

Inaugural-Dissertation  
zur Erlangung des Doktorgrades  
der Naturwissenschaften des Fachbereichs  
Mathematik und Informatik, Physik,  
Geographie  
der Justus-Liebig-Universität Gießen

**Electron-impact ionization  
of xenon and tin ions**

( Elektronenstoßionisation  
von Xenon- und Zinnionen )

vorgelegt von

**Alexander Borovik**  
aus Uzhgorod (Ukraine)

Gießen, 2010

Justus-Liebig-Universität Gießen  
Institut für Atom- und Molekülphysik

Dekan: Prof. Dr. C. Diller

1. Berichtstatter: Prof. Dr. A. Müller

2. Berichtstatter: Prof. Dr. S. Schippers

# Abstract

Electron-impact single- and multiple ionization cross sections of xenon and tin ions have been experimentally studied.

An animated crossed-beams method has been applied with the angle of 90 degrees between the beams. The ion beam was extracted from a 10 GHz Electron-Cyclotron-Resonance (ECR) ion source and mass-over-charge analysed using a dipole magnet. The electron beam was produced using a high-current electron gun. Space-charge limited electron currents were up to 450 mA at 1000 eV. Ion currents ranged from 0.1 to 200 nA. The reaction products were separated from the primary ion beam by another dipole magnet and registered by a single particle detector, whereas the primary ion beam was collected by a moveable Faraday cup.

Ionization cross sections have been measured for the energy regions from threshold up to 1000 eV. For  $\text{Xe}^{q+}$  ions single-ionization cross sections have been measured for all charge states  $q = 1, 2, 3, \dots, 25$ , double-ionization for  $q = 1, 2, 3, \dots, 17$ . Triple- and fourfold-ionization cross-sections have been obtained for charge states  $q = 1, 6, 7$ . For  $\text{Xe}^+$  cross sections for all final charge states  $q' = 2, 3, \dots, 10$  have been measured for multiple ionization processes  $q \rightarrow q'$ . For  $\text{Sn}^{q+}$  ions single-ionization cross sections for charge states 1 through 13 and double-ionization cross sections for charge states 1 through 12 have been obtained. The magnitude of the smallest measured cross section was of the order of  $10^{-24} \text{ cm}^2$  with error bars of about  $10^{-25} \text{ cm}^2$ . This is one order of magnitude smaller than the smallest ionization cross section ever measured using interacting beam techniques.

The obtained data reveal an important, sometimes dominant role of inner electron subshell ionization or excitation of ions giving rise to indirect ionization mechanisms, which can cause strong contributions to ionization cross sections.

In addition, in primary-ion beams fractions of ions in metastable states have been found. Excitation energies for some of them reach up to 850 eV and lifetimes were found to range at least from few to several tens of microseconds.



# Contents

<b>List of Figures</b>	<b>iii</b>
<b>List of Tables</b>	<b>vii</b>
<b>List of Abbreviations</b>	<b>ix</b>
<b>1 Introduction</b>	<b>1</b>
<b>2 Basics of electron-impact ionization of atomic ions</b>	<b>9</b>
2.1 Ionization mechanisms . . . . .	9
2.2 Theoretical Methods . . . . .	12
2.3 Semiempirical predictor formulae . . . . .	15
<b>3 Experimental Setup</b>	<b>17</b>
3.1 Production of xenon and tin ions in the ECR ion source . . . . .	20
3.2 Background . . . . .	22
3.3 Electron-current correction function . . . . .	24
3.4 Calibration of the energy scale . . . . .	24
3.5 Single-particle detection of product ions . . . . .	26
<b>4 Experimental Results</b>	<b>29</b>
4.1 Single ionization of xenon ions . . . . .	29
4.1.1 Overview . . . . .	29
4.1.2 Role of excited metastable states . . . . .	32
4.1.3 Comparison with previous experimental data . . . . .	39
4.1.4 Comparison with previous theoretical data . . . . .	43
4.2 Multiple ionization of xenon ions . . . . .	56
4.2.1 Double ionization of $\text{Xe}^{q+}$ ions ( $q = 1, 2, \dots, 17$ ) . . . . .	56
4.2.2 Multiple ionization of $\text{Xe}^+$ ions . . . . .	58
4.2.3 Multiple ionization of $\text{Xe}^{6+}$ and $\text{Xe}^{7+}$ ions . . . . .	58
4.2.4 Role of excited metastable states . . . . .	61
4.2.5 Comparison with previous experimental data . . . . .	61
4.3 Single ionization of tin ions . . . . .	68
4.3.1 Overview . . . . .	68

---

4.3.2	Role of excited metastable states . . . . .	70
4.4	Multiple ionization of tin ions . . . . .	72
4.4.1	Overview . . . . .	72
4.5	Recommendations for plasma physics . . . . .	74
<b>5</b>	<b>Conclusions and outlook</b>	<b>77</b>
	<b>Bibliography</b>	<b>79</b>
<b>A</b>	<b>Experimental details on the absolute cross-section measurements</b>	<b>87</b>
A.1	Properties of the primary ion target beam used in the experiments .	87
A.2	Electron-current correction functions . . . . .	89
<b>B</b>	<b>Details on the ionization of xenon ions</b>	<b>91</b>
B.1	Single ionization . . . . .	92
B.2	Double ionization . . . . .	105
B.3	Triple ionization . . . . .	114
B.4	Fourfold ionization . . . . .	116
B.5	Fivefold and higher multiple ionization . . . . .	118
<b>C</b>	<b>Details on the ionization of tin ions</b>	<b>121</b>
C.1	Single ionization . . . . .	122
C.2	Double ionization . . . . .	129
<b>D</b>	<b>Tabulated absolute values of the present cross sections</b>	<b>135</b>
<b>E</b>	<b>Calculated lifetimes of excited states</b>	<b>171</b>
<b>F</b>	<b>Ionization energies</b>	<b>187</b>
	<b>Acknowledgements</b>	<b>191</b>

# List of Figures

2.1	Direct Ionization . . . . .	9
2.2	Excitation-autoionization . . . . .	10
2.3	Ionization-autoionization . . . . .	11
2.4	REDA and READI . . . . .	12
3.1	Experimental setup . . . . .	18
3.2	Electron gun . . . . .	19
3.3	Observed mass spectrum of $\text{Xe}^{q+}$ ions ( $q = 13, 14, \dots, 21$ ) . . . . .	21
3.4	Observed mass spectrum of highly charged $\text{Xe}^{q+}$ ions ( $q \geq 21$ ) . . . . .	21
3.5	Schematic view of the oven for evaporating metallic tin . . . . .	22
3.6	Oven for evaporating metallic tin . . . . .	23
3.7	Product-ion detector . . . . .	27
3.8	Multipulsing . . . . .	27
4.1	Overview over the present single-ionization cross sections of $\text{Xe}^{q+}$ ions ( $q = 1, 2, \dots, 25$ ). . . . .	31
4.2	Single ionization of $\text{Xe}^{23+}$ , $\text{Xe}^{24+}$ and $\text{Xe}^{25+}$ . . . . .	34
4.3	Direct and indirect ionization processes of metastable $\text{Xe}^{7+}$ ions. . . . .	36
4.4	Single ionization of $\text{Xe}^{7+}$ . Below-threshold energy region. . . . .	37
4.5	Example of the distinguishing of the metastable component present in the experiment (single ionization of $\text{Xe}^{9+}$ ). . . . .	38
4.6	Single ionization of $\text{Xe}^{+}$ . Comparison with previous experimental data. . . . .	40
4.7	Single ionization of $\text{Xe}^{2+}$ . Comparison with previous experimental data. . . . .	41
4.8	Single ionization of $\text{Xe}^{3+}$ . Comparison with previous experimental data. . . . .	42
4.9	Single ionization of $\text{Xe}^{4+}$ . Comparison with previous experimental data. . . . .	43
4.10	Single ionization of $\text{Xe}^{5+}$ . Comparison with previous experimental data. . . . .	44
4.11	Single ionization of $\text{Xe}^{6+}$ . Comparison with previous experimental data. . . . .	44
4.12	Single ionization of $\text{Xe}^{8+}$ . Comparison with previous experimental data. . . . .	45

---

4.13	Single ionization of $\text{Xe}^{9+}$ . Comparison with previous experimental data. . . . .	46
4.14	Single ionization of $\text{Xe}^{10+}$ . Comparison with previous experimental data. . . . .	46
4.15	Single ionization of $\text{Xe}^+$ . Comparison with theoretical data. . . .	47
4.16	Single ionization of $\text{Xe}^{2+}$ . Comparison with theoretical data. . . .	47
4.17	Single ionization of $\text{Xe}^{3+}$ . Comparison with theoretical data. . . .	48
4.18	Single ionization of $\text{Xe}^{4+}$ . Comparison with theoretical data. . . .	49
4.19	Single ionization of $\text{Xe}^{5+}$ . Comparison with theoretical data. . . .	49
4.20	Single ionization of $\text{Xe}^{6+}$ . Comparison with theoretical data. . . .	51
4.21	Single ionization of $\text{Xe}^{8+}$ . Comparison with theoretical data. . . .	52
4.22	Single ionization of $\text{Xe}^{22+}$ . Comparison with theoretical data. . . .	54
4.23	Single ionization of $\text{Xe}^{23+}$ . Comparison with theoretical data. . . .	54
4.24	Single ionization of $\text{Xe}^{24+}$ . Comparison with theoretical data. . . .	55
4.25	Single ionization of $\text{Xe}^{25+}$ . Comparison with theoretical data. . . .	55
4.26	Overview over the present double-ionization cross sections of $\text{Xe}^{q+}$ ions ( $q = 1, 2, \dots, 17$ ). . . . .	57
4.27	Overview over the present multiple-ionization cross sections of $\text{Xe}^+$ ions. . . . .	59
4.28	Overview over the present multiple-ionization cross sections of $\text{Xe}^{6+}$ ions. . . . .	60
4.29	Overview over the present multiple-ionization cross sections of $\text{Xe}^{7+}$ ions. . . . .	60
4.30	Double ionization of $\text{Xe}^+$ . Comparison with previous experimental data. . . . .	63
4.31	Double ionization of $\text{Xe}^{2+}$ . Comparison with previous experimental data. . . . .	63
4.32	Double ionization of $\text{Xe}^{3+}$ . Comparison with previous experimental data. . . . .	64
4.33	Double ionization of $\text{Xe}^{4+}$ . Comparison with previous experimental data. . . . .	64
4.34	Double ionization of $\text{Xe}^{6+}$ . Comparison with previous experimental data. . . . .	65
4.35	Double ionization of $\text{Xe}^{8+}$ . Comparison with previous experimental data. . . . .	65
4.36	Double ionization of $\text{Xe}^{10+}$ . Comparison with previous experimental data. . . . .	66
4.37	Triple ionization of $\text{Xe}^+$ . Comparison with previous experimental data. . . . .	66
4.38	Triple ionization of $\text{Xe}^{6+}$ . Comparison with previous experimental data. . . . .	67
4.39	Fourfold ionization of $\text{Xe}^+$ . Comparison with previous experimental data. . . . .	67

---

4.40	Overview over the present single-ionization cross sections of $\text{Sn}^{q+}$ ions ( $q = 1, 2, \dots, 13$ ). . . . .	69
4.41	Single ionization of $\text{Sn}^{3+}$ . Below-threshold energy region. . . . .	70
4.42	Overview over the present double-ionization cross sections of $\text{Sn}^{q+}$ ions ( $q = 1, 2, \dots, 12$ ). . . . .	73
B.1	Single ionization of $\text{Xe}^+$ . . . . .	92
B.2	Single ionization of $\text{Xe}^{2+}$ . . . . .	92
B.3	Single ionization of $\text{Xe}^{3+}$ . . . . .	93
B.4	Single ionization of $\text{Xe}^{4+}$ . . . . .	93
B.5	Single ionization of $\text{Xe}^{5+}$ . . . . .	94
B.6	Single ionization of $\text{Xe}^{6+}$ . . . . .	94
B.7	Single ionization of $\text{Xe}^{7+}$ . . . . .	95
B.8	Single ionization of $\text{Xe}^{8+}$ . . . . .	95
B.9	Single ionization of $\text{Xe}^{9+}$ . . . . .	96
B.10	Single ionization of $\text{Xe}^{10+}$ . . . . .	96
B.11	Single ionization of $\text{Xe}^{11+}$ . . . . .	97
B.12	Single ionization of $\text{Xe}^{12+}$ . . . . .	97
B.13	Single ionization of $\text{Xe}^{13+}$ . . . . .	98
B.14	Single ionization of $\text{Xe}^{14+}$ . . . . .	98
B.15	Single ionization of $\text{Xe}^{15+}$ . . . . .	99
B.16	Single ionization of $\text{Xe}^{16+}$ . . . . .	99
B.17	Single ionization of $\text{Xe}^{17+}$ . . . . .	100
B.18	Single ionization of $\text{Xe}^{18+}$ . . . . .	100
B.19	Single ionization of $\text{Xe}^{19+}$ . . . . .	101
B.20	Single ionization of $\text{Xe}^{20+}$ . . . . .	101
B.21	Single ionization of $\text{Xe}^{21+}$ . . . . .	102
B.22	Single ionization of $\text{Xe}^{22+}$ . . . . .	102
B.23	Single ionization of $\text{Xe}^{23+}$ . . . . .	103
B.24	Single ionization of $\text{Xe}^{24+}$ . . . . .	103
B.25	Single ionization of $\text{Xe}^{25+}$ . . . . .	104
B.26	Double ionization of $\text{Xe}^+$ . . . . .	105
B.27	Double ionization of $\text{Xe}^{2+}$ . . . . .	105
B.28	Double ionization of $\text{Xe}^{3+}$ . . . . .	106
B.29	Double ionization of $\text{Xe}^{4+}$ . . . . .	106
B.30	Double ionization of $\text{Xe}^{5+}$ . . . . .	107
B.31	Double ionization of $\text{Xe}^{6+}$ . . . . .	107
B.32	Double ionization of $\text{Xe}^{7+}$ . . . . .	108
B.33	Double ionization of $\text{Xe}^{8+}$ . . . . .	108
B.34	Double ionization of $\text{Xe}^{9+}$ . . . . .	109
B.35	Double ionization of $\text{Xe}^{10+}$ . . . . .	109
B.36	Double ionization of $\text{Xe}^{11+}$ . . . . .	110
B.37	Double ionization of $\text{Xe}^{12+}$ . . . . .	110
B.38	Double ionization of $\text{Xe}^{13+}$ . . . . .	111

---

B.39	Double ionization of $\text{Xe}^{14+}$	111
B.40	Double ionization of $\text{Xe}^{15+}$	112
B.41	Double ionization of $\text{Xe}^{16+}$	112
B.42	Double ionization of $\text{Xe}^{17+}$	113
B.43	Triple ionization of $\text{Xe}^+$	114
B.44	Triple ionization of $\text{Xe}^{6+}$	114
B.45	Triple ionization of $\text{Xe}^{7+}$	115
B.46	Fourfold ionization of $\text{Xe}^+$	116
B.47	Fourfold ionization of $\text{Xe}^{6+}$	116
B.48	Fourfold ionization of $\text{Xe}^{7+}$	117
B.49	Fivefold ionization of $\text{Xe}^+$	118
B.50	Sixfold ionization of $\text{Xe}^+$	118
B.51	Sevenfold ionization of $\text{Xe}^+$	119
B.52	Eightfold ionization of $\text{Xe}^+$	119
B.53	Ninefold ionization of $\text{Xe}^+$	120
C.1	Single ionization of $\text{Sn}^+$	122
C.2	Single ionization of $\text{Sn}^{2+}$	122
C.3	Single ionization of $\text{Sn}^{3+}$	123
C.4	Single ionization of $\text{Sn}^{4+}$	123
C.5	Single ionization of $\text{Sn}^{5+}$	124
C.6	Single ionization of $\text{Sn}^{6+}$	124
C.7	Single ionization of $\text{Sn}^{7+}$	125
C.8	Single ionization of $\text{Sn}^{8+}$	125
C.9	Single ionization of $\text{Sn}^{9+}$	126
C.10	Single ionization of $\text{Sn}^{10+}$	126
C.11	Single ionization of $\text{Sn}^{11+}$	127
C.12	Single ionization of $\text{Sn}^{12+}$	127
C.13	Single ionization of $\text{Sn}^{13+}$	128
C.14	Double ionization of $\text{Sn}^+$	129
C.15	Double ionization of $\text{Sn}^{2+}$	129
C.16	Double ionization of $\text{Sn}^{3+}$	130
C.17	Double ionization of $\text{Sn}^{4+}$	130
C.18	Double ionization of $\text{Sn}^{5+}$	131
C.19	Double ionization of $\text{Sn}^{6+}$	131
C.20	Double ionization of $\text{Sn}^{7+}$	132
C.21	Double ionization of $\text{Sn}^{8+}$	132
C.22	Double ionization of $\text{Sn}^{9+}$	133
C.23	Double ionization of $\text{Sn}^{10+}$	133
C.24	Double ionization of $\text{Sn}^{11+}$	134
C.25	Double ionization of $\text{Sn}^{12+}$	134

# List of Tables

1.1	List of published data on electron-impact ionization of xenon atom and ions . . . . .	3
1.2	List of published data on electron-impact ionization of tin ions . . . . .	7
3.1	Energy scale calibration . . . . .	25
3.2	Systematic uncertainties . . . . .	28
4.1	Groups of the single-ionization cross sections of $Xe^{q+}$ ions. . . . .	30
4.2	Information on the metastable components in the primary $Xe^{q+}$ ion beams. . . . .	39
4.3	Information on the metastable components in the primary $Sn^{q+}$ ion beams. . . . .	71
A.1	Experimental ion current conditions for xenon ions . . . . .	87
A.2	Experimental ion current conditions for tin ions . . . . .	89
A.3	Electron-current correction functions . . . . .	90
D.1	Absolute cross-section values of electron-impact single ionization of xenon ions . . . . .	135
D.2	Absolute cross-section values of electron-impact double ionization of xenon ions . . . . .	147
D.3	Absolute cross-section values of electron-impact triple ionization of xenon ions . . . . .	153
D.4	Absolute cross-section values of electron-impact fourfold ionization of xenon ions . . . . .	155
D.5	Absolute cross-section values of electron-impact fivefold ionization of xenon ions . . . . .	156
D.6	Absolute cross-section values of electron-impact sixfold ionization of xenon ions . . . . .	156
D.7	Absolute cross-section values of electron-impact sevenfold ionization of xenon ions . . . . .	157
D.8	Absolute cross-section values of electron-impact eightfold ionization of xenon ions . . . . .	157
D.9	Absolute cross-section values of electron-impact ninefold ionization of xenon ions . . . . .	157

---

D.10	Absolute cross-section values of electron-impact single ionization of tin ions . . . . .	158
D.11	Absolute cross-section values of electron-impact double ionization of tin ions . . . . .	165
E.1	Calculated lifetimes of excited states of the studied $Xe^{q+}$ ions. . .	171
E.2	Calculated lifetimes of excited states of the studied $Sn^{q+}$ ions. . .	180
F.1	Threshold energies for ground-state single ionization of the studied $Xe^{q+}$ ions. . . . .	187
F.2	Threshold energies for ground-state double ionization of the studied $Xe^{q+}$ ions. . . . .	188
F.3	Threshold energies for ground-state triple ionization of the studied $Xe^{q+}$ ions. . . . .	188
F.4	Threshold energies for ground-state fourfold ionization of the studied $Xe^{q+}$ ions. . . . .	188
F.5	Threshold energies for ground-state multiple-ionization of $Xe^+$ ion.	189
F.6	Threshold energies for ground-state single ionization of the studied $Sn^{q+}$ ions. . . . .	189
F.7	Threshold energies for ground-state double ionization of the studied $Sn^{q+}$ ions. . . . .	189

## List of Abbreviations

DI .....	direct ionization
EA .....	excitation-autoionization
EDA .....	excitation-double-autoionization
REDA .....	resonant-excitation-double-autoionization
READI .....	resonant-excitation-auto-double-ionization
RETA .....	resonant-excitation-triple-autoionization
IA .....	ionization-autoionization
EUV .....	extreme ultra violet
PBWA .....	plane-wave Born approximation
CBA .....	coulomb Born approximation
DWBA .....	distorted-wave Born approximation
CS .....	cross section
ECCF .....	electron current correction function
RF .....	radio frequency
CEM .....	channel electron multiplier



# 1 Introduction

Electron-impact ionization is a fundamental process in atomic physics. It results in the release of one or more electrons from an atomic system by collision with an incident electron. Applications where electron-impact ionization plays an important role range from ion source, accelerator and plasma physics to planetary and stellar atmospheres and further on even to cancer irradiation therapy. The present thesis deals with electron-impact ionization of atomic ions, particularly of xenon and tin ions.

Xenon ions have been a topic of extensive research previously. However, new interest has been motivated by different applications. Xenon is envisaged as a coolant gas to be injected into the edge plasma of future tokamaks ([1] and references therein). Further, xenon admixtures in fusion plasmas serve to diagnose a variety of plasma properties including electron temperature and density, as well as ion temperature and impurity transport. In order to predict the effect of xenon injection on the performance of fusion plasmas accurate cross section data are needed.

Recent interest in applying EUV radiation to lithography has led to the construction of appropriate light sources. Xenon and tin ions produced under high-temperature plasma conditions emit strongly in the extreme ultraviolet spectral range and are established as suitable generators of 13.5 nm wavelength radiation for EUV lithography of the next generation of semiconductor nano-structured devices employed e.g., in computer chips [2, 3, 4]. In the effort to optimize for maximum radiation output detailed understanding of the origin of the radiation and the production of the radiating ions is necessary.

In another application accelerated xenon ions produced by electron impact ionization provide the propulsion of micro thrusters for modern space crafts and satellites [5].

For the purpose of plasma modeling, where huge amounts of data are needed, ionization cross section data are usually generated using theoretical codes. Lately, for few-electron systems, powerful theoretical approaches have been developed which can deliver data that are in a good agreement with experimental values [6]. In electron-impact ionization of two- and more-electron systems containing inner electron subshells there is a probability for the incident electron to interact with one or more inner electrons. This leads to indirect ionization mechanisms, which contribute to the total ionization cross section. For light elements, modern calculation already include some of those contributions and deliver reasonable results

[7, 8]. However, with an increasing number of electrons in the system the character of indirect mechanisms becomes more complex, and their contributions become significant, in some cases even dominant. This makes it enormously challenging to correctly include the whole variety of possible processes into the calculations and to predict the correct value of a cross section. Hence, only experiment is able to deliver reliable data on ionization of such complicated systems as xenon and tin ions.

From a fundamental point of view, with their many subshells at comparatively low binding energies xenon and tin ions offer rich opportunities to observe and study the complicated character of the processes of interaction of energetic electrons with complex atomic systems. This work is devoted to the study of electron-impact ionization of xenon and tin ions with the attention focused on mechanisms of indirect ionization and their contributions to the ionization cross sections.

The first experiments on electron-atom scattering were performed at the end of the 19th century by Lenard [9],[10]. The very first attempt to theoretically describe the electron-impact ionization process was made by Thomson in 1912 [11]. 18 years later Bethe published his first quantum-mechanical calculations [12]. First relevant measurements on absolute electron-impact ionization cross sections for ions were performed after the development of the crossed-beams method by Dolder *et al.* [13]. However, this method requires determination of the overlap between the two beams. This is a potential source of significant uncertainty. It was eliminated after the development of the animated-crossed-beams method by Defrance [14],[15] that considerably increased the measurement's accuracy and made the determination of absolute cross sections from the measurement more simple. Later on, the energy-scan method developed by Müller *et al.* [16] allowed for revealing fine structures in the energy dependence of the measured cross sections that correspond to indirect ionization processes [17].

Compilations of cross sections of electron-impact ionization have been published by Dere [18] and Mattioli *et al.* [19] for elements up to Zn and Ge respectively. A large collection of electron-impact ionization data for atoms and ions from hydrogen through uranium has been published by Tawara and Kato [20]. An overview on the electron and photon cross sections with xenon atoms and clusters until the year 2000 has been provided by Hayashi [21]. Systematic calculations of single-ionization cross sections for different isonuclear sequences including xenon ions have been performed by Povyshev *et al.* in 2001 [22] and more recently by Loch *et al.* [23]. The compilation of the energy levels and observed spectral lines of the xenon atom, in all stages of ionization for which experimental data are available, has been reported by Saloman [24].

A compilation of previous studies of electron-impact ionization cross sections of xenon and its ions is provided in Tab. 1.1. Apparently much attention has already been paid to the xenon isonuclear sequence. However, a systematic experimental study of single- and/or multiple ionization of xenon ions covering a significant number of xenon ion charge states has never been performed previously.

**Table 1.1:** List of published data on electron-impact ionization of xenon atom and ions. (I, II, ... correspond to single-, double-, ... ionization)

Target species	Ionization	Energy range (eV)	exp./theory	Reference
Xe	total	threshold - 100 eV	exp.	[25]
	total	threshold - 100 eV	exp.	[26]
	total	threshold - 1000 eV	exp.	[27]
	total	600 - 20000 eV	exp.	[28]
	total	100 - 600 eV	exp.	[29]
	I,II,...,XII	500 - 18000 eV	exp.	[30]
	I,II,...,V	2000 - 14000 eV	exp.	[31]
	total	11 - 10000 eV	theor.	[32]
	I,II,III	500 - 5000 eV	exp.	[33]
	I,II,III	threshold - 180 eV	exp.	[34]
	I,II,III	threshold - 100 eV	exp.	[35]
	I,II,III	threshold - 200 eV	exp.	[36]
	4 <i>d</i>	threshold - 560 eV	theor.	[37]
	I,II,...,V	threshold - 1000 eV	exp.	[38]
	I,II,...,V	threshold - 700 eV	exp.	[39]
	I,II,III	threshold - 200 eV	exp.	[40]
	I,II,...,VI	threshold - 470 eV	exp.	[41]
	I	threshold - 1000 eV	theor.	[42]
	I	threshold - 200 keV	theor.	[22]
	I,II,...,V	threshold - 1000 eV	exp.	[43]
	II,... VIII	100 - 2500 eV	exp.	[44]
	I	threshold - 3000 eV	theor.	[45]
	I	threshold - 100 eV	theor.	[46]
I	threshold - 500 eV	theor.	[47]	
I	threshold - 7000 eV	theor.	[23]	
Xe <sup>+</sup>	I	threshold - 830 eV	exp.	[48]
	II	threshold - 700 eV	exp.	[49]
	II	threshold - 165 eV	theor.	[50]
	I	threshold - 700 eV	exp.	[51]
	II,III,IV	threshold - 700 eV	exp.	[52]
	I	threshold - 110 eV	theor.	[53]
	I, 4 <i>d</i>	threshold - 160 eV	theor.	[54]
	4 <i>d</i>	threshold - 650 eV	theor.	[37]
	4 <i>d</i>	threshold - 810 eV	theor.	[55]
	I	threshold - 2000 eV	exp.	[56]
	II	threshold - 500 eV	theor.	[57]

Table 1.1(continued)

Target species	Ionization	Energy range (eV)	exp./theory	Reference
Xe <sup>2+</sup>	I	threshold - 100 eV	exp.	[58]
	I	threshold - 20000 eV	theor.	[59]
	I	threshold - 90 eV	exp.	[60]
	I	threshold - 200 eV	exp.	[61]
	I	threshold - 7000 eV	theor.	[23]
	II	threshold - 700 eV	exp.	[49]
	I	threshold - 700 eV	exp.	[51]
	I	threshold - 1000 eV	exp.	[62]
	I	threshold - 1500 eV	exp.	[53]
	I	threshold - 150 eV	theor.	[53]
	II,III,IV	threshold - 700 eV	exp.	[52]
	I, 4d	threshold - 185 eV	theor.	[54]
	I	threshold - 100 eV	exp.	[58]
	I	threshold - 20000 eV	theor.	[59]
	Xe <sup>3+</sup>	I	threshold - 1000 eV	exp.
I		threshold - 2000 eV	exp.	[64]
I		threshold - 200 keV	theor.	[22]
I		threshold - 7000 eV	theor.	[23]
II		threshold - 700 eV	exp.	[49]
I		threshold - 1500 eV	exp.	[65]
I		threshold - 700 eV	exp.	[51]
II,III		threshold - 700 eV	exp.	[52]
I, 4d		threshold - 200 eV	theor.	[54]
I		threshold - 150 eV	theor.	[53]
I		threshold - 105 eV	exp.	[58]
I		threshold - 20000 eV	theor.	[59]
I		threshold - 200 keV	theor.	[22]
I		70 - 90 eV	exp.	[66]
Xe <sup>4+</sup>		I	threshold - 7000 eV	theor.
	II	threshold - 700 eV	exp.	[49]
	I	threshold - 700 eV	exp.	[51]
	II	threshold - 700 eV	exp.	[52]
	II	threshold - 1500 eV	exp.	[54]
	I, 4d, 4p	threshold - 1500 eV	theor.	[54]
	I	threshold - 1500 eV	exp.	[53]
	I	threshold - 150 eV	theor.	[53]

**Table 1.1**(continued)

Target species	Ionization	Energy range (eV)	exp./ theory	Reference
Xe <sup>5+</sup>	I	threshold - 250 eV	exp.	[58]
	I	threshold - 20000 eV	theor.	[59]
	I	threshold - 200 keV	theor.	[22]
	I	threshold - 7000 eV	theor.	[23]
	I	threshold - 1200 eV	exp.	[53]
	I	threshold - 120 eV	theor.	[53]
	I	threshold - 200 eV	exp.	[58]
Xe <sup>6+</sup>	I	threshold - 20000 eV	theor.	[59]
	I	threshold - 200 keV	theor.	[22]
	I	threshold - 7000 eV	theor.	[23]
	I	threshold - 1500 eV	exp.	[67]
	I	threshold - 150 eV	theor.	[68]
	I	threshold - 125 eV	theor.	[53]
	II	threshold - 990 eV	exp.	[69]
Xe <sup>7+</sup>	III	threshold - 1500 eV	exp.	[69]
	I	threshold - 520 eV	exp.	[58]
	I	threshold - 20000 eV	theor.	[59]
	I	threshold - 200 keV	theor.	[22]
	I	threshold - 7000 eV	theor.	[23]
	I	threshold - 200 keV	theor.	[22]
	I	threshold - 7000 eV	theor.	[23]
Xe <sup>8+</sup>	I	threshold - 910 eV	theor.	[70]
	I	threshold - 1500 eV	exp.	[71]
	II	threshold - 1500 eV	exp.	[72]
	I,II	threshold - 1000 eV	exp.	[73]
	I	600 - 4000 eV	exp.	[74]
	II	threshold - 4800 eV	exp.	[74]
	III	600 - 4800 eV	exp.	[74]
Xe <sup>9+</sup>	IV	1000 - 4800 eV	exp.	Hofmann <i>et al.</i> (unpublished)
	I	threshold - 6500 eV	exp.	[75]
	I	threshold - 200 keV	theor.	[22]
	I	threshold - 7000 eV	theor.	[23]
	I	450 - 4800 eV	exp.	[74]
	III	600 - 4800 eV	exp.	[74]

**Table 1.1**(continued)

Target species	Ionization	Energy range (eV)	exp./theory	Reference
Xe <sup>10+</sup>	I	threshold - 200 keV	theor.	[22]
	I	threshold - 7000 eV	theor.	[23]
	I	threshold - 1000 eV	theor.	Ludlow <i>et al.</i> (priv. comm.)
	I	700 - 4800 eV	exp.	[74]
	II	800 - 4800 eV	exp.	Hofmann <i>et al.</i> (unpublished)
	III	800 - 4800 eV	exp.	[74]
	I	threshold - 200 keV	theor.	[22]
	I	threshold - 1000 eV	exp.	Brandau <i>et al.</i> (unpublished)
Xe <sup>11+</sup> , ..., Xe <sup>15+</sup>	I	threshold - 7000 eV	theor.	[23]
	I	threshold - 1000 eV	theor.	Ludlow <i>et al.</i> (priv. comm.)
	I	threshold - 200 keV	theor.	[22]
	I	threshold - 7000 eV	theor.	[23]
Xe <sup>16+</sup> , ..., Xe <sup>21+</sup>	I	threshold - 1000 eV	theor.	Ludlow <i>et al.</i> (priv. comm.)
	I	threshold - 200 keV	theor.	[22]
	I	threshold - 7000 eV	theor.	[23]
Xe <sup>22+</sup>	I	threshold - 200 keV	theor.	[22]
	I	threshold - 1500 eV	theor.	[76]
	I	threshold - 7000 eV	theor.	[23]
Xe <sup>23+</sup>	I	threshold - 200 keV	theor.	[22]
	I	threshold - 1400 eV	theor.	[77]
	I	threshold - 7000 eV	theor.	[23]
Xe <sup>24+</sup>	I	threshold - 200 keV	theor.	[22]
	I	threshold - 1500 eV	theor.	[78]
	I	threshold - 7000 eV	theor.	[23]
	I	threshold - 3000 eV	theor.	[79]
Xe <sup>25+</sup>	I	threshold - 200 keV	theor.	[22]
	I	threshold - 1500 eV	theor.	[80]
	I	threshold - 7000 eV	theor.	[23]
Xe <sup>26+</sup> , ..., Xe <sup>53+</sup>	I	threshold - 200 keV	theor.	[22]
	I	threshold - 7000 eV	theor.	[23]

Reviewing data on ionization cross sections of tin ions we have found that only little attention has been given to this isonuclear sequence. Only the ionization of neutral tin and  $\text{Sn}^{4+}$  ions has been studied experimentally. However, ionization of the whole tin isonuclear sequence has been studied theoretically. The entire literature is summarized in Tab. 1.2.

**Table 1.2:** List of published data on electron-impact ionization of tin ions. The notation is the same as in Tab. 1.1

Target species	Ionization	Energy range (eV)	exp./ theory	Reference
Sn	I,II,III	threshold - 200 eV	exp.	[40]
	I	threshold - 200 keV	theor.	[81]
	I	threshold - 7000 eV	theor.	[23]
$\text{Sn}^+$	4d	threshold - 420 eV	theor.	[55]
	I	threshold - 200 keV	theor.	[81]
	I	threshold - 7000 eV	theor.	[23]
$\text{Sn}^{2+}, \text{Sn}^{3+}$	I	threshold - 200 keV	theor.	[81]
	I	threshold - 7000 eV	theor.	[23]
$\text{Sn}^{4+}$	4d	threshold - 780 eV	theor.	[70]
	I	threshold - 900 eV	exp.	[58]
	II	threshold - 1000 eV	exp.	[58]
	I	threshold - 200 keV	theor.	[81]
	I	threshold - 7000 eV	theor.	[23]
$\text{Sn}^{5+}, \dots, \text{Sn}^{49+}$	I	threshold - 200 keV	theor.	[81]
	I	threshold - 7000 eV	theor.	[23]

In the current work we present systematic experimental studies of electron-impact single- and multiple ionization cross sections of xenon and tin ions performed at the Institute of Atomic and Molecular Physics of the Justus-Liebig University Giessen. The next chapter follows with a detailed description of the experimental setup and the experimental methods and discusses sources and magnitudes of errors. Chapter 4 contains the present results, their comparison with available literature data as well as their discussion. Chapter 5 presents conclusions and outlook. In the Appendix A experimental details are provided. Appendix B shows all cross sections measured with xenon ions as a function of energy. Appendix C shows all cross sections measured with tin ions as a function of energy. In the Appendix D all absolute cross-section values are provided. Finally, Appendix E provides information on long-lived excited states of the investigated ion species.

In Appendix F, ground-state ionization potentials of the investigated  $\text{Xe}^{q+}$  and  $\text{Sn}^{q+}$  ions are provided.

## 2 Basics on electron-impact ionization of atomic ions

When an electron scatters off an atomic ion the following reactions are possible:

- elastic or inelastic collision without change of ion charge
- recombination, whereby the ion charge state decreases by one
- further ionization, whereby the ion charge state is increased

The present work deals with ionization processes. Detailed overviews of electron-ion interaction mechanisms, intermediate processes, experimental access to data and the theoretical methods have been given by Müller [82, 83].

### 2.1 Ionization mechanisms

The simplest ionization process - *direct ionization* (DI) is sketched in Fig. 2.1 and expressed with equation (2.1):

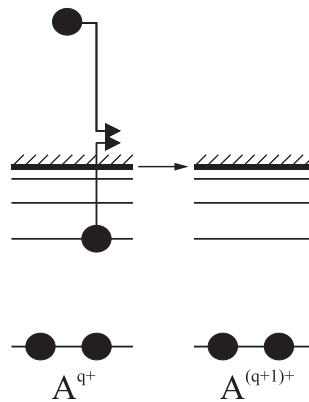
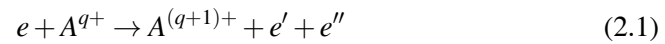


**Figure 2.1:** Direct ionization (DI).

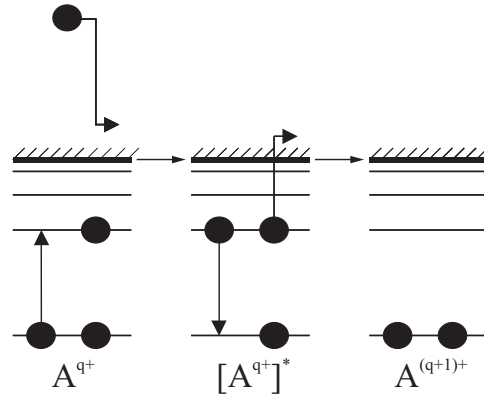
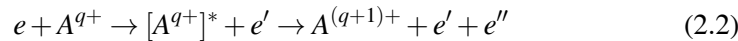


**Figure 2.2:** Excitation-autoionization process (EA).

The incident electron interacts inelastically with one of the target electrons and knocks it out of the ion. The transferred energy must be at least as high as the binding energy of the target electron. If the incident electron energy is sufficiently high, two or more electrons may be removed, which leads to double or multifold ionization, respectively.

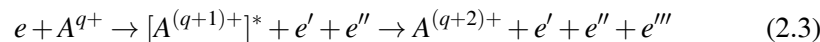
Possible are also processes, where excitation or ionization of a core electron results in the formation of an intermediate highly excited state which subsequently decays by autoionization. Such processes are called *indirect*. They can be *resonant* and *non-resonant*.

One non-resonant process is the two-step *excitation-autoionization* process (EA). Here, the incident electron excites one of the inner-shell target electrons to an intermediate autoionizing state. This state decays by the Auger-process resulting in net single ionization (Fig. 2.2, eq. 2.2):



If the excitation energy is sufficiently high, a cascade of Auger-processes may occur contributing to net multiple ionization.

If the incident electron ionizes an inner-shell electron creating a "hole" which can be "filled" by one of the outer-shell electrons after one or more subsequent Auger-processes (Fig. 2.3 eq. 2.3), such mechanism is called *ionization-autoionization* (IA). It leads to multiple ionization:



At certain incident-electron energies different kinds of *resonant* processes are possible. The starting point here is the capture of the incident electron by the target ion in a radiationless way with simultaneous excitation of an inner-shell electron, i.e., a *dielectronic capture* process. This, however, can only occur when the energy

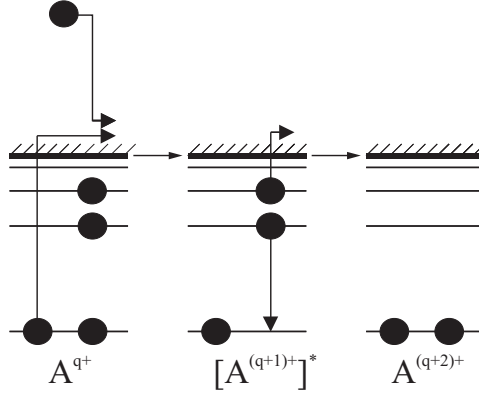


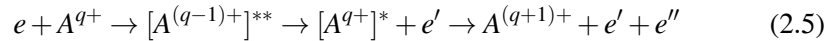
**Figure 2.3:** Ionization-autoionization (IA).

of the incident electron matches the resonance condition

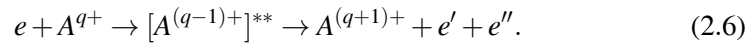
$$E_{res} = E(j) - E(i), \quad (2.4)$$

where  $E(j)$  and  $E(i)$  are the total binding energies of all electrons in the excited ion and the parent ion, respectively.

For net single ionization, an excited (in this sense intermediate) state must be available having sufficiently high energy for being able to emit two electrons. There are two possible decay mechanisms involving such intermediate states as shown in Fig. 2.4. The upper process is called *resonant-excitation-double-autoionization* (REDA) and results in net single ionization through two subsequent Auger processes (eq. 2.5). The existence of this process has been postulated by Lagattuta and Hahn [84] and has experimentally been demonstrated by Müller *et al.* [17].



In the lower process in Fig. 2.4 the  $A^{(q+1)+}$  ion charge state is reached with two electrons emitted at the same time. This ionization process is called *resonant-excitation-auto-double-ionization* (READI). It has been postulated by Henry and Msezane [85] and has been experimentally demonstrated by Müller *et al.* [86]. It can be described as



Whenever REDA is energetically allowed, READI can also occur, although the probability for the READI process is generally much smaller than for the REDA processes. These two processes cannot be experimentally distinguished without spectroscopy of the outgoing electrons, but REDA cannot occur if there is no suitable intermediate state in the parent target ion. Hence, READI may become the only possible resonant contribution to net ionization at sufficiently low incident

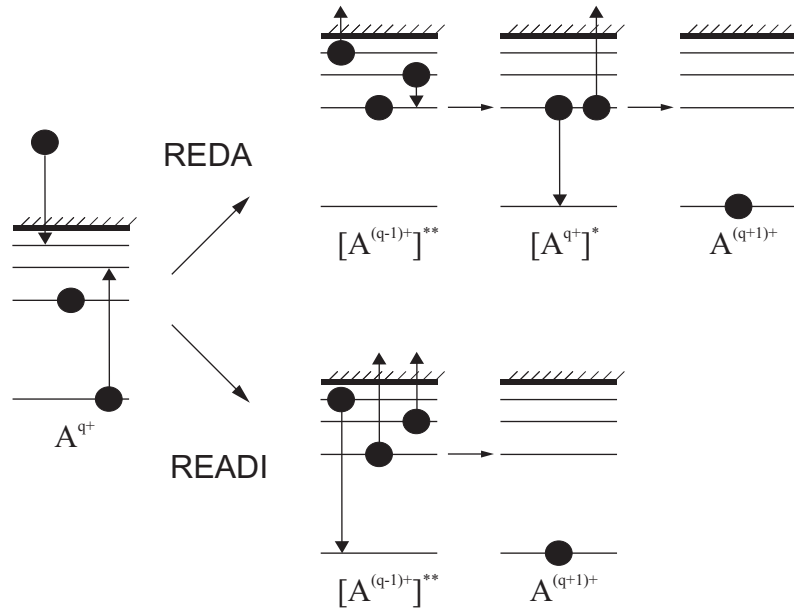


**Figure 2.4:** Resonant-excitation-double-autoionization (REDA) and resonant-excitation-auto-double-ionization (READI).

electron energies and resonances found in that energy range can be unambiguously identified with the READI mechanism.

If the excitation energy of the intermediate state after dielectronic capture is sufficiently high, net multiple ionization of the target ion can occur, as it was experimentally seen e.g. by Müller *et al.* [17] and Tinschert [58].

The energy that is gained by capture of the incident electron can also be released by emission of a photon, such that the  $q - 1$  charge state is stabilized. This process is called *dielectronic recombination*. It is not considered within the present work.

A variety of combinations of the processes described above is possible for net multiple ionization. Due to their huge number they are not individually described at this point, but they will be explained if necessary in the further sections.

Multiply excited states can generally also decay by emission of photon. This is particularly important for highly charged ions. In the theoretical treatment of resonant ionization mechanisms this effect is called *radiative damping*. It reduces the strength of the ionization resonances.

## 2.2 Theoretical Methods

The theoretical description of electron-impact ionization of ions is a complicated task because of the inherent three-body nature of the process. In the final state there are three free charged particles interacting via long range Coulomb forces. As we

know, there is no analytical solution for the three-body problem. Additionally, the theoretical description can be complicated due to the presence of the core electrons as well as due to the rich variety of different possible ionizations mechanisms. Therefore, theoretical investigations concentrate mainly on the development of approximation methods.

Thomson was the first who described electron-impact ionization in classical terms [11]. He considered electrons of the target as free and assumed that if the energy transferred by the incident particle exceeds the ionization potential, the ionization process will occur with 100% probability. However, the results obtained using this model were only qualitative. The simplicity of the model and the neglect of all quantum effects of the target resulted in significant deviations of the calculated cross sections from the experimental values both in low- and high-energy regions.

First quantum-mechanical models using perturbation methods have been developed by employing the Born-approximation. Unfortunately, the results possess good accuracy only in the region of high energies  $E_e \geq 20 \cdot E_i$  and they are restricted to direct single ionization. In the non-relativistic case, the starting point is the Schrödinger equation for the system of  $(N + 1)$  electrons for the scattering problem:

$$H(Z, N + 1)\Psi = i\hbar \frac{\partial}{\partial t} \Psi, \quad (2.7)$$

where  $N$  denotes the number of electrons and  $Z$  is the nuclear charge number. The Hamilton operator in equation (2.7) consists of three terms:

$$H = H_I + H_e + H_{int}. \quad (2.8)$$

where  $H_I$  is the Hamilton operator for the unperturbed ion,  $H_e$  is the Hamilton operator for the incident free electron, and  $H_{int}$  the Hamilton operator for interaction. There are different methods for dividing the Hamilton operator into an unperturbed part  $H_0$  and a perturbation  $H_{int}$ .

- In 1930 Bethe used the *Plane-Wave Born Approximation* (PWBA) which neglects the influence of the core electrons on the incident electron [12]. The unperturbed Hamiltonian included the sum of  $H_I + H_e$  and the perturbation  $H_{int}$  accounted for the electron-electron and electron-nucleus interactions. This approach works in the high-energy region  $E_e > 30 \cdot E_i$ .
- Within the *Coulomb Born Approximation* (CBA) the Coulomb interaction of the incident electron interaction with the nucleus is included in the unperturbed Hamiltonian, and the perturbation consists of the interaction of the incident electron with bound core electrons. This approach works well for highly charged ions and results in much better agreement with experimental data than the previous one.

- The *Distorted-wave Born Approximation* (DWBA) is an extension of the CBA. It replaces a constant screening charge by a screening function that changes during the collision. In practice, a potential  $V_{DW}$  has to be considered which describes the interaction of the incident electron with the spherically averaged potential of the core electrons.

The basic numerical method for the determination of DWBA cross sections is to expand the continuum waves into partial waves. At low incident-electron energies the number of contributing waves is rather limited, but with increasing electron energy an increasing number of partial waves has to be included in the calculation, making the computational efforts enormous. In comparison with the CBA and PWBA approaches, the DWBA provides much better agreement with experimental data also at low energies especially if additionally the exchange interaction is included (*Distorted wave Born exchange approximation*).

- In case of many-electron systems each configuration can split into many angular-momentum components, which highly increases the computational efforts for the state-selective calculation. With the aim to decrease the computational efforts a *Configuration-Average-Distorted-Wave* method (CADW) was developed. Here, the calculation averages over the multiplett-splittings, and cross sections are obtained for the given configuration only [50], [87]. In recent years, the method has been used to calculate electron-impact single ionization cross sections for the isonuclear sequences of several elements including Sn, Xe, W etc. [79] (and references therein).

An alternative to the above listed perturbative approaches is the *Close Coupling* method. This approach works very well for slow collisions, particularly for the detailed study of threshold behavior and resonances. Within this method the incident electron is treated on the same footing as the bound electrons. The difficulty, yet, is that there is an infinite number of states for the free electrons in the continuum. This, however, can be eliminated by treating the continuum via introduction of pseudostates or approximating it using appropriate functions.

A specific close coupling approach is the R-matrix theory. In 1971, Burke for the first time applied it to electron-ion collisions. The R-matrix method separates the interaction volume into two regions. In the inner (spherical) region the full quantum-mechanical problem is solved including exchange and correlation effects between target- and scattered electrons. In the outer region both the target and the incident electron move in a weak long-range multipole potential. This reduces the full many-body problem to the two-body problem, which is much more simple to solve. Finally, partial solutions for both inner- and outer regions are matched to each other. General R-matrix calculation methods for all possible processes including DI, EA, REDA and READI have been proposed by Berrington [88]. The result of successful application has been presented by Teng *et al.* [7]. A detailed description of the different facets of the R-matrix method in a general framework

was recently presented in [89].

## 2.3 Semiempirical predictor formulae

The theoretical approximation methods described above sometimes lead to huge computational efforts and, hence, are not suitable for quick cross section estimations. Therefore, it is much more convenient to use simpler empirical or scaling formulae based on theoretical and experimental findings. A general overview over such methods has been provided by Younger [90].

One of the most successful formulae for electron-impact single ionization is that of Lotz [91], [92]. Here, it is assumed that the ionization cross section below the cross section maximum follows the classical Thomson theory and the quantum-mechanical Bethe theory at high energies. The Lotz formula is:

$$\sigma = \sum_{i=1}^N a_i n_i \frac{\ln(E_e/E_i)}{E_e E_i} \{1 - b_i \exp[-c_i(E_e/E_i - 1)]\}, \quad (2.9)$$

where  $E_e \geq E_i$  is the incident electron energy,  $E_i$  is the ionization potential of subshell number  $i$ , and  $n_i$  is the number of equivalent electrons in this subshell. The parameters  $a_i$ ,  $b_i$  and  $c_i$  are the free parameters to be adjusted to best reproduce experimental and theoretical cross section data. These parameters are tabulated for a variety of atoms and ions [93],[94]. For ions with charge  $q = (Z - N) \geq 4$ , the numbers  $a_i = 4.5 \cdot 10^{-14}$ ,  $b_i = c_i = 0$  are recommended. In this case eq. 2.9 becomes the one-parameter Lotz formula. But in any form the Lotz formula can only describe cross sections for direct removal of a single electron from a given subshell within an uncertainty of  $\pm 40\%$  in cases where tabulated values for the parameters  $a_i$ ,  $b_i$  and  $c_i$  are available. Already the summation over different subshells has to be performed with care: autoionizing intermediate states resulting from inner-shell ionization can decay by the emission of electrons. An Auger process subsequent to inner-shell ionization contributes to net double ionization and should not appear in the sum described by eq. 2.9 for single ionization.

Unfortunately there is no general method for the treatment of multiple ionization of ions. However, there are several semiempirical and semiclassical approaches such as, e.g., the binary encounter approach by Gryziński [95]. For double ionization, it considers two possibilities for the removal of two electrons. The incident electron may hit a target electron which is ejected and then the projectile electron, although now having reduced energy, has a certain probability of knocking a second electron off the same ion. It is also possible that the first ejected electron hits a second target electron which also becomes ionized. The sum over these two contributions is given as

$$\sigma_i^{2e} = \frac{\sigma_0^2}{P_1^2 P_2^2} \frac{n_i^{5/3} (n_i - 1)}{4\pi R^2} g \left( \frac{E}{P_1 + P_2} \right). \quad (2.10)$$

Here,  $P_1(= E_i)$  and  $P_2$  are the binding energies of the first two electrons which can be removed from the target ion, respectively,  $n_i$  is the number of equivalent electrons in the outermost shell,  $R$  is the gas kinetic radius of this shell and  $\sigma_0 = 6.56 \times 10^{-14} \text{ cm}^2 (\text{eV})^2$ . Function  $g$  is a general function given by Gryziński in graphical form [95]. It can be well approximated by

$$g(x) = \frac{\ln x}{a_1 x^2 + a_2 x + a_3} + a_4(x-1) + a_5(x-1)^2, \quad (2.11)$$

with  $a_1 = 1.59$ ,  $a_2 = -3.71$ ,  $a_3 = 16.20$ ,  $a_4 = 2.14 \times 10^{-4}$  and  $a_5 = -3.67 \times 10^{-6}$ .

### 3 Experimental Setup

The apparatus employed in this work (Fig. 3.1) has been successfully used previously in a number of experiments on electron-impact ionization of various ions. Details of the experimental setup were provided in publications on single and multiple ionization of  $\text{Sc}^+$  [96], [97]. Therefore, only a short description of the experimental arrangement is provided, while the specific procedures and peculiarities of the present studies are comprehensively discussed. Ions produced in the 10-GHz all-permanent-magnet electron-cyclotron-resonance (ECR) ion source [98] were extracted and accelerated by a voltage of 12 kV. After selection of the desired ion species by a  $90^\circ$  dipole magnet and subsequent charge cleaning by an electrostatic  $90^\circ$  spherical deflector, the ion beam was collimated in front of the interaction region using two pairs of slits about 18.5 cm apart from one another. There it was crossed by an intense ribbon-shaped electron beam produced by a high-power electron gun (Fig. 3.2). The electron beam is space-charge limited and reaches a current of about 450 mA at 1 keV energy thus providing an electron density unsurpassed in other electron-ion crossed beam arrangements [99]. Products of electron-ion collisions were separated from the primary ion beam by a second  $90^\circ$ -dipole magnet and were registered by a single-particle detector [100] after passing an electrostatic  $180^\circ$ -spherical deflector. The additional deflection of the product ions minimized background of stray electrons released by ions hitting surfaces. The primary ion beam was collected in a movable Faraday cup positioned at an appropriate location inside the second-magnet chamber.

The signal detection efficiency was determined in previous works for a variety of ions at given energies to be  $(97 \pm 3)\%$  [100, 101]. Moreover, for 16 keV  $\text{Xe}^{q+}$  ions ( $q = 1, \dots, 6$ ) it was shown that the detection efficiency does not depend on the charge state of the detected ions [100].

Absolute electron-impact single-ionization cross sections of xenon and tin ions were measured in the energy range from threshold to a maximum of 1000 eV employing the well-established animated-beams method [14, 99]. The high-current electron gun is mounted on a linear translation feedthrough with its (vertical) axis perpendicular to the ion beam direction. Thus, the electron beam can be moved up and down across the ion beam between two zero-overlap positions below and above the ion beam. At positions with no overlap this technique allows for a separate measurement of the background count rate while in the overlap region a position-dependent ionization signal on top of that background is recorded. The integral of

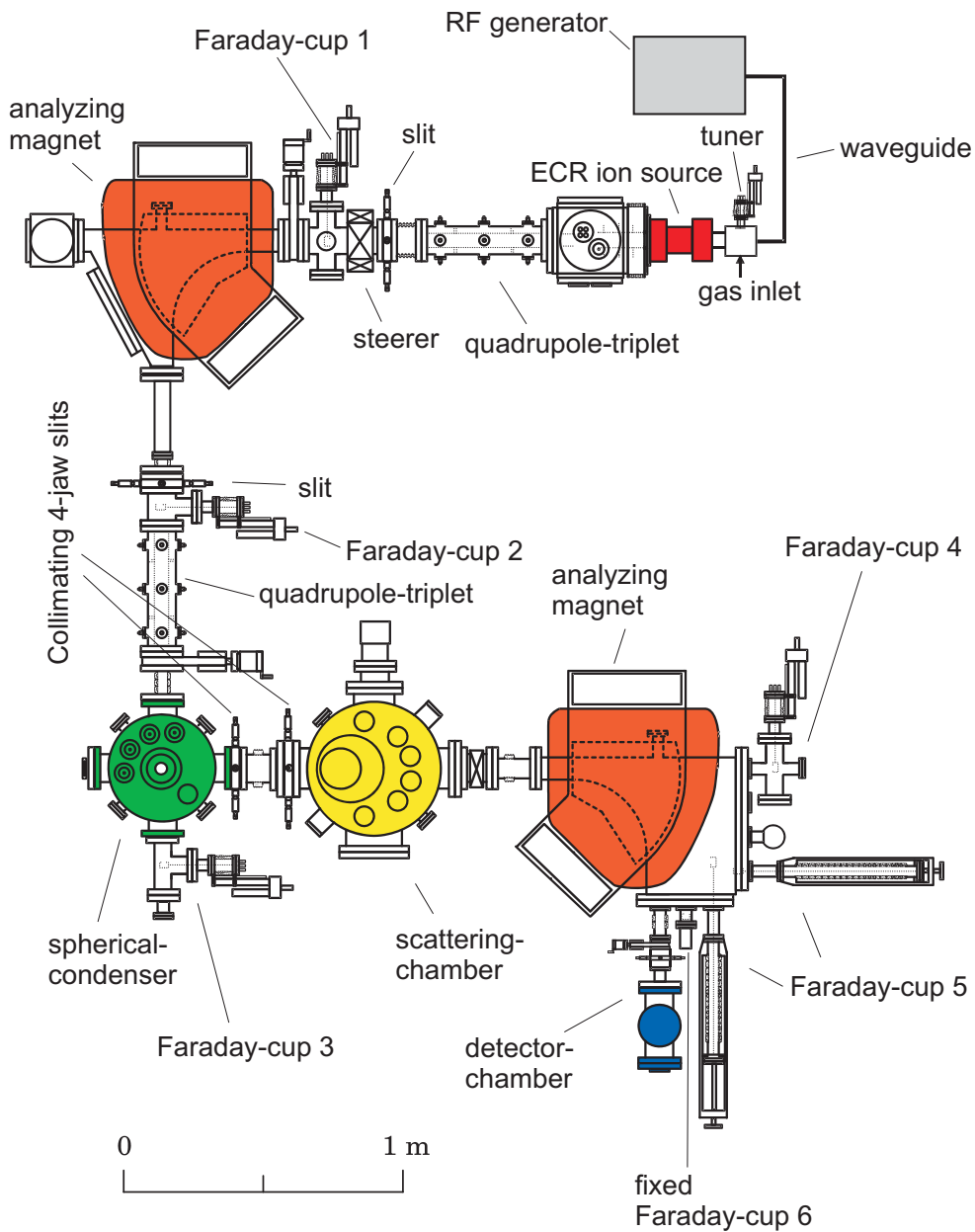


**Figure 3.1:** Experimental "crossed-beams" setup used for the present studies.

the signal peak directly provides the cross section without additional measurement of any overlap form factors [99].

For absolute measurements xenon and tin parent ion beams were collimated typically to the size of  $0.7 \times 0.7 \text{ mm}^2$ . Only in some cases the lack of signal forced us to increase the ion beam current by opening the collimator slits. The maximum

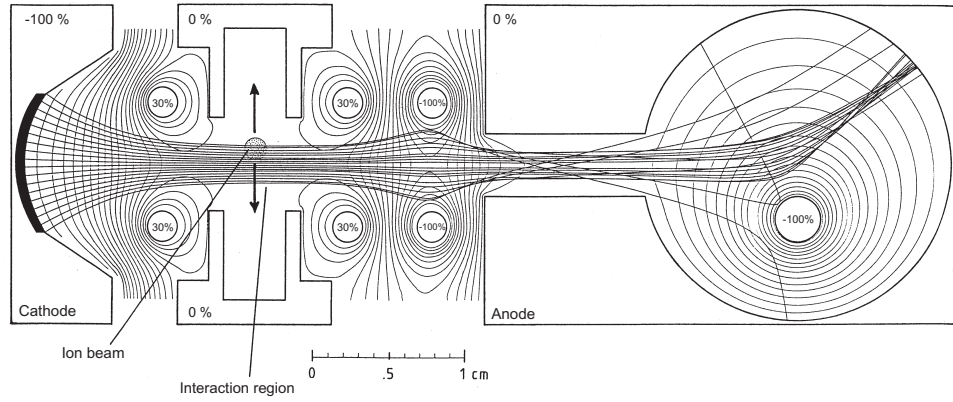


**Figure 3.2:** Schematic view of the electron gun used in the present experiments. The electron beam is emitted by the cathode, focused by the 3 pairs of cylindrical rods and collected in the anode with the defocusing electrode inside. The percent numbers represent the relative potential distribution on the gun electrodes. Thin lines show the field distribution inside the gun.

beam size used in the present experiments for absolute cross section measurements was  $1.0 \times 1.0 \text{ mm}^2$  (see Tab. A.1 for detailed information considering every single measurement). Tight collimation ensured complete transmission of both the parent ion beam to the Faraday cup and the product ions to the detector while the ion beam had to cross different regions of the moving electron beam. Because of the electron-beam space-charge an electric field especially at the upper and lower surfaces of the electron beam can lead to deflection of the traversing ion beam and, hence, to losses of off-center components of parent and product ions not reaching the cup or the detector, respectively. In the experiments, however, the negative space charge of the electrons was at least partly compensated by trapped positive ions formed from purposely introduced Kr background gas in the collision chamber [16].

Finally, the cross-section values were calculated as:

$$\sigma = \frac{N\Delta z}{I_e I_i \epsilon \Delta t} \frac{K}{M}, \quad (3.1)$$

where  $H$  is the number of registered product ions during the measurement time interval  $\Delta t$ ,  $I_i$  and  $I_e$  are measured ion- and electron currents respectively,  $M$  is the kinematic factor,  $\Delta z$  is the displacement of the electron gun along the  $z$  axis during the time interval  $\Delta t$ , and  $\epsilon$  is the efficiency of the product-ion detector [102].

In addition to the animated-beams technique employed for the measurement of independently absolute cross sections a high-resolution energy-scan technique was used to access details in the energy dependence of the cross sections [16]. Measurements covering a maximum electron energy range of 200 eV in a single sweep with about 1000 energy steps were carried out at optimum overlap of the

electron and ion beams. The dwell time on each energy step was chosen to be 3 ms. With a settling time as low as 0.3 ms for each energy a sweep over 1000 steps took 3.3 s. Slow fluctuations of experimental conditions with a time constant of 0.1 s and slower were therefore averaged over wide ranges of the energy-dependent spectrum measured. Real changes in the cross section function due to fine energy-dependent structures are thus conserved and made accessible to experimental observation. The number of sweeps was chosen such that statistical uncertainties were reduced to below a desired level. The resulting relative cross sections were then normalized to the absolute cross sections determined by the animated-beams method. The systematic uncertainty of these normalized energy-scan cross sections is therefore almost identical with that of the cross sections obtained with the animated-beams method.

The collimation conditions for the ion beam can be relaxed for the energy-scan measurements. During an energy scan the ion beam crosses the static electron beam in the center where the space charge electric field has its minimum. Deflection is a less critical issue in this geometry and therefore the ion beam size can be increased up to  $2 \text{ mm} \times 2 \text{ mm}$ . By this, the usable ion current passing the interaction region can be significantly enhanced.

### 3.1 Production of xenon and tin ions in the ECR ion source

As mentioned above, a 10 GHz ECR ion source has been used for the production of xenon and tin ions. This section reports on the procedure and some general source settings used for the generation of ion currents suitable for the experiments.

$\text{Xe}^{q+}$  ions ( $q \leq 9$ ) were produced by introducing only xenon gas to the source without admixtures. The gas pressures needed for maximum ion currents varied in the region of  $0.5 - 1 \times 10^{-4}$  mbar measured in the gas inlet region. For producing highly charged  $\text{Xe}^{q+}$  ions ( $q > 9$ ) the xenon gas had to be mixed with oxygen as support gas. Unfortunately, it was possible to measure only the sum of the partial pressures of both gases. It amounted to  $1.3 - 1.5 \times 10^{-4}$  mbar. However, the monitoring of the valve controls allowed to roughly estimate the partial pressure of oxygen to be 90% or even more. Oxygen admixtures led to great improvements in the production of highly-charged ions. Hence, hundreds of nano Amperes of ion current for charge states  $q = 10, 11, \dots, 20$  were available after mass-over-charge selection. An example of the observed mass spectrum<sup>1</sup> is shown in Fig. 3.3. Furthermore, for the investigated most highly-charged ion,  $\text{Xe}^{25+}$ , a current of more than 30 nA could be measured with Faraday cup 2 behind the first analyzing magnet. Finally, the mass spectrum with the ion source optimized on  $\text{Xe}^{21+}$  and the

---

<sup>1</sup>This mass spectrum has been taken with the ion current measured in the Faraday cup behind the second dipole magnet, i.e. behind the collimator used in the experiment. This is the reason for the much weaker ion currents than mentioned above. However, the collimation in the much longer flight path resulted in an excellent resolution of the mass spectrum. The isotopic composition of the ion source output could be resolved.

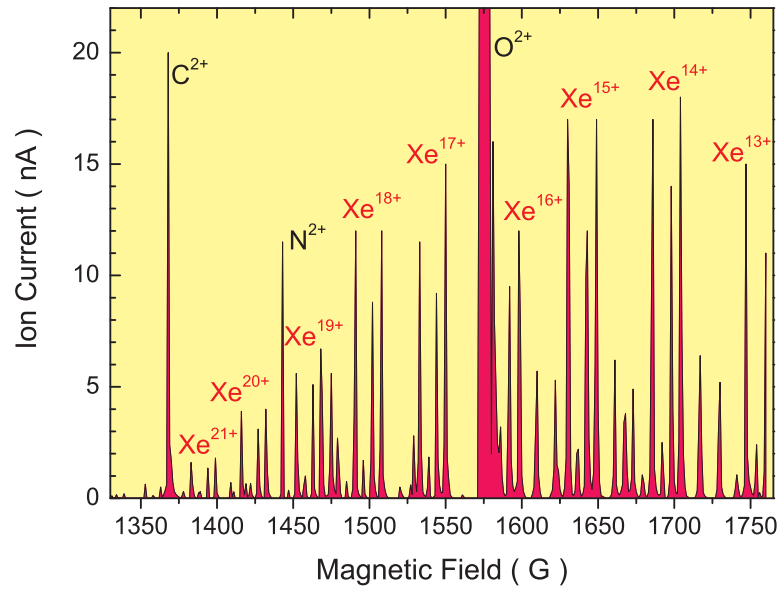


**Figure 3.3:** Observed mass spectrum of  $\text{Xe}^{q+}$  ions ( $q = 13, 14, \dots, 21$ ) measured in Faraday cup 4 (see Fig. 3.1). The current of  $\text{Xe}^{14+}$  was optimized.

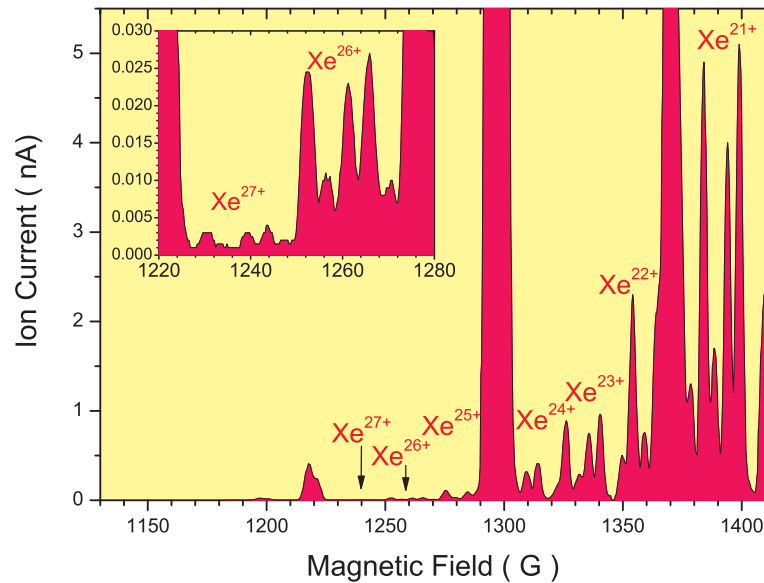


**Figure 3.4:** Observed mass spectrum of highly charged  $\text{Xe}^{q+}$  ions ( $q \geq 21$ ) measured in Faraday cup 4 with the setting optimized for  $\text{Xe}^{21+}$ . Individual Xe isotopes are clearly resolved. The observed isotopic distribution corresponds to the natural abundances of the various Xe isotopes.

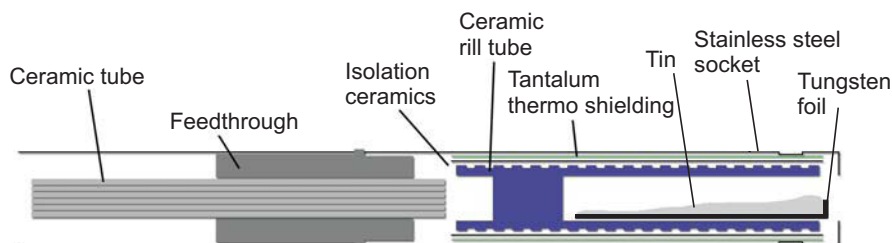


**Figure 3.5:** Schematic view of the improved oven for evaporating metallic tin.

collimated ion current measured in the Faraday cup 4 behind the second dipole magnet revealed up to 4 pA of  $\text{Xe}^{27+}$  (Fig. 3.4).

Tin ions were produced by evaporating metallic tin in an oven inside the ECR ion source. Although the melting point for tin is relatively low (231.93 °C) the temperatures needed for acquiring optimal vapor pressures were higher than 1000 °C with the heating power applied to the oven being about 50 W. At these high temperatures, melted tin becomes very liquid and, due to the horizontal position of the oven, can easily flow out. This problem was solved by introducing a stripe of tungsten foil to the bottom of the aluminium-oxide ceramic container (Fig. 3.5 and 3.6). The point of this improvement is that hot liquid tin does not moisten the aluminium-oxide ceramic, but does moisten the tungsten foil very well. Hence, the liquid tin remains on the foil inside the container for the entire time of the experiment without flowing out.

For the production of low-charged  $\text{Sn}^{q+}$  ions ( $q \leq 6$ ), helium gas was used as a support gas at pressures ranging from 6 to  $9 \times 10^{-4}$  mbar. For higher charge states ( $q = 7, 8$ ) helium was mixed with oxygen and for  $q = 9, 10, \dots, 13$  helium was almost completely replaced by oxygen. As in the case of xenon ions, it was possible to measure only the sum of the partial pressures of the gases. This was around  $1.4 \times 10^{-4}$  mbar. In analogy with highly charged  $\text{Xe}^{q+}$  ions, where relatively lower partial pressure of xenon gas was required for better ion current production, the lower tin vapor pressure helped for more efficient production of highly charged  $\text{Sn}^{q+}$  ions.

The ion current values available for each of the cross-section measurements can be found in Tables A.1 and A.2 in Appendix A.

## 3.2 Background

One of the major problems in electron-ion crossed beams experiments is the background produced by collisions of ions with residual gas atoms or molecules. In such collisions the ions can strip off an electron and the ionized ions produced in the residual gas all along the ion flight path between beam deflectors before and

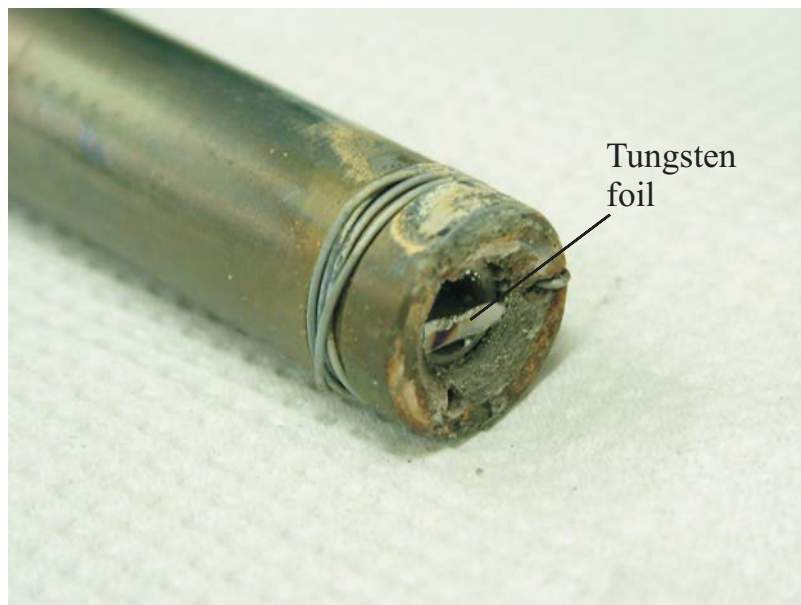


**Figure 3.6:** The oven for evaporating metallic tin with inserted tungsten foil to protect liquid tin from flowing out.

behind the interaction region are recorded by the signal detector. One of the measures that can be taken against such stripping background is energy-labeling of secondary ions produced just within the electron-ion interaction region. This is accomplished by applying a voltage (a few hundred Volts) to the interaction region. As a result, ions formed in the interaction region have a different kinetic energy compared to the ones formed elsewhere and can, therefore, be separated in the analyzing magnetic field.

For the sake of avoiding additional problems the voltage labeling was not used for the absolute cross-section measurements. Applying a voltage to the electron gun during the animated-beam measurements would have implied variations of electric fields seen by the ions while the position of the electron gun was scanned. In particular, focusing or de-focusing of background produced by stripping collisions before and inside the interaction region could possibly have corrupted the absolute cross-section measurement.

Generally, there was no drastic need in applying the energy-labeling technique for measurements involving xenon and tin ions. The energy-labeling method was employed only for several energy-scan measurements when the signal/background ratios were unsatisfying, as has been the case in earlier experiments performed with the setup, e.g., on  $\text{Li}^+$  [6]. Mainly, the studied processes possessed relatively large cross sections and, hence, tolerable signal/background ratio values. Detailed information on the background conditions of every single measurement also can be found in Tables A.1 and A.2 in Appendix A.

### 3.3 Electron-current correction function

For the determination of ionization cross sections accurate values of the particle currents in the interaction region are required. While the geometry of the ion beam allows for an accurate determination of the ion current in the interaction region, the electron current in this region cannot be directly measured. The reason for this is the construction of the electron gun (Fig. 3.2) that leads to electron current losses on the electrodes. A separate investigation showed that the effective electron current  $I_{eff}$  can be obtained as a result of multiplication of the measured electron current  $I_{cath}$  by the acceleration-voltage dependent correction factor  $C(U_e)$ , where

$$C(U_e) = \frac{I_{cath} - I_{rods}}{I_{cath}}. \quad (3.2)$$

Here  $I_{cath}$  is the measured electron current emitted from the cathode and  $I_{rods}$  is the separately measured electron current collected on the first pair of the focusing rod electrodes (see Fig. 3.2). The correction factors  $C(U_e)$  measured at different electron energies constitute the *electron-current correction function* (ECCF). This function is unique for a given gun assembly since it is influenced, amongst others, by cathode emission properties, slight changes of the gun geometry etc. Therefore, it has to be newly determined after performing any manipulations on the electron gun, e.g., cathode replacement.

During the present study of xenon and tin ions 5 different electron-current correction functions have been used which were obtained in April 2007, March 2008, November 2008, July 2009 and August 2009. Each of these functions was used for the measurements as long as changes of the electron gun were necessary and hence a new ECCF had to be measured. All data considering the presently used electron-current correction functions are given in Tab. A.3 in Appendix A.

A conservative estimate of the uncertainty of the resulting effective electron current is  $\pm I_{rods}$ . Thus, the energy-dependent determination of the electron current through the interaction region has a possible error of about 15% at 20 eV and less than 1% for energies greater than 120 eV.

### 3.4 Calibration of the energy scale

For the identification of the observed structure in the measured ionization cross sections it is particularly important to have a reliable energy scale. The energy channels in the measured raw spectra correspond to nominal, i.e., set energies of the electrons in the laboratory frame. The true laboratory energies depend on possible contact potentials between the electrodes of the voltage power supply and the electrodes of the electron gun which are connected via different cables, wires and vacuum feedthroughs. For the determination of possible potential shifts the well known 54.42 eV threshold for ionization of  $\text{He}^+$  ions was scanned. The set energies were transformed to the electron-ion centre-of-mass (c.m.) frame taking the

velocity of the ions into account. Assuming laboratory energies  $E_e$  and  $E_i$  of the electrons and ions, respectively, the c.m. energy  $E_{cm}$  in a crossed-beam experiment with a  $90^\circ$  crossing angle was obtained from [83]

$$E_{cm} = m_i c^2 (1 + m_e/m_i) \times \left[ \sqrt{1 + \frac{2m_e/m_i}{(1 + m_e/m_i)^2} (\gamma_i \gamma_e - 1)} - 1 \right] \quad (3.3)$$

with the Lorentz factors

$$\gamma_i = 1 + \frac{E_i}{m_i c^2} \quad (3.4)$$

and

$$\gamma_e = 1 + \frac{E_e}{m_e c^2}. \quad (3.5)$$

The scan spectrum was then plotted as a function of the nominal c.m. energy determined from the above equations. The contact potential shift could be determined by comparison with the known ionization threshold of H-like  $\text{He}^+$ .

Since contact potential differences strongly depend on the materials used for the gun electrodes, insulators and wiring, a new electron energy scale calibration measurement has to be performed after every new gun assembly, just as for the ECCF. In addition, the energy scale can also slightly change with time as a result of contaminations of the gun surfaces with tungsten evaporated from the cathode. For the present measurements the experimental energy scale was calibrated four times. These calibrations have been performed mostly together with the ECCF measurements and have been used for the same corresponding time periods. The energy corrections are listed in Tab. 3.1. They are estimated to be correct within  $\pm 0.5$  eV.

**Table 3.1:** Energy scale calibration

Measurement	Energy shift (eV)
April 2007	+0.3
March 2008	-0.9
November 2008	-1.8
July 2009	-1.6

Space charge potentials of the electron beam can lower the actual electron energy. This effect is compensated by introducing Kr gas into the collision region at an apparent pressure of about  $2.0 \times 10^{-7}$  mbar. This has to be corrected by a factor 0.5 to account for the Kr gas "atmosphere" around a vacuum gauge calibrated for the measurement of  $\text{N}_2$ . The electron beam produces slow positive ions from that gas and traps them within its own negative space charge potential well. Electron optics calculations of the present electron gun have shown that the maximum potential depression by an uncompensated electron space charge inside the

interaction region is 4% of the acceleration voltage applied between the cathode and interaction region. At 1000 eV this would imply a 40 eV energy spread in the electron beam. In experiments with multiply charged barium ions [103], as well as within current experiments, resonances have been observed even near 1000 eV with a width of 3 eV. Even if one would assume that the space charge depression of the potential inside the electron beam alone is responsible for this energy spread, the comparison with the theoretically expected 40-eV spread would require more than 90% compensation of the electron space charge by slow trapped ions. At lower electron energies, resonances with smaller widths have been observed. Hence, the electron space charge potential does not have a big influence on the present electron energy scale.

### 3.5 Single-particle detection of product ions

The construction of the detector used for detecting the reaction products is described by Timphus [101] and by Rinn *et al.* [100]. Briefly, inside the detector the product ions hit the surface of the converter plate, where secondary electrons are released. These electrons are accelerated towards the input of the channel-electron-multiplier (CEM) by the voltage between the converter plate and the cone of the CEM. The potential difference of about 100 eV between the cone and the repeller plate prevents the secondary electrons produced on the CEM cone surface from being lost. The amplified pulse signal is read from the pulse output of the CEM. During the measurements it was found that the number of pulses coming from the detector is higher than the number of the incoming product ions. This effect was observed previously for fullerene ions [104]. Here, it has been observed for heavy atomic ions for the first time.

The electron-impact ionization process can be treated as a Poisson process, i.e., single identical events are statistically independent of each other. The number of these events per time unit has a statistical spread around some mean value. It can be described with a Poisson distribution. Consequently, the time-differences between two events follow an exponential distribution. The distribution of these time differences was measured and by that a certain deviation from the expected exponential behavior could be revealed. An unexpected higher number of pulses was detected in the region of the shortest intervals up to 4  $\mu\text{s}$  (Fig. 3.8a) indicating the effect of multiple pulsing. Measurements with xenon and tin ions showed an increase of the count rate of approximately 1-8%. No systematic dependence either on ion charge state or on ion energy has been found.

This problem can be solved by introducing a significantly long artificial dead time [105]. For the present measurements an artificial paralyzing deadtime of  $\tau_a = 5 \mu\text{s}$  was chosen that resulted in suppression of multiple pulse counting (Fig. 3.8b). The paralyzing deadtime was corrected for by considering the count rates of the measurements. For the measurements performed before the introduction of the artificial deadtime, the raw data have been revised and corrected by subtraction of

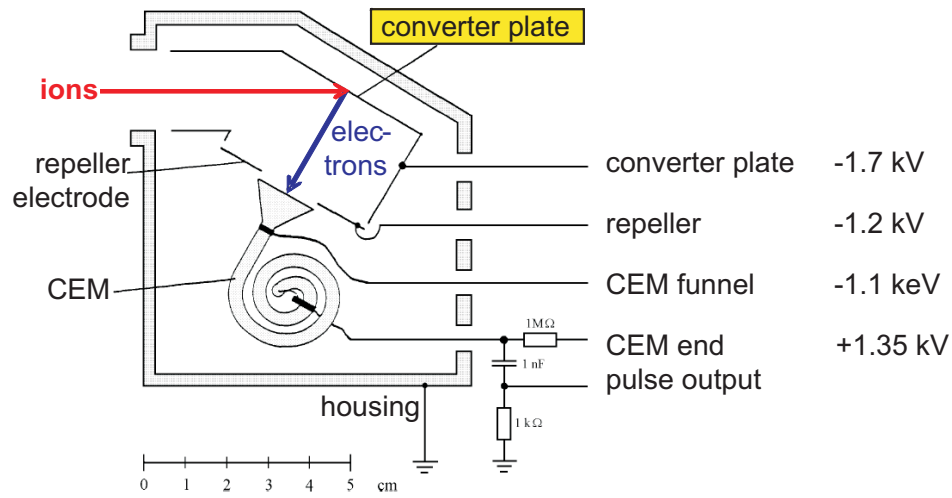


**Figure 3.7:** Schematic view of the product-ion detector employed in the present studies.

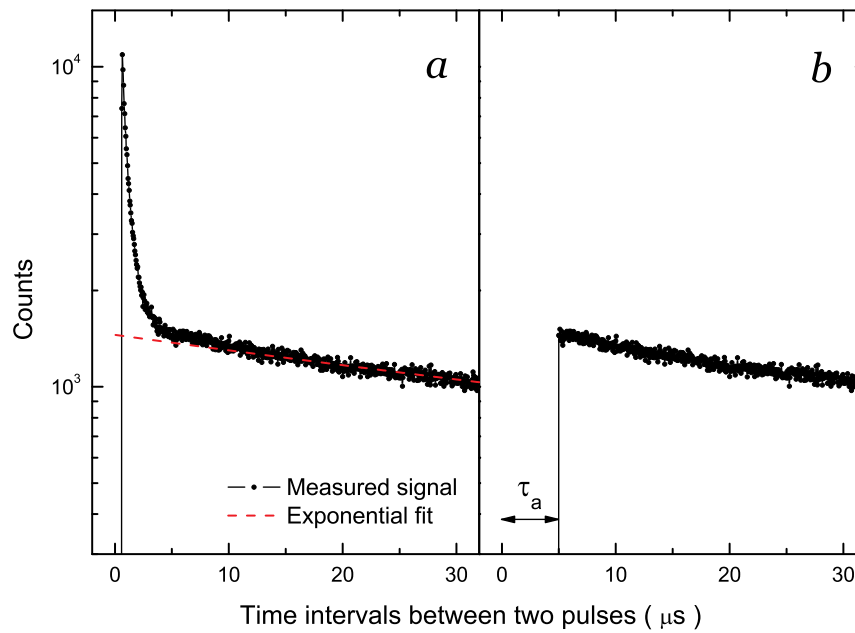


**Figure 3.8:** Measured distribution of the registered product ions against time-interval length between two counting pulses (*a*). The dashed curve is an exponential fit that represents the Poisson distribution. Section (*b*) shows the result of applying an artificial paralyzing deadtime  $\tau_a = 5 \mu\text{s}$ .

5% of the signal counts. Also, additional 5% have been quadratically added to the total systematic error of the measurements.

The systematic uncertainty of the absolute cross-section is determined as the quadrature sum of the systematic uncertainties of the parameters that enter the cross section determination (equation (3.1)) and are listed in Tab. 3.2. Excluding the above described additional uncertainties from the ECCF and multiple pulse counting this was determined to be 6.3%. Statistical uncertainties varied depending on the experimental conditions and remained within 1-2% at 95% confidence interval for most of the data. Total uncertainties of cross sections were determined from the square root of the squared individual uncertainties listed above plus the squared statistical uncertainty.

**Table 3.2:** Systematic uncertainties

Magnitude	Uncertainty
Kinematic factor $M$	1 %
Detector efficiency $\epsilon$	3%
Displacement $\Delta z$	1 %
Ion current $I_i$	5 %
Electron current $I_e$	2 %

## 4 Experimental Results

The results of the present study on electron impact ionization of xenon and tin ions comprise 78 measured energy-dependent cross sections. In the current chapter, these cross sections are described and compared with previously available experimental and theoretical cross-section data. Effects and influences of excited metastable-state primary-beam impurities on the experimental results are discussed. Recommendations for application of the present data in plasma physics are given.

Detailed illustrations of the measured cross sections together with explanations of contributions arising from direct and indirect ionization mechanisms are given in Appendix B and Appendix C. The absolute values of the measured cross sections are tabulated in Appendix D.

### 4.1 Single ionization of xenon ions

#### 4.1.1 Overview

Within the present work cross sections for single ionization of xenon ion charge states from 1 through 25 have been measured in the range from threshold up to 1000 eV electron energy.  $\text{Xe}^{25+}$  is the highest charge state for which the single-ionization cross section can be investigated employing the current electron gun with its energy limitation to 1000 eV.  $\text{Xe}^{25+}$  is also the most highly charged ion, for which ionization has ever been investigated employing the crossed-beams method. The record has been held previously with measurements for  $\text{Kr}^{18+}$  carried out by Khouilid *et al.* [106].

The data for all 25 ionization stages are presented in Fig. 4.1 in the form of the energy scan data normalized to the separately measured absolute cross-section values. For better viewing, the data sets (except for  $\text{Xe}^+$ ) have been multiplied by appropriate factors provided individually for the each data set in the figure.

For the ionization stages up to  $\text{Xe}^{21+}$ , the statistical uncertainties of the absolute measurements in the cross-section maxima (or at 1000 eV, where these could not be reached) were 2% or lower. Thus, the total uncertainties are mostly determined by the systematic uncertainty (see Chapter 3) and resulted in 9% or better. At lower electron energies the total uncertainties are, however, significantly increased due to poor statistics as a result of poor signal/background ratios. For the higher charge states, statistical uncertainties reached 7%, resulting in 11% total uncer-

tainty of the measurement. The relative uncertainties of the energy scans varied on the average from 3% for the ion stages above  $\text{Xe}^{20+}$  down to 0.1% for  $\text{Xe}^{2+}$ . The maximum measured cross-section value is  $2.55 \times 10^{-16} \text{ cm}^2$  at 34.3 eV for  $\text{Xe}^+$ .

According to the electron configuration and, hence, the processes defining the cross-section function behavior, the data presented here can be classified into several groups as shown in Tab. 4.1.

**Table 4.1:** Groups of the single-ionization cross sections of  $\text{Xe}^{q+}$  ions.

	Ion charge states	Electron configurations
I	$\text{Xe}^+, \dots, \text{Xe}^{7+}$	$4d^{10}5s^25p^5, \dots, 4d^{10}5s$
II	$\text{Xe}^{8+}, \dots, \text{Xe}^{17+}$	$4d^{10}, \dots, 4d$
III	$\text{Xe}^{18+}, \dots, \text{Xe}^{25+}$	$3d^{10}4s^24p^6, \dots, 3d^{10}4s$

The first group includes the ionization cross sections for the ion charge stages 1 through 7 with ground electron configurations  $4d^{10}5s^25p^5, \dots, 4d^{10}5s$ . Typical for this group is a rather steep increase of the cross section at the ionization threshold and occurrence of strong, amongst others, resonant structures in the energy range 50 eV to 200 eV. These are caused by processes mostly involving  $4d$ -subshell excitation with subsequent autoionization resulting in net single ionization of the parent ions (see e.g. [53]). For the ion stages from  $\text{Xe}^{4+}$  and further, structure corresponding to the indirect ionization processes involving excitation of the  $4p$  subshell could also be identified. For all cross sections of the first group the maximum is located below 200 eV. Beyond the maximum, the measured single-ionization cross sections generally exhibit a smooth behavior as function of energy, except for small resonant structures at 600 - 700 eV which become discussible for  $\text{Xe}^{5+}$  and the higher charge states. These resonant structures can be assigned to the processes of resonant excitation of an electron from the  $3d$  subshell with incident-electron capture by the target ion followed by autoionization finally resulting in net single ionization.

In the case of the last ion of the first group,  $\text{Xe}^{7+}$ , a small non-zero cross section has been observed in a wide range below the ground-state ionization threshold. To our understanding, this effect is caused by metastable states arising from excitation of the outermost filled  $4d$  subshell which are populated in the ion source. The lifetime of these excited states is sufficiently long so that they can survive the passage from the ion source to the region of the intersection with the electron beam. This and other effects involving excited metastable-state admixtures in the parent ion beam are discussed in Section 4.1.2.

The second group comprises 10 ionization stages from  $\text{Xe}^{8+}$  to  $\text{Xe}^{17+}$ , for which the  $4d$  subshell is the outermost shell. The cross section functions exhibit a relatively smooth increase above threshold dominated by direct outer-shell electron removal. Additional weak structures stem from indirect ionization processes

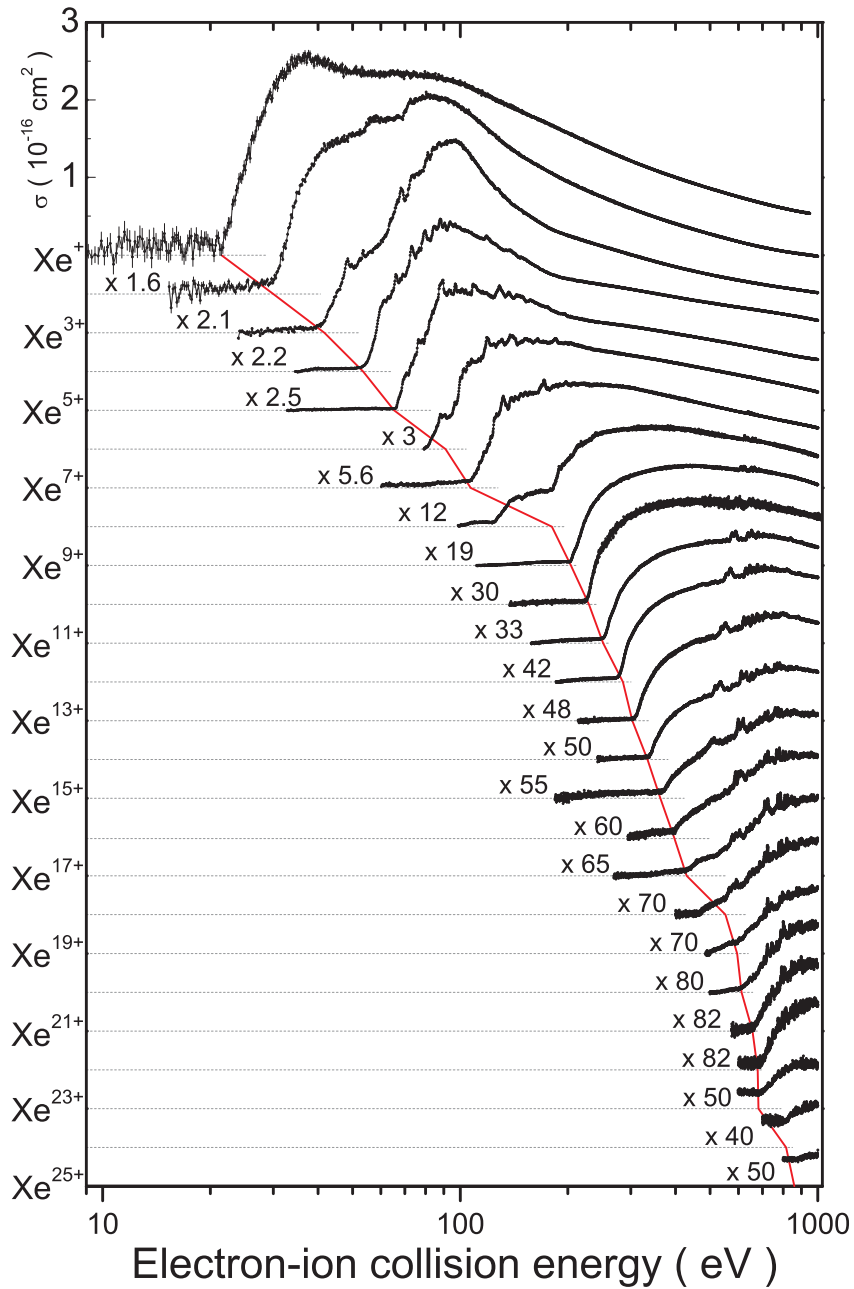


**Figure 4.1:** Overview over the present single-ionization cross sections of  $\text{Xe}^{q+}$  ions ( $q = 1, 2, \dots, 25$ ). The cross-section scale is in units of  $10^{-16} \text{ cm}^2$  and the cross section for each ion stage is shifted downwards by  $0.5 \times (q - 1) \times 10^{-16} \text{ cm}^2$ . The thin solid line connects the observed ground-state ionization thresholds.

involving excitation of the  $4p$ - and, probably, of the  $4s$  subshell. At higher energies beyond 600 eV features indicating indirect ionization processes caused by  $3d$ -subshell excitation can be recognized. The ionization onsets below the ground-state ionization thresholds indicate the presence of excited metastable states. These do not seem to influence the measured cross sections much, except for  $\text{Xe}^{8+}$ , where the most distinct contributions due to ionization of the metastable admixture are present. Bannister *et al.* explained these rather large contributions by indirect ionization processes (via excitations of  $4d$  and  $4p$  subshells) occurring in the metastable admixture [71].

With the ion charge states further increasing, structures due to indirect ionization via excitation of the  $4p$ - and  $3d$ -subshells gain significance. In the case of  $\text{Xe}^{17+}$  resonances are observed over the whole experimental energy range. Moreover, from  $\text{Xe}^{9+}$  on, the data contain recognizable structures above the  $3d$ -subshell ionization thresholds from processes involving excitation of the  $3p$  subshell.

The third group contains ionization stages 18 through 25 with ground electron configurations  $3d^{10}4s^24p^6, \dots, 3d^{10}4s$ . Over the entire experimental energy ranges, the measured cross sections exhibit clear features of indirect ionization involving excitation of the  $3d$ - and  $3p$  subshells. These processes strongly dominate over the direct outer-shell electron knock-off process (see [79],[80] and references therein).

An important issue concerning the third single-ionization cross-section group is the presence of non-zero cross sections below both the ground-state- and the low-lying excited metastable-state ionization thresholds. Their relative magnitudes have a tendency to increase with higher charge states and eventually comprises  $\sim 85\%$  of the total measured cross section for  $\text{Xe}^{25+}$  at 1000 eV (see Fig. B.25). The preliminary explanation for the origin of the observed features is similar to the one proposed for  $\text{Xe}^{7+}$ : metastable components arising from excitation of an electron from the outermost filled  $3d$  subshell might be present in the parent ion beam. A detailed discussion of the role of metastable ions in all of the present single-ionization cross sections will be given in the following Section 4.1.2.

### 4.1.2 Role of excited metastable states

In atomic collision experiments, an atomic or ion beam often contains a certain fraction of excited metastable species which depends strongly on the conditions of beam production. As confirmed in numerous publications, this complication becomes significant especially for experiments in which ions are produced in ECR ion sources. Clearly, an ion source that is used to produce intense beams of ions in high charge states must provide sufficiently high energies of the ionizing electrons. These energies are also sufficiently high to excite ions present in the plasma to any excited state below the ionization threshold. Population of long lived excited states of multiply of highly charged ions is practically unavoidable.

According to our experience with the operation of the present ECR source, one can influence the amount of metastables but not in a controlled manner, as it was possible with a Penning source, where the fraction of metastable ions could be

varied by adjusting ion source parameters [107]. For  $\text{Li}^+$  ions it was shown that the magnitudes of metastable admixtures very much depend on the Li-containing parent material used in the ion source and that the metastable fraction can be even reduced to zero [6]. No similar solution has been found for  $\text{Xe}^{q+}$  ions.

As already mentioned, each of the present single-ionization cross sections reveals that the primary beam contained an excited metastable-ion component. A clear signature for the presence of the metastable ions in the ion beam is ionization signal at energies below the ground-state ionization threshold. Single-ionization cross sections of excited metastable ions vary depending on the electron configuration excited. The cross sections for ionization from excited states of the ground configuration usually possess magnitudes similar to those for ground-state ionization. Hence, the admixtures of such states to the primary ion beam results generally in a slight shift of the observed ionization threshold towards lower energies. The situation may change significantly when the primary ion beam contains metastable states of configurations where an electron of the outer-shell  $nl$  has been excited to a higher subshell  $n'l'$ :

$$nl^k \rightarrow nl^{k-1}n'l', \quad (4.1)$$

where  $k$  is the number of electrons in subshell  $nl$  for an ion in its ground state. This results in a significant shift of the measured ionization threshold towards lower energies. Moreover, the interaction of incident electrons with the  $nl$  subshell (which contain  $k - 1$  electrons) may invoke indirect ionization processes, as has been observed, e.g., for  $\text{Xe}^{6+}$  and  $\text{Xe}^{8+}$ . As a result, the measured cross sections can be seriously affected by even small amounts of metastable ions admixed to the primary ion beam (see Figs.B.6 and B.8).

In ions with configurations containing one, or few electrons above the outermost filled subshell it may occur that an electron from this subshell gets excited to higher subshells. In such cases, even higher excitation energies are to be expected. For example, for ions isoelectronic to alkali atoms there are long-lived states whose excitation energies exceed the ground-state ionization potential [108, 109].

It turns out in the present work, that for highly charged xenon ions possessing electron configurations with one or few electrons above the filled  $nd$  subshell, the measured cross sections reveal non-zero values at relatively very low energies. Figure 4.2 shows the present single-ionization cross sections of  $\text{Xe}^{23+}$ ,  $\text{Xe}^{24+}$  and  $\text{Xe}^{25+}$ . The data suggest strong contributions of ionization of long-living primary-ion-beam components with high excitation energies. Because of poor signal/background ratio, detailed energy-scan measurements of the cross sections in the whole energy regions below the ground-state ionization thresholds would have been extremely time consuming and, hence, have not been performed.

In order to obtain more information on the subject of these components we have performed extensive calculations of the lifetimes of states of different possible excited electron configurations using the Cowan code [110]. The results of these calculations for all  $\text{Xe}^{q+}$  ion species studied in this work are listed in table

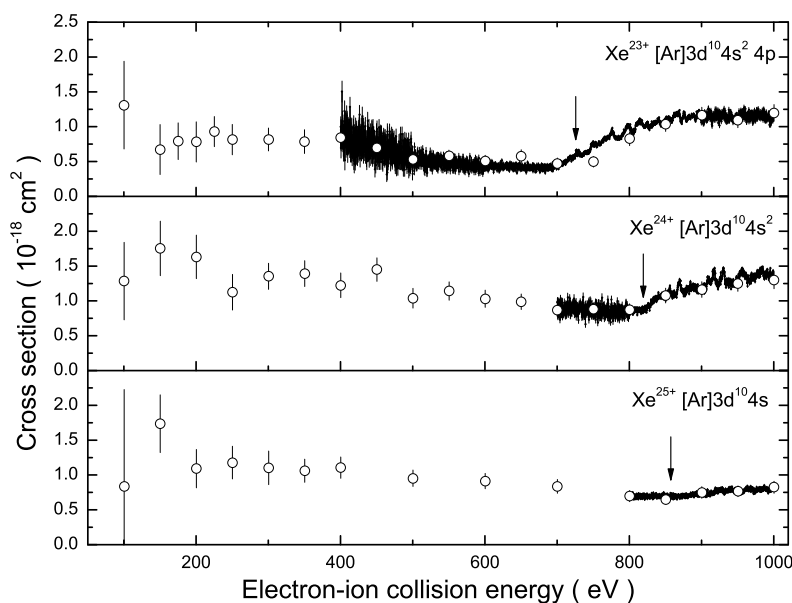


**Figure 4.2:** Single ionization of  $\text{Xe}^{23+}$ ,  $\text{Xe}^{24+}$  and  $\text{Xe}^{25+}$ . Open circles represent absolute cross section values and small filled circles are the energy scan data. Vertical arrows represent ground-state ionization potentials.

E.1 in Appendix E. It has been revealed by the calculations that for highly charged xenon ions  $\text{Xe}^{23+}(3d^{10}4s^24p)$  to  $\text{Xe}^{25+}(3d^{10}4s)$  the excitation of the  $3d$  subshell leads to formation of states with the energies slightly below (and in some cases even beyond) the ground-state ionization potential. According to the calculations, at the same time, these states possess lifetimes of the order of ten to hundred microseconds. Comparing these with the times required for the passage of the ions from the ion source to the point of the interaction with the electron beam (also listed in Tab. E.1) suggests it to be possible that ions in such highly excited states could have been present in the interaction region during the experiments and, hence, have influenced the measured cross sections. Surprising, however, are the proportions of ground-state- and metastable ionization contributions. In the studied energy intervals the contributions of ionization from the metastable states are of the same order or even higher than the ones from ground-state ionization. Considering the low ionization potential of such highly excited states it is probably only a small fraction of metastable states in the primary ion beam that produces such a strong contribution to the apparent cross sections.

A similar behavior has been observed for the single ionization cross section of  $\text{Xe}^{7+}$ , with the  $4d^{10}5s$  electron configuration (which is similar to the one of  $\text{Xe}^{25+}$ ). In this case, the signal/background ratio allowed for relatively easy performance of the energy scan measurement in the below-threshold region. The result for  $\text{Xe}^{7+}$  is

shown in Fig. 4.4. In order to account for a huge background originating from ionization of (mainly metastable) ions by collisions with residual gas particles (see the inset) a linear fit of the data below the visible onset at 10 eV was subtracted. The fact that the obtained fitting line is not horizontal suggests that the background is influenced by the electron beam. Reason for such influence can be increased background gas load released from the electron collector with increasing electron beam current and energy or electron impact ionization of ions in very highly excited states present in the incoming ion beam. However, the present explicit investigations of the lifetimes of excited states (see Appendix E) revealed no long-living states with energies above 88 eV. This is almost 18 eV below the ground-state ionization potential of  $\text{Xe}^{7+}$ . Nevertheless, an apparent ionization threshold is found near 12 eV which can only arise from long lived ions in the primary beam with excitation energies 94 eV or higher. Given the insufficient knowledge of the origin of the background below 10 eV, the straight fit line may not represent the real background at higher energies. Therefore, the cross-section scale in this figure is uncertain.

By referring to the behavior of the measured absolute cross-section values (Fig. B.7) and comparing with the situation for highly charged ions, it can be seen that the relative contributions of metastable-state ionization are much smaller for  $\text{Xe}^{7+}$  than for the cases of the more highly charged ions.

The energy scan measurement shown in Fig. 4.4 revealed rather unique cross section behavior. Within a few eV above the apparent threshold at about 12 eV the cross section rises to a maximum.

Attempting to determine the origin of this cross section behavior observed for single ionization of  $\text{Xe}^{7+}$ , one can refer to the results of the lifetimes calculations provided in Tab. E.1. The  ${}^4F_{9/2}$  state of the  $4d^9 5s 5p$  and several states of the  $4d^9 4f 5s$  configuration which possess sufficiently long lifetimes and sufficiently high excitation energies to be responsible for the observed cross section shape below the ground-state ionization threshold. The calculated excitation energies are about 68 eV and 83–88 eV respectively (see Tab. E.1). At the same time the calculated lowest energies required for direct removal of an electron from  $\text{Xe}^{7+}$  ions with  $4d^9 5s 5p$  and  $4d^9 4f 5s$  electron configurations (leading, e.g., to  $4d^9 5s$ , see Fig. 4.3) are approximately 92 eV and 77 eV [111], while the observed ionization signal starts at much lower energies. An explanation for this is the possibility of indirect ionization by the mechanism of excitation-autoionization as shown in Fig. 4.3. Different from ordinary EA, excitation of one of the outer-shell electrons in the inner-shell excited metastable ions is sufficient to produce autoionizing states. Apparently, excitation of levels with a threshold near 12 eV is sufficient to produce a cross section step function typical for EA contributions.

According to the calculation using the LANL code [111] the energetically lowest (inner-shell excited) configuration of  $\text{Xe}^{7+}$  which contains states more than 106 eV above the ground state is the  $4d^9 5s 6s$  configuration. These autoionizing states can be accessed from  $4d^9 5s 5p {}^4F_{9/2}$  metastable excited states by electron-impact excitations with thresholds near 40 eV. Figure 4.4 shows a step feature in the apparent cross section in that energy range indicating EA contributions

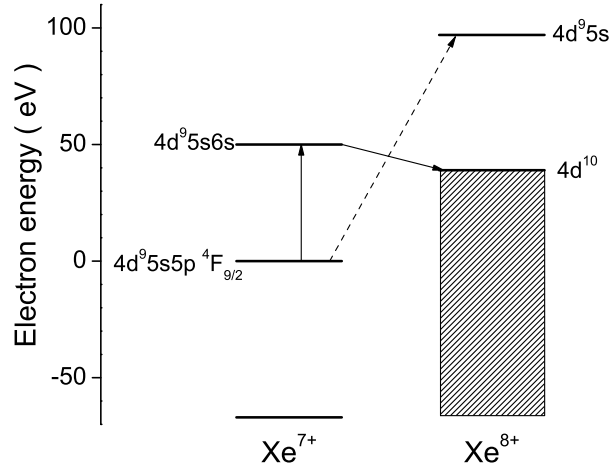


**Figure 4.3:** Direct (dashed arrow) and indirect (solid arrows) ionization processes of metastable  $4d^9 5s 5p \ ^4F_{9/2}$  states present in the primary ion beam.

which might be assigned to  $e + \text{Xe}^{7+}(4d^9 5s 5p \ ^4F_{9/2}) \rightarrow \text{Xe}^{7+}(4d^9 5s 6s)$  excitations. The much stronger step feature at about 15 eV may be associated with excitation  $e + \text{Xe}^{7+}(4d^9 4f 5s) \rightarrow \text{Xe}^{7+}(4d^9 4f nl)$  to autoionizing configurations at energies just above the  $\text{Xe}^{7+}$  ground-state ionization potential. Exact identification of the states or even configurations involved in these processes are hampered by the limited accuracy of atomic structure calculation for such complex multielectron problems.

In order to take into account possible effects induced by ionization of metastable primary-beam admixtures beyond the respective ground-state ionization thresholds, their fractions have to be known. Several experimental methods for the determination of metastable fractions have been described previously (e.g. in Ref. [113]) and there have even been methods developed for separating a single-state fraction from the other fractions in the beam [114]. However, these methods work well only for ions with only few metastable states with sufficiently large excitation energies. Moreover, they lead to a drastic reduction of the ion current and, therefore, they require large experimental installations. As a result, they could not be used here. Another method for extracting information on the presence of metastable states from the already measured data has been adopted previously in a number of references (see, e.g., [6, 71, 115]). This consists in fitting of the measured data below the ground-state ionization threshold by a theoretically calculated cross section  $\sigma_{th}$  for the ionization from a metastable initial state. A scaling factor  $f$  (which represents the fraction of the metastable admixture) is used as a fit parameter which is determined by the fit such that  $f \times \sigma_{th}$  matches the experimental data. The accuracy of the thus determined metastable fractions depends of course on the quality of the theoretical data which is not always easily known.

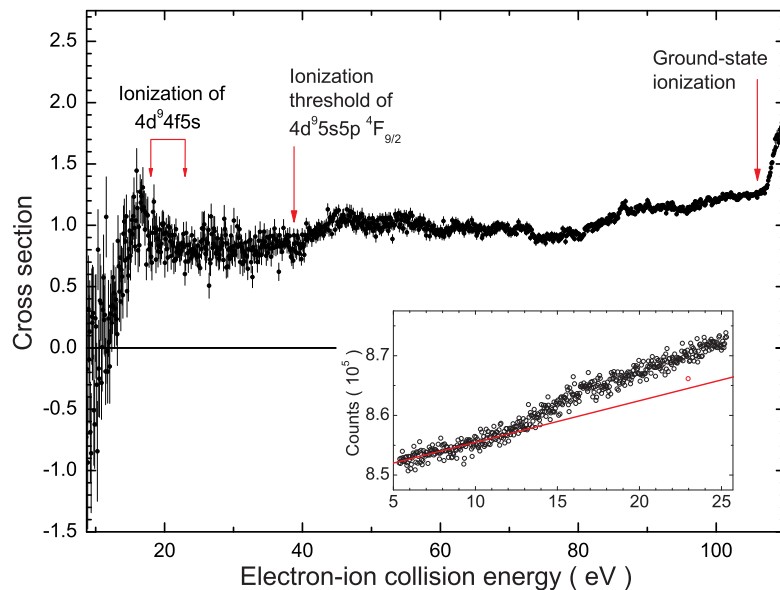


**Figure 4.4:** Single ionization of  $\text{Xe}^{7+}$ . Energy scan data, taken in the below-threshold energy region after subtraction of background. The inset illustrates the determination of this background by a fit to the observed countrate at energies below 10 eV. The ground-state ionization potential is 105.98 eV [112].

A widely used theoretical description of electron-impact ionization of many-electron atomic systems is the configuration-averaged distorted wave (CADW) method as implemented, e.g., in the LANL Atomic Physics Code package [111]. This code has been used in the present work for calculating both energies (see above) and the ionization cross sections of metastable ions. Due to the relatively complicated procedure of including possible indirect-ionization processes, the cross section calculations were only carried out for the direct ionization channels. This, however, limits the applicability of the above described procedure for quantifying the metastable fraction to cases where indirect-ionization processes are absent or insignificant.

As an example, the case of  $\text{Xe}^{9+}$  is shown in Fig. 4.5. In the inset, the below-threshold region is fitted by the sum of the calculated cross sections for removal of an outer electron from  $\text{Xe}^{9+}$  in  $4d^8 5s$  and  $4d^8 4f$  excited configurations. The corresponding scaling factors resulting from the fit are 0.15 and 0.1 respectively.

The uncertainties of the presently determined metastable fractions are different for each considered ion. The uncertainty of the fitting procedure does not exceed 20%. Another significant source of uncertainty is related to the question in how far the CADW calculations are able to reproduce the measured shape of the ionization cross section. The CADW calculations deliver reasonable results for direct ionization (where it could be judged) with a maximum discrepancy of 70% as observed for the case of  $\text{Xe}^+$ . Hence, being overcautious, we expect no error larger

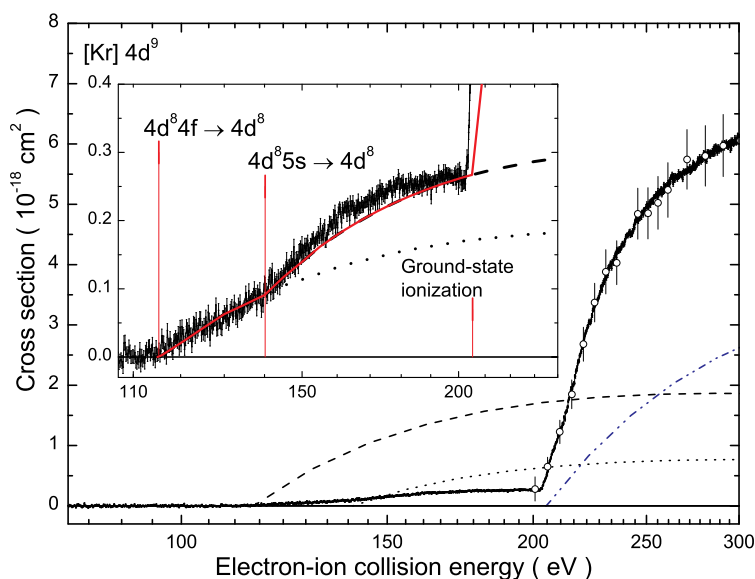


**Figure 4.5:** Single-ionization cross section of  $\text{Xe}^{9+}$  in the threshold region with the results of the CADW calculations [111] for the ionization of  $4d^8 5s$  and  $4d^8 4f$  excited configurations (dashed and dotted curves respectively) and for the ground-state ionization (dash-dotted curve). In the inset, the experimental data are fitted by the sum of these (the solid curve).

than 100% for the direct ionization of metastable ions by the CADW calculations. An additional source of error is the presence of contributions of indirect-ionization processes if they cannot be estimated reliably. In such cases the current method results therefore in an upper limit of the metastable fraction, however, not more than by 50%, since such strong indirect-ionization contributions should give rise to distinct and clearly recognizable cross-section features which were not observed. Therefore, we believe that the uncertainty of the whole procedure varies between 20 and 100% in the case where it can be applied at all. For these cases, the results are presented in the table 4.2. The first and the second columns identify the investigated ions and excited configurations. The energies given in the third column are the averaged excitation energies of the corresponding electron configurations calculated by the LANL Atomic Structure Code. Finally, the resulting fit coefficients representing the metastable fractions are given in the fourth column.

**Table 4.2:** Information on the metastable components in the primary  $\text{Xe}^{q+}$  ion beams.

Primary ion	Configuration	Excitation energy (eV)	Scaling factor $f$
$\text{Xe}^{3+}$	$5s^25p^25d$	17.57	0.09
$\text{Xe}^{5+}$	$5s5p5d$	33.98	0.05
$\text{Xe}^{9+}$	$4d^85s$	65.06	0.15
$\text{Xe}^{9+}$	$4d^84f$	89.96	0.1
$\text{Xe}^{10+}$	$4d^74f$	92.52	0.09
$\text{Xe}^{11+}$	$4d^64f$	94.72	0.2
$\text{Xe}^{12+}$	$4d^54f$	96.64	0.2
$\text{Xe}^{13+}$	$4d^44f$	98.34	0.11
$\text{Xe}^{14+}$	$4d^34f$	99.78	0.2
$\text{Xe}^{16+}$	$4d4f$	102.15	0.7
$\text{Xe}^{17+}$	$4p^65s$	128.98	0.45

### 4.1.3 Comparison with previous experimental data

The current section contains comparisons of the present cross sections with previously available experimental data. Cross sections for ionization of charge states 1 through 6 as well as for 8, 9 and 10 have been measured previously. In general, the overall agreement with the present data is found to be good, although small discrepancies occur. These will be discussed here. Probable discrepancy sources will be proposed.

The single-ionization cross section of  $\text{Xe}^+$  has been previously reported by Achenbach *et al.* [51], Man *et al.* [56] and Bell *et al.* [61]. The comparison with the present data (Fig. 4.6) shows agreement within the error bars with each of the previous cross-section data. All of the data sets generally follow the same trend of the cross section except for the data of Achenbach *et al.* which possess somewhat higher values at energies below 70 eV. Earlier measurements by Müller *et al.* [48] had been performed without the possibility to monitor beam overlap during the ionization experiments and have been found to underestimate the cross section. They are not compared here.

The available data sets show more scatter in the case of  $\text{Xe}^{2+}$ . Fig. 4.7 compares the present cross section with previous experimental data of Achenbach *et al.* [51], Griffin *et al.* [53], Danjo *et al.* [62], Matsumoto *et al.* [63] and of Man *et al.* [64]. Here, the present data and the data of Achenbach *et al.* are approximately 20% above the other data sets. The agreement of the present data with the results of Achenbach *et al.* is within the error bars. The fact that the present data are also in very good agreement with the data of Matsumoto *et al.* and Danjo *et al.* at energies above 350 eV and also in the threshold region and below. This would imply that similar metastable components were present in the different experiments. With this in mind, the discrepancy of the data sets between 30 eV and 300 eV is not clear.

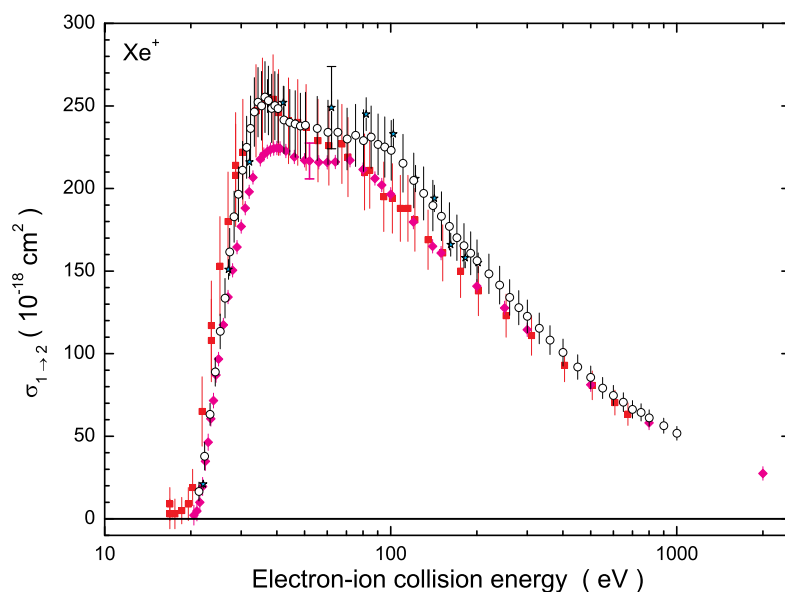


**Figure 4.6:** Single ionization of  $\text{Xe}^+$ . Comparison with previous experimental data. Open circles represent the present data. The solid squares are the data of Achenbach *et al.* [51], the solid diamonds are the data of Man *et al.* [56], and the open stars denote the data of Bell *et al.* [61]. The error bars represent the total uncertainties except for the data of Man *et al.* and Bell *et al.*. For these, the displayed error bars represent statistical uncertainties and the total uncertainties are given by the capped error bars in the cross-section maxima.

A similar situation can be observed for  $\text{Xe}^{3+}$  in Fig. 4.8, where the comparison of the present data to the data of Achenbach *et al.* [51] and of Gregory *et al.* [65] is shown. The present data exceed the data of Gregory *et al.* by about 25%, but are in a good agreement with the data of Achenbach *et al.* The present data, however, clearly reveal non-zero cross sections below the ground-state ionization threshold at 40.9 eV [112] meaning that excited metastable ion species were present in the primary ion beam during the measurement. Gregory *et al.* also reported on the metastable content present in their experiment. This, however, is assumed to be due to ions in the excited states within the ground state configuration because the reported ionization onset is located at around 40 eV which is only 0.9 eV below the ground-state ionization threshold [112]. The cross section onset in the present data set for  $\text{Xe}^{3+}$  is at around 24.5 eV as revealed by a detailed energy scan measurement (see Fig. B.3). This indicates the presence of a (probably small) much more highly excited metastable component in the parent beam in addition to possible excited components within the ground state configuration, that is in the entire coincidence with the results of performed life times calculations (see Appendix E). This may explain the slight discrepancy between the trends of the two discussed cross sections in the energy region below maximum which can be noticed after

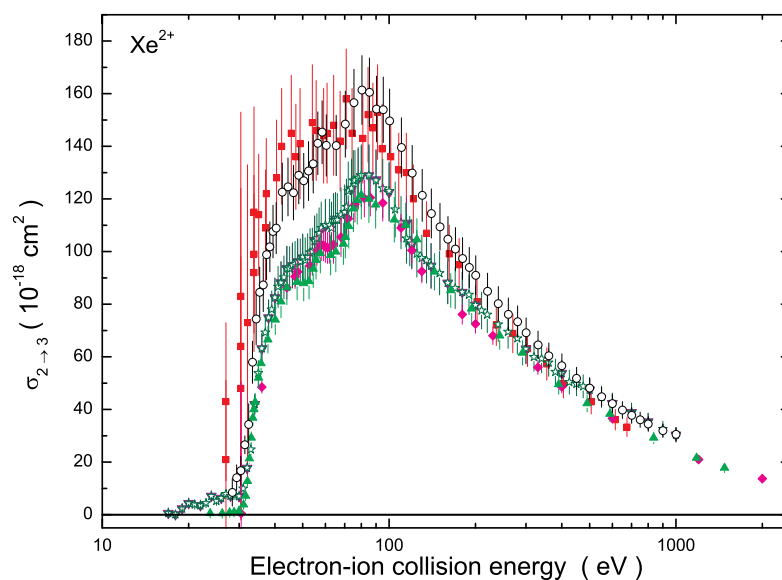


**Figure 4.7:** Single ionization of  $\text{Xe}^{2+}$ . Comparison with previous experimental data. Open circles represent the present data, solid squares are the data of Achenbach *et al.* [51], solid diamonds are the data of Man *et al.* [64], solid triangles are the data of Griffin *et al.* [53], flipped solid triangles are the data of Danjo *et al.* [62] and stars denote the data of Matsumoto *et al.* [63]. The error bars represent the total uncertainties for all data sets.

scaling both data sets together.

Clearly noticeable discrepancies between the cross-section trends of the present and previous measurements can be observed for xenon charge states 4, 5, and 6 (Figs.4.9–4.11). Single-ionization cross sections for these charge states have been measured previously by the Oak Ridge group and reported in the papers by Griffin *et al.* ( $\text{Xe}^{4+}$  and  $\text{Xe}^{5+}$ ) [53] and by Gregory and Crandall ( $\text{Xe}^{6+}$ ) [67]. The data for  $\text{Xe}^{4+}$  have also been reported by Achenbach *et al.* [51]. For all of the mentioned cross sections, the present data possess values which exceed those from Oak Ridge at the energies around and below the cross-section maxima. The agreement of the present data with the data of Achenbach *et al.*, however, is within the error bars in the entire experimental energy range and is especially good beyond 100 eV. The discrepancies between the present and the Oak Ridge data may be attributed to the presence of different metastable contents in the primary beams used in the experiments. This is supported by the fact that the observed cross-section onsets in the present experiment (see Figs. B.4–B.6) are located significantly lower than those observed by the Oak Ridge groups. This is especially pronounced for  $\text{Xe}^{6+}$  (Fig. 4.11), where a 10 eV difference can be seen between the ionization onsets.

For  $\text{Xe}^{4+}$  and  $\text{Xe}^{6+}$ , the present and the Oak Ridge data are in quite good agreement with one another above 300 eV, whereas for  $\text{Xe}^{5+}$ , the data of Griffin *et*

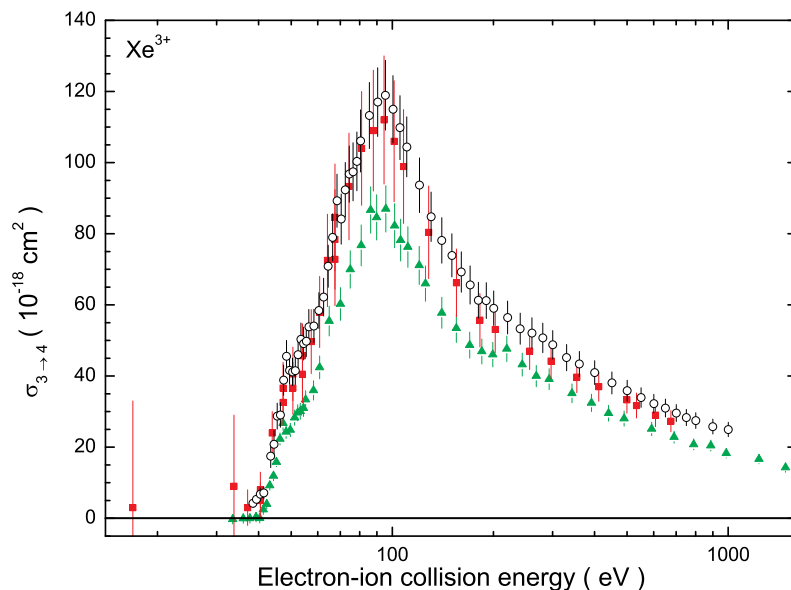


**Figure 4.8:** Single ionization of  $\text{Xe}^{3+}$ . Comparison with previous experimental data. Open circles represent the present data, solid squares are the data of Achenbach *et al.* [51] and solid triangles are the data of Gregory *et al.* [65]. The error bars represent the total uncertainties for all data sets.

*al.* tend to increase beyond the present data from around 200 eV on.

No data have been reported previously on single ionization of  $\text{Xe}^{7+}$ . The present data are provided in Fig. B.7.

Data on single-ionization cross section of  $\text{Xe}^{8+}$  are available from the works of Bannister *et al.* [71], of Hofmann *et al.* [74], and of Stenke *et al.* [75]. The comparison in Fig. 4.12 reveals good agreement of the present data with the data of Bannister *et al.*. Comparison with the data of Hofmann *et al.* and of Stenke *et al.* shows differences between the present and the previous cross-section values of up to about 15%. Nevertheless, agreement within the given error bars can still be stated. Non-zero cross-section values are reported by Stenke *et al.* below 90 eV, where no ionization signal have been seen in the present measurements.

For  $\text{Xe}^{9+}$  and  $\text{Xe}^{10+}$ , comparison of the present data with the previous measurements reported by Hofmann *et al.* (Figs. 4.13 and 4.14) shows again up to 15% difference between the data sets. Still, the cross sections agree within the mutual given uncertainty limits. To our knowledge, no previous data have been reported on single ionization of  $\text{Xe}^{11+}$  and higher ionization stages.

In summary, the comparisons made in this section reveal agreement of the present data with the data sets reported previously. Practically all of the existing measurements are within margins of  $\pm 20\%$  from their average. Mostly, the observed discrepancies may be attributed to different metastable contamination of

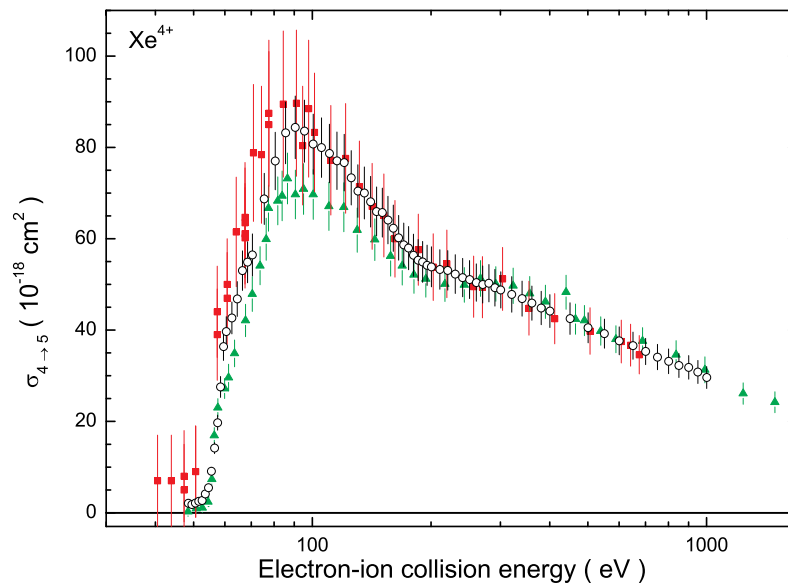


**Figure 4.9:** Single ionization of  $\text{Xe}^{4+}$ . Comparison with previous experimental data. Open circles represent the present data, solid squares are the data of Achenbach *et al.* [51] and solid triangles are the data of Griffin *et al.* [53]. The error bars represent the total uncertainties for all data sets.

the primary ion beams which is associated with larger discrepancies in the threshold energy region.

#### 4.1.4 Comparison with previous theoretical data

Many calculations on single ionization of xenon and its ionization stages employing different methods have been reported. An overview is given in Tab. 1.1 in Chapter 1. Loch *et al.* have performed cross-section calculations for the entire xenon isonuclear sequence, employing the semi-relativistic configuration-average distorted-wave method [23]. However, their results are not fully available yet. Povyshev *et al.* have compiled data sets of single-ionization cross sections for isonuclear sequences of several elements including xenon on the basis of experimental data and calculations performed by using the ATOM code [22].

In this section we compare the present experimental data with available results of those calculations which include processes of indirect ionization via interaction of the incident electron with inner-shell electrons. Restricting the calculations to direct ionization processes is not adequate and leads to strong underestimation of the single-ionization cross sections.

Single-ionization cross sections for xenon ionization stages from 1 through 6 have been calculated by Griffin *et al.* [53]. The comparison of their results with the

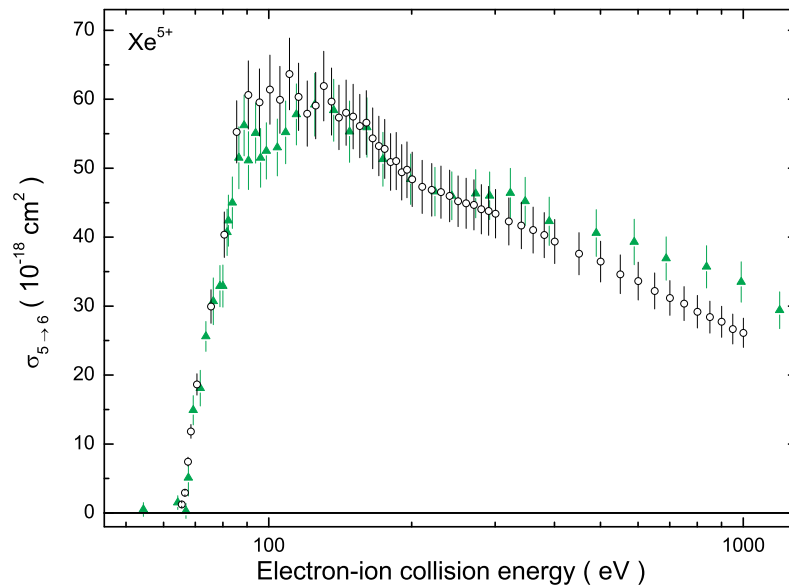


**Figure 4.10:** Single ionization of  $\text{Xe}^{5+}$ . Comparison with previous experimental data. Open circles represent the present data, solid triangles are the data of Griffin *et al.* [53]. The error bars represent the total uncertainties for all data sets.

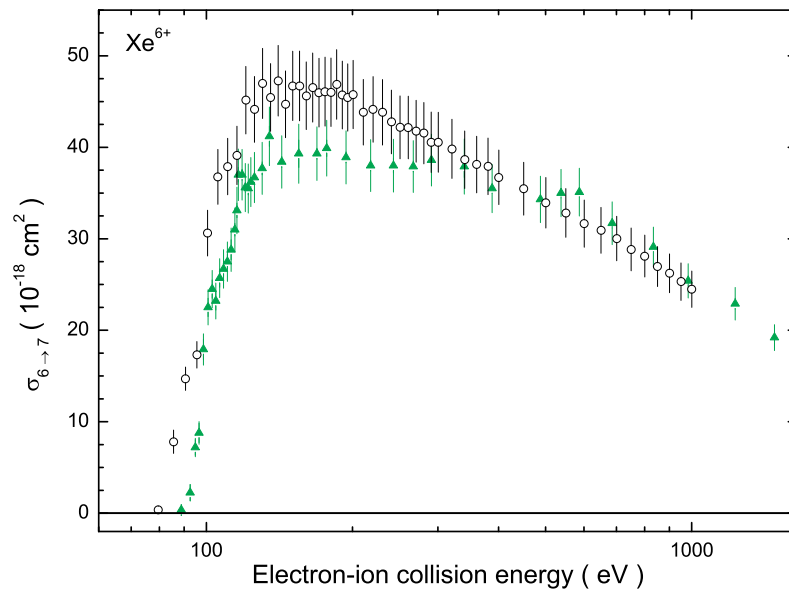


**Figure 4.11:** Single ionization of  $\text{Xe}^{6+}$ . Comparison with previous experimental data. Open circles represent the present data, solid triangles are the data of Gregory and Crandall [67]. The error bars represent the total uncertainties for all data sets.

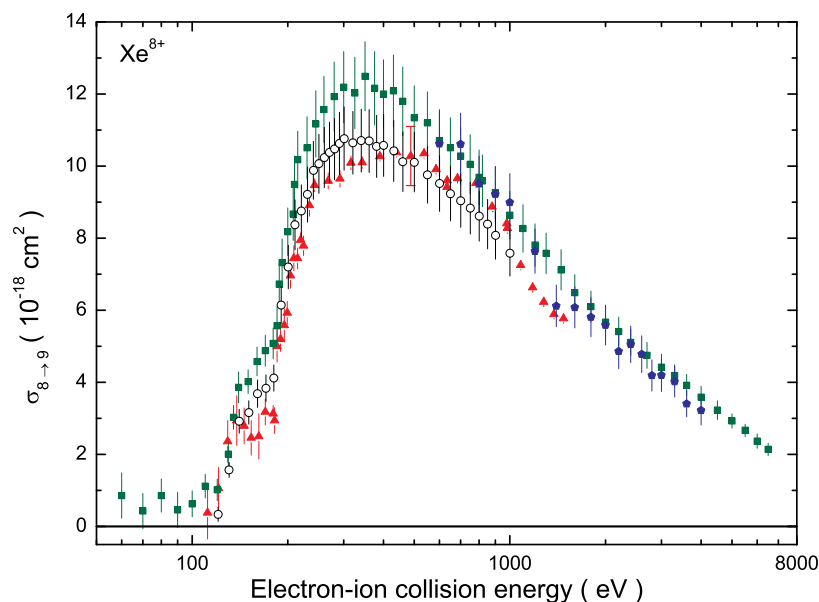


**Figure 4.12:** Single ionization of  $\text{Xe}^{8+}$ . Comparison with previous experimental data. Open circles represent the present data, solid triangles are the data of Bannister *et al.* [71], solid pentagons are the data of Hofmann *et al.* [74] and solid squares denote the data of Stenke *et al.* [75]. The error bars represent the total uncertainties except for the data of Bannister *et al.*. For these, the shown error bars represent statistical uncertainties and the total uncertainties are given by the bolder capped error bar in the cross-section maximum.

present experimental data is shown in Figs. 4.15 – 4.20. In their calculations, Griffin *et al.* included direct-ionization and excitation-autoionization processes. For  $\text{Xe}^{6+}$ , they also report on calculations of resonant-excitation-double-autoionization processes but those are not shown here.

The comparison of the data sets for  $\text{Xe}^+$  reveals rather poor agreement (see Fig. 4.15). The data of Griffin *et al.* describe the measured cross section well only for energies below 32 eV. At higher energies, where the experimental cross section reaches its maximum, the theoretical cross-section curve does not reproduce the form of the experimental data. It increases further up to a maximum at 53 eV, where the discrepancy from the present experimental results reaches 40%. The contributions from EA processes involving excitation of the  $4d$  subshell which were predicted by Griffin *et al.* at 73 eV do not show up in the experiment so prominently. Also, the contribution of direct ionization of the  $4d$  subshell seems to be overestimated. In addition, we compare the present data on  $\text{Xe}^+$  with the direct ionization cross sections calculated using the Los Alamos National Laboratory (LANL) code package [111] which employs the CADW method. The result of this overestimates the experimental data at energies beyond 40 eV. This is surprising in view of the fact that the CADW calculation includes only direct ionization.

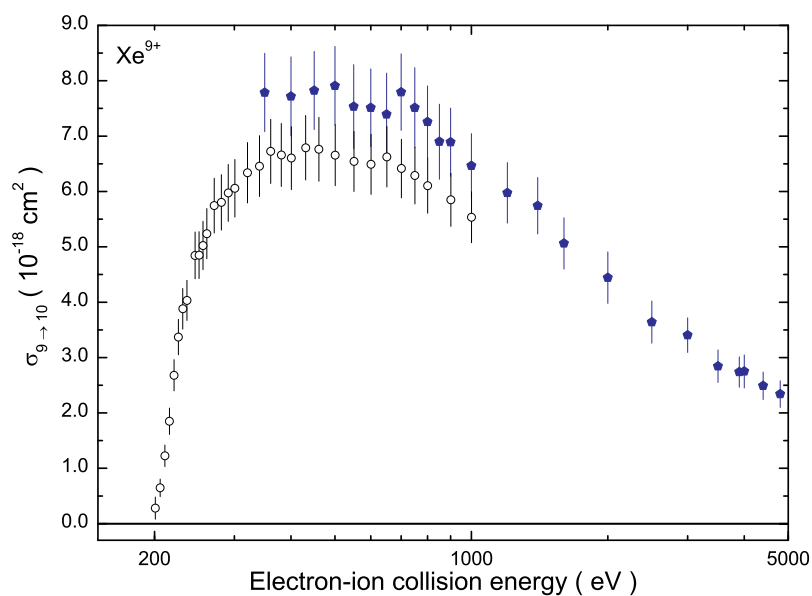


**Figure 4.13:** Single ionization of  $\text{Xe}^{9+}$ . Comparison with previous experimental data. Open circles represent the present data, solid pentagons are the data of Hofmann *et al.* [74]. The error bars represent the total uncertainties for both data sets.

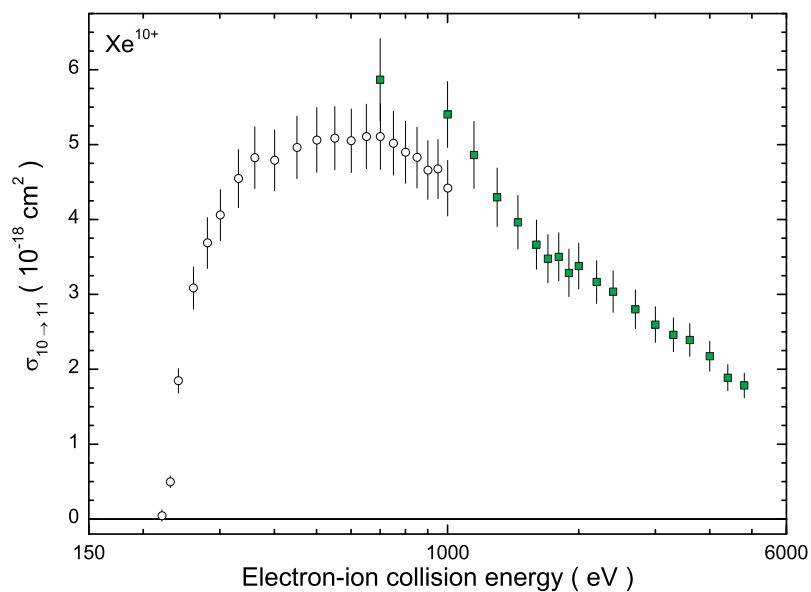


**Figure 4.14:** Single ionization of  $\text{Xe}^{10+}$ . Comparison with previous experimental data. Open circles represent the present data, solid pentagons are the data of Hofmann *et al.* [74]. The error bars represent the total uncertainties for both data sets.

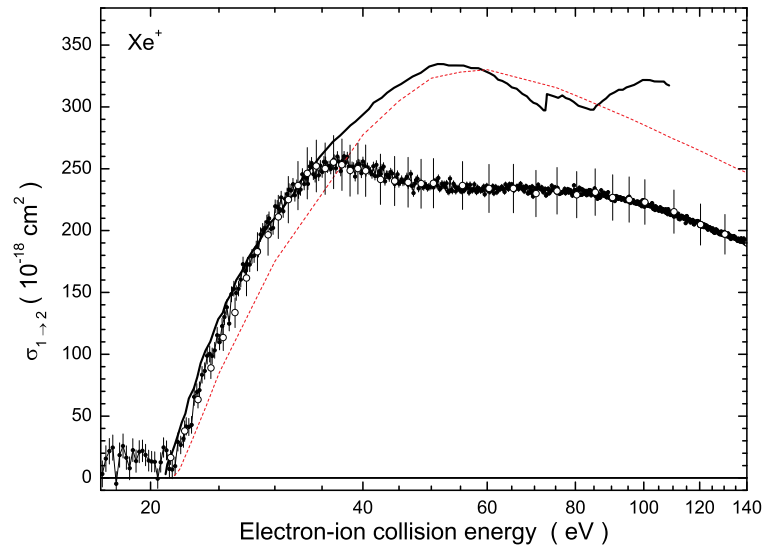


**Figure 4.15:** Single ionization of  $\text{Xe}^+$ . The present experimental results are compared with theoretical data. Open circles represent the present absolute data points, smaller filled circles represent the energy scan data. The thick curve is the result of Griffin *et al.* [53] and the thin dashed curve shows the outcome of the present CADW calculation DI [111].

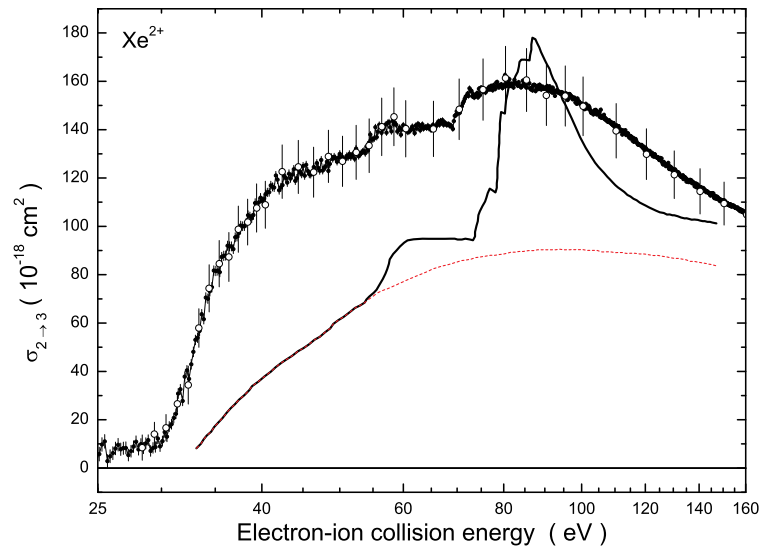


**Figure 4.16:** Single ionization of  $\text{Xe}^{2+}$ . The present experimental results are compared with theoretical data. Open circles represent the present absolute data points, smaller filled circles represent the energy scan data. The calculated data of Griffin *et al.* [53]: the thin dashed curve is the direct ionization cross section and the thick black curve is the excitation-autoionization cross section added to the direct ionization cross section.

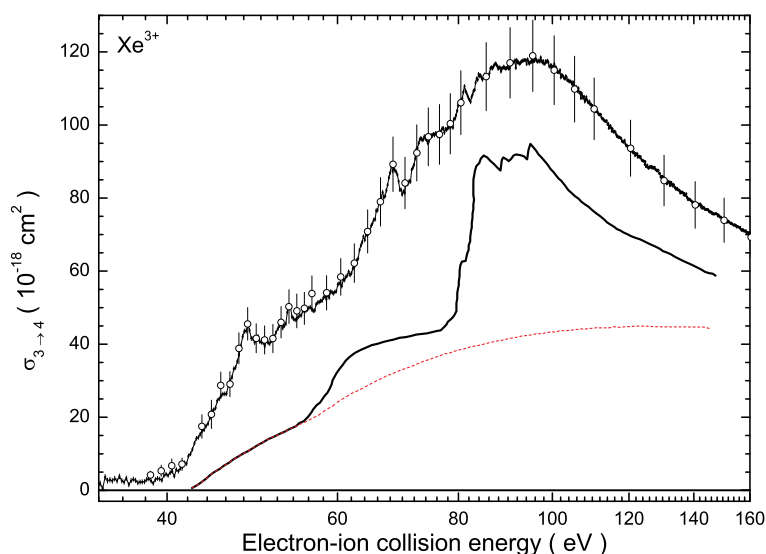


**Figure 4.17:** Single ionization of  $\text{Xe}^{3+}$ . The present experimental results are compared with theoretical data. Open circles represent the present absolute data points, smaller filled circles represent the energy scan data. The calculated data of Griffin *et al.* [53]: the thin dashed curve is the direct ionization cross section and the thick black curve is the excitation-autoionization cross section added to the direct ionization cross section.

In Fig. 4.16, the present experimental cross section for  $\text{Xe}^{2+}$  is compared to the theoretical calculations of Griffin *et al.* and the present CADW direct-ionization calculations. The agreement of theory with the experiment is poor. The theoretical data mostly underestimate the total cross section. Possible reasons of this could be that resonant processes have not been included in the calculation and that metastable ions were present in the experiment. On the other hand, the excitation-autoionization contribution associated with the  $4d \rightarrow 4f$  transition [53] has been overestimated. The calculated direct-ionization cross-section curve suggests that the contribution of the indirect ionization processes to the total cross section is in general about 50% over the entire experimental energy range with larger contributions at lower energies.

The theoretical and experimental data for  $\text{Xe}^{3+}$  (Fig. 4.17) are quite similar in shape, though the theoretical curve of Griffin *et al.* somewhat underestimates the experimentally obtained cross-section values. At energies below 40 eV the scan measurement reveals a metastable content in the primary ion beam of the present experiment. The role of resonant contributions below the cross section maximum can be seen from this comparison as well. The calculated direct-ionization cross section suggests that the indirect-ionization contributions are at least half of the measured cross section at its maximum (even when taking into account metastable-ionization contributions).

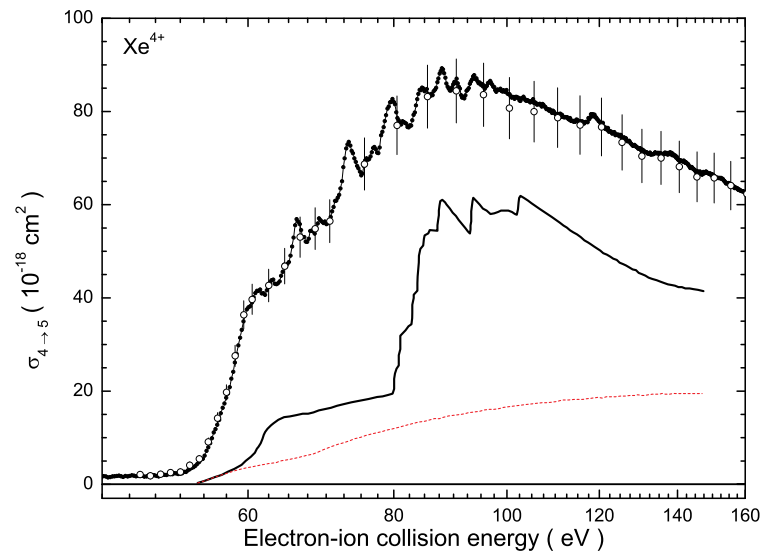


**Figure 4.18:** Single ionization of  $\text{Xe}^{4+}$ . The present experimental results are compared with theoretical data. Open circles represent the present absolute data points, small filled circles represent the energy scan data. The calculated data of Griffin *et al.* [53]: the thin dashed curve is the direct ionization cross section and the thick black curve is the excitation-autoionization cross section added to the direct ionization cross section.

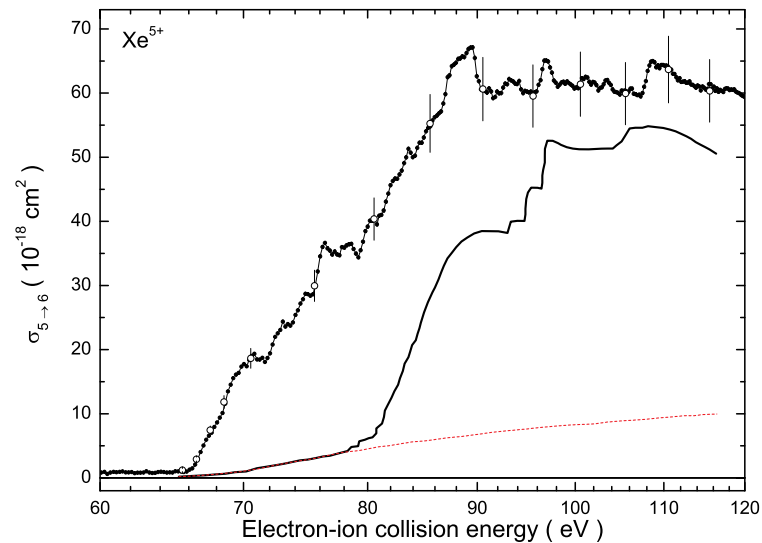


**Figure 4.19:** Single ionization of  $\text{Xe}^{5+}$ . The present experimental results are compared with theoretical data. Open circles represent the present absolute data points, small filled circles represent the energy scan data. The calculated data of Griffin *et al.* [53]: the thin dashed curve is the direct ionization cross section and the thick black curve is the excitation-autoionization cross section added to the direct ionization cross section.

For  $\text{Xe}^{4+}$ , the discrepancy between the present experimental and the theoretical data of Griffin *et al.* is larger than for  $\text{Xe}^{3+}$  (Fig. 4.18). Besides the effects due to small metastable admixtures to the primary ion beam, this can be caused by the increasing role of resonant processes, as suggested by the rich resonant structure observed in the experiment. In addition, indirect ionization processes involving excitation of the  $4p$ -subshell which show up in the experimental cross section at energies above 110 eV have not been included in the calculations. The calculated direct-ionization cross section curve suggests that indirect ionization clearly dominates the total single-ionization cross section.

The comparison for  $\text{Xe}^{5+}$  (Fig. 4.19) reveals the clearly dominant role of indirect channels in single ionization of this ion. The cross section calculated by Griffin *et al.* suggests high contributions due to excitation-autoionization processes. The theoretical results, however, are lower than the present data, probably, because REDA processes were not included in the calculation. Also the scan measurement reveals a small fraction of metastable ions admixed to the primary beam of the present experiment.

Finally, the comparison for  $\text{Xe}^{6+}$  is shown in Fig. 4.20. In their paper, Griffin *et al.* [53] reported on the remarkable agreement of their calculations with the experimental data of Gregory and Crandall [67]. As has been shown in the previous section, because of different metastable primary beam components, the present data exceed those of Gregory and Crandall and, hence, the discrepancy in the current comparison appears to be larger. However, to our opinion, the calculated contribution due to the  $4d \rightarrow 4f$  excitation (from 101 eV on) is somewhat overestimated since the obtained theoretical curve exceeds the experimental data of Gregory and Crandall leaving no space for the resonant processes observed in the present work. In their paper, Griffin *et al.* have also presented their calculations for resonant-excitation-double-autoionization contributions. We do not compare these here because of the present data contain massive (amongst others resonant) contributions of indirect ionization of the metastable content present in the primary ion beam. These contributions could possibly twist the structure above the ionization threshold as well and make the comparison irrelevant. The calculated by Griffin *et al.* direct-ionization cross section curve suggests that the role of direct ionization is minor.

CADW calculations of the single-ionization cross section of  $\text{Xe}^{8+}$  were reported by Bannister *et al.* [71]. Fig. 4.21 shows their results for total ionization of the ground-state  $\text{Xe}^{8+}$  (lower solid curve) and of ions in the first-excited  $4d^9 5s$  configuration (upper solid curve) compared to the present experimental results. The calculations reveal that the presence of metastable ions in the experiment dramatically affects the measured total ionization cross section. Indirect ionization due to  $3d$ -subshell excitation have not been included in these calculations. Corresponding structures show up in the experimental cross section at energies of about 600 eV and higher (see Fig. B.8). The long-dashed and short-dashed curves represent the calculations for direct ionization of ions in the ground state and in the first excited configuration, respectively, indicating that the relative importance of the direct ion-

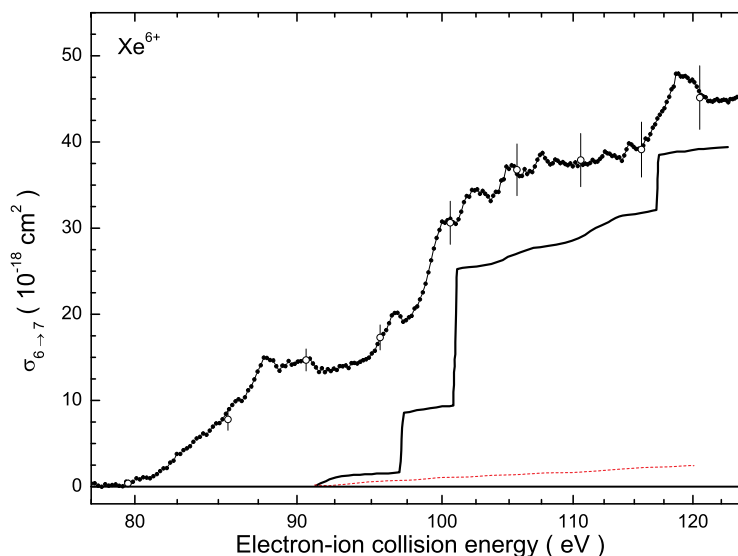


**Figure 4.20:** Single ionization of  $\text{Xe}^{6+}$ . The present experimental results are compared with theoretical data. Open circles represent the present absolute data points, small filled circles represent the energy scan data. The calculated data of Griffin *et al.* [53]: the thin dashed curve is the direct ionization cross section and the thick black curve is the excitation-autoionization cross section added to the direct ionization cross section.

ization contributions is enhanced as compared to the lower charge states such as  $\text{Xe}^{6+}$ .

Comprehensive theoretical studies on single ionization of  $\text{Xe}^{22+}$  through  $\text{Xe}^{25+}$  were reported in Refs. [76, 77, 78, 79, 80]. All these calculations include direct-ionization and excitation-autoionization processes involving excitations of the  $3d$ - and  $3p$  subshells. The comparisons of the theoretical cross sections with the present experimental data are shown in Figs. 4.22–4.25. For these comparisons the contributions (extrapolated up to 1000 eV) of the very highly excited metastable ions discussed in Section 4.1.2 have been subtracted from the measured apparent cross sections (see Fig. 4.2). It is assumed that the fractions of such metastable states are very small but provide large contributions to the ionization signal because of their low ionization threshold. Thus, the experimental cross sections in Figs. 4.22–4.25 represent cross sections for the ionization of ground-state ions. They might be considered lower limits of the true cross sections since they are normalized to the sum of the ground-state and (small) metastable-ion components in the parent ion beams.

Fig. 4.22 displays the present experimental data on single ionization of  $\text{Xe}^{22+}$  in comparison with the calculations by Mandelbaum *et al.* [76]. In Fig. 4.23, for  $\text{Xe}^{23+}$ , the ionization-threshold energy reported by Mandelbaum *et al.* [77] is roughly 45 eV higher than that observed in the experiment. The calculated cross

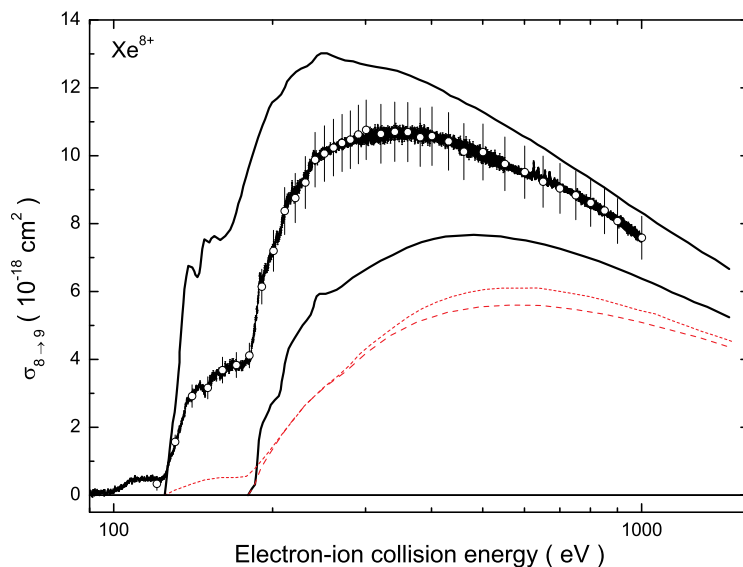


**Figure 4.21:** Single ionization of  $\text{Xe}^{8+}$ . The present experimental results are compared with theoretical data. Open circles represent the present absolute data points, small filled circles represent the energy scan data. The thick lower curve is the result of Bannister *et al.* [71] for ionization of the ground-state ions. The upper solid curve is their result for ionization of the  $4d^9 5s$  excited configuration. The thin dashed and short-dashed curves are the results for the direct ionization of ground-state ions and of ions in the the  $4d^9 5s$  excited configuration, respectively.

sections of Mitnik *et al.* [78] and of Pindzola *et al.* [79] for  $\text{Xe}^{24+}$  are compared to the present data in Fig. 4.24. Surprisingly, the data of Pindzola *et al.* are significantly lower than both the experiment and the calculations of Mitnik *et al.*. In addition, their calculated threshold is located 35 eV higher than the one calculated by Mitnik *et al.* which perfectly matches the experimental value of 815 eV. The  $\text{Xe}^{25+}$  data of Mitnik *et al.* [80] are compared to the present data in Fig. 4.25. The comparison reveals that the slope of the experimental data is somewhat less steep than theoretically predicted. Therefore, it is possible that the role of excitation-autoionization processes just beyond the ground-state ionization threshold is overestimated in the calculations.

In summary, the comparison of the present data with the available theoretical calculations on single ionization of the various xenon ionization stages revealed theoretical difficulties to accurately describe ionization in such complicated atomic systems as xenon ions, where inclusion of indirect ionization mechanisms is mandatory. As shown above, these mechanisms play an important role and often dominate the total ionization cross section. A special issue are resonant capture processes followed by autoionization (REDA). Inclusion of these leads to significant complications in the calculations and have, therefore, been considered only

in a few theoretical calculations so far. However, the present experimental data for highly charged ions reveal that these processes make significant contributions to the total cross sections.

Generally, quantitative comparisons between experimental and theoretical data bear significant uncertainties because of the unknown content of metastable ions in the primary ion beam.

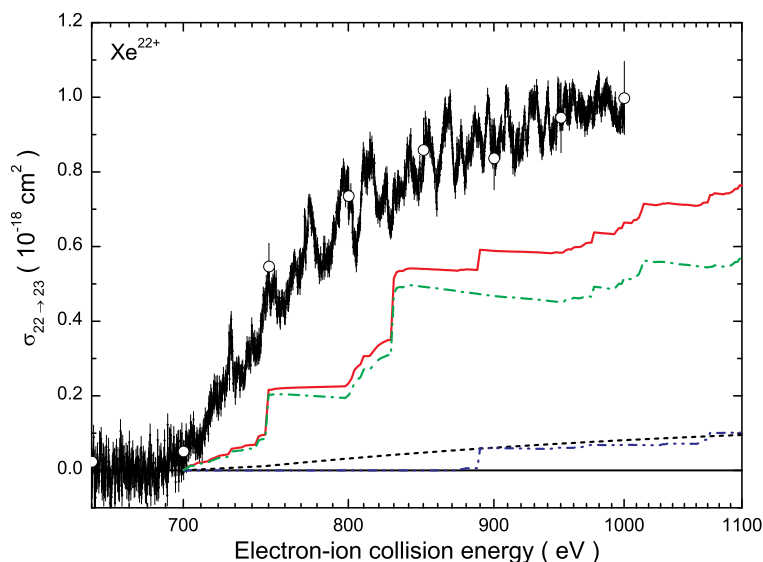


**Figure 4.22:** Single ionization of  $\text{Xe}^{22+}$ . The present experimental results are compared with theoretical data. Open circles represent the present absolute data points, small filled circles represent the energy scan data, both after subtraction of "background" arising from very highly excited metastable ions (see text). Theoretical calculations of Mandelbaum *et al.* [76]: the dashed curve is the DI cross section, the dash-dotted- and dash-dot-dotted curves are the cross sections of EA processes involving excitations of  $3d$  and  $3p$  subshells respectively and the solid curve represents the sum of DI+EA.

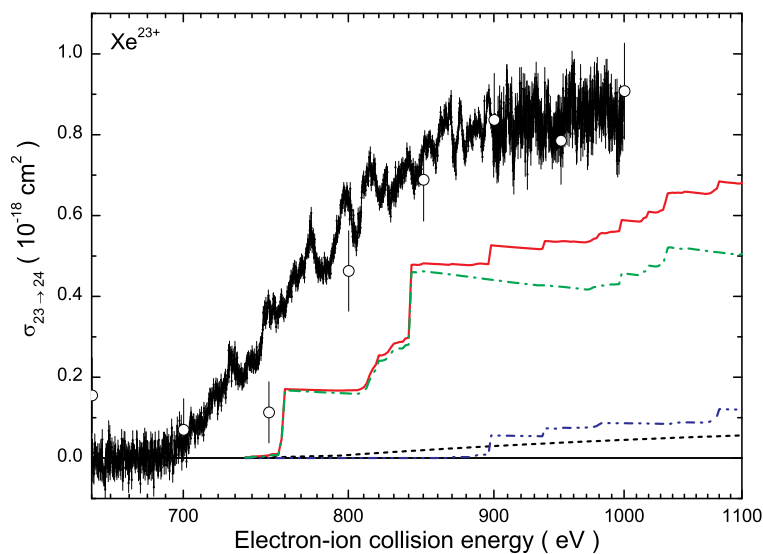


**Figure 4.23:** Single ionization of  $\text{Xe}^{23+}$ . The present experimental results are compared with theoretical data. Opened circles represent the present absolute data points, small filled circles represent the energy scan data, both after subtraction of "background" arising from very highly excited metastable ions (see text). Theoretical calculations of Mandelbaum *et al.* [77]: the dashed curve is the DI cross section, the dash-dotted- and dash-dot-dotted curve are the cross sections of EA processes involving excitations of  $3d$ - and  $3p$  subshells respectively and the solid curve represents the sum of DI+EA.

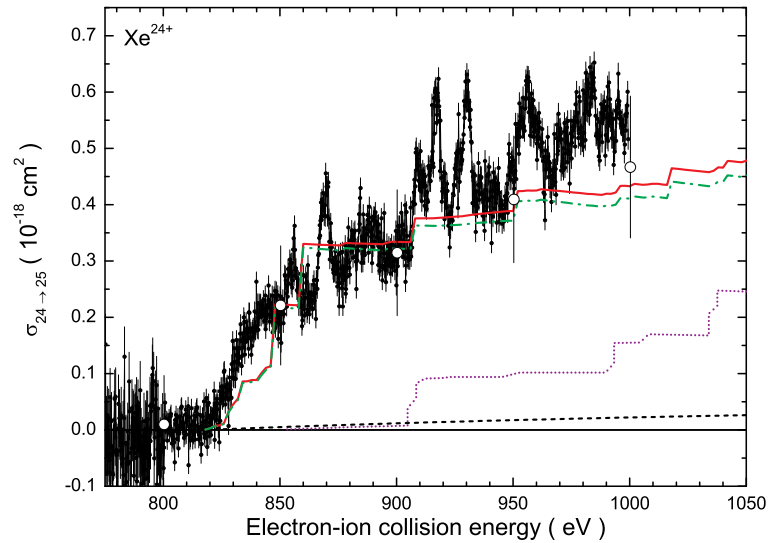


**Figure 4.24:** Single ionization of  $\text{Xe}^{24+}$ . The present experimental results are compared with theoretical data. Open circles represent the present absolute data points, small filled circles represent the energy scan data, both after subtraction of "background" arising from very highly excited metastable ions (see text). Theoretical calculations of Mitnik *et al.* [78]: the dashed curve is the cross section of the direct-ionization process, the dash-dotted curve is the cross section of EA processes involving excitations of  $3d$ - and  $3p$  subshells and the solid curve represents the sum of DI and EA contributions. The dotted curve denotes the data of Pindzola *et al.* [79]

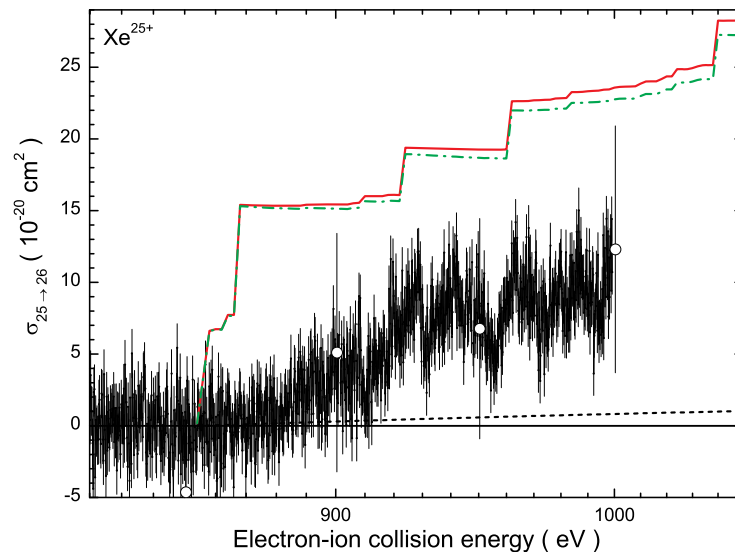


**Figure 4.25:** Single ionization of  $\text{Xe}^{25+}$ . The present experimental results are compared with theoretical data. Open circles represent the present absolute data points, small filled circles represent the energy scan data, both after subtraction of "background" arising from very highly excited metastable ions (see text). Theoretical calculations of Mitnik *et al.* [80]: the dashed curve is the DI cross section, the dash-dotted curve is the cross section of EA processes involving excitations of  $3d$ - and  $3p$  subshells and the solid curve represents the sum of DI+EA.

## 4.2 Multiple ionization of xenon ions

When the incident electron has a sufficiently high energy for removal of two or more electrons from a target ion multiple ionization may occur. In many cases, it is assumed that the cross sections for multiple ionization are significantly smaller than the cross sections for single ionization. Consequently, multiple ionization is often neglected in plasma modeling. However, it was experimentally shown, e.g., for  $\text{Xe}^{q+}$  ( $q = 1, 2, \dots, 4$ ) that multiple ionization can be as important as single ionization [49] and, therefore, should be considered in the modeling of high-temperature plasmas particularly for high- $Z$  elements.

In the following subsection, the data are presented in the form of energy scans normalized to the separately measured absolute cross-section values. For better viewing, each data set (except for the two top cross-section curves) has been multiplied by a certain factor provided individually for the each data set in the figure.

### 4.2.1 Double ionization of $\text{Xe}^{q+}$ ions ( $q = 1, 2, \dots, 17$ )

The present cross-section data on double-ionization of  $\text{Xe}^+$  through  $\text{Xe}^{17+}$  are displayed in Fig. 4.26. In previous papers on lower charged xenon ions, it has been concluded that the double ionization process is dominated by inner-shell ionization followed by autoionization, i.e., by ionization-autoionization (IA) processes. Accordingly, we can distinguish the first group of the data comprising cross sections for ionization stages 1 to 4. For these ions double ionization proceeds mainly via direct knock out of a  $4d$  electron with subsequent ejection of another electron from the O ( $n = 5$ ) shell. The pronounced cross-section maxima observed represent the giant-resonance features described previously [37, 55, 116].

The resonant structures observed in the cross sections of  $\text{Xe}^{3+}$  through  $\text{Xe}^{5+}$  result from *resonant-excitation-triple-autoionization* (RETA) processes involving excitation of the  $4s$  subshell. For  $\text{Xe}^{4+}$  and  $\text{Xe}^{5+}$ , the cross sections show evidences for contributions due to *excitation-double-autoionization* (or EDA) involving excitation of the  $4s$  subshell at around 215 eV and 217 eV respectively (see Figs. B.29 and B.30). In these cross sections, there are also humps which have onsets close to  $4s$ -subshell ionization thresholds (273 eV for  $\text{Xe}^{4+}$  and 287 eV for  $\text{Xe}^{5+}$ ), which probably correspond to IA processes involving this subshell.

The cross sections from  $\text{Xe}^{4+}$  onwards reveal resonant structure corresponding to RETA processes involving excitation of the  $3d$  subshell. For  $\text{Xe}^{7+}$  this is most pronounced. From  $\text{Xe}^{5+}$  onwards, the double-ionization cross sections show also well recognizable contributions due to EDA processes involving the  $3d$  subshell (starting at 670 eV for  $\text{Xe}^{5+}$ ). They become more significant with further increase of the charge state. RETA processes involving excitation of the  $3p$  subshell start to create visible structures in the cross section of the ionization stage 7 (at the energies from around 880 eV on). With further increase of ionization stage, these structures gain magnitude, extend and shift towards lower energies. Most of these cross sections have been separately investigated in some more details in the

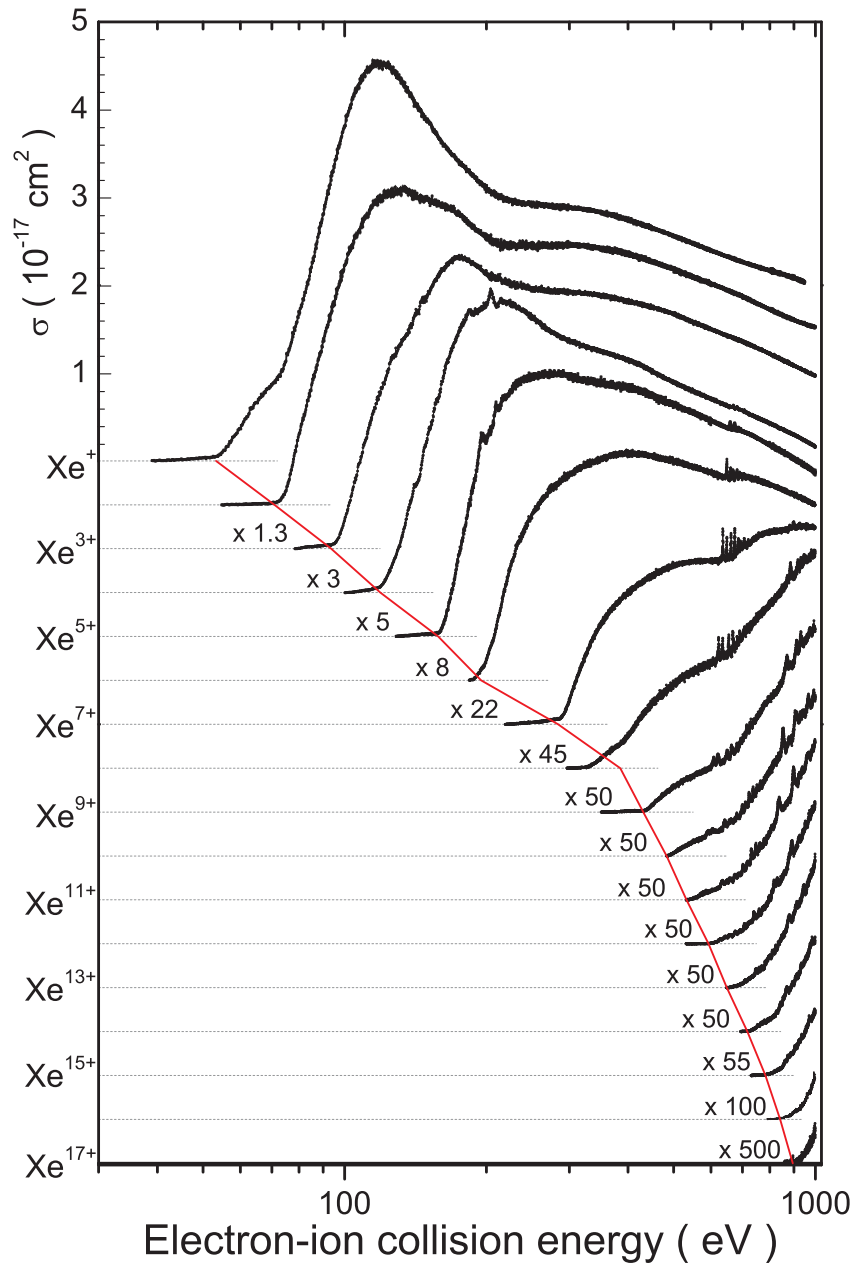


**Figure 4.26:** Overview over the present double-ionization cross sections of  $\text{Xe}^{q+}$  ions ( $q = 1, 2, \dots, 17$ ). The scale is in units of  $10^{-17} \text{ cm}^2$  and the cross section for each ion stage is shifted downwards by  $0.5 \times (q - 1) \times 10^{-17} \text{ cm}^2$ . The thin solid line connects the observed ground-state ionization thresholds.

Bachelor thesis of J. Rausch ( $\text{Xe}^{6+}, \dots, \text{Xe}^{10+}$ ) [117] and in the Diploma thesis of J. Rudolph ( $\text{Xe}^{11+}, \dots, \text{Xe}^{17+}$ ) [118].

Almost all cross-section curves possess non-zero values below the double-ionization thresholds of the respective ground states. This indicates the presence of metastable ions in the primary ion beams. Ionization of metastable ions, however, has a smaller influence on the double-ionization cross sections (at least in the near-threshold region) as compared to, e.g., single-ionization cross sections. The exceptions are double-ionization cross sections of  $\text{Xe}^{6+}$  and  $\text{Xe}^{8+}$ . The cross sections of these ions have somewhat higher values below threshold.

### 4.2.2 Multiple ionization of $\text{Xe}^+$ ions

Figure 4.27 shows the present experimental results on multiple ionization of singly charged xenon ions. It contains the energy scan data for single through eightfold ionization normalized to absolute cross-section measurements.

One can observe a dramatic decrease of the cross sections with increasing number of electrons removed. The measured values are between  $2.55 \times 10^{-16} \text{ cm}^2$  at 34.3 eV for single ionization and  $7.1 \times 10^{-24} \text{ cm}^2$  at 1000 eV for ninefold ionization (see Fig. B.53). The latter value is almost 3 times smaller than the smallest ionization cross section ever measured using interacting beam techniques [119]. The cross sections for single- and double ionization have already been shown and described in sections section 4.1.1 and section 4.2.1 respectively. The cross sections for triple and fourfold ionization show humps which could be attributed to the contributions from *ionization-double-* and *ionization-triple-autoionization* processes (IDA and ITA respectively) involving removal of an electron from the  $4s$ - and (for triple-ionization cross section only)  $4p$  subshells. In the fourfold-ionization cross section at 690 eV, there is a clear onset of an ITA process involving  $3d$ -electron removal. Contributions of *ionization-fourfold-autoionization* processes involving removal of an electron from the  $3d$ - and  $3p$  subshells can be clearly recognized at 690 and 960 eV in the fivefold ionization cross section of singly charged xenon ion. Removal of a  $3d$  electron with subsequent ejection of four outer electrons contributes more than 10% to the total cross section.

In the sixfold-ionization cross section, the steep onsets at the electron energies equal to the binding energies of  $3d$  and  $3p$  subshells (Fig. B.50) suggest that multi-electron-autoionization processes induced by direct removal of an electron out of these subshells are almost equally strong as multi-target-electron ionization processes. For seven- and eightfold-ionization cross sections (Figs. B.51 and B.52), they clearly dominate.

### 4.2.3 Multiple ionization of $\text{Xe}^{6+}$ and $\text{Xe}^{7+}$ ions

Results on multiple ionization of  $\text{Xe}^{6+}$  and  $\text{Xe}^{7+}$  ions are displayed in figures 4.28 and 4.29. The single- and double-ionization cross sections for both ions have already been described in sections section 4.1.1 and section 4.2.1 respectively. The

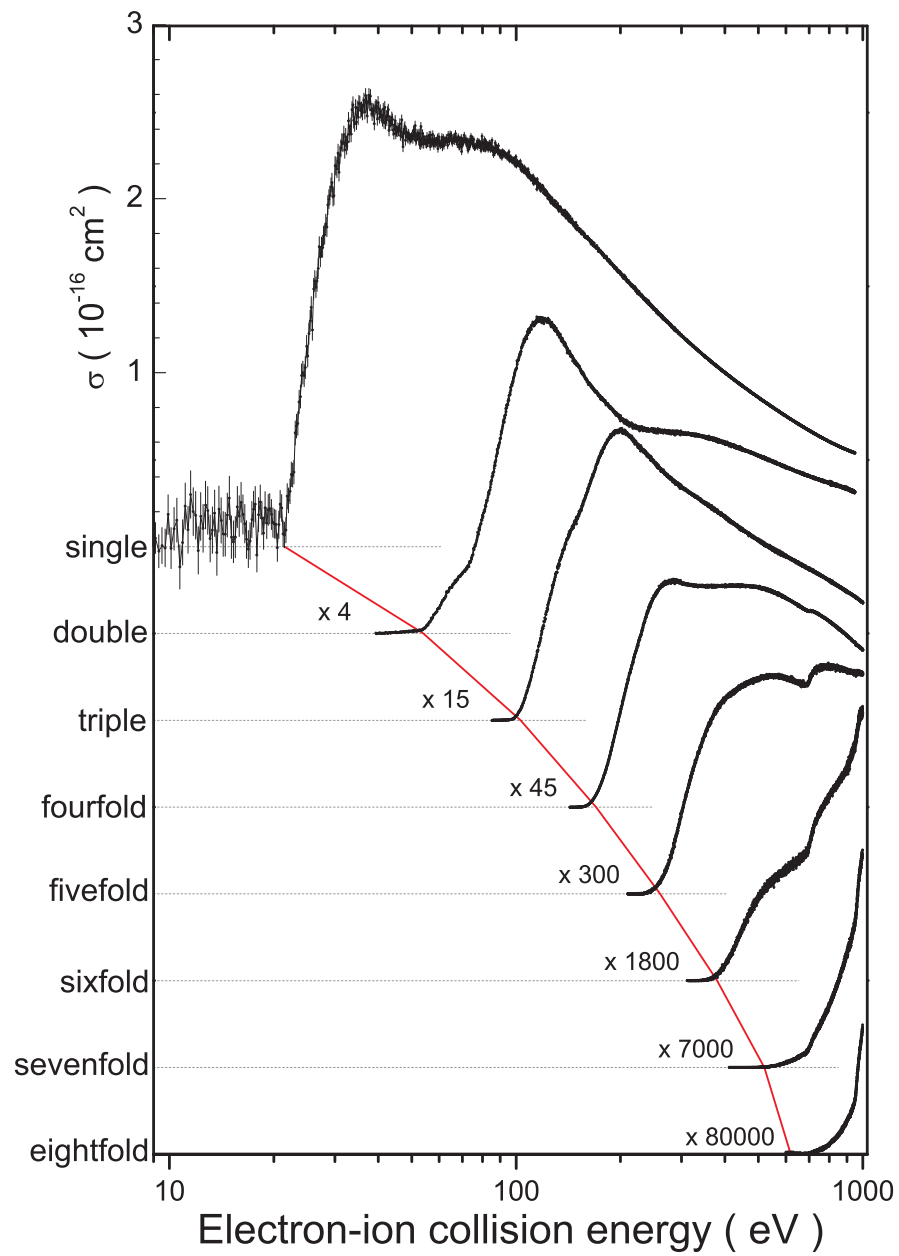


**Figure 4.27:** Overview over the present multiple-ionization cross sections of  $\text{Xe}^+$  ions. The scale is in units of  $10^{-16} \text{ cm}^2$  and the cross section for each ion stage is shifted downwards by  $0.5 \times (n - 1) \times 10^{-16} \text{ cm}^2$ , where  $n$  is the ionization multiplicity. The thin solid line connects the observed ground-state ionization thresholds.

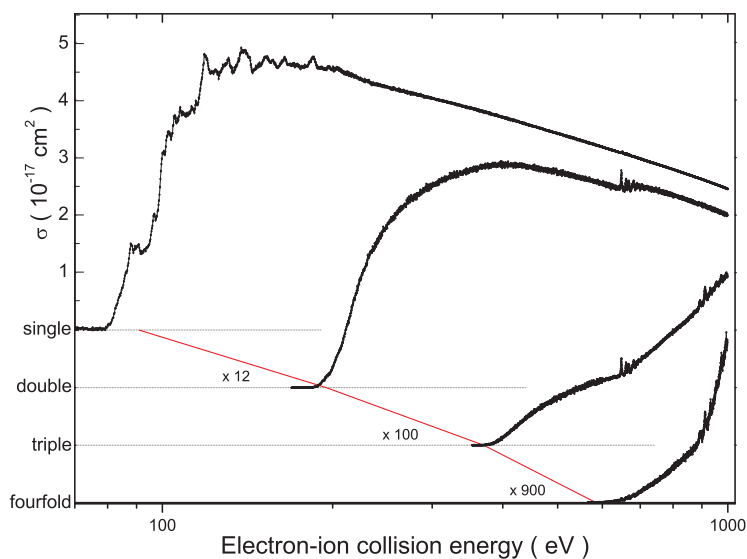


**Figure 4.28:** Overview over the present multiple-ionization cross sections of  $\text{Xe}^{6+}$  ions. The scale is in units of  $10^{-17} \text{ cm}^2$  and the cross section for each ion stage is shifted downwards by  $1 \times (n - 1) \times 10^{-17} \text{ cm}^2$ , where  $n$  is the ionization multiplicity. The thin solid line connects the observed ground-state ionization thresholds.

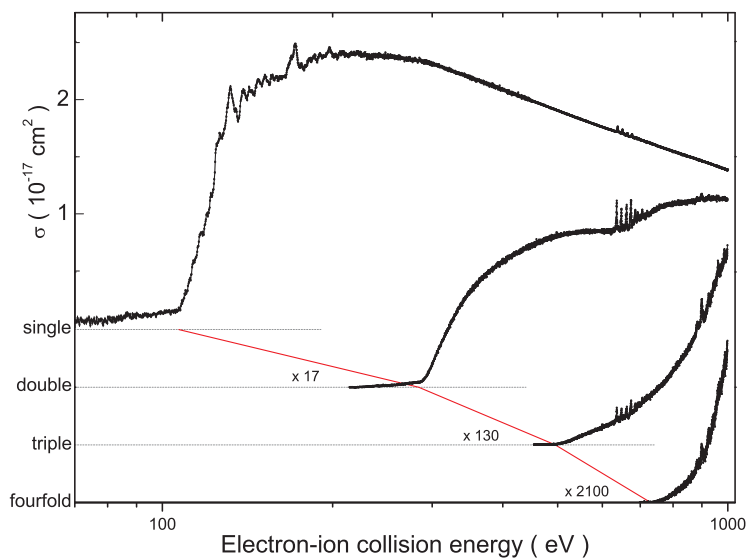


**Figure 4.29:** Overview over the present multiple-ionization cross sections of  $\text{Xe}^{7+}$  ions. The scale is in units of  $10^{-17} \text{ cm}^2$  and the cross section for each ion stage is shifted downwards by  $0.5 \times (n - 1) \times 10^{-17} \text{ cm}^2$ , where  $n$  is the ionization multiplicity. The thin solid line connects the observed ground-state ionization thresholds.

cross sections for triple- and fourfold ionization of both  $\text{Xe}^{6+}$  and  $\text{Xe}^{7+}$  reveal the important role of resonant excitation of  $3d$ - and  $3p$  electrons accompanied by capture of the incident electron with subsequent ejection of several target electrons. The steeper cross-section increases just beyond the thresholds for excitation of  $3d$ - and  $3p$  electron suggest also non-resonant indirect-ionization processes such as *excitation-triple-autoionization* and *excitation-fourfold-autoionization* to contribute to triple- and fourfold ionization of  $\text{Xe}^{6+}$  and  $\text{Xe}^{7+}$  ions, respectively. No significant role of ionization of metastable primary-ion-beam components is observed.

#### 4.2.4 Role of excited metastable states

Like the experiments on single ionization of xenon ions (see Section 4.1.2), the present multiple-ionization measurements are affected by metastable ions admixed to the primary ion beam. Detailed examination of the below-ground-state-threshold regions reveals the onsets for multiple ionization from metastable states. These are shifted towards lower energies by the same amount as in the single-ionization cross sections of the corresponding ions. This suggests that the same metastable species have been present in the experiments as those revealed for the single-ionization cross sections. The fractions, however, may differ from those listed in the Tab. 4.2. A detailed examination of the measured cross sections in the below-ground-state-threshold region revealed that for several charge states, where in the single-ionization cross section metastable species of two excited configurations have been detected to be present in the primary ion beam, e.g.  $\text{Xe}^{9+}$ , the double-ionization cross section contain visible onsets for the first (lower-excited) metastable primary-beam components only. The reason for this might be the low signal intensities in the corresponding energy regions.

For the case of  $\text{Xe}^{7+}$  described in detail in Section 4.1.2, the present double-ionization cross section has an onset around 67 eV below the ground-state ionization threshold. This is in perfect agreement with the suggested presence of the  $4d^9 5s 5p^4 F_{9/2}$  state with an excitation energy of 68 eV (see Tab. E.1) in the primary ion beam used in measurements of the single-ionization cross section of  $\text{Xe}^{7+}$ . An onset indicating the presence of the higher excited states of the  $4d^9 4f 5s$  configuration, however, is not observed.

The magnitudes of metastable fractions could not be determined from multiple ionization experiment. In general, contributions of metastable-state ionization to the measured multiple ionization cross sections below the ground-state ionization threshold are noticeably smaller than for single ionization.

#### 4.2.5 Comparison with previous experimental data

In this section, the present data on multiple ionization of xenon ions are compared to previously available experimental data. For the present data, the given error bars

represent the total uncertainties.

There is no general theoretical concept available to calculate multiple ionization cross sections for electrons incident on ions. The only available method for describing direct many-electron knock out is the classical binary-encounter approximation of Gryziński [95] (see section Section 2.3). For this reason, a comparison with previous theoretical data cannot be performed.

Figures 4.30, 4.31 and 4.32 show the present double-ionization cross sections of  $\text{Xe}^+$ ,  $\text{Xe}^{2+}$  and  $\text{Xe}^{3+}$  compared to the previous data of Achenbach *et al.* [49]. The corresponding data sets are in good agreement with one another.

The present data on double ionization of  $\text{Xe}^{4+}$  compared to previous data of Achenbach *et al.* [49] and of Pindzola *et al.* [54] are displayed in Fig. 4.33. While the agreement with the data of Achenbach *et al.* is very good, the data of Pindzola *et al.* are generally around 15–20% lower than the present results in the whole experimental energy range. The double-ionization cross section of  $\text{Xe}^{6+}$  has been studied previously by Howald *et al.* [69]. The comparison of their data with the present cross-section values is illustrated in Fig. 4.34. Both data sets show good agreement, except in the region 240–450 eV where the data of Howald *et al.* are up to 30% lower than the present cross-section values and, hence, the discrepancy exceeds the given error-bar limits. Good agreement is found in the comparison of the present double-ionization cross section of  $\text{Xe}^{8+}$  with previous data of Mueller *et al.* [72] and of Hofmann *et al.* [74] (Fig. 4.35). The data of Hofmann *et al.* on double ionization of  $\text{Xe}^{10+}$  [74] were measured in the energy region 800–4800 eV i.e. mostly beyond the energy range accessible by the electron gun employed in the present measurements. In the overlap region 800–1000 eV the data sets agree well within the error bars (Fig. 4.36). No double-ionization cross-section data for higher ionization stages of xenon have been reported so far.

The triple-ionization cross section of  $\text{Xe}^+$  was measured previously by Müller *et al.* [52]. Their result is compared with the present data in Fig. 4.37. The observed agreement is very good. Triple-ionization of  $\text{Xe}^{6+}$  has been investigated by Howald *et al.* [69]. Their data are compared to the present results in Fig. 4.38. The agreement is excellent. No triple-ionization cross-section data for higher ionization stages of xenon have been reported.

Finally, fourfold-ionization cross section of  $\text{Xe}^+$  has been measured previously by Müller *et al.* [52]. The comparison with the present data reveals very good agreement of the data sets, especially below 300 eV (Fig. 4.39).

In summary, the comparisons made in this section reveal good agreement of the present data with the data sets reported previously.

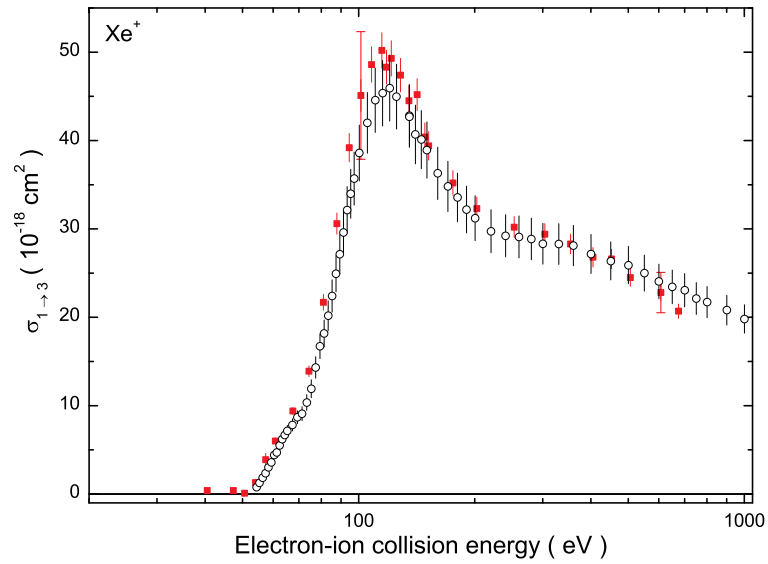


**Figure 4.30:** Double ionization of  $\text{Xe}^+$ . Comparison with previous experimental data. Open circles represent the present data and solid squares the data of Achenbach *et al.* [49]. Error bars of Achenbach *et al.* represent statistical uncertainties. Their total uncertainties are given by capped error bars.

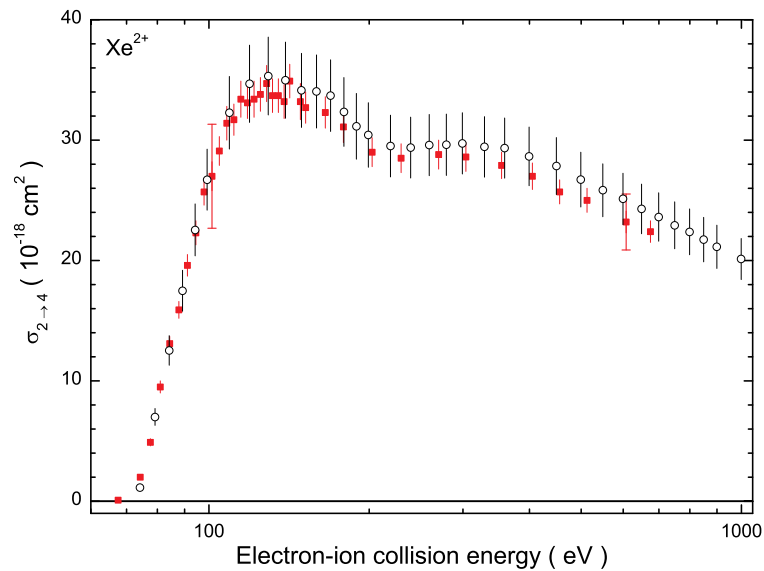


**Figure 4.31:** Double ionization of  $\text{Xe}^{2+}$ . Comparison with previous experimental data. Open circles represent the present data and solid squares the data of Achenbach *et al.* [49]. Error bars of Achenbach *et al.* represent statistical uncertainties. Their total uncertainties are given by capped error bars.

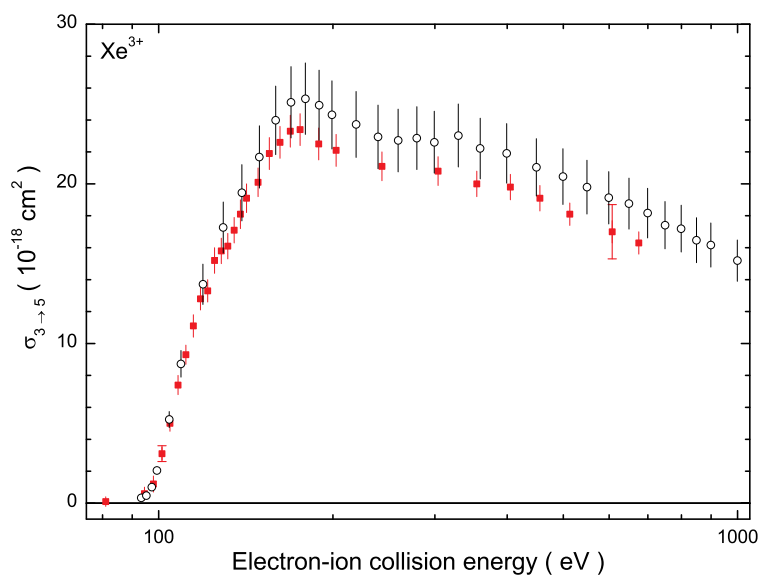


**Figure 4.32:** Double ionization of  $\text{Xe}^{3+}$ . Comparison with previous experimental data. Open circles represent the present data and solid squares are the data of Achenbach *et al.* [49]. Error bars of Achenbach *et al.* represent statistical uncertainties. Their total uncertainties are given by capped error bars.

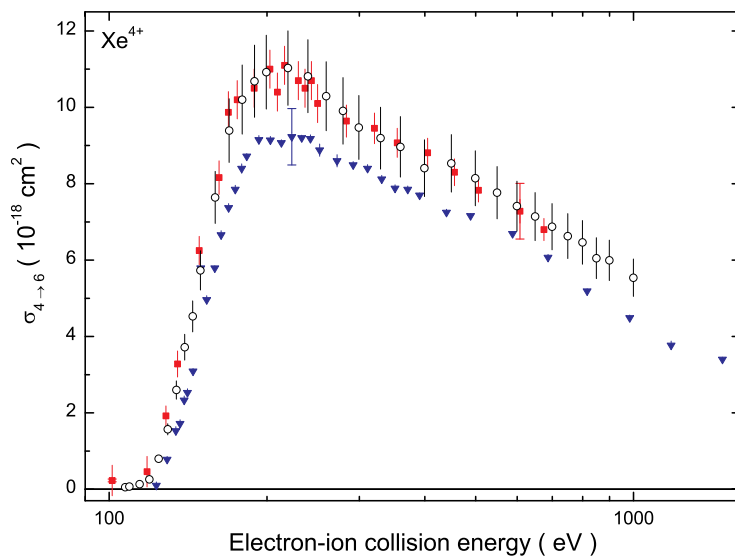


**Figure 4.33:** Double ionization of  $\text{Xe}^{4+}$ . Comparison with previous experimental data. Open circles represent the present data. Solid squares are the data of Achenbach *et al.* [49] and flipped triangles are the data of Pindzola *et al.* [54]. Error bars of Achenbach *et al.* and Pindzola *et al.* represent statistical uncertainties. The total uncertainties of both data sets are given by capped error bars.

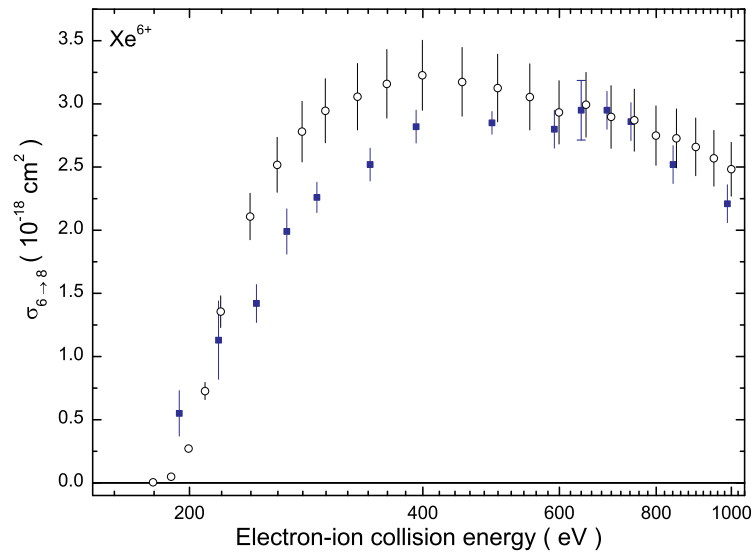


**Figure 4.34:** Double ionization of  $\text{Xe}^{6+}$ . Comparison with previous experimental data. Open circles represent the present data and solid squares the data of Howald *et al.* [69]. Error bars of Howald *et al.* represent statistical uncertainties. Their total uncertainties are given by capped error bars.

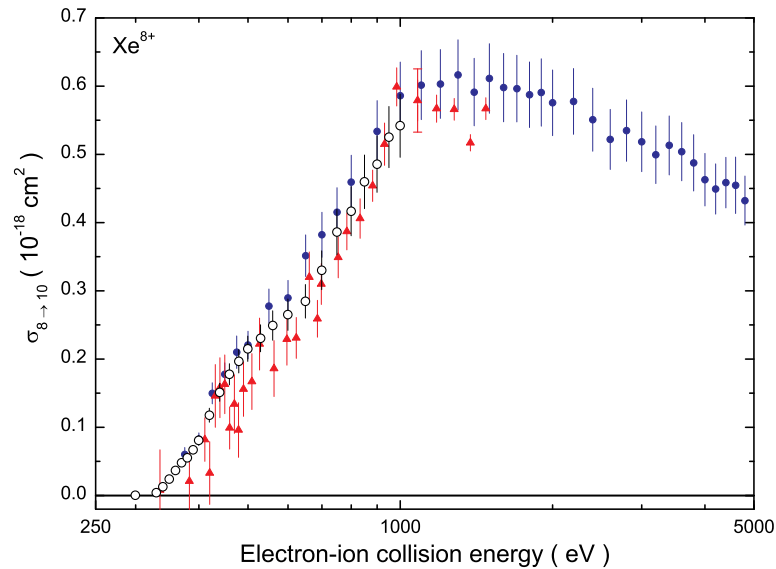


**Figure 4.35:** Double ionization of  $\text{Xe}^{8+}$ . Comparison with previous experimental data. Open circles represent the present data. Solid triangles are the data of Mueller *et al.* [72] and filled circles are the data of Hofmann *et al.* [74]. Error bars of Hofmann *et al.* show total uncertainties, while error bars of Mueller *et al.* represent statistical uncertainties. Their total uncertainties are given by capped error bars.

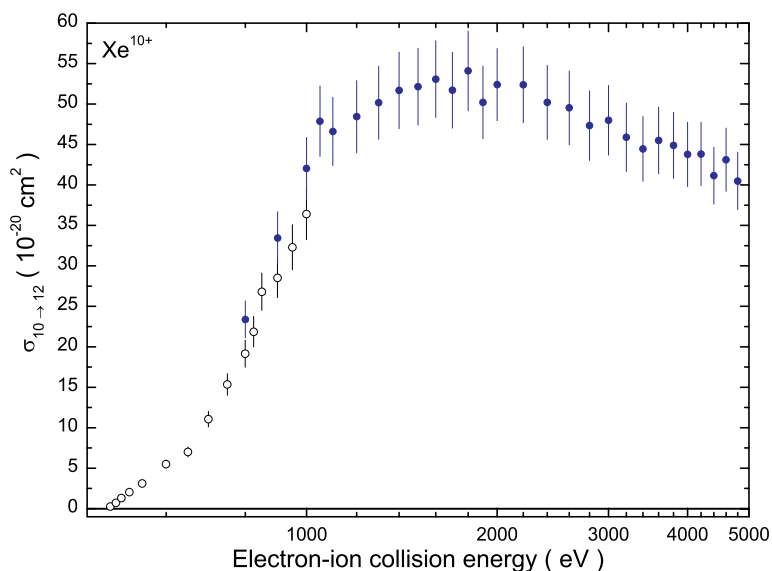


**Figure 4.36:** Double ionization of  $\text{Xe}^{10+}$ . Comparison with previous experimental data. Open circles represent the present data. Filled circles are the data of Hofmann *et al.* [74]. Error bars of Hofmann *et al.* represent total uncertainties.

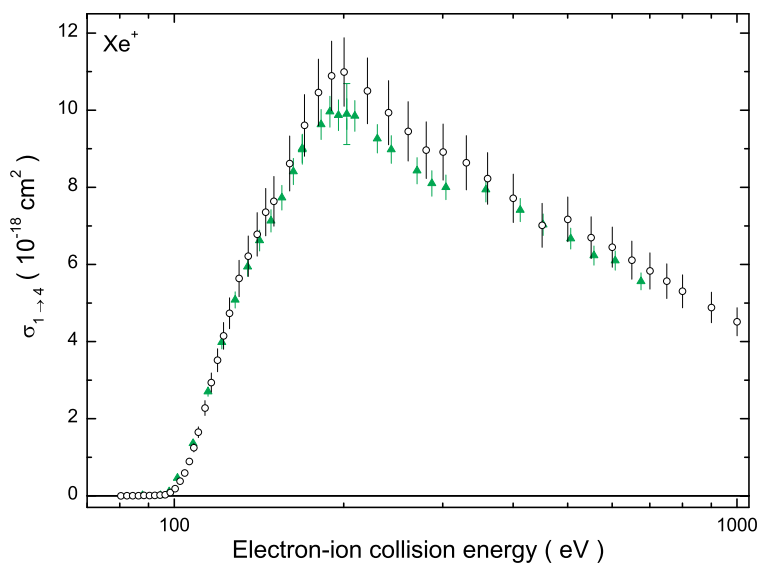


**Figure 4.37:** Triple ionization of  $\text{Xe}^+$ . Comparison with previous experimental data. Open circles represent the present data and squares the data of Müller *et al.* [52]. Error bars of Müller *et al.* represent statistical uncertainties. Their total uncertainties are given by capped error bars.

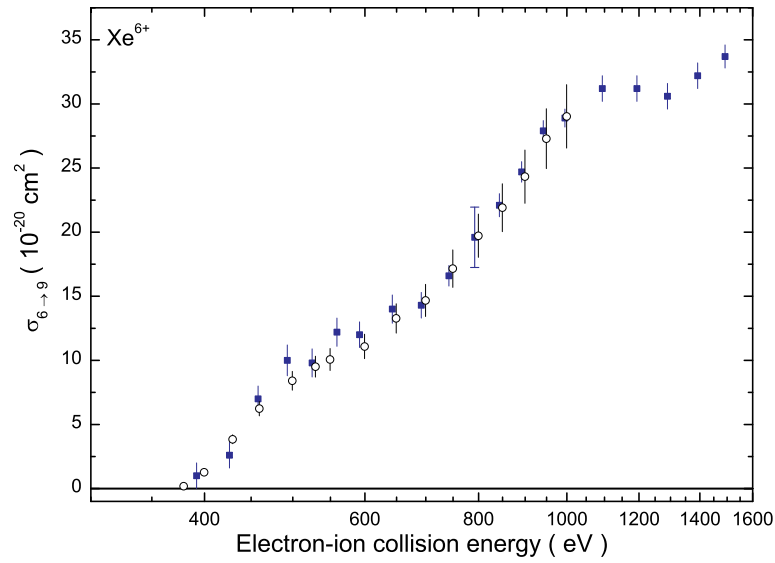


**Figure 4.38:** Triple ionization of  $\text{Xe}^{6+}$ . Comparison with previous experimental data. Open circles represent the present data. Squares are the data of Howald *et al.* [69]. Error bars of Howald *et al.* represent statistical uncertainties. Their total uncertainties are given by capped error bars.

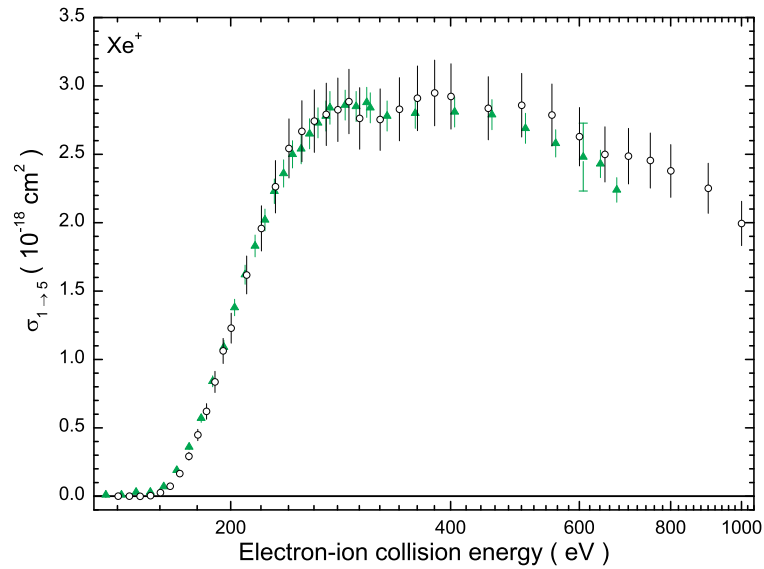


**Figure 4.39:** Fourfold ionization of  $\text{Xe}^+$ . Comparison with previous experimental data. Open circles represent the present data and squares the data of Müller *et al.* [52]. Error bars of Müller *et al.* represent statistical uncertainties. Their total uncertainties are given by capped error bars.

## 4.3 Single ionization of tin ions

### 4.3.1 Overview

Within the present work, cross sections for single ionization of tin ions with charge states ranging from 1 through 13 have been measured in the electron energy range from threshold up to 1000 eV. The measured data are displayed in Fig. 4.40 in the form of energy scans normalized to the separately measured absolute cross-section values. For better viewing, the data sets (except for  $\text{Sn}^+$ ) have been multiplied by certain factors provided individually for the each data set in the figure.

The statistical uncertainties of the absolute measurements at the cross-section maxima were 2% or lower for all charge states investigated. The total uncertainties are mostly determined by the systematic uncertainty originating from the factors described in Chapter 3. The systematic uncertainty was determined to be generally 9% or better. At lower electron energies the total uncertainties are, however, significantly increased due to poor statistics as a result of poor signal/background ratios. The relative uncertainties of the energy scans for all charge states are below 2%. The largest measured cross-section value is  $2.74 \times 10^{-16} \text{ cm}^2$  at 44.1 eV for  $\text{Sn}^+$ .

Similar to the  $\text{Xe}^{q+}$  data, the present data for  $\text{Sn}^{q+}$  can also be classified into several groups (namely two) according to the electron configuration of the parent ion. The first group includes the ionization cross sections for the ion charge stages 1, 2 and 3 with ground-state configurations  $4d^{10}5s^25p$ ,  $4d^{10}5s^2$  and  $4d^{10}5s$ , respectively. The cross section functions have similar energy dependencies as the cross section functions of isoelectronic  $\text{Xe}^{q+}$  ions. A steep increase of the cross section starts right above the ground-state ionization threshold. However, the structure induced by indirect ionization processes is less pronounced than the structure for equally charged xenon ions. In the maxima and beyond, the Sn cross sections are smooth (see Fig. 4.1).

For  $\text{Sn}^{3+}$ , a non-zero cross section below the ground-state ionization threshold indicates highly excited metastable states being present in the primary ion beam during the experiment. A similar situation has already been observed for the isoelectronic  $\text{Xe}^{7+}$  ions. For  $\text{Sn}^{3+}$ , The details are discussed in Section 4.3.2.

The second group comprises the 10 ionization stages from  $\text{Sn}^{4+}$  to  $\text{Sn}^{13+}$  with configurations  $4d^{10}$ ,  $4d^9$ , ...,  $4d$ . The cross sections exhibit a rapid increase above the ionization threshold caused by indirect ionization processes. These involve the excitation of  $4p$  and  $4s$  subshells, which for  $\text{Sn}^{q+}$  deliver noticeably larger contributions than for  $\text{Xe}^{q+}$  ions. The single-ionization cross section of  $\text{Sn}^{6+}$ , in the region 480–540 eV, contains resonant structure corresponding to indirect ionization processes via resonant excitation of the  $3d$  subshell. These contributions become more and more significant with increasing ion charge state. In the cross section of  $\text{Sn}^{8+}$ , the structure indicating indirect ionization via excitation of the  $3p$  subshell can already be recognized. For  $\text{Sn}^{13+}$ , which is the highest tin ionization stage investigated, indirect ionization processes via excitation of  $3d$ - and  $3p$  subshells

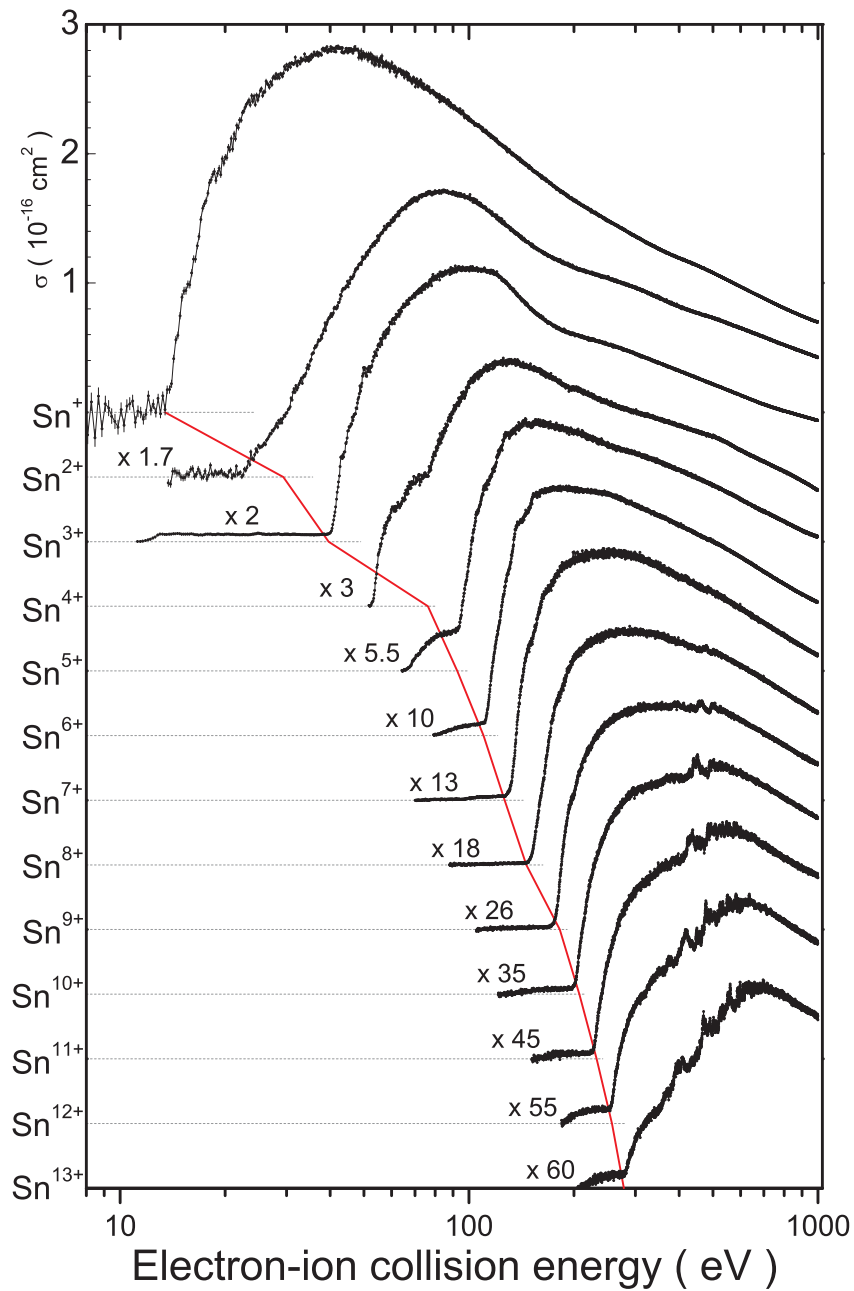


**Figure 4.40:** Overview over the present single-ionization cross sections of  $\text{Sn}^{q+}$  ions ( $q = 1, 2, \dots, 13$ ). The cross-section scale is in units of  $10^{-16} \text{ cm}^2$  and the cross section for each ion stage is shifted downwards by  $0.5 \times (q - 1) \times 10^{-16} \text{ cm}^2$ . The thin solid line connects the observed ground-state ionization thresholds.

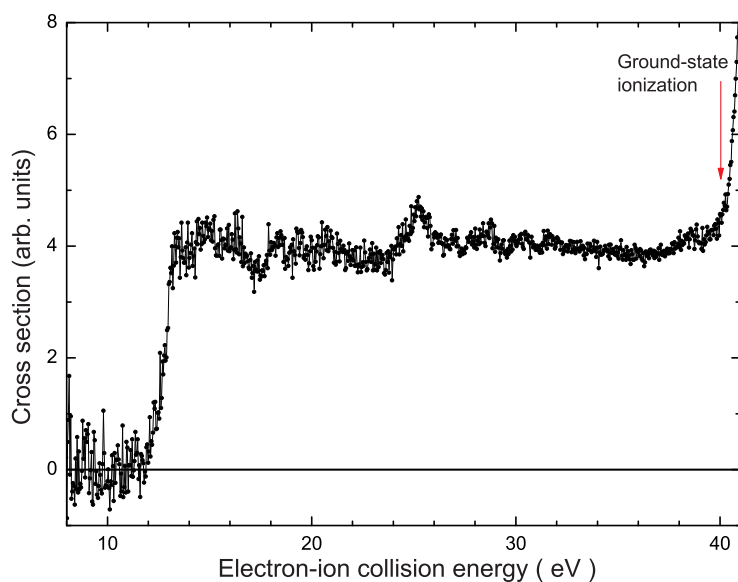


**Figure 4.41:** Single ionization of  $\text{Sn}^{3+}$ . Energy scan data, taken in the below-ground-state-threshold energy region.

contribute more than 50% to the total ionization cross section measured.

The measured non-zero ionization cross sections below the ground-state ionization thresholds indicate metastable contaminations being admixed to the primary ion beam during the experiments. For  $\text{Sn}^{4+}$ , analogously to  $\text{Xe}^{8+}$ , the behavior of the cross section below the ground-state ionization threshold reveals effective indirect ionization of the metastable admixture. Details regarding the metastable admixtures are presented in the next section.

### 4.3.2 Role of excited metastable states

In the present experiments, various amounts of metastable ions have been present in the ion beams as is revealed by ionization signal below the ground-state ionization threshold. Generally, these states belong to the ground-state configurations and/or to electron configurations with an excited outer-shell electron. A special case is  $\text{Sn}^{3+}$ , where analogously to  $\text{Xe}^{7+}$  an inner-shell  $4d$  electron is excited to the  $5s$  and  $5p$  subshells to form long-living  $4d^9 5s^2 \ ^2D_{5/2,3/2}$  and  $4d^9 5s 5p \ ^4F_{9/2}$  states (see Tab. E.2). Corresponding steps in the cross section curve are located at approximately 18 eV and 12 eV, respectively (Fig. 4.41).

The same method as described in Section 4.1.2 has been employed for quantifying metastable fractions. The results are given in the table 4.3. Uncertainties are the same as described in Section 4.1.2.

**Table 4.3:** Information on the metastable components in the primary  $\text{Sn}^{q+}$  ion beams.

Primary ion	Configuration	Excitation energy (eV)	Scaling factor $f$
$\text{Sn}^{2+}$	$5s5d$	16.56	0.02
$\text{Sn}^{6+}$	$4d^7 5s$	35.11	0.45
	$4d^7 4f$	64.29	0.01
$\text{Sn}^{7+}$	$4d^6 5s$	41.21	0.14
	$4d^6 4f$	68.34	0.01
$\text{Sn}^{8+}$	$4d^5 5s$	47.49	0.03
	$4d^5 4f$	71.66	0.02
$\text{Sn}^{9+}$	$4d^4 4f$	74.46	0.02
$\text{Sn}^{10+}$	$4d^3 4f$	76.86	0.1
$\text{Sn}^{11+}$	$4d^2 4f$	78.95	0.1

## 4.4 Multiple ionization of tin ions

### 4.4.1 Overview

Within the present work, double-ionization cross sections of  $\text{Sn}^{q+}$  ions with  $q = 1, 2, \dots, 12$  have been measured in the electron energy range from threshold up to 1000 eV. The energy scan data normalized to separately measured absolute cross-section values are represented in Fig. 4.42. For better viewing, the data sets (except for  $\text{Sn}^+$  and  $\text{Sn}^{2+}$ ) have been multiplied by certain factors provided individually for the each data set in the figure.

Double-ionization cross sections of  $\text{Sn}^+$  and  $\text{Sn}^{2+}$  are dominated by the process of direct removal of a  $4d$  electron followed by subsequent ejection of a second electron from an outer shell (IA process). Similar to double ionization of  $\text{Xe}^{q+}$ , the pronounced cross-section maxima represent giant-resonance features described previously [37, 55, 116]. The shape of the double-ionization cross section of  $\text{Sn}^{3+}$  suggests that IA involving removal of a  $4d$  electron contributes as well.

For  $\text{Sn}^{4+}$  and higher ionization stages, contributions from excitation-double-autoionization processes involving  $3d$  subshell excitations (at around 500 eV for  $\text{Sn}^{4+}$ ) can be observed. The double-ionization cross section of  $\text{Sn}^{5+}$  contains resonant structure corresponding to RETA processes involving the same subshell. In the cross section for  $\text{Sn}^{6+}$  it becomes more pronounced. An onset that corresponds to ionization-autoionization induced by direct removal of a  $3d$  electron can be observed at around 600 eV. Moreover, the resonant structure at 700–750 eV suggests the presence of RETA processes involving excitation of the  $3p$  subshell.

Resonant structures arising from RETA processes involving both  $3d$  and  $3p$  subshells almost completely "cover" the double-ionization cross sections of the higher tin ionization stages. This makes it hard to disentangle the contributions from IA and EDA. More detailed analysis of the structure observed in the cross sections of  $\text{Sn}^6, \dots, \text{Sn}^{12}$  ions has been performed in [120].

Neither experimental, nor theoretically calculated cross-section values for double ionization of  $\text{Sn}^{q+}$  are available in literature.

As in the case of single ionization, ionization signal below the threshold for ground-state ionization also shows up in various double-ionization cross sections. As well as for double-ionization experiments with  $\text{Xe}^{q+}$  ions, the magnitudes of metastable fractions could not be determined from the experiment data.

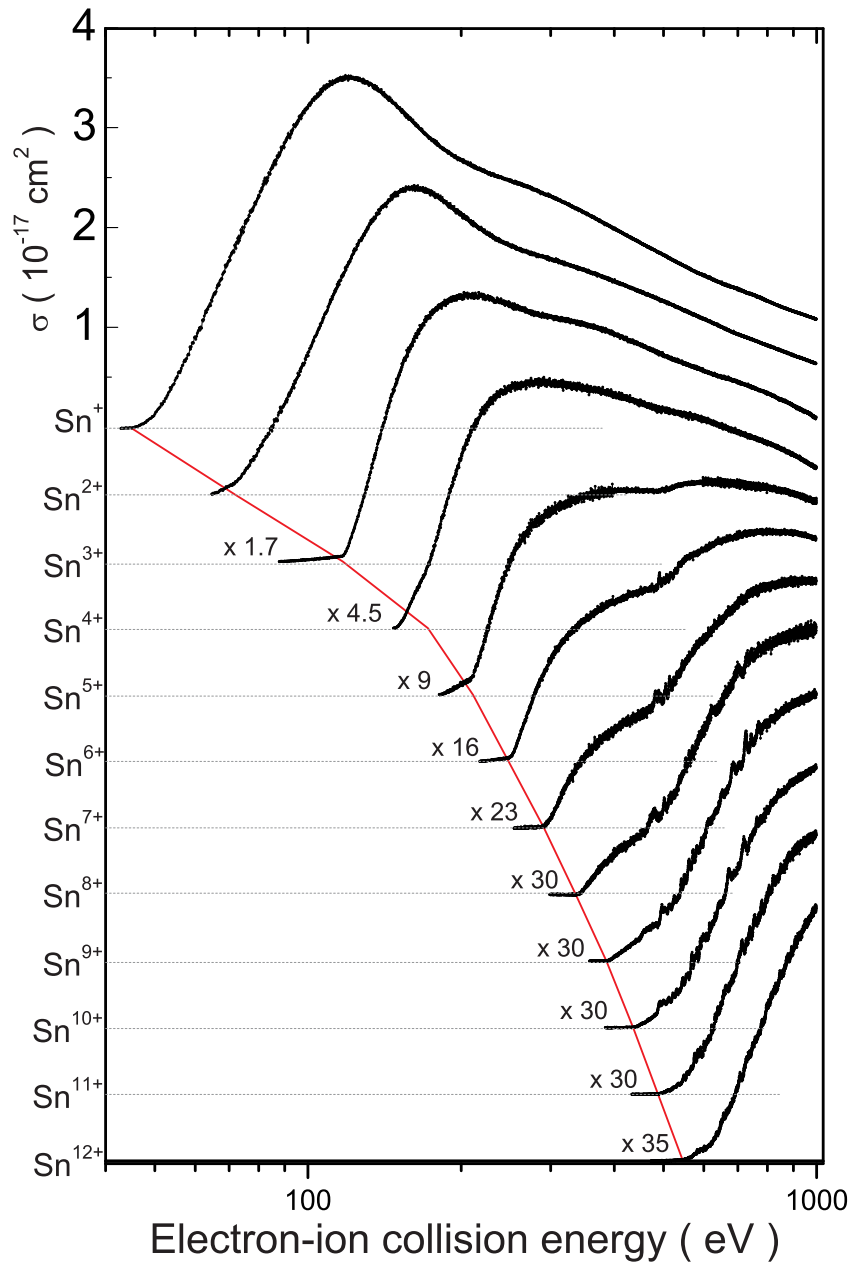


**Figure 4.42:** Overview over the present double-ionization cross sections of  $\text{Sn}^{q+}$  ions ( $q = 1, 2, \dots, 12$ ). The scale is in units of  $10^{-17} \text{ cm}^2$  and the cross section for each ion stage is shifted downwards by  $0.5 \times (q-1) \times 10^{-17} \text{ cm}^2$ . The thin solid line connects the observed ground-state ionization thresholds.

## 4.5 Recommendations for plasma physics

For the detailed modeling of plasmas huge amount of atomic data on the structure and dynamics of atoms and ions as well as cross sections and rate coefficients for collision processes of these particles are required. Like other processes occurring in plasmas, electron-impact ionization of atoms and ions is of a very fundamental nature. Data on single and multiple ionization of atoms and ions by electron impact are crucial to understand and to model the charge state distributions of ions in plasmas, which, in turn, determine all the macroscopic properties of a plasma environment and the emission of electromagnetic radiation from the plasma. The amount of required data can never be obtained by experiments. Theory has to provide the bulk of the information needed in plasma modeling. Experiments, though, are needed to test and to benchmark theoretical approaches. But even if a theoretical method is capable of delivering results that agree with the experiments [6], mass calculations of data using this theoretical method may not be feasible because of computational limitations. Especially for many-electron systems like the multi-charged xenon and tin ions studied in this thesis detailed calculations are very complex and time consuming. Therefore, calculations are often performed with simplifying approaches that can yield results in a reasonable time. Even simple predictor formulae are employed to generate data that are used in modeling the behavior of atoms and ions in wide isonuclear sequences. Such formulae may neglect, for example, all indirect processes contributing to electron-impact ionization [121]. As a consequence the resulting cross sections can be wrong by factors if the one order of 10.

With increasing computer power, systematic calculations at an increased level of sophistication can be carried out, e.g., for electron-impact single ionization of ions along an isonuclear sequence such as the  $\text{Xe}^{q+}$  sequence from  $q = 0$  to  $q = 53$ . Such calculations have been reported by Loch *et al.* [23]. They included excitation-autoionization processes in addition to plain direct ionization employing powerful approximations to keep the calculational effort in the range of feasibility. The comparison of such calculations with the present experiments has revealed unexpected difficulties of such theoretical approaches to reproduce the experimental findings. In particular, the measurements carried out in the framework of the present thesis clearly show that resonant contributions to the ionization cross sections must not be neglected. This is especially true for highly charged ions, where decreasing importance of resonant contributions was expected by theory.

On the other hand, experimental data on all studied ions are affected by the presence of unknown quantities of long-lived excited states in the primary ion beam employed for the experiments. Population of metastable ionic levels in an ion source that can produce high ion charge states appears to be unavoidable. By storing the ions prior to experiments most of the long-lived excited states, but not all, can be made to decay. Measurements of electron-impact ionization cross sections for selected ion species are therefore carried out at heavy-ion storage rings. The lifetime of ions in a storage ring can usually be enhanced by increasing the

energy of the circulating ions. This, in turn, leads to enhanced background in the ionization measurements due to electron-stripping collisions of the ions with residual gas atoms or molecules. No storage-ring measurement has therefore been able to deliver such detailed information on resonance features like the present experimental setup. Also, the complex and expensive operation of an accelerator for ion injection and of a storage ring itself preparing the ion beams prior to the measurements makes systematic measurements like the present ones unfeasible. Hence, in fact, only few ionization cross sections of selected ion species have been investigated using ion storage rings.

Given the difficulties with measurements employing ions exclusively in their ground state and considering the limited reliability of theoretical calculations that have to make compromises with respect to the level of sophistication of the approximations employed, one has to make a decision about the best strategy in selecting the data to be used in modeling a real plasma. In high-temperature plasmas, such as in magnetic-confinement fusion, the electron temperature and the electron density inevitably lead to the production of highly excited states in the ions  $A^{q+}$  which are abundant at the given plasma temperature. One can assume that long-lived states are populated with probabilities similar to the situation in the ECR ion source employed in the present experiments. Therefore, it can be assumed that the present data can be used in plasma modeling with good meaning. The cross sections resulting from the experiments must be considered superior to the results of theoretical calculations that do not include essential contributions to the ionization cross sections. Therefore, the use of experimental data even though subject to problems with metastable admixtures in the parent ion beams is recommended for plasma modeling whenever such experimental data are available [19].



## 5 Conclusions and outlook

In the present work, absolute electron-impact single- and multiple-ionization cross sections of xenon and tin ions have been measured employing the animated-beam method. More than two thirds of the cross-section datasets studied have not been measured previously. The charge states above 18 are the highest ones for which ionization has ever been investigated by employing the crossed-beams technique. The comparison with the previously available data mostly shows good agreement.

By employing the energy-scan technique, contributions from resonant and non-resonant indirect-ionization processes in the studied cross sections have been revealed in great detail. The deeper analysis of the data showed an important and often dominating role of contributions arising from interactions of the incident electrons with inner shells of the target ions, especially with  $nd$  subshells. Relative contributions to the measured cross sections originating from resonant ionization processes are up to 20% and sometimes even more at specific energies.

The measured cross sections are influenced to some extent by the excited metastable-ion components admixed to the primary ion beams employed in the present experiments. By comparison with the results of theoretical calculations suggestions for identification and quantification of the observed metastable fractions are provided. For highly charged xenon ions with charge states greater than 22, ionization signal has been observed at energies far below the ground-state ionization threshold. On the basis of theoretical calculations performed within the present study this was attributed to the presence of very highly excited (possibly even autoionizing) metastable primary-ion-beam components. For avoiding ambiguities it would be desirable to carry out ionization experiments at the storage rings where most of the metastable states can be made to decay before a measurement is started. Preparation of specific projectile ion states can be facilitated by ion-atom collisions in a gas cell prior to the ionization experiment.

In spite of the problem with metastable-ion admixtures, the present absolute cross sections (except for the very highly charged xenon ions  $\text{Xe}^{23+}, \dots, \text{Xe}^{25+}$ ) can be recommended for the use in plasma modeling calculations. Also in a plasma metastable states are produced and admixtures of long-lived states may be present similar to those found in the measurements described in this thesis.

The data of energy scan measurements clearly revealed structures in the studied cross sections indicating the importance of indirect ionization processes. The detailed information obtained by this techniques serve as a guidance for the the-

oretical groups on the way of further development of theoretical models for the description of electron-impact ionization of complex many-electron systems.

A limitation in this work was set by the voltage range accessible by the electron gun. Energies of incident electrons were limited to a maximum of 1000 eV. For highly charged ions, where ground-state ionization energies reach several hundreds of electronvolts, this restricts the measurements to the near-threshold region. The forthcoming implementation of a new electron gun will provide access to higher energies. With the new gun, electron beams with currents of 1 A at 3 keV could already be produced. A goal for the new setup is an energy range up to approximately 10 keV.

# Bibliography

- [1] C. H. Skinner, Phys. Scr. **T134**, 014022 (2009).
- [2] U. Stamm, H. Schwoerer, and R. Lebert, Physik Journal **1**, 33 (2002).
- [3] E. R. Kieft, K. Garloff, J. J. A. M. van der Mullen, and V. Banine, Phys. Rev. E **71**, 036402 (2005).
- [4] Y. Shimada, H. Nishimura, M. Nakai, K. Hashimoto, M. Yamaura, Y. Tao, K. Shigemori, T. Okuno, K. Nishihara, T. Kawamura, A. Sunahara, T. Nishikawa, A. Sasaki, K. Nagai, T. Norimatsu, S. Fujioka, S. Uchida, N. Miyanaga, Y. Izawa, and C. Yamanaka, Appl. Phys. Lett. **86**, 051501 (2005).
- [5] E. J. Lerner, The Industrial Physicist **6**, 16 (2000).
- [6] A. Borovik Jr., A. Müller, S. Schippers, I. Bray, and D. V. Fursa, J. Phys. B **42**, 025203 (2009).
- [7] H. Teng, H. Knopp, S. Ricz, S. Schippers, K. A. Berrington, and A. Müller, Phys. Rev. A **61**, 060704 (2000).
- [8] A. Müller, H. Teng, G. Hofmann, R. A. Phaneuf, and E. Salzborn, Phys. Rev. A **62**, 062720 (2000).
- [9] P. Lenard, Wied. Ann. **51**, 225 (1894).
- [10] P. Lenard, Ann. Phys. (Leipzig) **12**, 714 (1903).
- [11] S. J. J. Thomson, Philos. Mag. **23**, 449 (1912).
- [12] H. Bethe, Ann. Phys. (Leipzig) **397**, 325 (1930).
- [13] K. T. Dolder, M. F. A. Harrison, and P. Thonemann, Proc. R. Soc. A **264**, 367 (1961).
- [14] P. Defrance, F. Brouillard, W. Claeys, and G. V. Wassenhove, Phys. Rev. A **14**, 103 (1981).
- [15] F. Brouillard and P. Defrance, Phys. Scr. **T3**, 68 (1983).

- 
- [16] A. Müller, G. Hofmann, K. Tinschert, R. Sauer, and E. Salzborn, Nucl. Instrum. Methods B **24**, 369 (1987).
- [17] A. Müller, K. Tinschert, G. Hofmann, E. Salzborn, and G. Dunn, Phys. Rev. Lett. **61**, 70 (1988).
- [18] K. P. Dere, Astron. Astrophys. **466**, 771 (2007).
- [19] M. Mattioli, G. Mazzitelli, M. Finkenthal, P. Mazzotta, K. B. Fournier, J. Kaastra, and M. E. Puiatti, J. Phys. B **40**, 3569 (2007).
- [20] H. Tawara and M. Kato, *Electron Impact Ionization Data for Ions*, NIFS-DATA Series (National Institute for Fusion Science, Tokio, Japan, 1999).
- [21] M. Hayashi, *Bibliography of Electron and Photon Cross Sections with Atoms and Molecules (Xenon)*, NIFS-DATA Series, Vol. 79 (National Institute for Fusion Science, Tokio, Japan, 2003).
- [22] V. M. Povyshev, A. A. Sadovoy, V. P. Shevelko, G. D. Shirkov, E. G. Vasina, and V. V. Vatulín, in *Preprints and Communications* (Joint Inst. Nucl. Res. Dubna, 2001).
- [23] S. Loch, M. Pindzola, and D. Griffin, *Yong-Ki Kim Honour Issue*, Int. J. Mass Spectrom. **271**, 68 (2008).
- [24] E. B. Saloman, J. Phys. Chem. Ref. Data **33**, 765 (2004).
- [25] B. A. Tozer and J. D. Craggs, Journal of Electronics and Control **8**, 103 (1960).
- [26] R. K. Asundi and M. V. Kurepa, Journal of Electronics and Control **15**, 41 (1963).
- [27] D. Rapp and P. Englander-Golden, J. Chem. Phys. **43**, 1464 (1965).
- [28] B. L. Schram, F. J. D. Heer, M. J. van der Wiel, and J. Kistemaker, Physica **31**, 94 (1965).
- [29] B. L. Schram, H. R. Moustafa, J. Schutten, and F. J. de Heer, Physica **32**, 734 (1966).
- [30] B. L. Schram, Physica **32**, 197 (1966).
- [31] T. M. El-Sherbini, M. J. Van der Wiel, and F. J. de Heer, Physica **48**, 157 (1970).
- [32] E. J. McGuire, Phys. Rev. A **16**, 62 (1977).
- [33] P. Nagy, A. Skutlartz, and V. Schmidt, J. Phys. B **13**, 1249 (1980).

- 
- [34] K. Stephan and T. D. Märk, *J. Chem. Phys.* **81**, 3116 (1984).
- [35] D. Mathur and C. Badrinathan, *Phys. Rev. A* **35**, 1033 (1987).
- [36] Wetzel, R. C., Baiocchi, F. A., Hayes, T. R., Freund, and R. S., *Phys. Rev. A* **35**, 559 (1987).
- [37] S. M. Younger, *Phys. Rev. A* **35**, 2841 (1987).
- [38] E. Krishnakumar and S. K. Srivastava, *J. Phys. B* , 1055 (1988).
- [39] H. Lebius, J. Binder, H. R. Koslowski, K. Wiesemann, and B. A. Huber, *J. Phys. B* , 83 (1989).
- [40] R. S. Freund, R. C. Wetzel, R. J. Shul, and T. R. Hayes, *Phys. Rev. A* **41**, 3575 (1990).
- [41] J. A. Syage, *Phys. Rev. A* **46**, 5666 (1992).
- [42] D. L. Moores, *Nucl. Instrum. Methods B* **179**, 316 (2001).
- [43] R. Rejoub, B. G. Lindsay, and R. F. Stebbings, *Phys. Rev. A* **65**, 042713 (2002).
- [44] D. P. Almeida, *Journal of Electron Spectroscopy and Related Phenomena* **122**, 1 (2002).
- [45] P. L. Bartlett and A. T. Stelbovics, *Phys. Rev. A* **66**, 012707 (2002).
- [46] D. A. Erwin and J. A. Kunc, *J. Phys. B* , 4605 (2003).
- [47] D. A. Erwin and J. A. Kunc, *Phys. Rev. A* **70**, 022705 (2004).
- [48] A. Müller, E. Salzborn, R. Frodl, R. Becker, H. Klein, and H. Winter, *J. Phys. B* **13**, 1877 (1980).
- [49] C. Achenbach, A. Müller, E. Salzborn, and R. Becker, *Phys. Rev. Lett.* **50**, 2070 (1983).
- [50] M. S. Pindzola, D. C. Griffin, and C. Bottcher, *J. Phys. B* **16**, L355 (1983).
- [51] C. Achenbach, A. Müller, E. Salzborn, and R. Becker, *J. Phys. B* **17**, 1405 (1984).
- [52] A. Müller, C. Achenbach, E. Salzborn, and R. Becker, *J. Phys. B* **17**, 1427 (1984).
- [53] D. C. Griffin, C. Bottcher, M. S. Pindzola, S. M. Younger, D. C. Gregory, and D. H. Crandall, *Phys. Rev. A* **29**, 1729 (1984).

- [54] M. S. Pindzola, D. C. Griffin, C. Bottcher, D. H. Crandall, R. A. Phaneuf, and D. C. Gregory, *Phys. Rev. A* **29**, 1749 (1984).
- [55] S. M. Younger, *Phys. Rev. A* **35**, 4567 (1987).
- [56] K. F. Man, A. C. H. Smith, and M. F. A. Harrison, *J. Phys. B* **20**, 5865 (1987).
- [57] S. N. Chatterjee and B. N. Roy, *J. Phys. B* **20**, 2291 (1987).
- [58] K. Tinschert, *Experimentelle Untersuchung resonanter und nichtresonanter Ionisationsmechanismen bei der Elektronenstoßionisation von Ionen*, Ph.D. thesis, Justus-Liebig University Giessen (1989).
- [59] M. J. Higgins, M. A. Lennon, J. G. Hughes, K. L. Bell, H. B. Gilbody, A. E. Kingston, and F. J. Smith, *Atomic and Molecular Data for Fusion, Part III. Recommended Cross Sections and Rates for Electron Ionization of Atoms and Ions: Copper to Uranium*. (Culham Laboratory, 1989).
- [60] E. N. Nikolaev, M. V. Gorshkov, A. V. Mordekhai, and V. L. Tal'rose, *High Energy Chem.* **24**, 1 (1990).
- [61] E. W. Bell, N. Djurić, and G. H. Dunn, *Phys. Rev. A* **48**, 4286 (1993).
- [62] A. Danjo, A. Matsumoto, S. Ohtani, H. Suzuki, H. Tawara, K. Wakiya, and M. Yoshino, *Journal of the Physical Society of Japan* **53**, 4091 (1984).
- [63] A. Matsumoto, A. Danjo, S. Ohtani, H. Suzuki, H. Tawara, T. Takayanagi, K. Wakiya, I. Yamada, and M. Y. T. Hirayama, *Journal of the Physical Society of Japan* **59**, 902 (1990).
- [64] K. F. Man, A. C. H. Smith, and M. F. A. Harrison, *J. Phys. B* **26**, 1365 (1993).
- [65] D. C. Gregory, P. F. Dittner, and D. H. Crandall, *Phys. Rev. A* **27**, 724 (1983).
- [66] E. D. Emmons, A. Aguilar, M. F. Gharaibeh, S. W. J. Scully, R. A. Phaneuf, A. L. D. Kilcoyne, A. S. Schlachter, I. Alvarez, C. Cisneros, and G. Hinojosa, *Phys. Rev. A* **71**, 042704 (2005).
- [67] D. C. Gregory and D. H. Crandall, *Phys. Rev. A* **27**, 2338 (1983).
- [68] M. S. Pindzola, D. C. Griffin, and C. Bottcher, *Phys. Rev. A* **27**, 2331 (1983).
- [69] A. M. Howald, D. C. Gregory, R. A. Phaneuf, D. H. Crandall, and M. S. Pindzola, *Phys. Rev. Lett.* **56**, 1675 (1986).

- [70] S. M. Younger, Phys. Rev. A **34**, 1952 (1986).
- [71] M. E. Bannister, D. W. Mueller, L. J. Wang, M. S. Pindzola, D. C. Griffin, and D. C. Gregory, Phys. Rev. A **38**, 38 (1988).
- [72] D. W. Mueller, L. J. Wang, and D. C. Gregory, Phys. Rev. A **39**, 2381 (1989).
- [73] J. Neumann, *Untersuchungen an einer Elektronenkanone für den Energiebereich 300 - 5000 eV sowie vergleichende Messungen zur Elektronenstossionization von Ionen*, Master's thesis, Justus-Liebig Universität Giessen (1992).
- [74] G. Hofmann, J. Neumann, U. Pracht, K. Tinschert, M. Stenke, R. Völpel, A. Müller, and E. Salzborn, in *The Physics of Highly Charged Ions. AIP Conf. Proc.*, Vol. 274, edited by P. Richard, M. Stöckli, C. L. Cocke, and C. D. Lin (1993) p. 485.
- [75] M. Stenke, K. Aichele, D. Hathiramani, G. Hofmann, M. Steidl, R. Völpel, and E. Salzborn, Nucl. Instrum. Methods B **98**, 573 (1995).
- [76] P. Mandelbaum, M. Cohen, J. L. Schwob, and A. Bar-Shalom, Eur. Phys. J. D **33**, 213 (2005).
- [77] Mandelbaum, P., Schwob, and J., Eur. Phys. J. D **49**, 173 (2008).
- [78] D. Mitnik, P. Mandelbaum, J. L. Schwob, A. Bar-Shalom, and J. Oreg, Phys. Rev. A **55**, 310 (1997).
- [79] M. S. Pindzola, C. P. Ballance, J. A. Ludlow, S. D. Loch, and D. C. Griffin, J. Phys. B , 025201 (2010).
- [80] D. Mitnik, P. Mandelbaum, J. L. Schwob, A. Bar-Shalom, J. Oreg, and W. H. Goldstein, Phys. Rev. A **53**, 3178 (1996).
- [81] A. V. Philipov, V. M. Povyshev, A. A. Sadovoy, V. P. Shevelko, G. D. Shirkov, E. G. Vasina, and V. V. Vatulín, in *Preprints and Communications* (Joint Inst. Nucl. Res. Dubna, 2002).
- [82] A. Müller, in *Physics of Ion-Impact Phenomena*, Springer Series in Chemical Physics, Vol. 54, edited by D. Mathur (Springer, Berlin, Heidelberg, New York, 1991) p. 13.
- [83] A. Müller, Adv. At. Mol. Phys. **55**, 293 (2008).
- [84] K. J. LaGattuta and Y. Hahn, Phys. Rev. A **24**, 2273 (1981).
- [85] R. J. W. Henry and A. Z. Msezane, Phys. Rev. A **26**, 2545 (1982).

- [86] A. Müller, G. Hofmann, K. Tinschert, and E. Salzborn, *Phys. Rev. Lett.* **61**, 1352 (1988).
- [87] M. S. Pindzola, D. C. Griffin, and C. Bottcher, *Atomic processes in electron-ion and ion-ion collisions*, edited by F. Brouillard (Plenum Press, New York, 1986).
- [88] K. Berrington, J. Pelan, and L. Quigley, *J. Phys. B* **30**, 4973 (1997).
- [89] P. Descouvemont and D. Baye, *Reports on Progress in Physics* **73**, 036301 (2010).
- [90] S. M. Younger, in *Electron Impact Ionization*, edited by G. H. Dunn and M. T. D. (Springer Verlag, Wien-New York, 1985) p. 1.
- [91] W. Lotz, *Astrophys. J. Suppl. Ser.* **14**, 207 (1967).
- [92] W. Lotz, *Z. Phys.* **216**, 241 (1968).
- [93] W. Lotz, *Z. Phys.* **220**, 466 (1969).
- [94] W. Lotz, *Z. Phys.* **232**, 101 (1970).
- [95] Gryziński and M., *Phys. Rev. A* **138**, 336 (1965).
- [96] J. Jacobi, H. Knopp, S. Schippers, A. Müller, S. D. Loch, M. Witthoef, M. S. Pindzola, and C. P. Ballance, *Phys. Rev. A* **70**, 042717 (2004).
- [97] J. Jacobi, H. Knopp, S. Schippers, W. Shi, and A. Müller, *J. Phys. B* **38**, 2015 (2005).
- [98] F. Brötz, R. Trassl, R. W. McCullough, W. Arnold, and E. Salzborn, *Phys. Scr.* **T92**, 278 (2001).
- [99] A. Müller, K. Tinschert, C. Achenbach, R. Becker, and E. Salzborn, *Nucl. Instrum. Methods B* **10**, 204 (1985).
- [100] Rinn, K., Müller, A., Eichenauer, H., Salzborn, and E., *Rev. Sci. Instrum.* **53**, 829 (1982).
- [101] F. Timphus, *Ausbau einer Experimentieranlage mit gekreuzten Elektronen- und Ionenstrahlen*, Ph.D. thesis, Justus-Liebig University Giessen (1998).
- [102] A. Müller, K. Huber, K. Tinschert, R. Becker, and E. Salzborn, **18**, 2993 (1985).
- [103] H. Knopp, C. Böhme, J. Jacobi, S. Ricz, S. Schippers, and A. Müller, *Nucl. Instrum. Methods B* **205**, 433 (2003).
- [104] D. Hathiramani, *Ionisation und Fragmentation von Fulleren-Ionen durch Elektronenstoß*, Ph.D. thesis, Justus-Liebig-Universität Giessen (2000).

- [105] K. Huber, "Zählratenstatistik," Unpublished Internal Report, Institut für Atom- und Molekülphysik, Justus-Liebig University Giessen, (available at <http://www.strz.uni-giessen.de/ExpHelp/cntlrou/cntlrou.html>).
- [106] M. Khouilid, S. Cherkani-Hassani, S. Rachafi, H. Teng, and P. Defrance, *J. Phys. B* **34**, 1727 (2001).
- [107] R. A. Falk, G. Stefani, R. Camilloni, G. H. Dunn, R. A. Phaneuf, D. C. Gregory, and D. H. Crandall, *Phys. Rev. A* **28**, 91 (1983).
- [108] P. Feldman and R. Novick, *Phys. Rev.* **160**, 143 (1967).
- [109] M. Lu and R. A. Phaneuf, *Phys. Rev. A* **66**, 012706 (2002).
- [110] R. D. Cowan, *The Theory of Atomic Structure and Spectra* (University of California Press, Berkeley, 1981).
- [111] Atomic and Optical Theory Group Los Alamos National Laboratory (LANL), "Atomic physics codes package," (available at <http://aphysics2.lanl.gov/cgi-bin/ION/runlanl08d.pl>).
- [112] National Institute of Standards and Technology, "Atomic Spectra Database," (available at <http://www.nist.gov/pml/data/asd.cfm>).
- [113] A. Matsumoto, S. Ohtani, and T. Iwai, *J. Phys. B* **15**, 1871 (1982).
- [114] J. B. Greenwood, D. Burns, R. W. McCullough, J. Geddes, and H. B. Gilbody, *J. Phys. B* **29**, 5867 (1996).
- [115] N. Djurić, E. W. Bell, X. Q. Guo, G. H. Dunn, R. A. Phaneuf, M. E. Bannister, M. S. Pindzola, and D. C. Griffin, *Phys. Rev. A* **47**, 4786 (1993).
- [116] S. M. Younger, *Phys. Rev. Lett.* **56**, 2618 (1986).
- [117] J. Rausch, *Untersuchung der Elektronenstoß-Doppelionisation hochgeladener Xenonionen*, Bachelor thesis, Justus-Liebig University Giessen (2008).
- [118] J. Rudolph, *Zweifachionisation hochgeladener Xenonionen durch Elektronenstoß*, Diploma thesis, Justus-Liebig University Giessen (2009).
- [119] J. Jacobi, *Indirekte Prozesse bei der Elektronenstoßionisation von Zwei- und Quasi-Zwei-Elektronen-Systemen*, Ph.D. thesis, Justus-Liebig University Giessen (2004).
- [120] P.-M. Hillenbrand, *Doppelionisation hochgeladener Zinn-Ionen durch Elektronenstoß*, Diploma thesis, Justus-Liebig University Giessen (2009).
- [121] R. A. Phaneuf, *Physica Scripta* **T47**, 124 (1993).



# A Experimental details on the absolute cross-section measurements

## A.1 Properties of the primary ion target beam used in the experiments

In this section, the properties of the primary ion beams used in the present measurements of absolute cross-section values are given. The data are listed in Tables A.1 and A.2 and comprise the reactions investigated, magnitudes of the available ion current, slit width (i.e., sizes of the ion beams used), backgrounds in the units of frequency per 1 nA of ion current and the signal/background ratios at the cross-section maxima or at 1000 eV where these could not be reached.

**Table A.1:** Experimental conditions for measurements of ionization of Xe ions.

Reaction	$I_i$ [nA]	Slits [mm]	Background [Hz nA <sup>-1</sup> ]	Signal/backgr.
Xe <sup>+</sup> → Xe <sup>2+</sup>	0.074	0.6 × 0.6	4320	2.83
Xe <sup>+</sup> → Xe <sup>3+</sup>	0.049	0.6 × 0.6	44	467
Xe <sup>+</sup> → Xe <sup>4+</sup>	0.21	0.6 × 0.6	10	352
Xe <sup>+</sup> → Xe <sup>5+</sup>	0.18	0.6 × 0.6	5	475
Xe <sup>+</sup> → Xe <sup>6+</sup>	2.9	0.8 × 0.8	4.4	252
Xe <sup>+</sup> → Xe <sup>7+</sup>	2.9	0.8 × 0.8	0.7	276
Xe <sup>+</sup> → Xe <sup>8+</sup>	2.9	0.8 × 0.8	0.16	333
Xe <sup>+</sup> → Xe <sup>9+</sup>	8.6	0.5 × 0.7	0.007	606
Xe <sup>+</sup> → Xe <sup>10+</sup>	45.6	1.0 × 1.0	0.004	16.2
Xe <sup>2+</sup> → Xe <sup>3+</sup>	0.144	0.6 × 0.6	1180	6.01
Xe <sup>2+</sup> → Xe <sup>4+</sup>	0.38	0.3 × 0.3	24.1	911
Xe <sup>3+</sup> → Xe <sup>4+</sup>	0.23	0.6 × 0.6	270	14.36
Xe <sup>3+</sup> → Xe <sup>5+</sup>	0.5	0.3 × 0.3	9.2	817
Xe <sup>4+</sup> → Xe <sup>5+</sup>	0.62	0.7 × 0.7	47.3	42.9
Xe <sup>4+</sup> → Xe <sup>6+</sup>	1.9	0.3 × 0.3	3.6	380
Xe <sup>5+</sup> → Xe <sup>6+</sup>	1.1	0.7 × 0.7	23	120
Xe <sup>5+</sup> → Xe <sup>7+</sup>	1.3	0.4 × 0.4	1	879
Xe <sup>6+</sup> → Xe <sup>7+</sup>	0.96	0.7 × 0.7	53	32.6

**Table A.1**(continued)

Reaction	$I_i$ [nA]	Slits [mm]	Background [Hz nA <sup>-1</sup> ]	Signal/backgr.
Xe <sup>6+</sup> → Xe <sup>8+</sup>	7	0.8 × 0.8	0.5	978
Xe <sup>6+</sup> → Xe <sup>9+</sup>	17.7	0.7 × 0.7	0.05	1293
Xe <sup>6+</sup> → Xe <sup>10+</sup>	17.7	0.7 × 0.7	0.02	511
Xe <sup>7+</sup> → Xe <sup>8+</sup>	0.75	0.7 × 0.7	112	4.38
Xe <sup>7+</sup> → Xe <sup>9+</sup>	9.2	0.7 × 0.7	0.07	1764
Xe <sup>7+</sup> → Xe <sup>10+</sup>	20	0.7 × 0.5	0.02	1409
Xe <sup>7+</sup> → Xe <sup>11+</sup>	20	0.7 × 0.5	0.008	298
Xe <sup>8+</sup> → Xe <sup>9+</sup>	0.9	0.7 × 0.7	7	55.9
Xe <sup>8+</sup> → Xe <sup>10+</sup>	7.8	0.7 × 0.7	0.03	1954
Xe <sup>9+</sup> → Xe <sup>10+</sup>	0.217	0.8 × 0.8	8	354
Xe <sup>9+</sup> → Xe <sup>11+</sup>	8.2	0.7 × 0.7	0.03	1796
Xe <sup>10+</sup> → Xe <sup>11+</sup>	0.480	0.7 × 0.5	5.8	152
Xe <sup>10+</sup> → Xe <sup>12+</sup>	4.4	0.7 × 0.7	0.02	2535
Xe <sup>11+</sup> → Xe <sup>12+</sup>	4.7	1.0 × 1.0	5.4	86.8
Xe <sup>11+</sup> → Xe <sup>13+</sup>	7	0.7 × 0.7	0.03	45.7
Xe <sup>12+</sup> → Xe <sup>13+</sup>	3.8	1.0 × 1.0	2.7	146
Xe <sup>12+</sup> → Xe <sup>14+</sup>	5.08	0.7 × 0.7	0.03	1220
Xe <sup>13+</sup> → Xe <sup>14+</sup>	3.2	1.0 × 1.0	2.7	103
Xe <sup>13+</sup> → Xe <sup>15+</sup>	5	0.7 × 0.7	0.03	987
Xe <sup>14+</sup> → Xe <sup>15+</sup>	3.2	1.0 × 1.0	4.5	51.6
Xe <sup>14+</sup> → Xe <sup>16+</sup>	4.2	0.8 × 0.8	0.03	571
Xe <sup>15+</sup> → Xe <sup>16+</sup>	3.2	1.0 × 1.0	14.1	13.6
Xe <sup>15+</sup> → Xe <sup>17+</sup>	2.8	0.8 × 0.8	0.03	636
Xe <sup>16+</sup> → Xe <sup>17+</sup>	22	0.7 × 0.7	9	31
Xe <sup>16+</sup> → Xe <sup>18+</sup>	1.9	0.9 × 0.8	0.04	178
Xe <sup>17+</sup> → Xe <sup>18+</sup>	38	0.7 × 0.7	6	32.6
Xe <sup>17+</sup> → Xe <sup>19+</sup>	3	1.0 × 1.0	0.02	54.9
Xe <sup>18+</sup> → Xe <sup>19+</sup>	38	0.7 × 0.7	5.4	29.9
Xe <sup>19+</sup> → Xe <sup>20+</sup>	30	0.7 × 0.7	4.5	49.9
Xe <sup>20+</sup> → Xe <sup>21+</sup>	35	0.7 × 0.7	5.8	39.1
Xe <sup>21+</sup> → Xe <sup>22+</sup>	9.3	0.7 × 0.7	33.7	6.1
Xe <sup>22+</sup> → Xe <sup>23+</sup>	5	0.7 × 0.7	19.8	22.3
Xe <sup>23+</sup> → Xe <sup>24+</sup>	2.5	0.7 × 0.7	42.4	34.9
Xe <sup>24+</sup> → Xe <sup>25+</sup>	2.6	0.7 × 0.7	11.4	40.3
Xe <sup>25+</sup> → Xe <sup>26+</sup>	1.7	0.8 × 0.8	32.7	40

**Table A.2:** Experimental conditions for measurements of ionization of Sn ions

Reaction	$I_i$ [nA]	Slits [mm]	Background [kHz nA <sup>-1</sup> ]	Signal/backgr.
Sn <sup>+</sup> → Sn <sup>2+</sup>	0.45	1.0 × 1.0	11500	1.83
Sn <sup>+</sup> → Sn <sup>3+</sup>	0.45	1.0 × 1.0	32.9	717
Sn <sup>2+</sup> → Sn <sup>3+</sup>	0.83	0.8 × 0.8	370	17.3
Sn <sup>2+</sup> → Sn <sup>4+</sup>	0.83	0.8 × 0.8	17.5	562
Sn <sup>3+</sup> → Sn <sup>4+</sup>	0.4	0.7 × 0.7	87.9	103
Sn <sup>3+</sup> → Sn <sup>5+</sup>	0.4	0.7 × 0.7	6.8	678
Sn <sup>4+</sup> → Sn <sup>5+</sup>	0.26	0.8 × 0.8	20.3	278
Sn <sup>4+</sup> → Sn <sup>6+</sup>	0.26	0.8 × 0.8	2.69	137
Sn <sup>5+</sup> → Sn <sup>6+</sup>	1.8	1.0 × 1.0	8.9	360
Sn <sup>5+</sup> → Sn <sup>7+</sup>	1.8	1.0 × 1.0	0.51	674
Sn <sup>6+</sup> → Sn <sup>7+</sup>	2	0.6 × 0.6	3.5	164
Sn <sup>6+</sup> → Sn <sup>8+</sup>	6.2	0.8 × 0.8	1.03	142
Sn <sup>7+</sup> → Sn <sup>8+</sup>	1.7	0.8 × 0.8	2.78	219
Sn <sup>7+</sup> → Sn <sup>9+</sup>	2.9	0.8 × 0.8	0.09	1196
Sn <sup>8+</sup> → Sn <sup>9+</sup>	4.2	0.8 × 0.8	1.94	171
Sn <sup>8+</sup> → Sn <sup>10+</sup>	6	1.0 × 1.0	0.07	960
Sn <sup>9+</sup> → Sn <sup>10+</sup>	7.1	0.6 × 0.6	1.7	178
Sn <sup>9+</sup> → Sn <sup>11+</sup>	6.05	0.6 × 0.6	0.04	1479
Sn <sup>10+</sup> → Sn <sup>11+</sup>	3.7	0.6 × 0.6	1.7	144
Sn <sup>10+</sup> → Sn <sup>12+</sup>	3.8	0.6 × 0.6	0.02	1899
Sn <sup>11+</sup> → Sn <sup>12+</sup>	4.3	0.6 × 0.6	2.13	107
Sn <sup>11+</sup> → Sn <sup>13+</sup>	4.5	0.6 × 0.6	0.03	1573
Sn <sup>12+</sup> → Sn <sup>13+</sup>	5	0.6 × 0.6	3.74	82.7
Sn <sup>12+</sup> → Sn <sup>14+</sup>	5.3	0.6 × 0.6	0.03	1266
Sn <sup>13+</sup> → Sn <sup>14+</sup>	4.7	0.8 × 0.8	6.2	23.1

## A.2 Electron-current correction functions

This section describes the electron-current correction functions (ECCF) that were used in the course of the present measurements. There were five ECCF measurements performed: April 2007, March 2008, November 2008, July 2009 and August 2009. The electron currents on each electrode of the gun were measured separately as functions of electron acceleration voltage. For more comfortable use the measured data except for April 2007 were fitted with the following function

$$C(U_e) = C_0 + A_1 \exp(-U_e/t_1) + A_2 \exp(-U_e/t_2). \quad (\text{A.1})$$

The electron-current correction function measured in April 2007 was fitted using the function

$$C(U_e) = C_0 + A_1[1 - \exp(-U_e/t_1)] + A_2[1 - \exp(-U_e/t_2)]. \quad (\text{A.2})$$

In the both equations  $U_e$  is the electron acceleration voltage and  $A_1, A_2, t_1, t_2$  and  $C_0$  are the fitting coefficients, the values of which for each used electron-current correction function are listed in table Tab. A.3 below.

**Table A.3:** Fitting coefficients for electron-current correction functions.

Function	$C_0$	$A_1$	$A_2$	$t_1$	$t_2$
April 2007 <sup>1</sup>	0.3399	0.30945	0.33791	61.3211	14.16874
March 2008	0.9748	-0.40894	-0.0769	13.00698	78.12314
November 2008	0.96722	-0.20777	-0.443	33.96317	3.38886
July 2009	0.95206	0.00152	-0.15504	-416.90686	18.00624
August 2009	0.95393	0.00159	-0.10278	-453.36509	18.39305

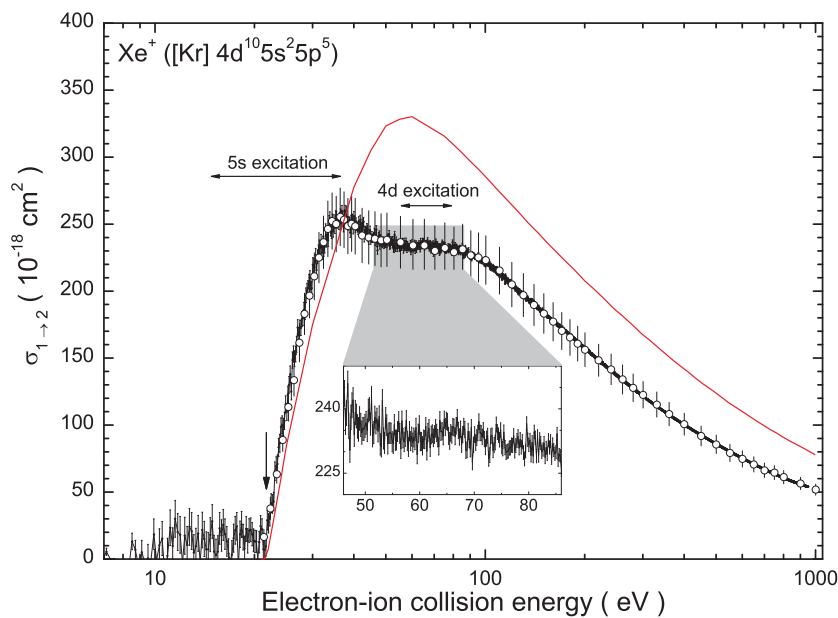
<sup>1</sup>For this ECCF the given coefficients are to be applied into eq. A.2.

## B Details on the ionization of xenon ions

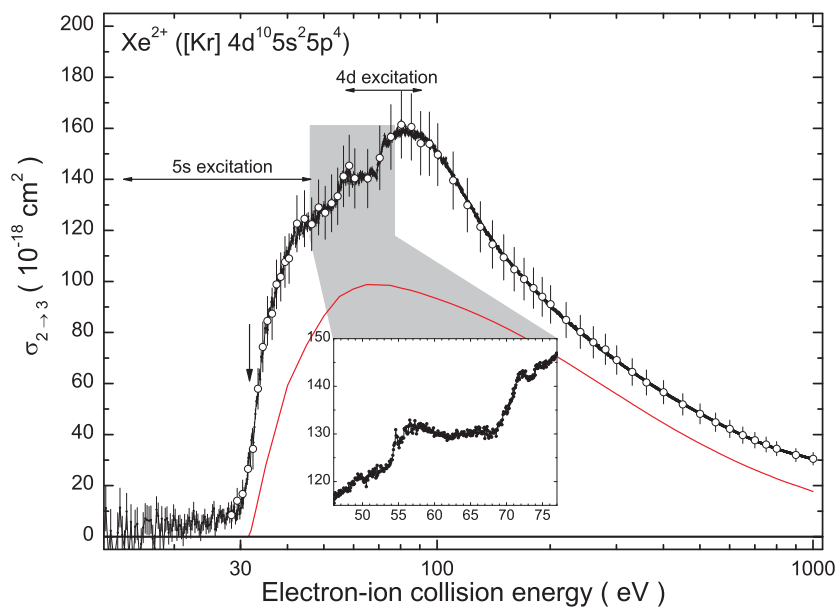
The detailed illustrations of the measured single- and multiple-ionization cross sections of xenon ions together with explanations of individual contributions arising from direct and indirect ionization mechanisms are given here. For all figures, open circles are absolute cross-section data and small filled circles represent energy scan data. For single-ionization, thin solid curves denote the results of CADW direct-ionization cross section calculations using the LANL Atomic Physics Code package [111]. For the cross sections, for which the present metastable-state fractions could be estimated (see Tab. 4.2 in Section 4.1.2) they have been included in the calculations. For those cross sections, for which the metastable fraction could not be estimated the CADW calculations include only ionization from the ground state.

Horizontal arrows represent the energy ranges from the lowest energy required to excite an electron of the corresponding subshell to the nearest available vacancy up to the energy needed to remove it to the continuum. These energies have also been obtained using the LANL code. Vertical arrows show the ground-state ionization potentials.

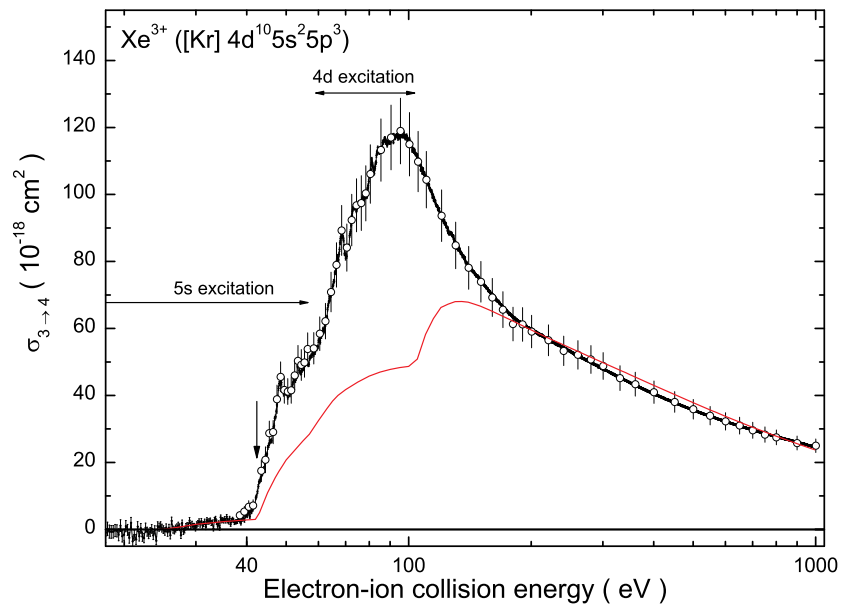
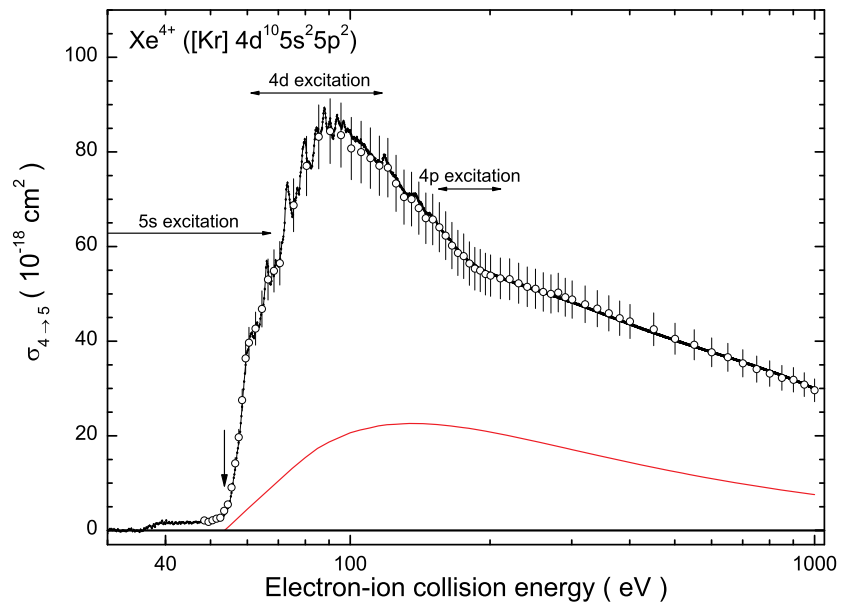
## B.1 Single ionization

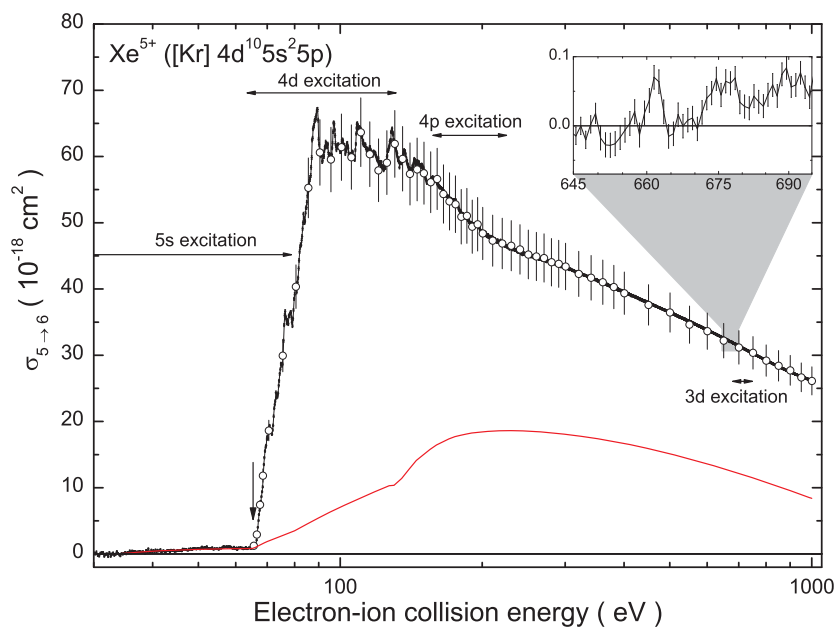


**Figure B.1:** Single ionization of  $\text{Xe}^+$ .

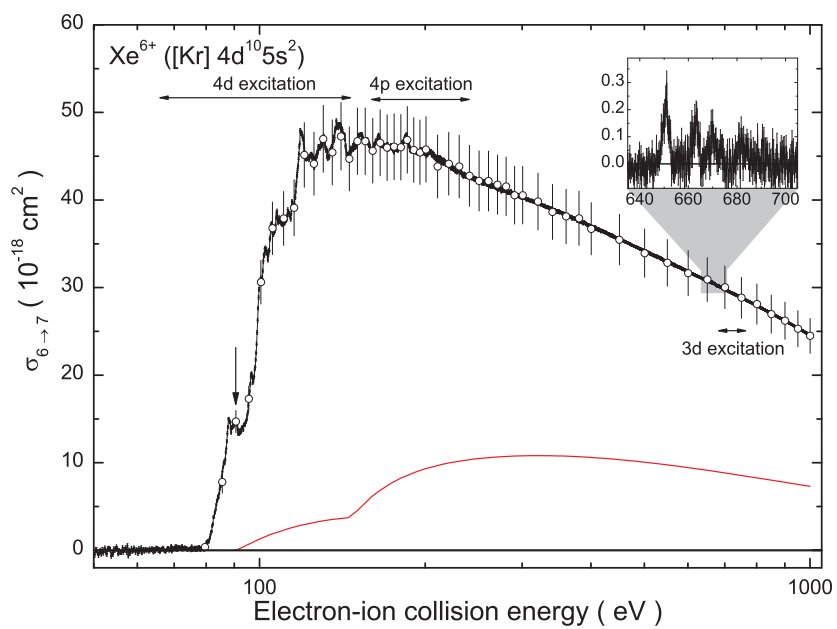


**Figure B.2:** Single ionization of  $\text{Xe}^{2+}$ .

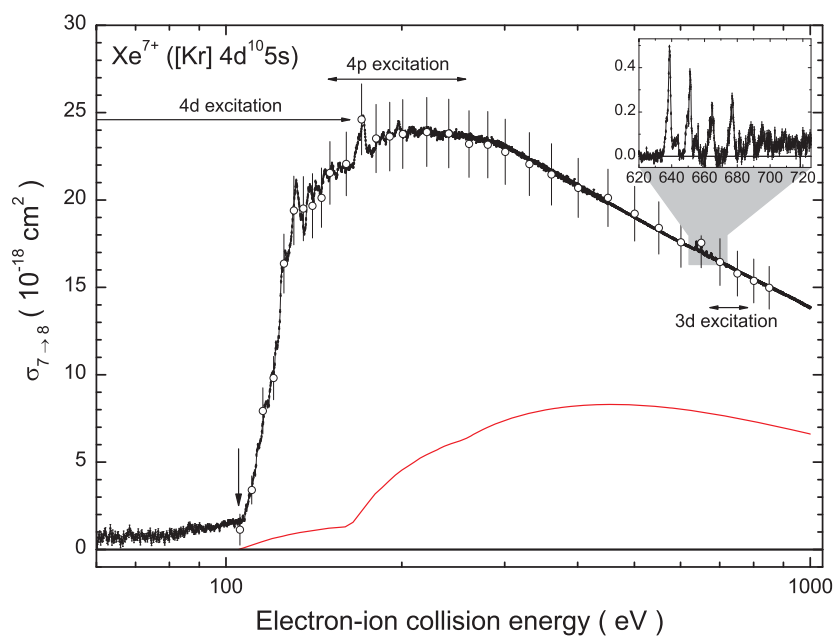
**Figure B.3:** Single ionization of  $\text{Xe}^{3+}$ .**Figure B.4:** Single ionization of  $\text{Xe}^{4+}$ .



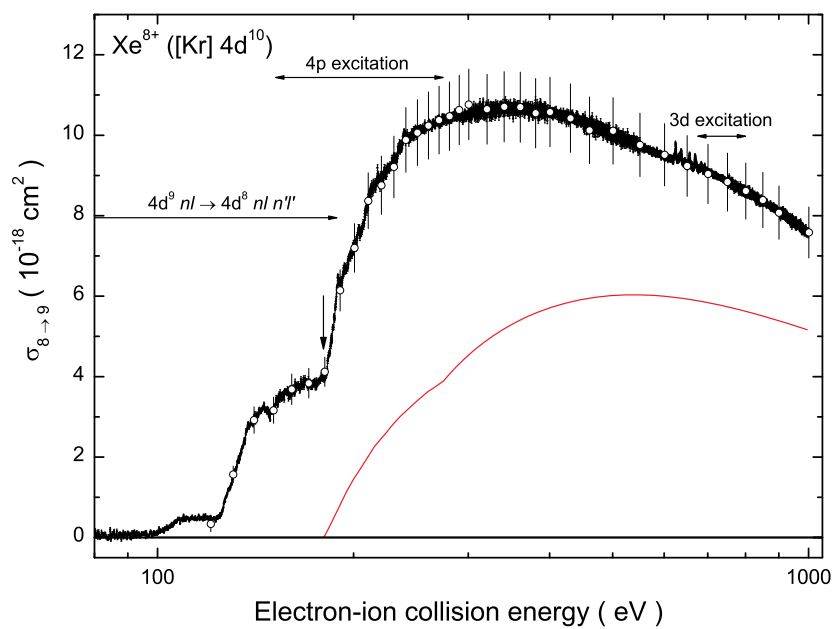
**Figure B.5:** Single ionization of  $\text{Xe}^{5+}$ .



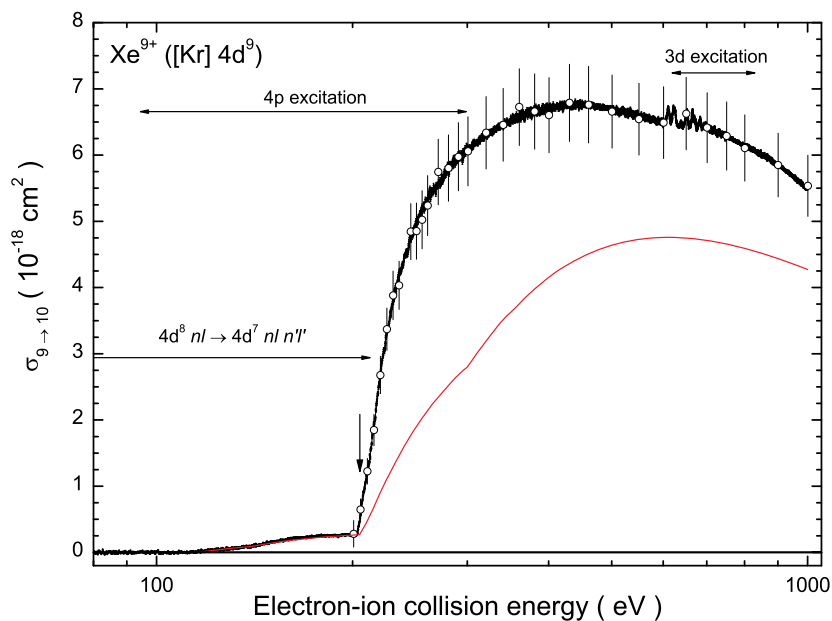
**Figure B.6:** Single ionization of  $\text{Xe}^{6+}$ .



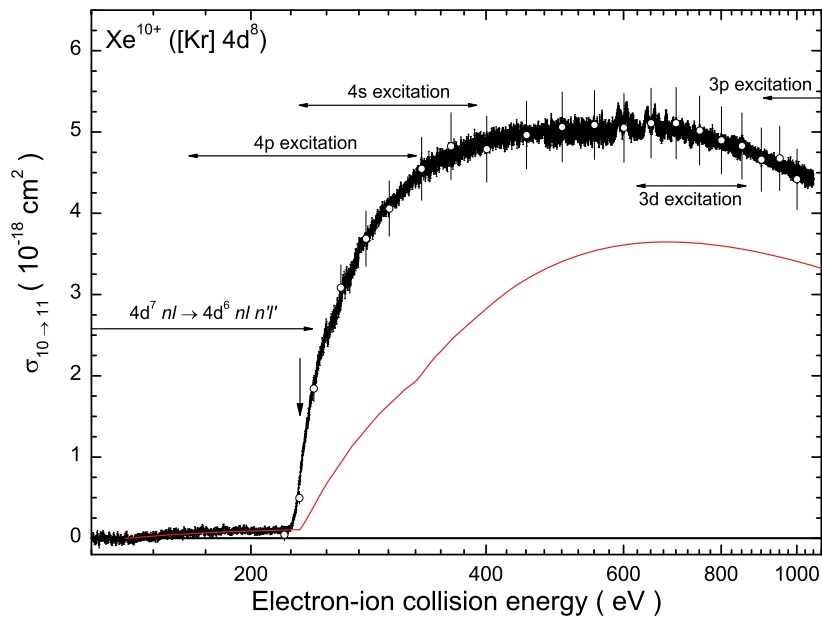
**Figure B.7:** Single ionization of  $\text{Xe}^{7+}$ .



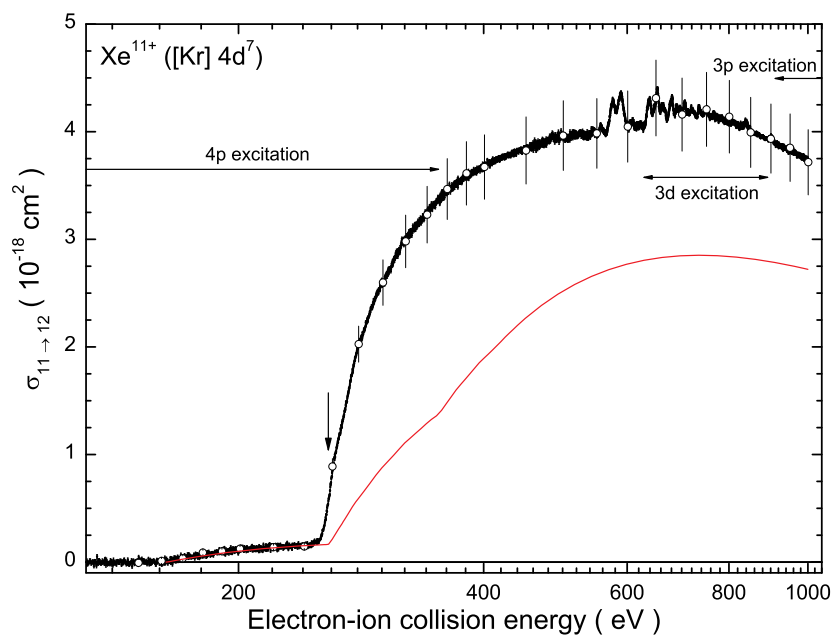
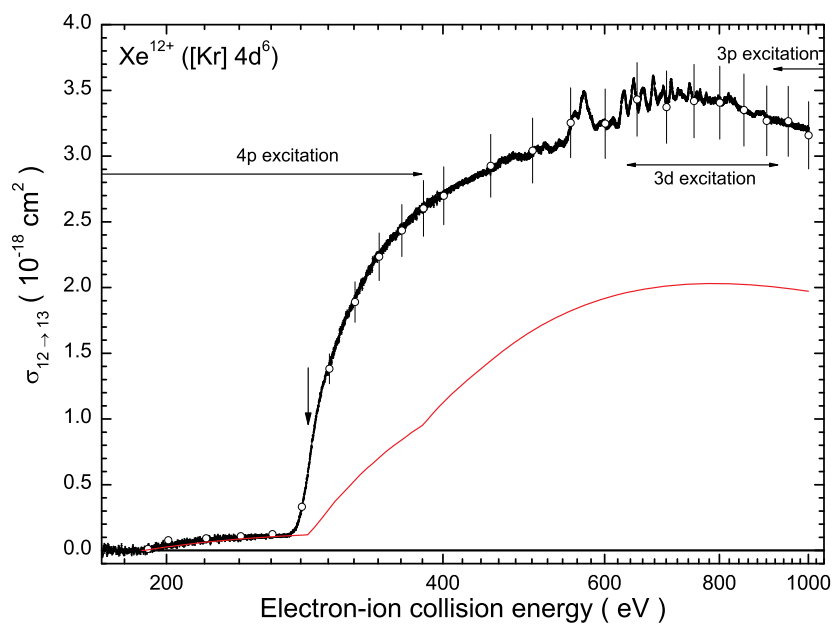
**Figure B.8:** Single ionization of  $\text{Xe}^{8+}$ .



**Figure B.9:** Single ionization of  $\text{Xe}^{9+}$ .



**Figure B.10:** Single ionization of  $\text{Xe}^{10+}$ .

**Figure B.11:** Single ionization of  $\text{Xe}^{11+}$ .**Figure B.12:** Single ionization of  $\text{Xe}^{12+}$ .

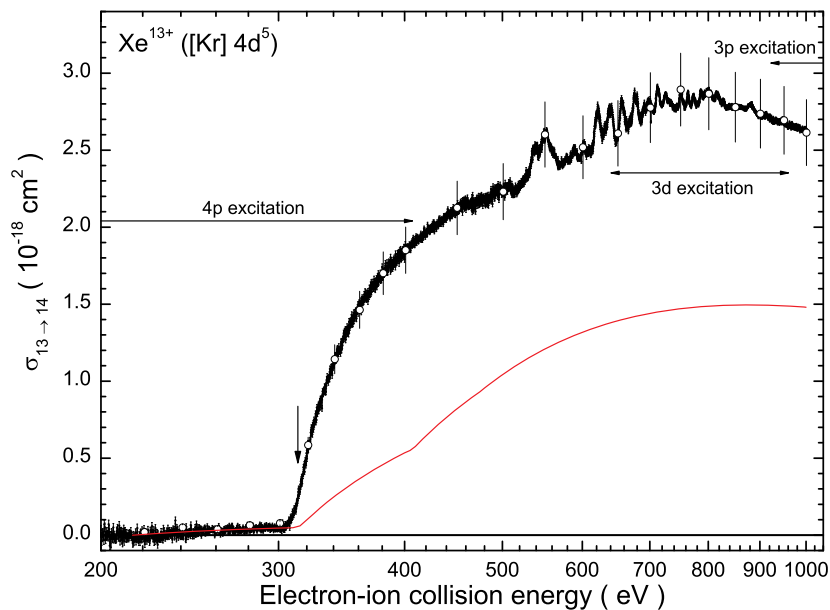


Figure B.13: Single ionization of  $\text{Xe}^{13+}$ .

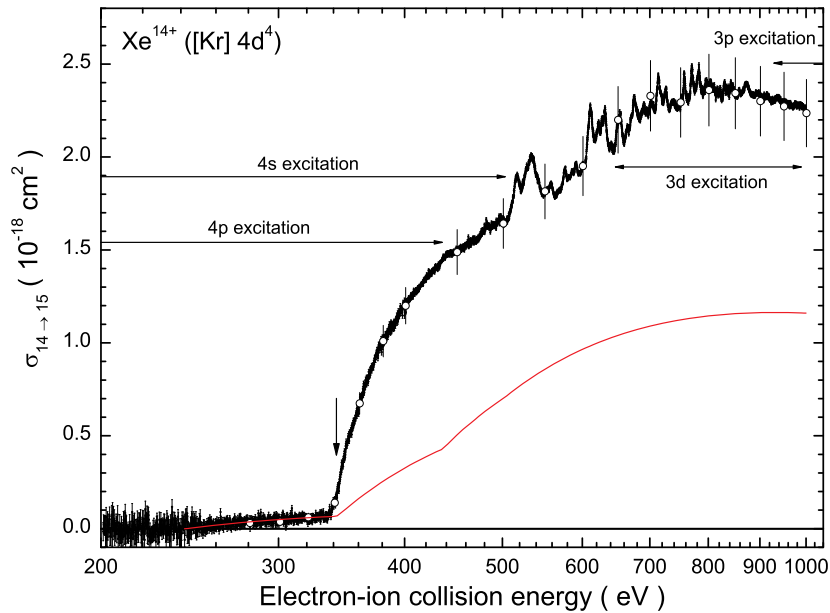


Figure B.14: Single ionization of  $\text{Xe}^{14+}$ .

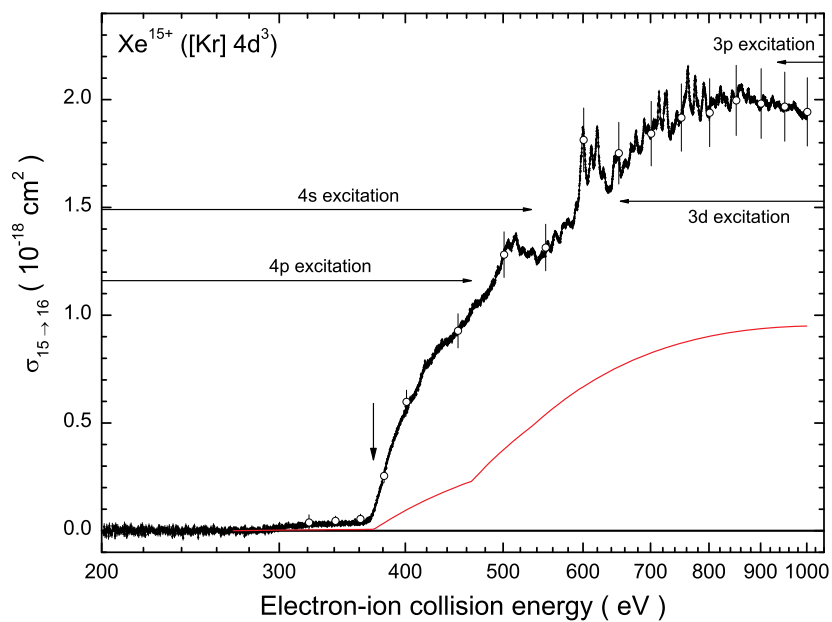


Figure B.15: Single ionization of  $\text{Xe}^{15+}$ .

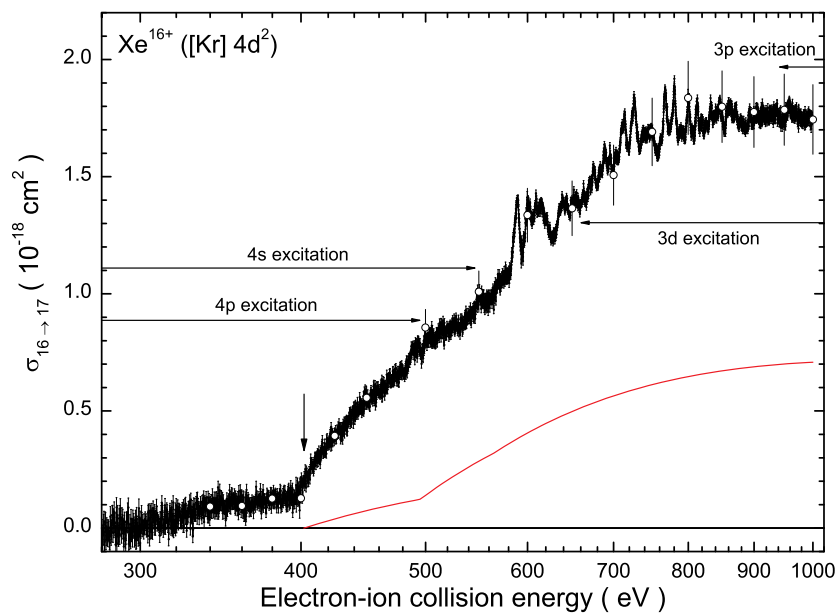


Figure B.16: Single ionization of  $\text{Xe}^{16+}$ .

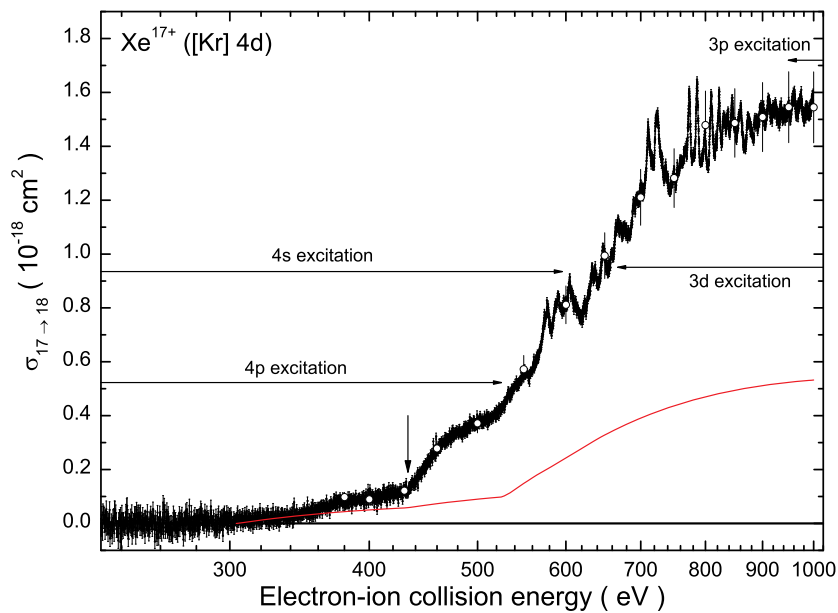


Figure B.17: Single ionization of  $\text{Xe}^{17+}$ .

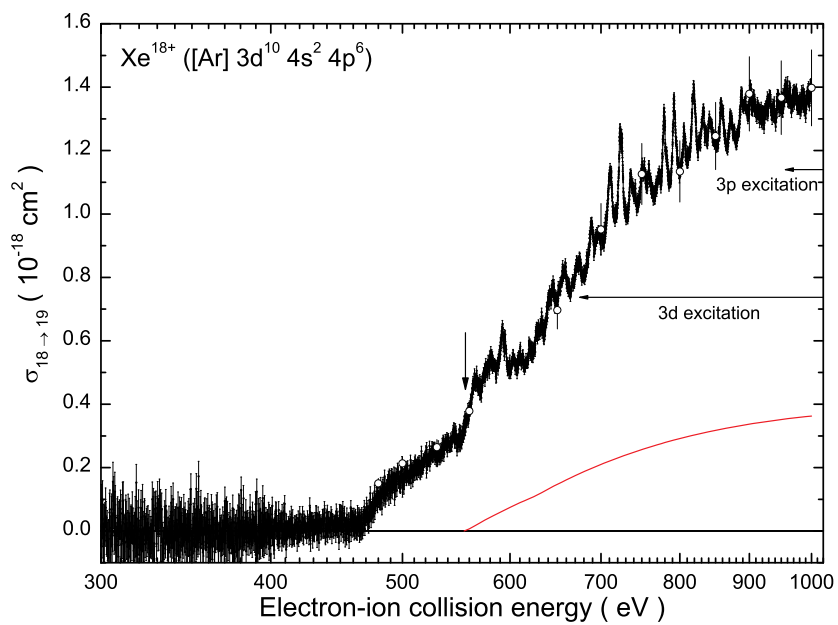


Figure B.18: Single ionization of  $\text{Xe}^{18+}$ .

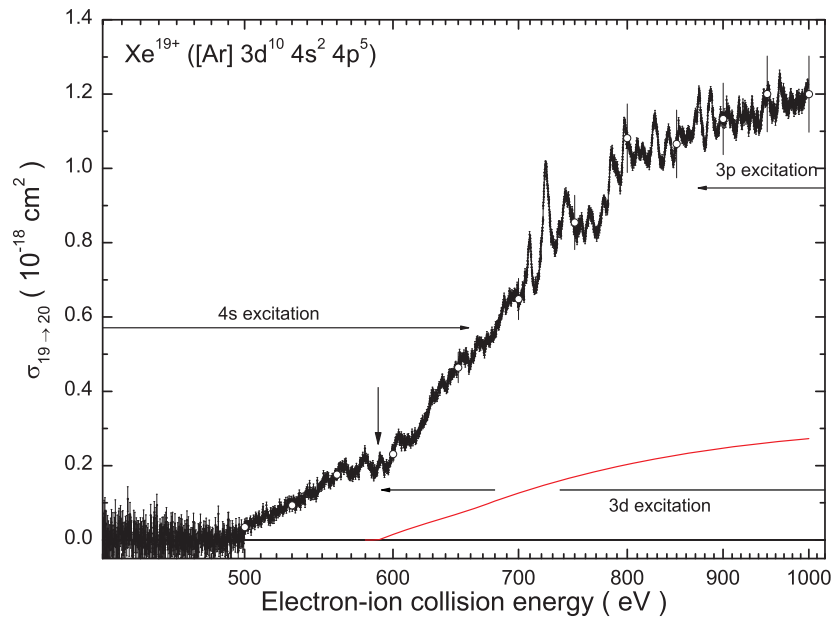


Figure B.19: Single ionization of  $\text{Xe}^{19+}$ .

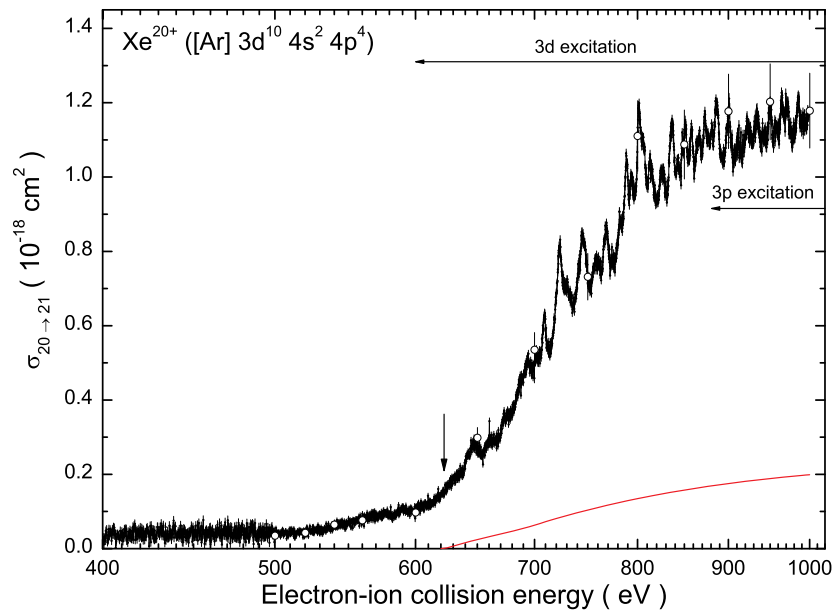


Figure B.20: Single ionization of  $\text{Xe}^{20+}$ .

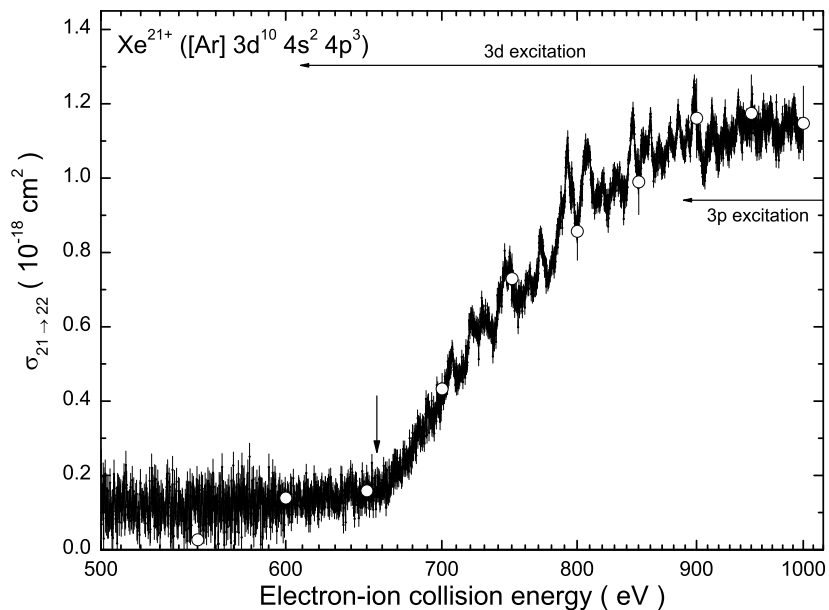


Figure B.21: Single ionization of  $\text{Xe}^{21+}$ .

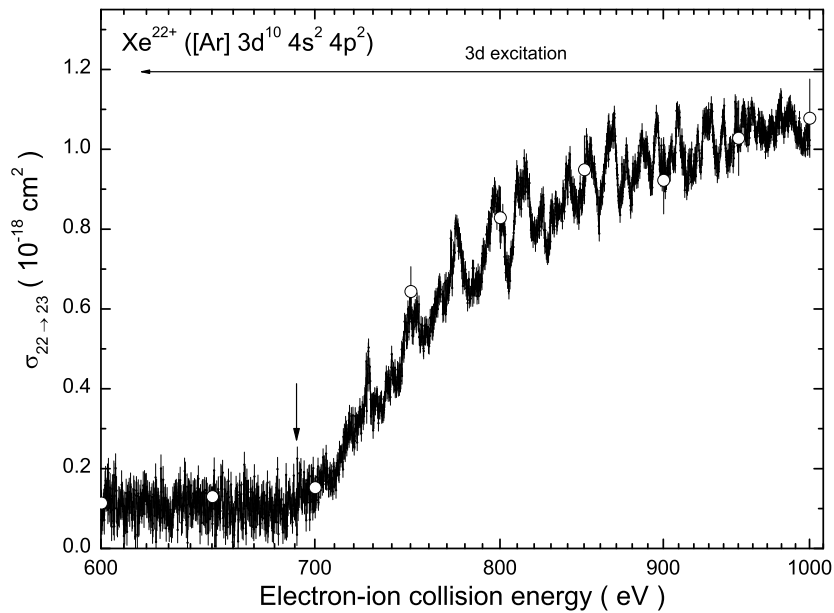
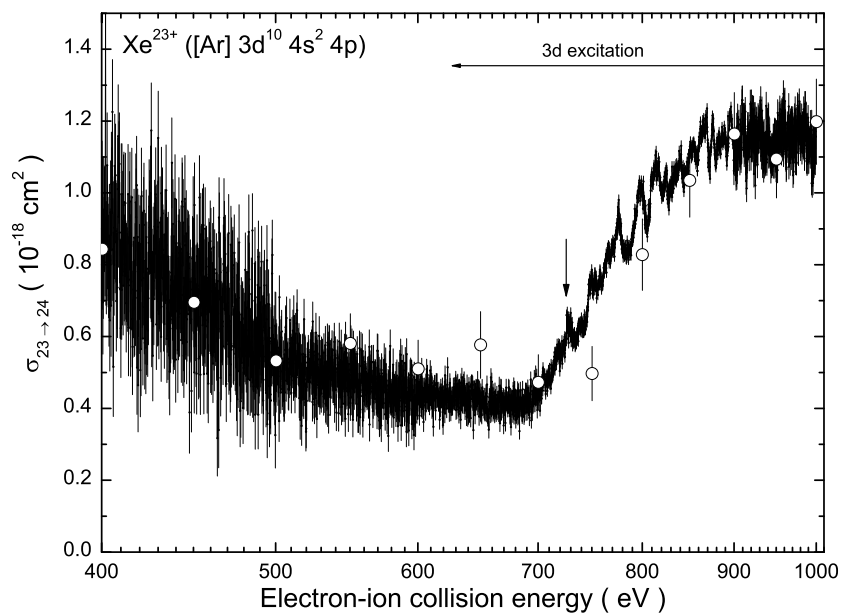
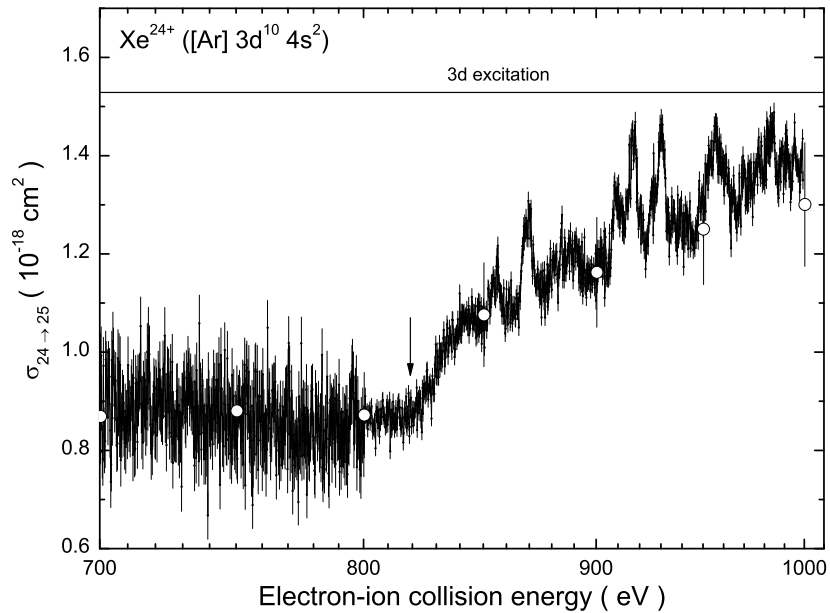
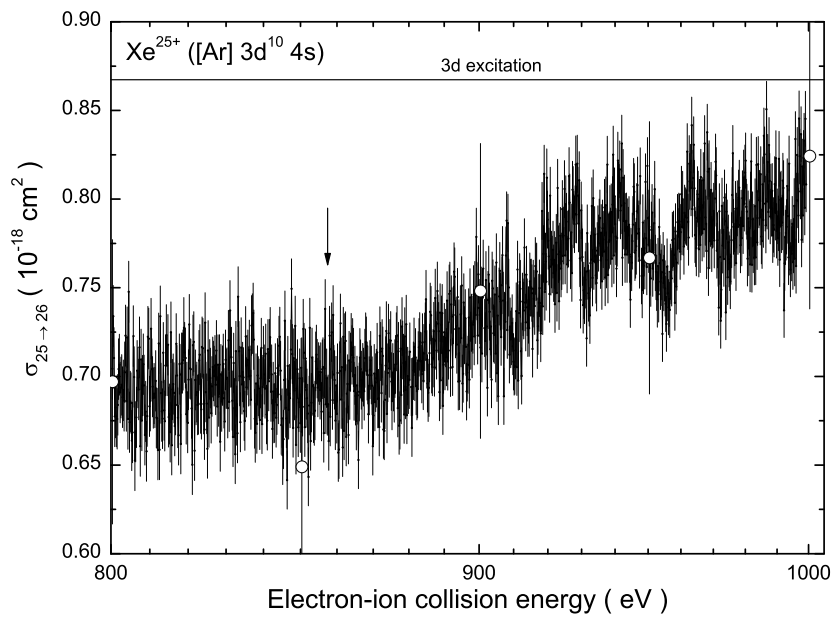
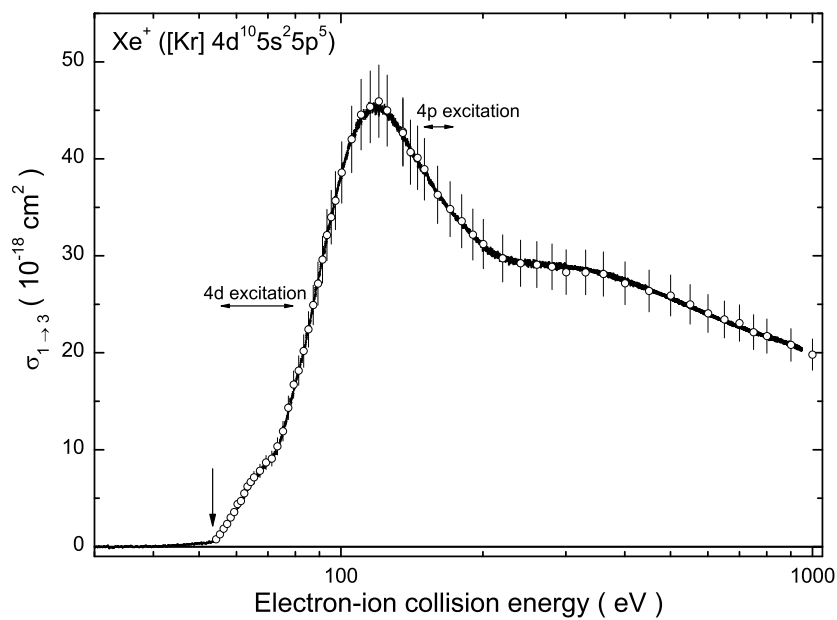
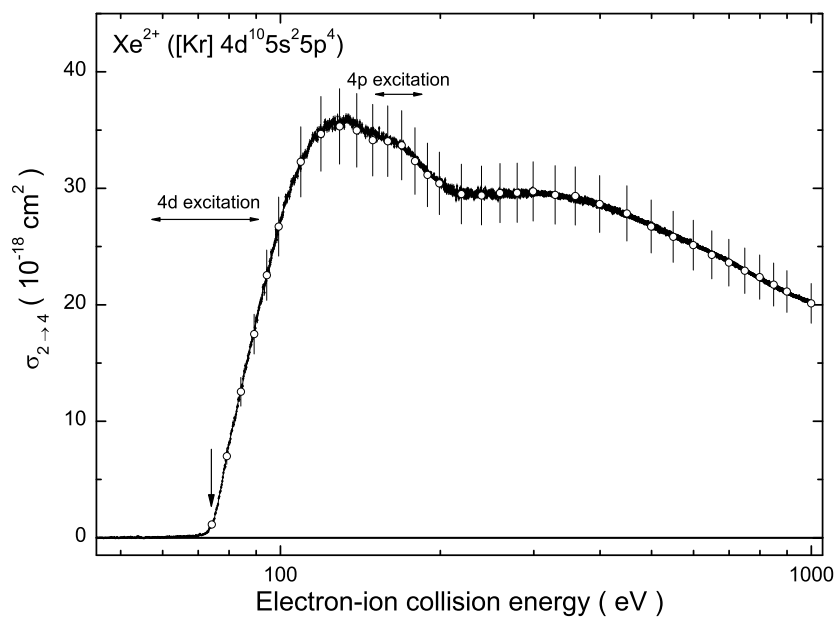


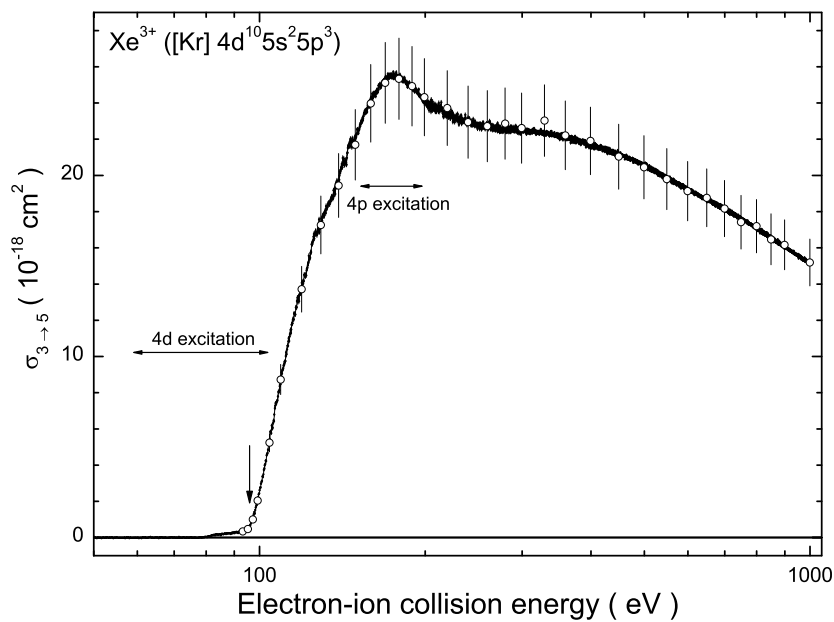
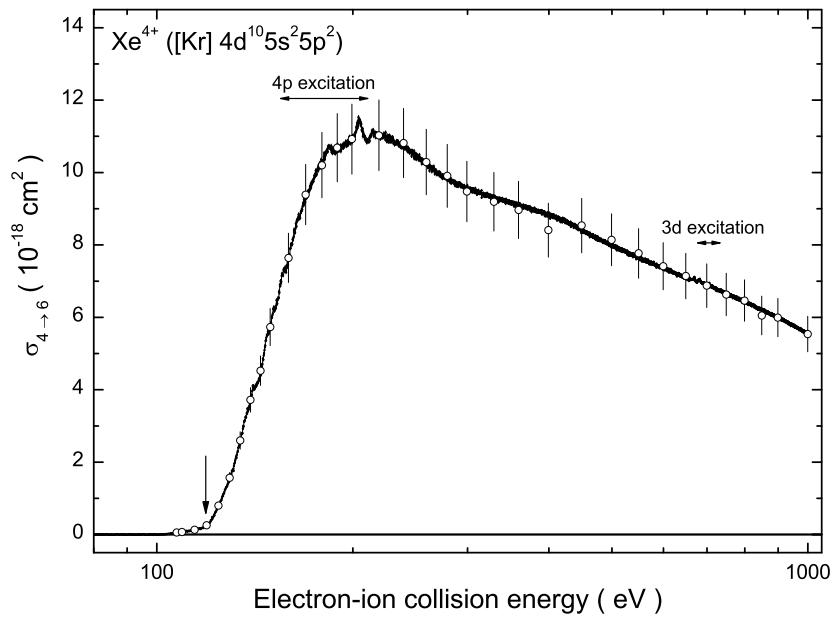
Figure B.22: Single ionization of  $\text{Xe}^{22+}$ .

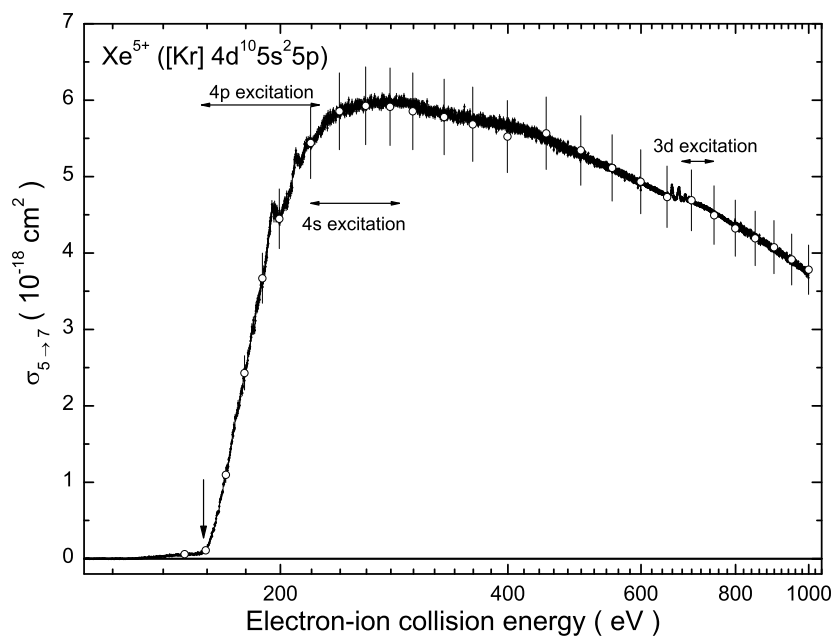
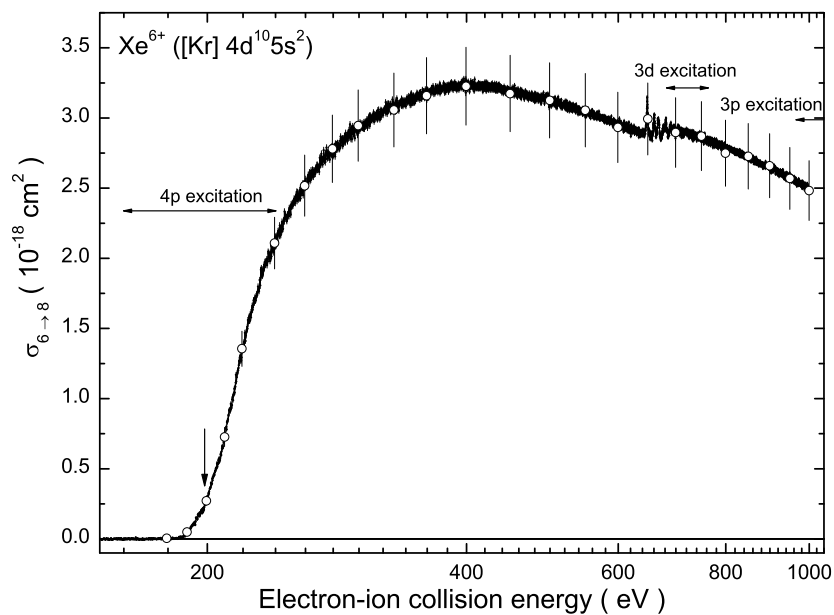
**Figure B.23:** Single ionization of  $\text{Xe}^{23+}$ .**Figure B.24:** Single ionization of  $\text{Xe}^{24+}$ .



**Figure B.25:** Single ionization of Xe<sup>25+</sup>.

**B.2 Double ionization****Figure B.26:** Double ionization of  $\text{Xe}^+$ .**Figure B.27:** Double ionization of  $\text{Xe}^{2+}$ .

**Figure B.28:** Double ionization of  $\text{Xe}^{3+}$ .**Figure B.29:** Double ionization of  $\text{Xe}^{4+}$ .

**Figure B.30:** Double ionization of  $\text{Xe}^{5+}$ .**Figure B.31:** Double ionization of  $\text{Xe}^{6+}$ .

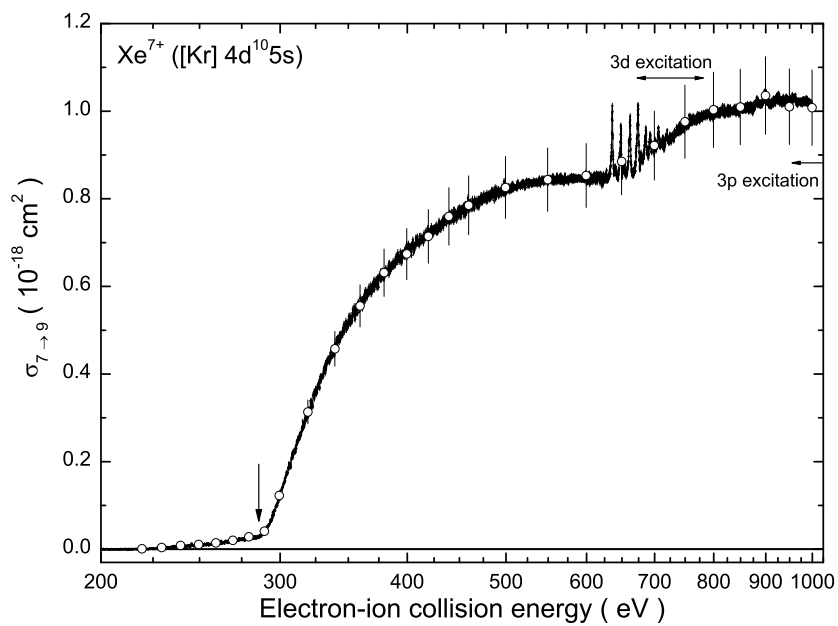


Figure B.32: Double ionization of  $\text{Xe}^{7+}$ .

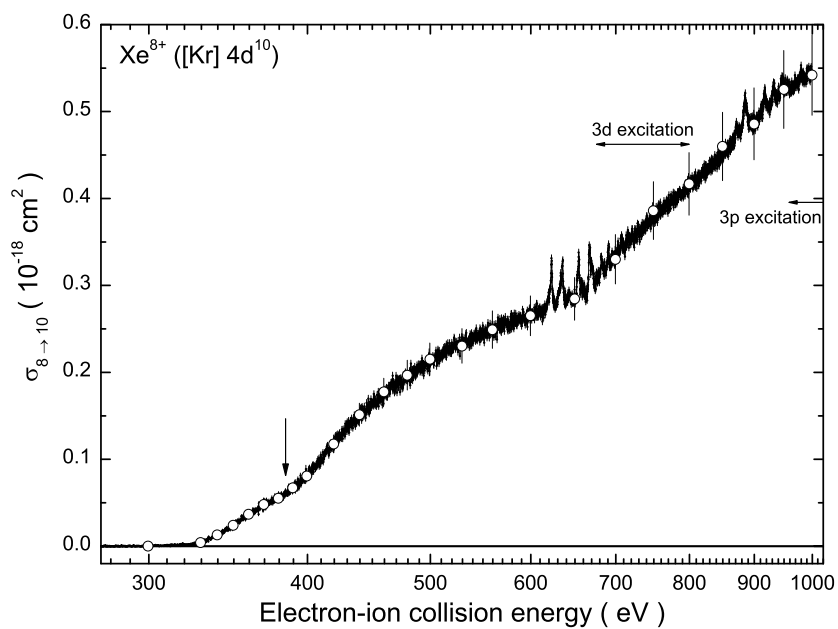
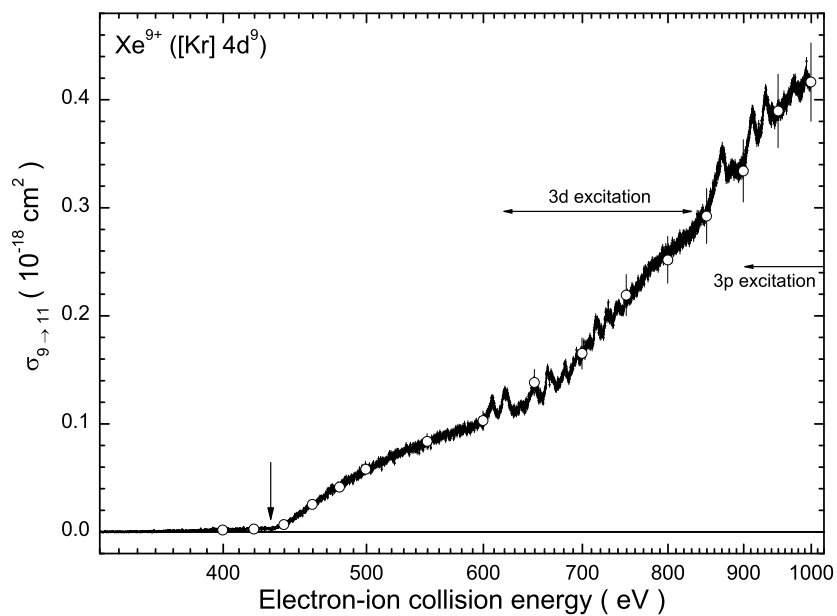
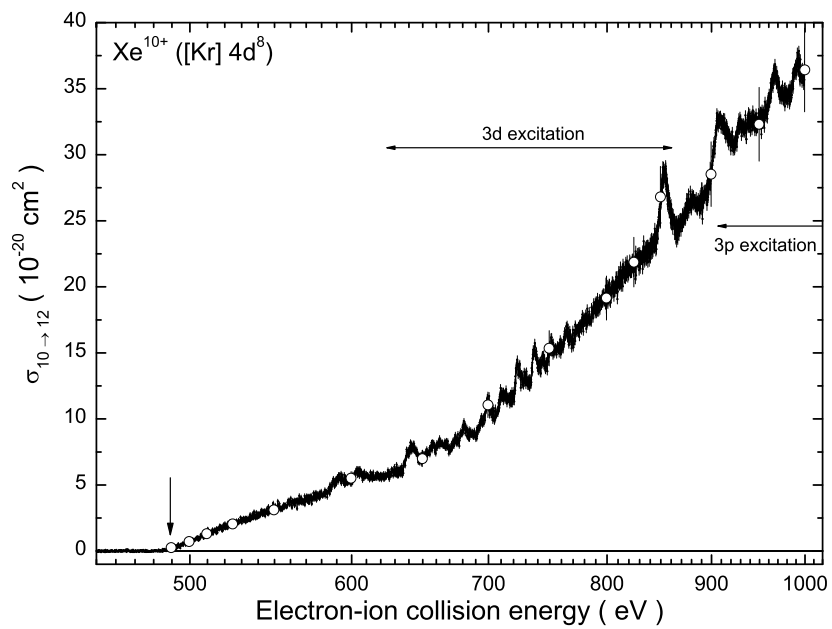


Figure B.33: Double ionization of  $\text{Xe}^{8+}$ .

**Figure B.34:** Double ionization of  $\text{Xe}^{9+}$ .**Figure B.35:** Double ionization of  $\text{Xe}^{10+}$ .

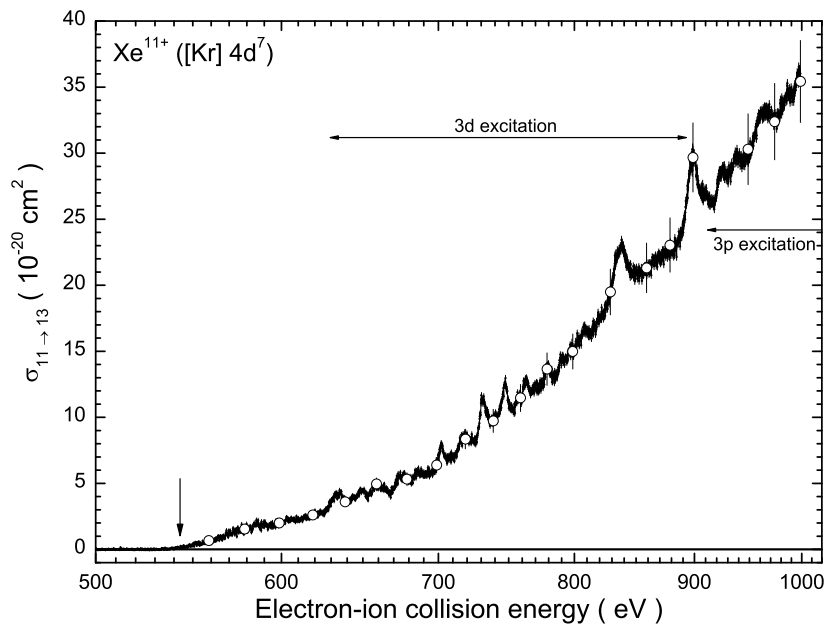


Figure B.36: Double ionization of  $\text{Xe}^{11+}$ .

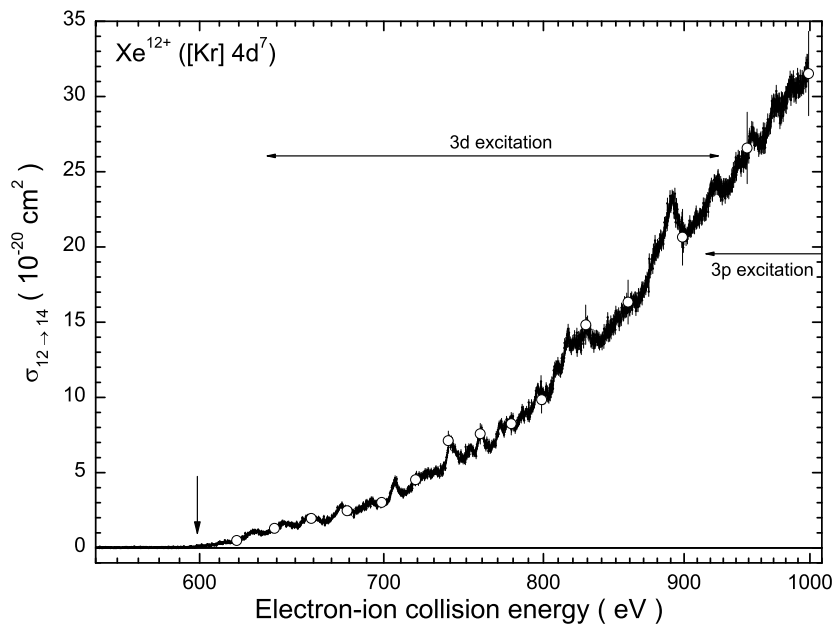


Figure B.37: Double ionization of  $\text{Xe}^{12+}$ .

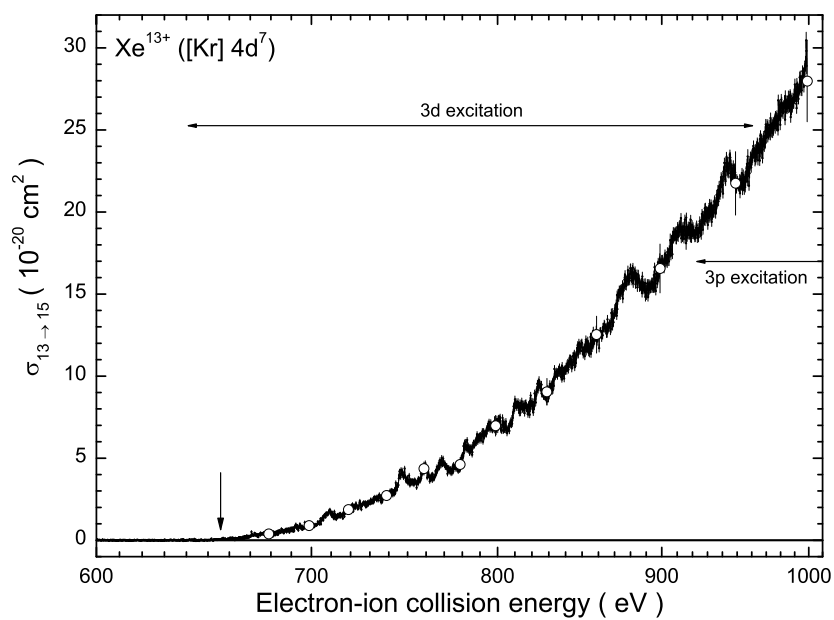


Figure B.38: Double ionization of  $\text{Xe}^{13+}$ .

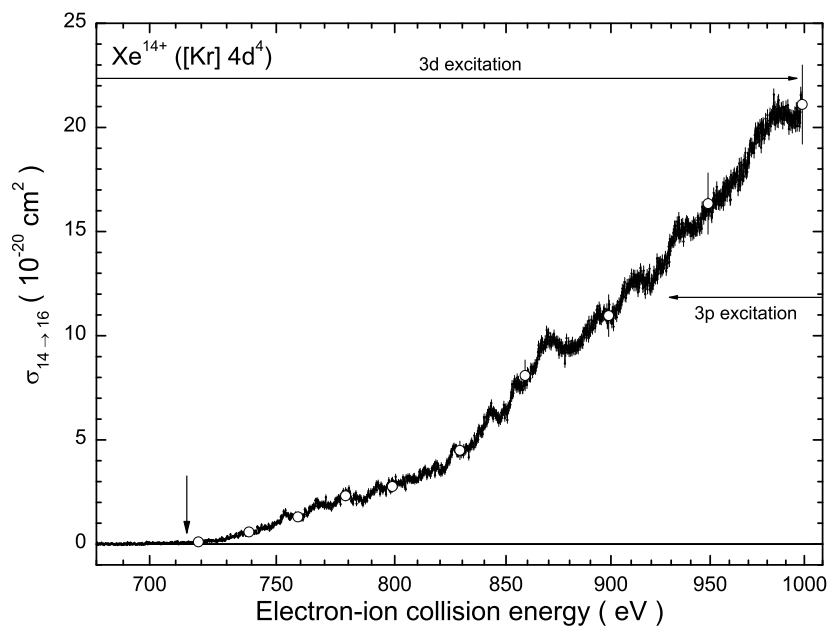


Figure B.39: Double ionization of  $\text{Xe}^{14+}$ .

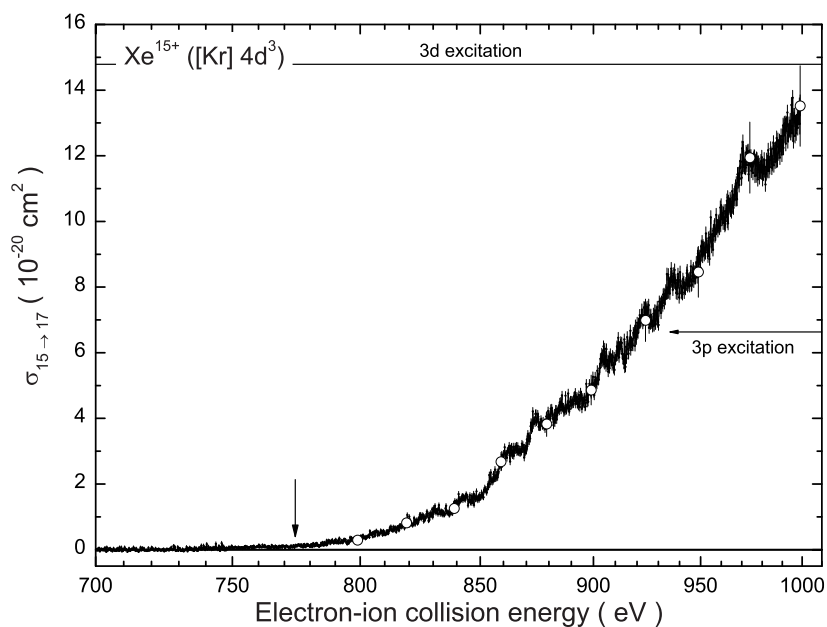


Figure B.40: Double ionization of  $\text{Xe}^{15+}$ .

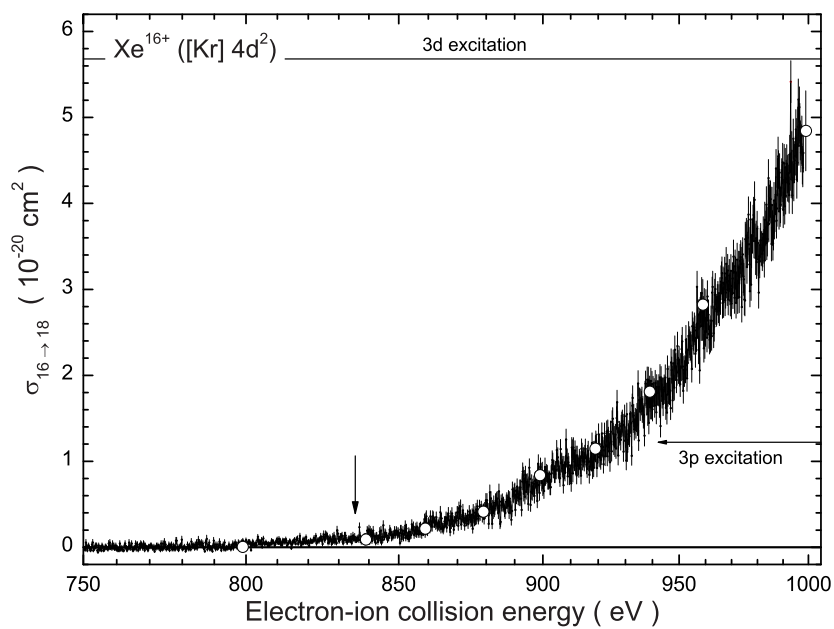
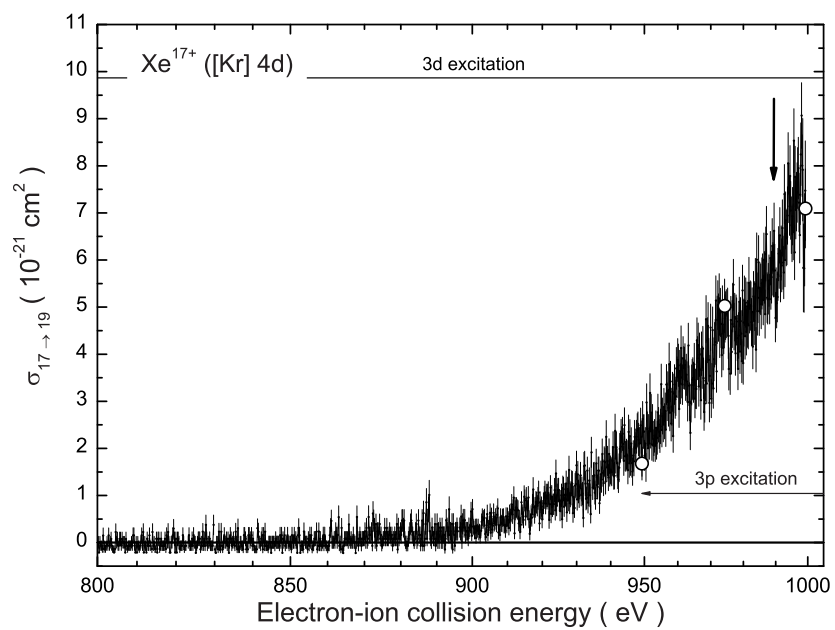


Figure B.41: Double ionization of  $\text{Xe}^{16+}$ .



**Figure B.42:** Double ionization of  $\text{Xe}^{17+}$ .

### B.3 Triple ionization

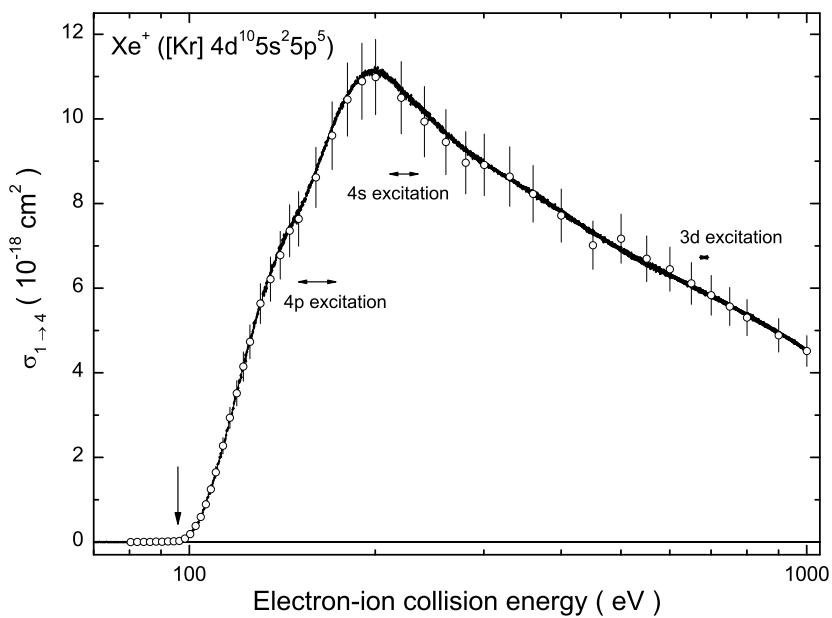


Figure B.43: Triple ionization of  $\text{Xe}^+$ .

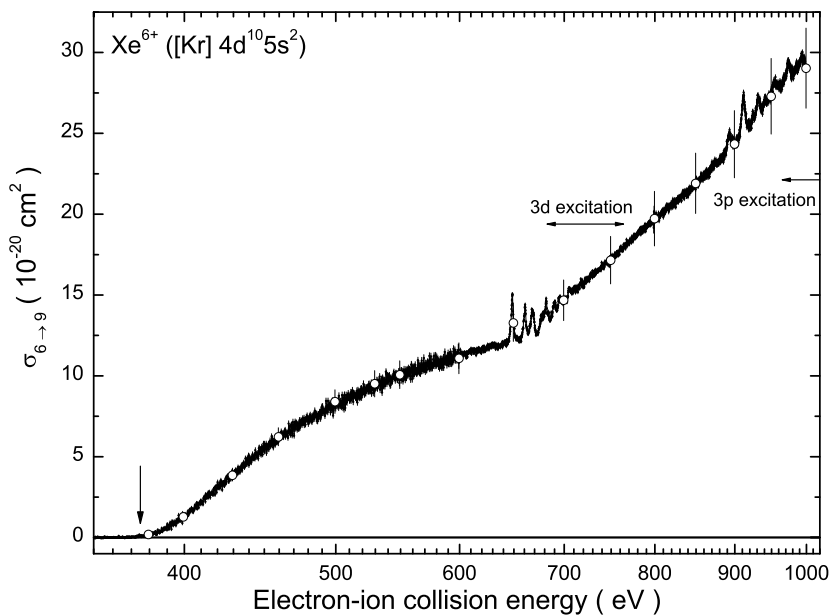
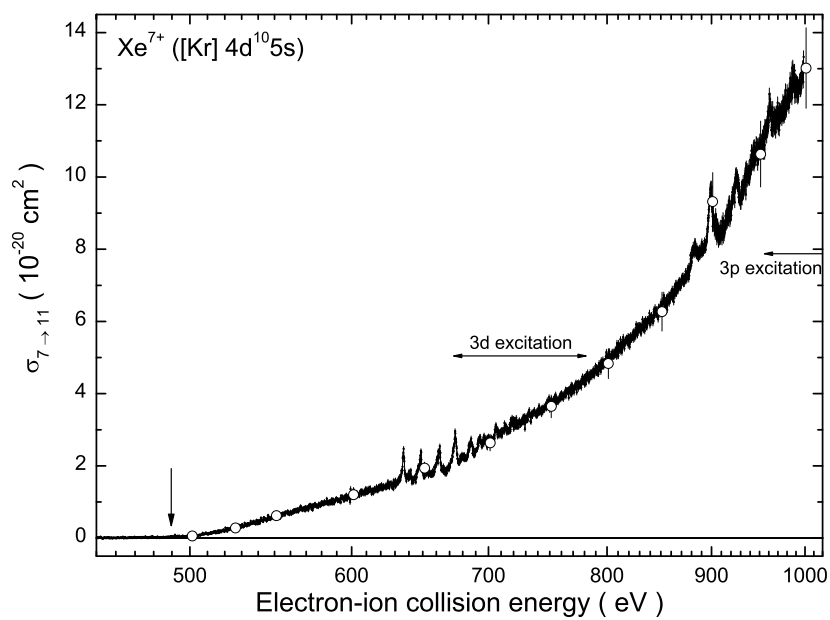


Figure B.44: Triple ionization of  $\text{Xe}^{6+}$ .



**Figure B.45:** Triple ionization of  $\text{Xe}^{7+}$ .

## B.4 Fourfold ionization

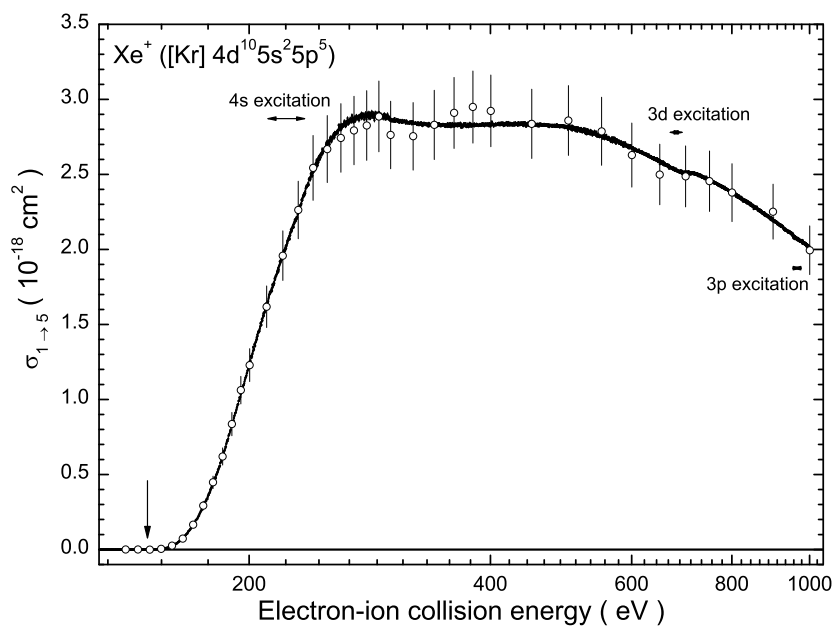


Figure B.46: Fourfold ionization of  $\text{Xe}^+$ .

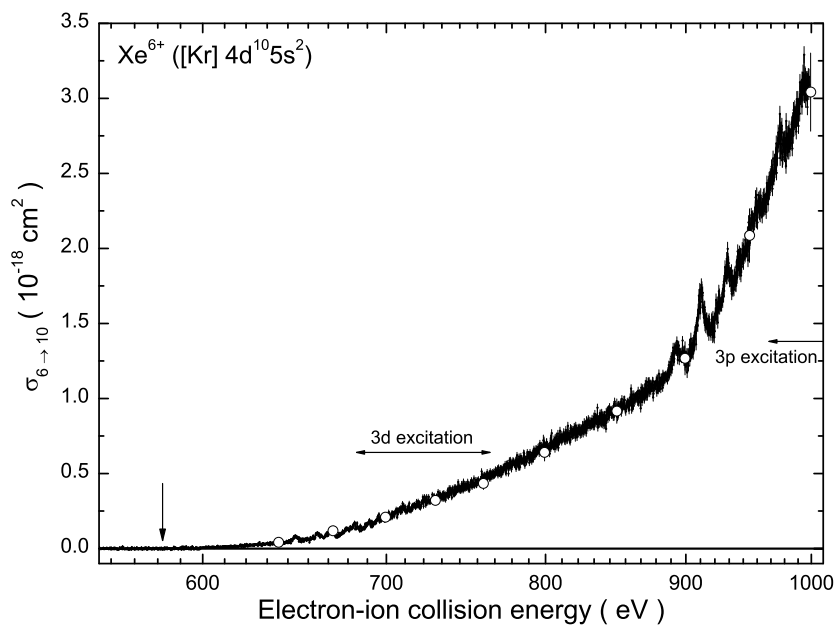
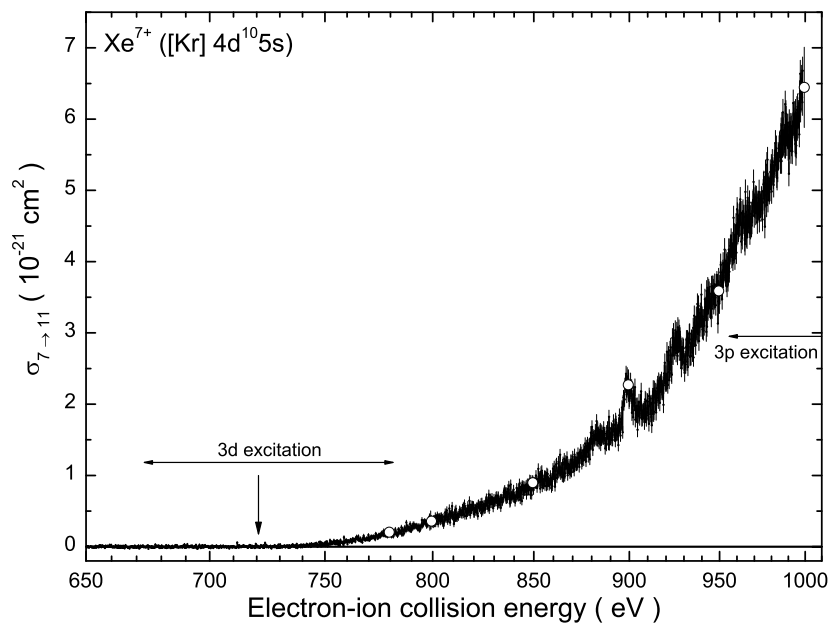


Figure B.47: Fourfold ionization of  $\text{Xe}^{6+}$ .



**Figure B.48:** Fourfold ionization of  $\text{Xe}^{7+}$ .

## B.5 Fivefold and higher multiple ionization

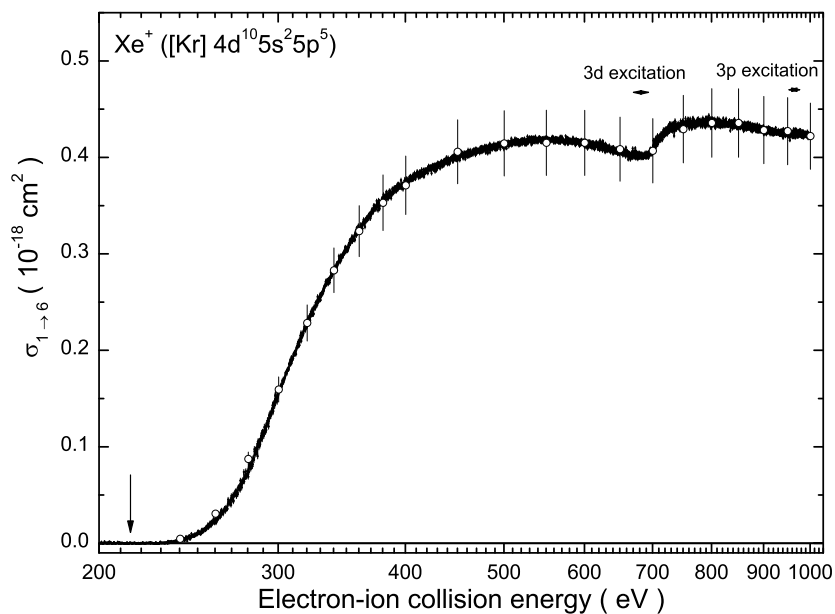


Figure B.49: Fivefold ionization of  $\text{Xe}^+$ .

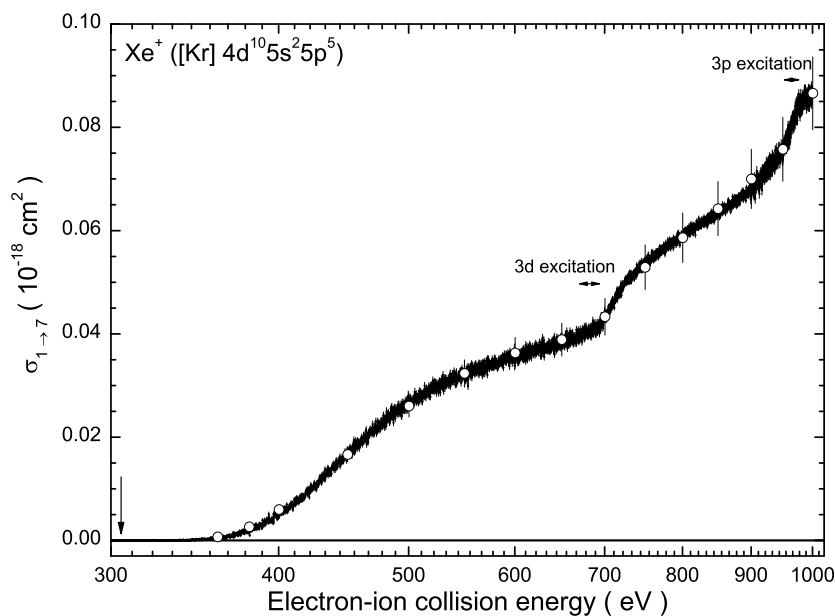
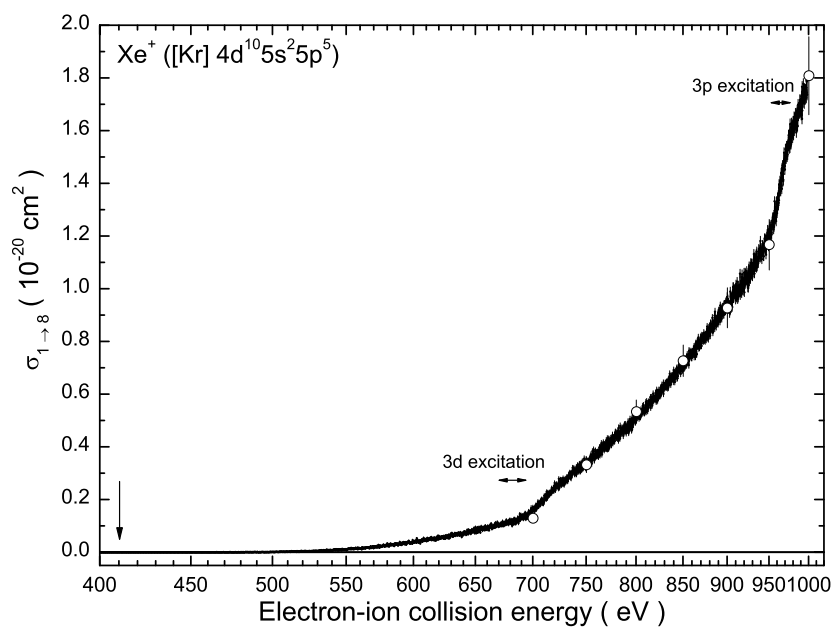
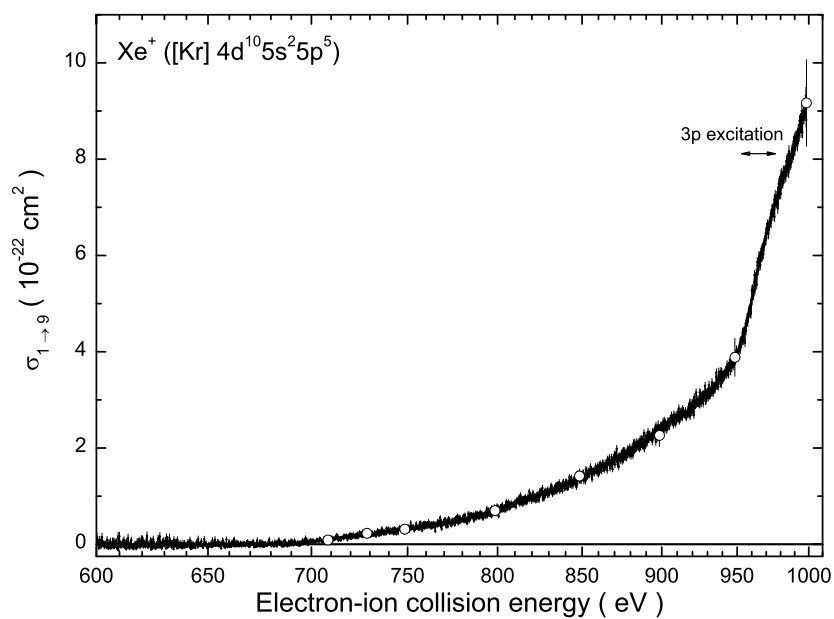


Figure B.50: Sixfold ionization of  $\text{Xe}^+$ .



**Figure B.51:** Sevenfold ionization of  $\text{Xe}^+$ .



**Figure B.52:** Eightfold ionization of  $\text{Xe}^+$ . The estimated ground-state ionization threshold position (589.63 eV) is below the studied energy region.

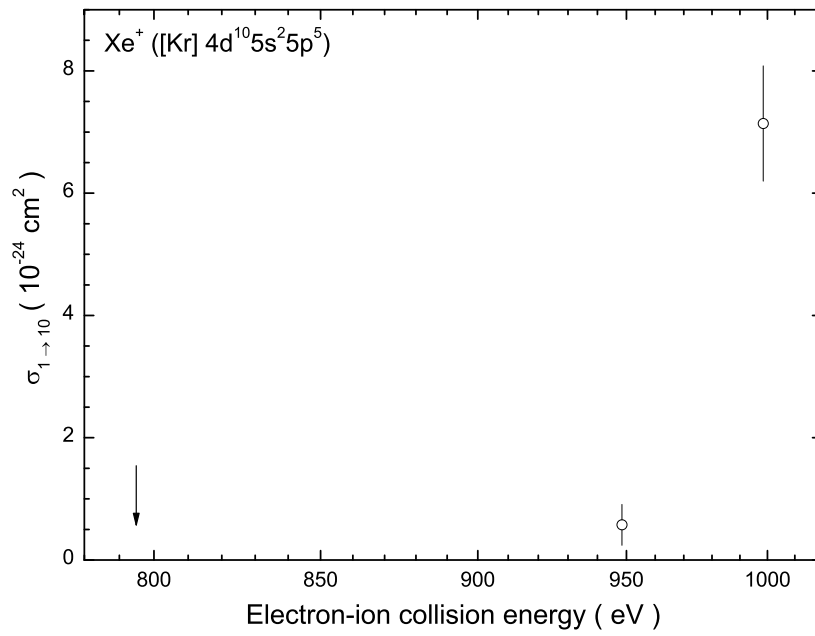


**Figure B.53:** Ninefold ionization of  $\text{Xe}^+$ .

## C Details on the ionization of tin ions

The detailed illustrations of the measured single- and multiple-ionization cross sections of tin ions together with explanations of individual contributions arising from direct and indirect ionization mechanisms are given here. For all figures, open circles are absolute cross-section data and small filled circles represent energy scan data. For single-ionization, thin solid curves denote the results of CADW direct-ionization cross section calculations using the LANL Atomic Physics Code package [111]. For the cross sections, for which the present metastable-state fractions could be estimated (see Tab. 4.3 in Section 4.3.2) they have been included in the calculations. For those cross sections, for which the metastable fraction could not be estimated the CADW calculations include only ionization from the ground state.

Horizontal arrows represent the energy ranges from the lowest energy required to excite an electron of the corresponding subshell to the nearest available vacancy up to the energy needed to remove it to the continuum. These energies have also been obtained using the LANL code. Vertical arrows show the ground-state ionization potentials.

## C.1 Single ionization

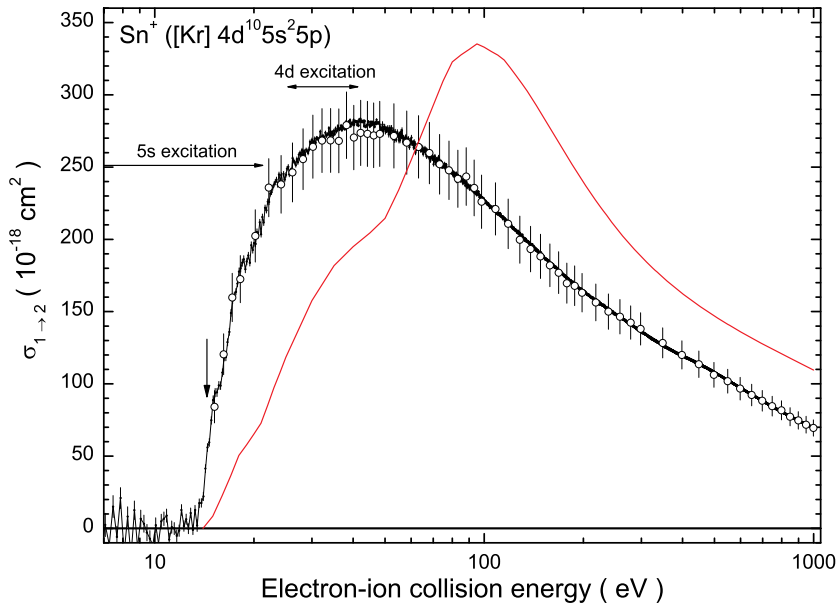


Figure C.1: Single ionization of  $\text{Sn}^+$ .

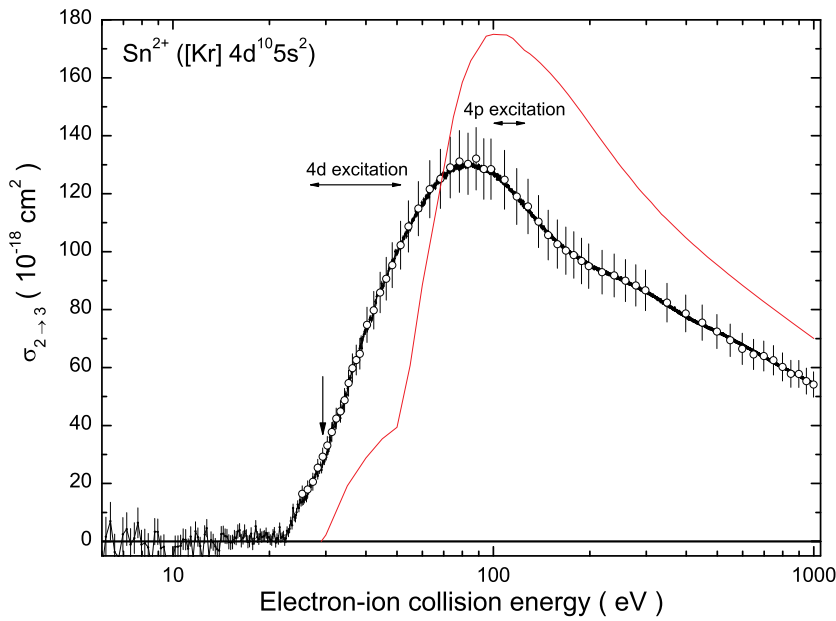
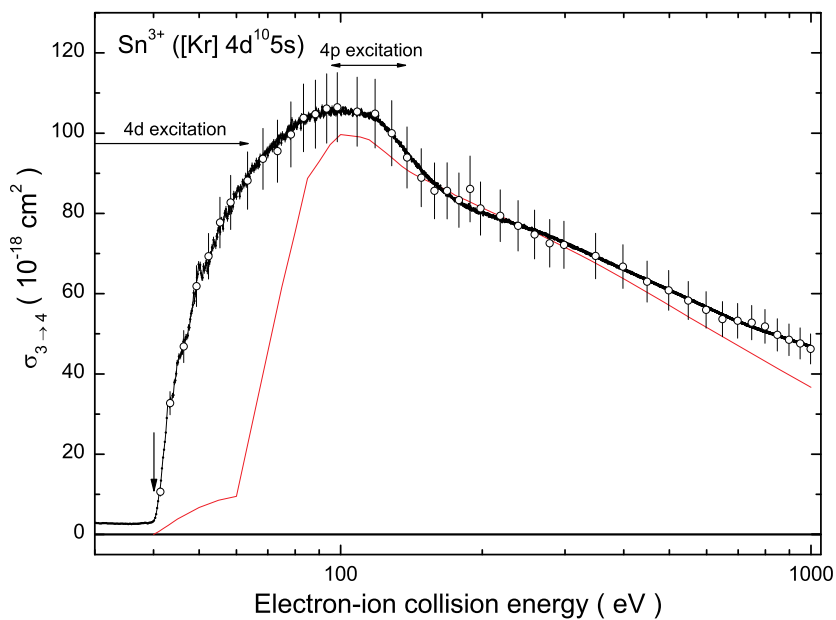
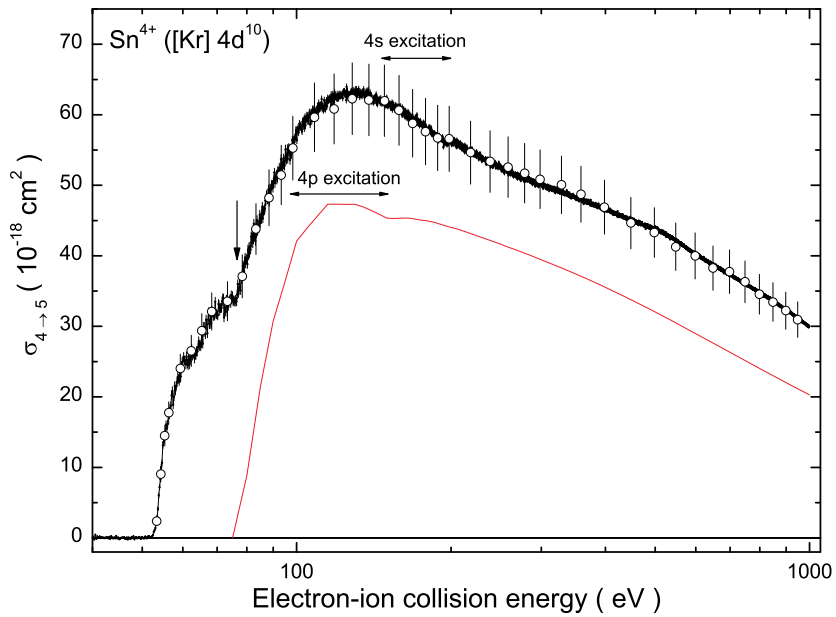


Figure C.2: Single ionization of  $\text{Sn}^{2+}$ .

**Figure C.3:** Single ionization of  $\text{Sn}^{3+}$ .**Figure C.4:** Single ionization of  $\text{Sn}^{4+}$ .

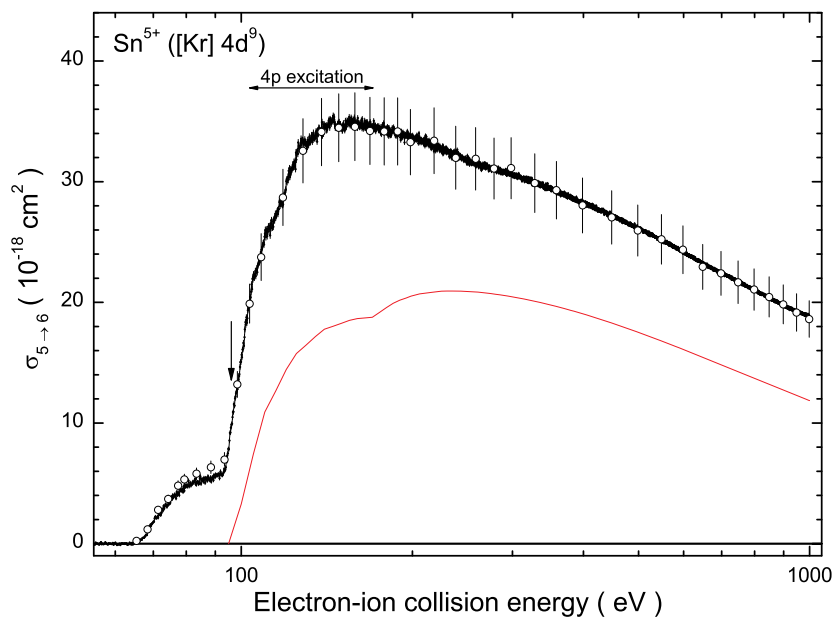


Figure C.5: Single ionization of  $\text{Sn}^{5+}$ .

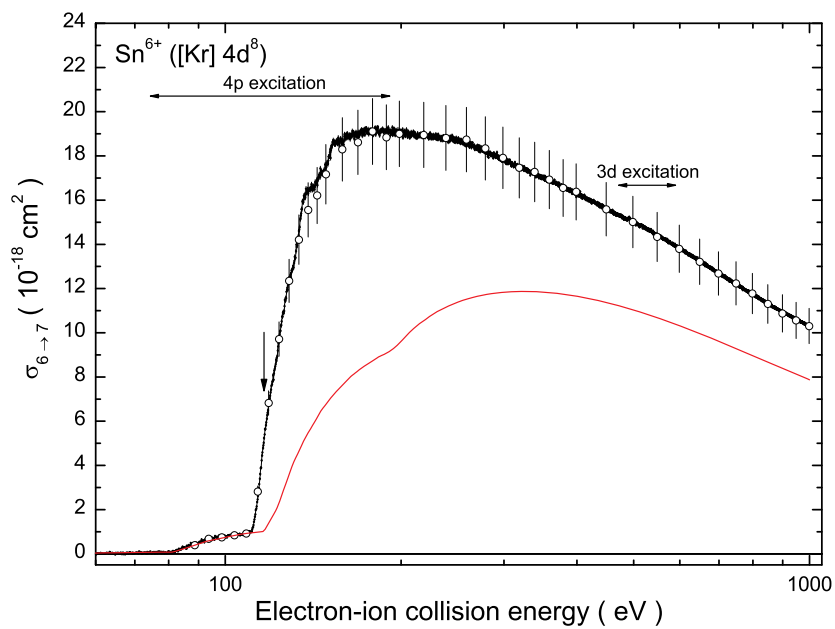
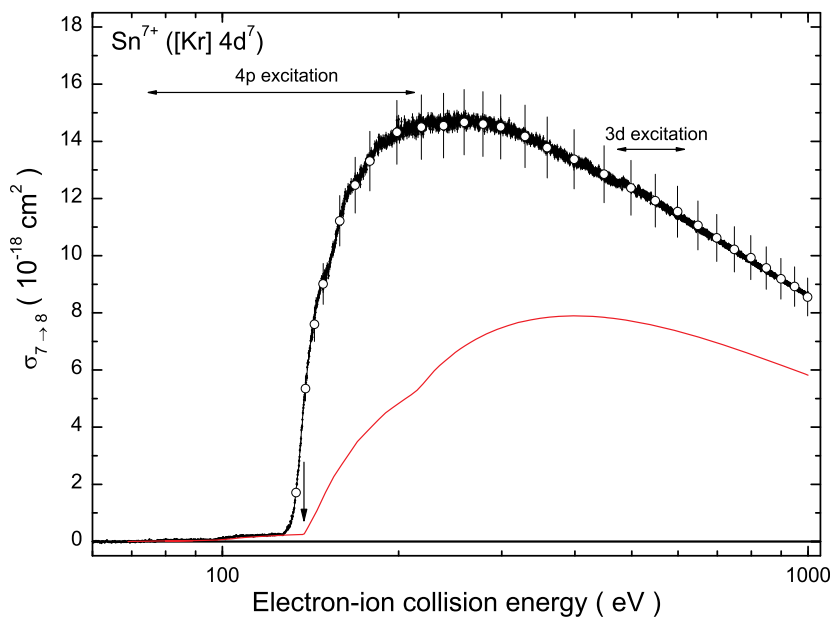
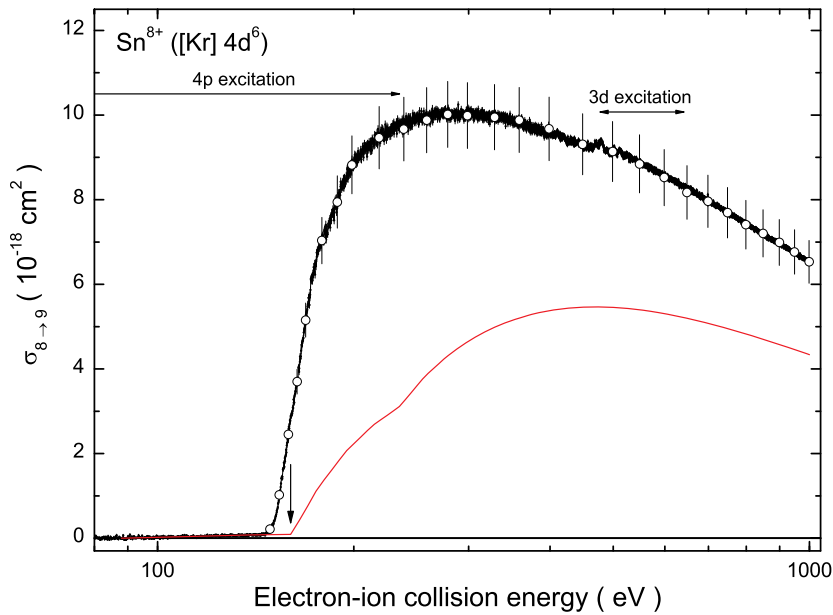
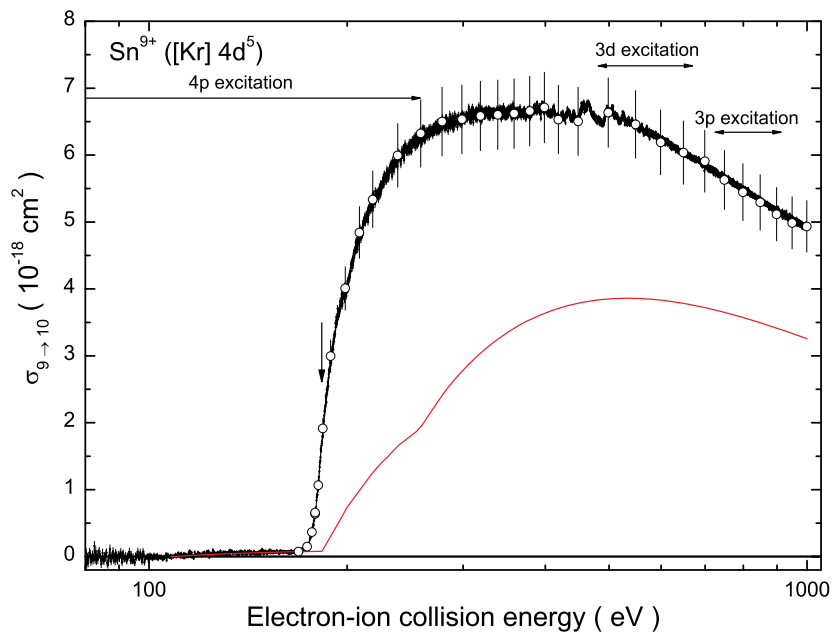
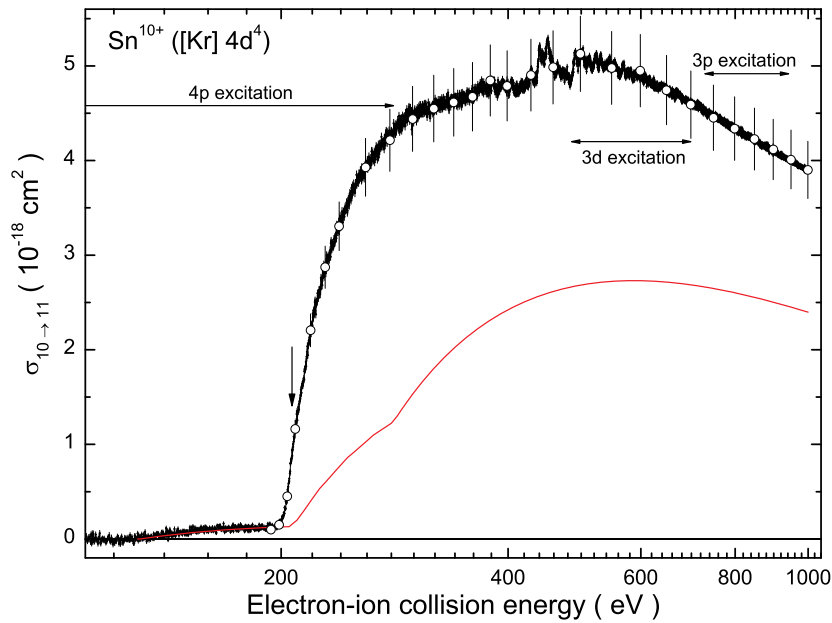


Figure C.6: Single ionization of  $\text{Sn}^{6+}$ .

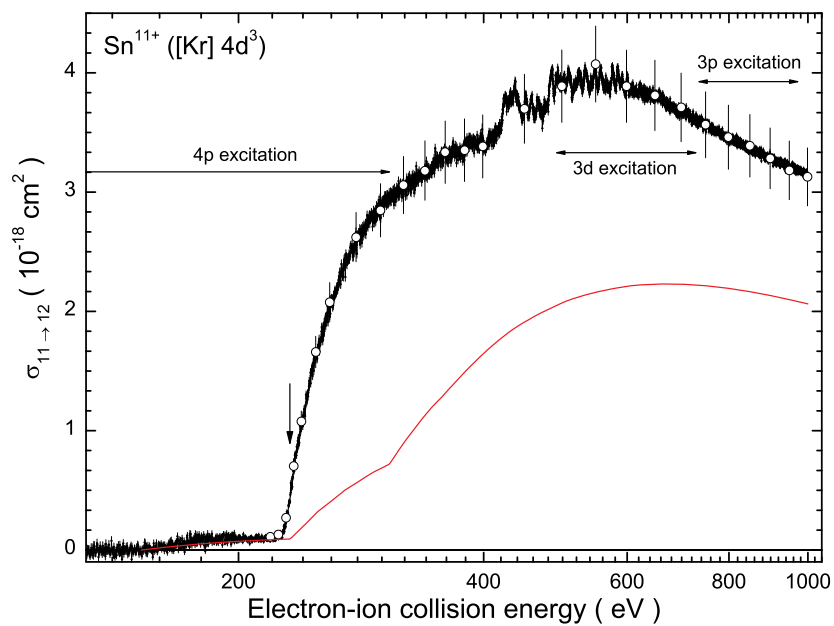
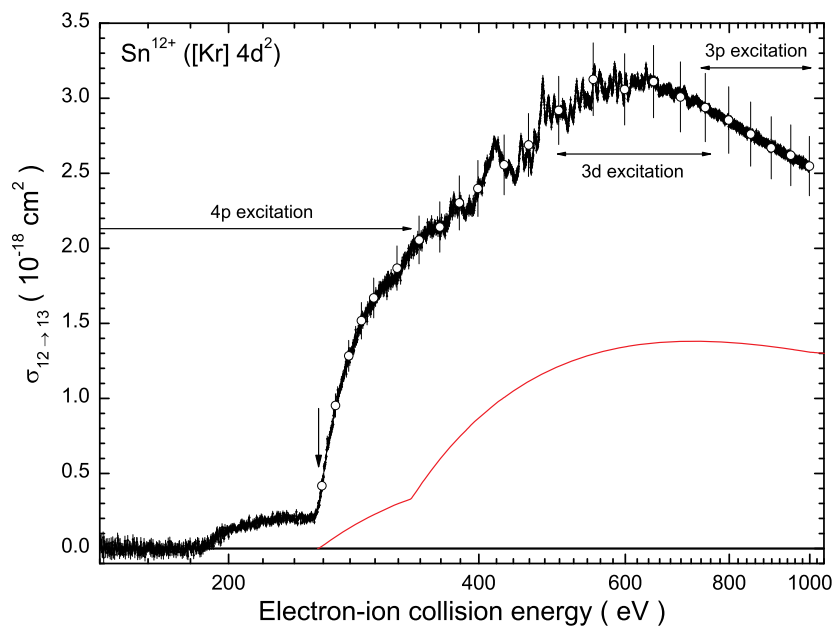
**Figure C.7:** Single ionization of  $\text{Sn}^{7+}$ .**Figure C.8:** Single ionization of  $\text{Sn}^{8+}$ .



**Figure C.9:** Single ionization of  $\text{Sn}^{9+}$ .



**Figure C.10:** Single ionization of  $\text{Sn}^{10+}$ .

**Figure C.11:** Single ionization of  $\text{Sn}^{11+}$ .**Figure C.12:** Single ionization of  $\text{Sn}^{12+}$ .

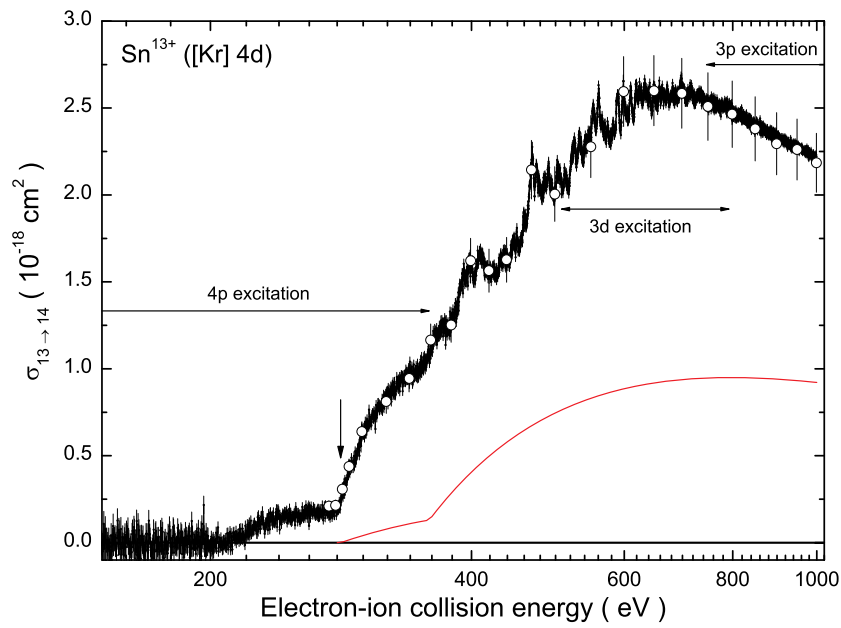


**Figure C.13:** Single ionization of  $\text{Sn}^{13+}$ .

## C.2 Double ionization

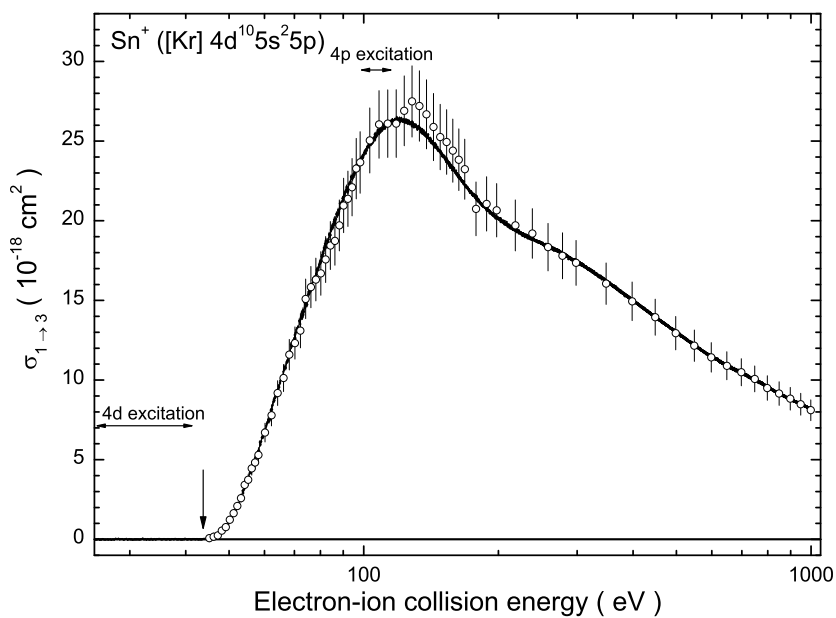


Figure C.14: Double ionization of  $\text{Sn}^+$ .

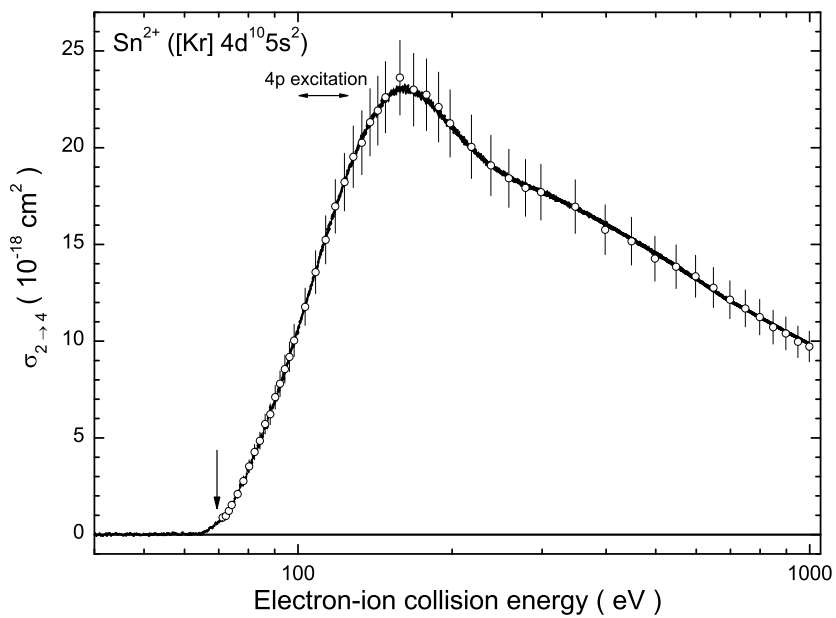
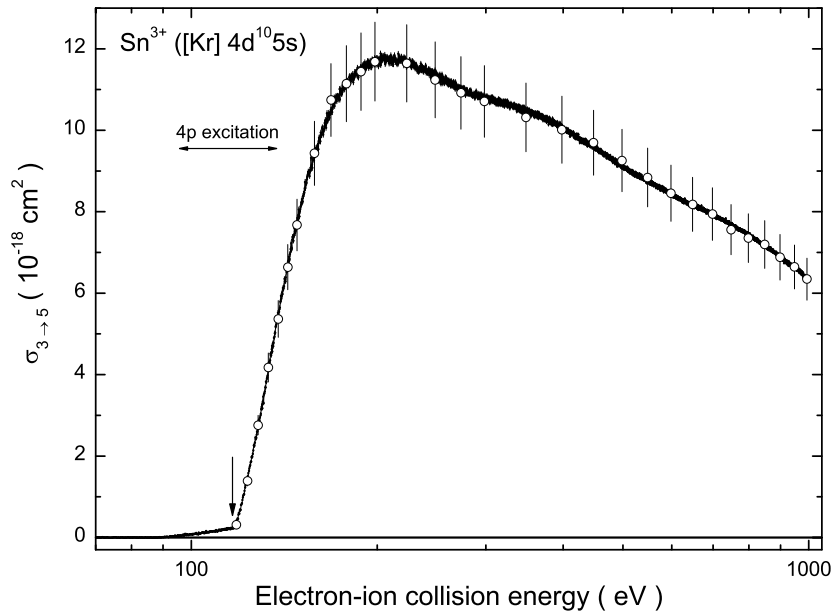
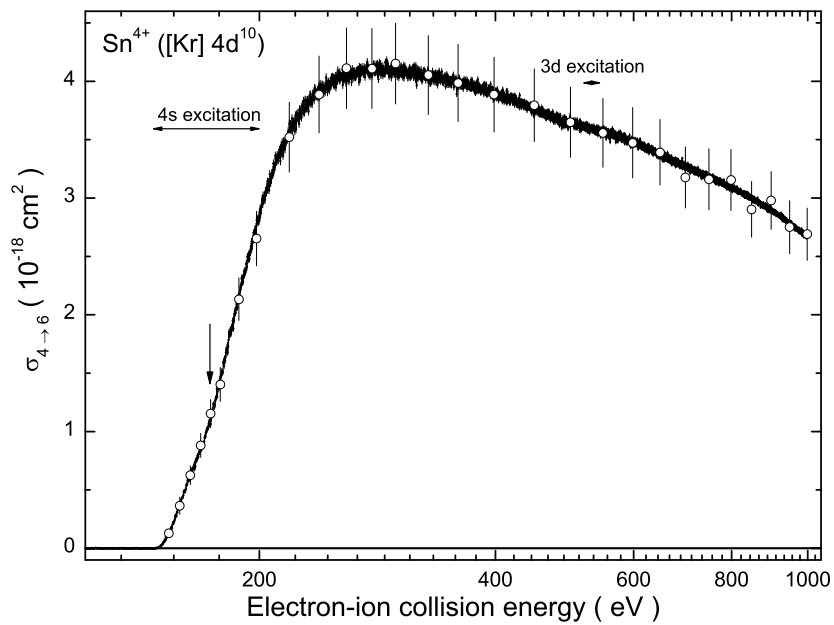
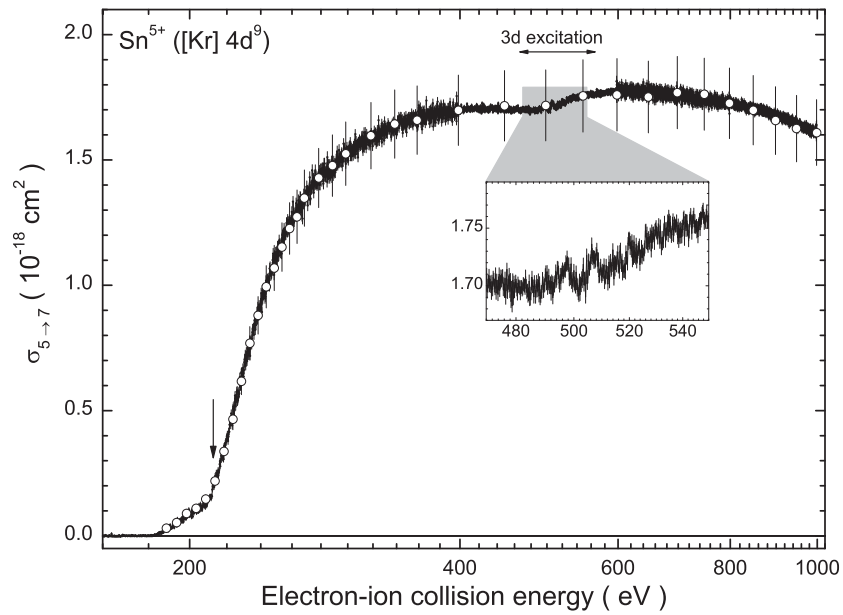
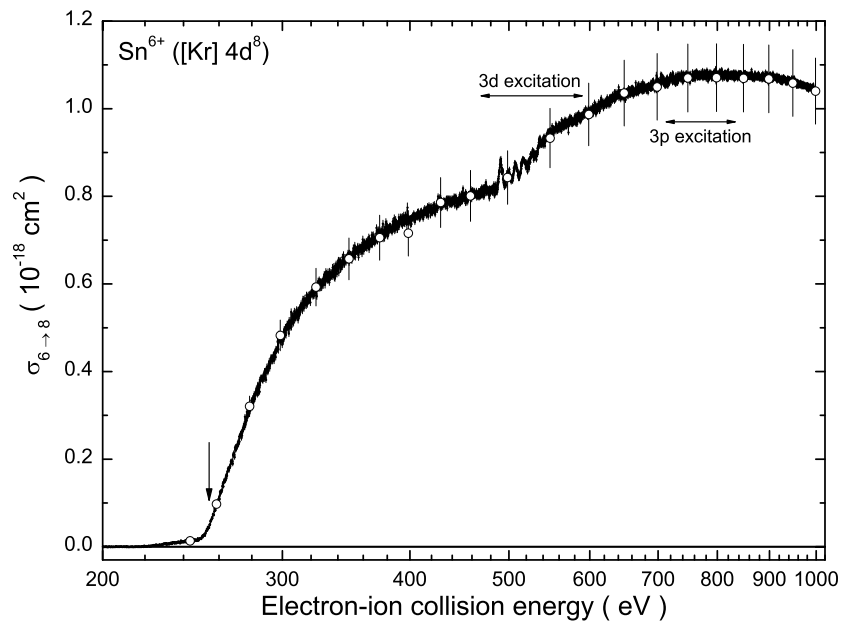


Figure C.15: Double ionization of  $\text{Sn}^{2+}$ .

**Figure C.16:** Double ionization of  $\text{Sn}^{3+}$ .**Figure C.17:** Double ionization of  $\text{Sn}^{4+}$ .

**Figure C.18:** Double ionization of  $\text{Sn}^{5+}$ .**Figure C.19:** Double ionization of  $\text{Sn}^{6+}$ .

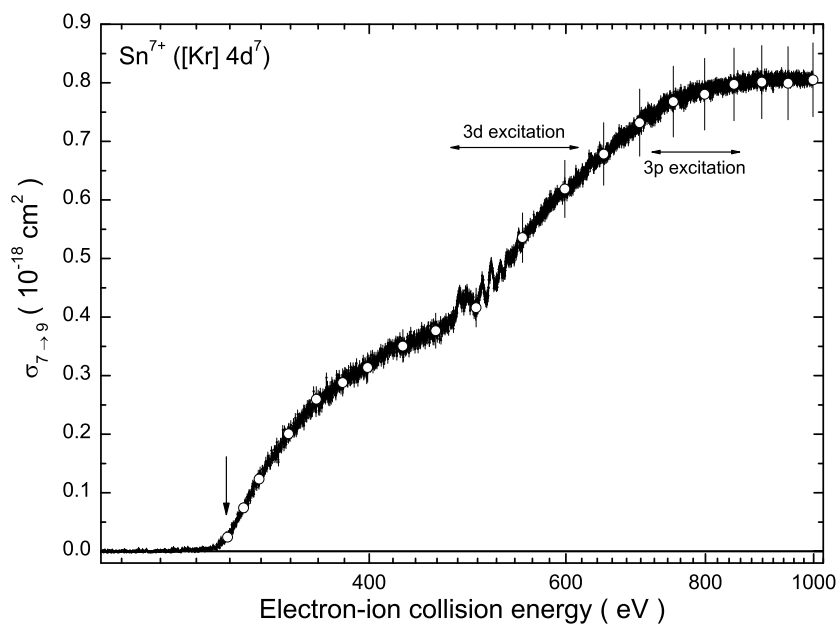


Figure C.20: Double ionization of  $\text{Sn}^{7+}$ .

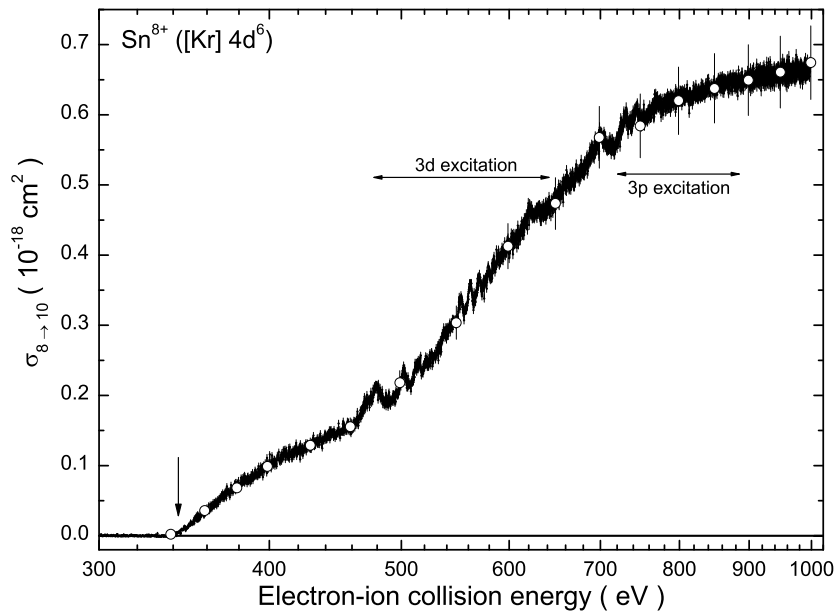


Figure C.21: Double ionization of  $\text{Sn}^{8+}$ .

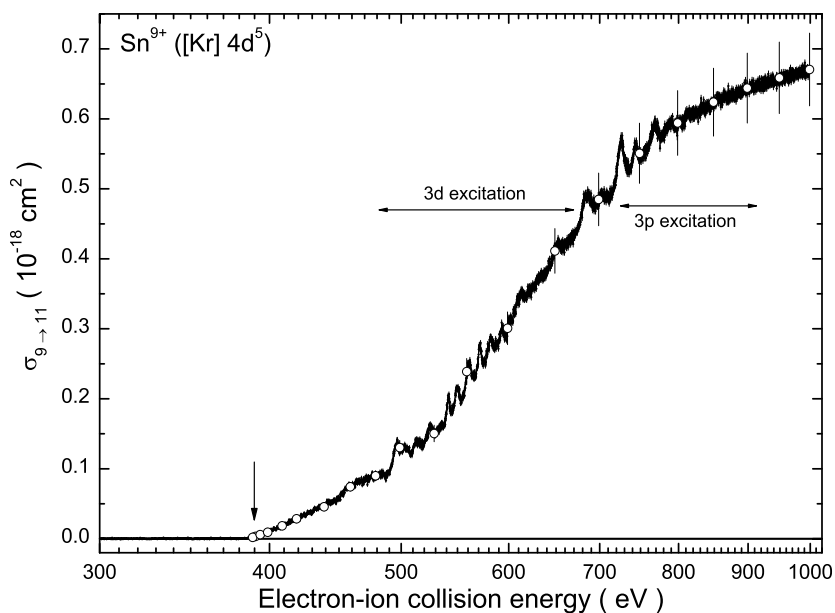


Figure C.22: Double ionization of  $\text{Sn}^{9+}$ .

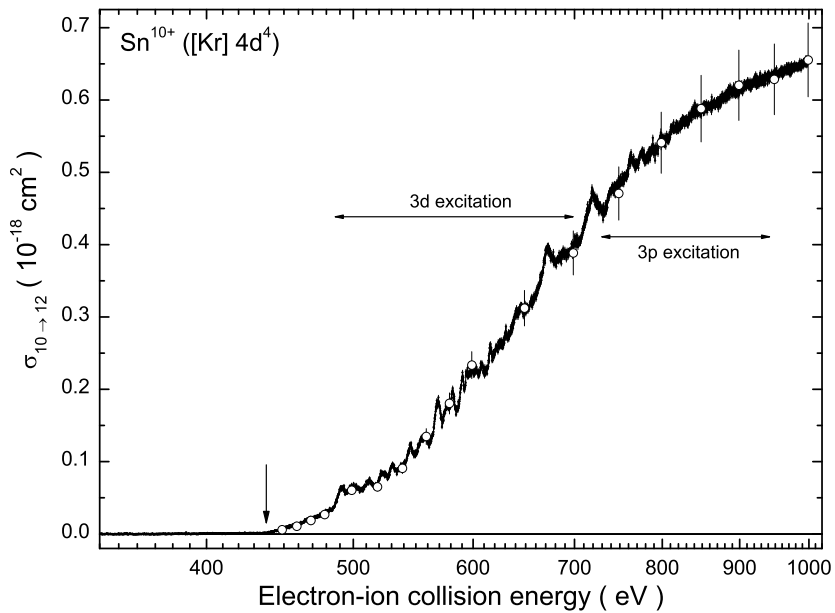


Figure C.23: Double ionization of  $\text{Sn}^{10+}$ .

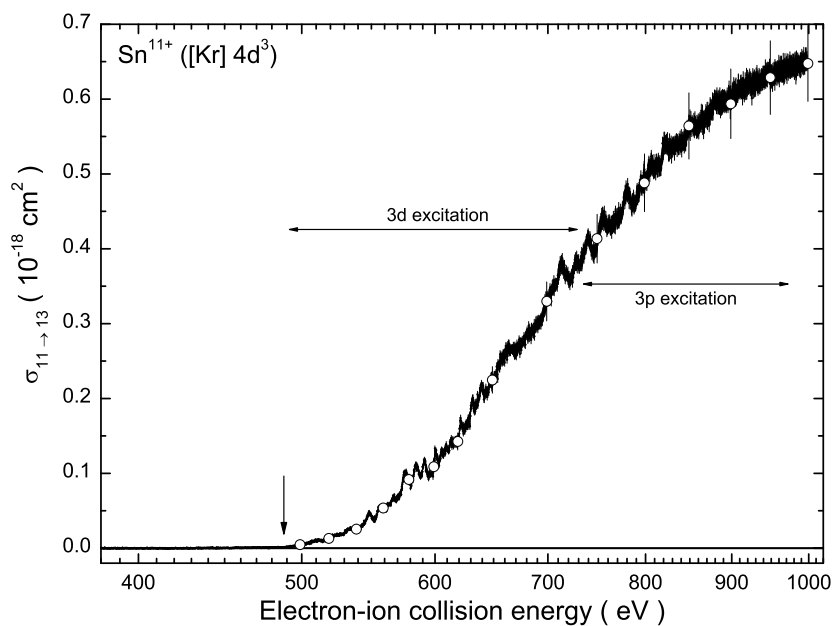


Figure C.24: Double ionization of  $\text{Sn}^{11+}$ .

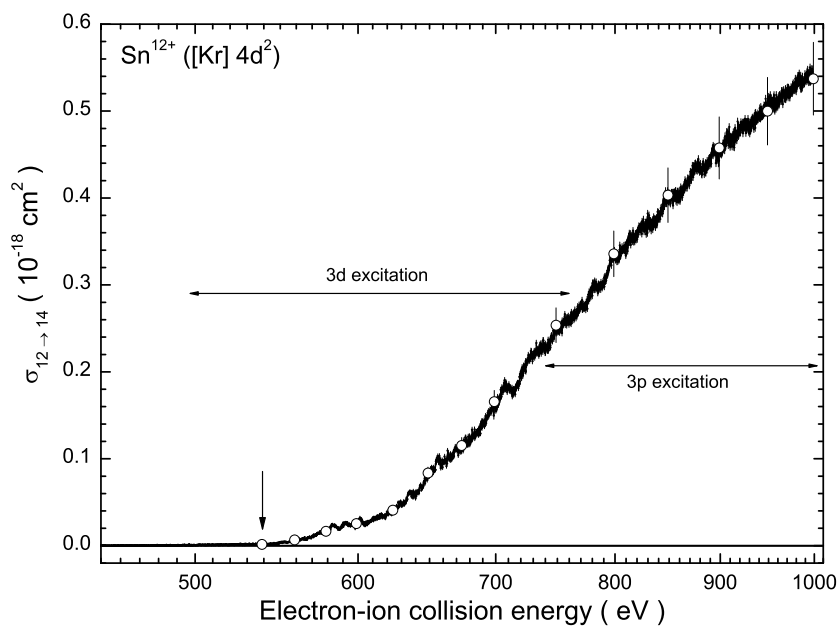


Figure C.25: Double ionization of  $\text{Sn}^{12+}$ .

## D Tabulated absolute values of the present cross sections

Here, the tabulated data on absolute single- and multiple electron-impact ionization cross sections of xenon and tin ions measured within the present work are listed. The following tables contain electron-ion collision energy corrected for the contact potential differences given in electronvolts, values of absolute cross sections and total uncertainty values both given in squared centimeters and multiplied by the factor given in each table header.

**Table D.1:** Absolute cross-section values of electron-impact single ionization of xenon ions

Collision energy (eV)	Cross section ( $10^{-18}\text{cm}^2$ )	Total error	Collision energy (eV)	Cross section ( $10^{-18}\text{cm}^2$ )	Total error
$\text{Xe}^+ \rightarrow \text{Xe}^{2+}$					
21.3	16.6	5.7	85.3	231	19
22.3	37.9	8.4	90.3	227	18
23.3	63.3	6.7	95.3	225	18
24.3	89.0	8.6	100.3	223	18
25.3	113	11	110.3	215	17
26.3	134	12	120.3	205	17
27.3	162	14	130.3	197	16
28.3	183	15	140.3	190	15
29.3	197	17	150.3	183	15
30.3	211	18	160.3	177	14
31.3	225	19	170.3	170	14
32.3	236	20	180.3	165	13
33.3	246	21	190.3	161	13
34.3	252	21	200.3	156	13
35.3	250	21	220.3	148	12
36.3	255	22	240.3	142	11
37.3	253	21	260.3	134	11
38.3	248	21	280.3	128	10
39.3	250	21	300.3	123	9.9

**Table D.1**(continued)

Collision energy (eV)	Cross section ( $10^{-18}\text{cm}^2$ )	Total error	Collision energy (eV)	Cross section ( $10^{-18}\text{cm}^2$ )	Total error
40.3	248	21	330.3	115	9.3
42.3	242	20	360.3	108	8.8
44.3	240	20	400.3	101	8.2
46.3	239	20	450.3	91.9	7.4
48.3	238	20	500.3	85.6	6.9
50.3	238	20	550.3	79.2	6.4
55.3	236	19	600.3	74.8	6.0
60.3	234	19	650.3	70.6	5.7
65.3	234	20	700.3	66.3	5.4
70.3	230	19	750.3	64.5	5.2
75.3	232	19	800.3	61.1	4.9
80.3	229	19	900.3	56.4	4.6
			1000.3	51.8	4.2
 $\text{Xe}^{2+} \rightarrow \text{Xe}^{3+}$					
28.4	8.48	5.2	95.4	154	12
29.4	14.1	4.9	100.4	150	12
30.4	16.7	5.5	110.4	140	11
31.4	26.6	3.4	120.4	130	11
32.4	34.3	7.9	130.4	121	9.9
33.4	57.9	8.0	140.4	114	9.4
34.4	74.4	9.8	150.4	109	8.9
35.4	84.6	9.6	160.4	105	8.6
36.4	87.3	10	170.4	101	8.2
37.4	98.8	9.6	180.4	97.4	7.9
38.4	102	9.5	190.4	94.0	7.7
39.4	108	10.0	200.4	91.0	7.4
40.4	109	9.7	220.4	84.9	6.9
42.4	123	11	240.4	80.2	6.5
44.4	125	11	260.4	76.2	6.2
46.4	122	10	280.4	73.4	6.0
48.4	129	11	300.4	69.2	5.6
50.4	127	10	330.4	64.5	5.3
52.4	131	11	360.4	60.4	4.9
54.4	133	11	400.4	56.6	4.6
56.4	141	12	450.4	51.8	4.2
58.4	145	12	500.4	48.1	3.9
60.4	140	12	550.4	44.8	3.6
65.4	140	11	600.4	42.2	3.4

**Table D.1**(continued)

Collision energy (eV)	Cross section ( $10^{-18}\text{cm}^2$ )	Total error	Collision energy (eV)	Cross section ( $10^{-18}\text{cm}^2$ )	Total error
70.4	148	13	650.4	39.8	3.2
75.4	157	13	700.4	37.8	3.1
80.4	161	13	750.4	36.1	2.9
85.4	161	13	800.4	34.5	2.8
90.4	154	12	900.4	31.9	2.6
			1000.4	30.5	2.5
 $\text{Xe}^{3+} \rightarrow \text{Xe}^{4+}$					
38.4	4.21	1.1	90.4	117	9.7
39.4	5.35	1.5	95.4	119	9.8
40.4	6.76	1.8	100.4	115	9.5
41.4	7.14	1.7	105.4	110	9.0
43.4	17.5	3.2	110.4	104	8.4
44.4	20.8	3.9	120.4	93.6	7.7
45.4	28.7	3.6	130.4	84.8	6.9
46.4	29.1	3.5	140.4	78.1	6.4
47.4	38.9	4.2	150.4	73.9	6.1
48.4	45.6	4.5	160.4	69.2	5.7
49.4	41.6	4.0	170.4	65.6	5.4
50.4	41.2	3.9	180.4	61.3	5.0
51.4	41.5	3.9	190.4	61.2	5.0
52.4	46.0	4.3	200.4	59.1	4.8
53.4	50.3	4.6	220.4	56.5	4.6
54.4	49.1	4.6	240.4	53.3	4.4
55.4	49.8	4.4	260.4	52.1	4.3
56.4	53.9	4.9	280.4	50.7	4.2
58.4	54.1	4.7	300.4	48.8	4.0
60.4	58.4	5.0	330.4	45.2	3.7
62.4	62.2	5.3	360.4	43.4	3.6
64.4	70.9	5.9	400.4	41.0	3.4
66.4	79.0	6.6	450.4	38.1	3.1
68.4	89.3	7.5	500.4	35.9	2.9
70.4	84.1	7.1	550.4	34.0	2.8
72.4	92.4	7.7	600.4	32.3	2.6
74.4	96.8	7.9	650.4	31.0	2.5
76.4	97.4	8.2	700.4	29.6	2.4
78.4	100	8.3	750.4	28.3	2.3
80.4	106	8.7	800.4	27.5	2.2
85.4	113	9.3	900.4	25.8	2.1

**Table D.1**(continued)

Collision energy (eV)	Cross section ( $10^{-18}\text{cm}^2$ )	Total error	Collision energy (eV)	Cross section ( $10^{-18}\text{cm}^2$ )	Total error
			1000.4	25.0	2.0
$\text{Xe}^{4+} \rightarrow \text{Xe}^{5+}$					
48.5	2.09	0.52	160.5	62.3	5.1
49.5	1.80	0.36	165.5	60.2	4.9
50.5	2.15	0.38	170.5	58.7	4.8
51.5	2.50	0.33	175.5	58.0	4.7
52.5	2.67	0.40	180.5	56.4	4.6
53.5	4.12	0.47	185.5	55.3	4.5
54.5	5.47	0.57	190.5	54.9	4.5
55.5	9.09	0.86	195.5	54.2	4.4
56.5	14.2	1.2	200.5	53.9	4.4
57.5	19.7	1.6	210.5	53.3	4.3
59.5	36.4	3.0	220.5	53.1	4.3
60.5	39.7	3.3	230.5	52.3	4.2
62.5	42.7	3.5	240.5	51.5	4.2
64.5	46.8	3.8	250.5	51.1	4.2
58.5	27.6	2.3	260.5	50.4	4.1
66.5	53.0	4.3	270.5	50.0	4.1
68.5	54.9	4.5	280.5	50.3	4.1
70.5	56.5	4.6	290.5	49.3	4.0
75.5	68.7	5.6	300.5	48.8	4.0
80.5	77.0	6.3	320.5	47.8	3.9
85.5	83.2	6.8	340.5	46.9	3.8
90.5	84.4	6.9	360.5	45.9	3.7
95.5	83.6	6.8	380.5	44.8	3.7
100.5	80.7	6.6	400.5	44.2	3.6
105.5	80.0	6.5	450.5	42.5	3.5
110.5	78.7	6.4	500.5	40.5	3.3
115.5	77.1	6.3	550.5	39.2	3.2
120.5	76.7	6.2	600.5	37.6	3.0
125.5	73.4	5.9	650.5	36.6	3.0
130.5	70.5	5.7	700.5	35.3	2.9
135.5	70.0	5.7	750.5	34.1	2.8
140.5	68.1	5.5	800.5	33.2	2.7
145.5	66.0	5.4	850.5	32.3	2.6
150.5	65.7	5.4	900.5	31.8	2.6
155.5	64.1	5.2	950.5	30.8	2.5
			1000.5	29.6	2.4

**Table D.1**(continued)

Collision energy (eV)	Cross section ( $10^{-18}\text{cm}^2$ )	Total error	Collision energy (eV)	Cross section ( $10^{-18}\text{cm}^2$ )	Total error
$\text{Xe}^{5+} \rightarrow \text{Xe}^{6+}$					
65.5	1.23	0.24	195.5	50	4.0
66.5	2.94	0.31	200.5	48	3.9
67.5	7.44	0.63	210.5	47	3.9
68.5	11.8	1.0	220.5	47	3.8
70.5	18.6	1.6	230.5	47	3.8
75.5	29.9	2.4	240.5	46	3.7
80.5	40.4	3.3	250.5	45	3.7
85.5	55.3	4.5	260.5	45	3.7
90.5	60.6	5.0	270.5	45	3.6
95.5	59.5	4.9	280.5	44	3.6
100.5	61.4	5.0	290.5	44	3.6
105.5	59.9	4.9	300.5	43	3.5
110.5	63.7	5.2	320.5	42	3.4
115.5	60.3	4.9	340.5	42	3.4
120.5	57.9	4.7	360.5	41	3.3
125.5	59.1	4.8	380.5	40	3.3
130.5	61.9	5.0	400.5	39	3.2
135.5	59.7	4.9	450.5	38	3.1
140.5	57.4	4.7	500.5	36	3.0
145.5	58.0	4.7	550.5	35	2.8
150.5	57.5	4.7	600.5	34	2.7
155.5	56.1	4.6	650.5	32	2.6
160.5	56.6	4.6	700.5	31	2.5
165.5	54.3	4.4	750.5	30	2.5
170.5	53.2	4.3	800.5	29	2.4
175.5	52.8	4.3	850.5	28	2.3
180.5	50.9	4.1	900.5	28	2.3
185.5	51.0	4.2	950.5	27	2.2
190.5	49.4	4.0	1000.5	26	2.1
$\text{Xe}^{6+} \rightarrow \text{Xe}^{7+}$					
79.6	0.363	0.38	220.6	44.1	3.6
85.6	7.81	1.3	230.6	43.8	3.6
90.6	14.7	1.3	240.6	42.8	3.5
95.6	17.3	1.5	250.6	42.2	3.4
100.6	30.6	2.5	260.6	42.2	3.4
105.6	36.8	3.0	270.6	41.8	3.4
110.6	37.9	3.1	280.6	41.6	3.4

**Table D.1**(continued)

Collision energy (eV)	Cross section ( $10^{-18}\text{cm}^2$ )	Total error	Collision energy (eV)	Cross section ( $10^{-18}\text{cm}^2$ )	Total error
115.6	39.1	3.2	290.6	40.6	3.3
120.6	45.2	3.7	300.6	40.6	3.3
125.6	44.2	3.6	320.6	39.8	3.2
130.6	47.0	3.8	340.6	38.6	3.1
135.6	45.4	3.7	360.6	38.1	3.1
140.6	47.3	3.9	380.6	37.9	3.1
145.6	44.7	3.6	400.6	36.7	3.0
150.6	46.7	3.8	450.6	35.5	2.9
155.6	46.7	3.8	500.6	33.9	2.8
160.6	45.6	3.7	550.6	32.8	2.7
165.6	46.5	3.8	600.6	31.7	2.6
170.6	46.0	3.8	650.6	30.9	2.5
175.6	46.1	3.8	700.6	30.0	2.4
180.6	46.0	3.7	750.6	28.8	2.3
185.6	46.9	3.8	800.6	28.1	2.3
190.6	45.7	3.7	850.6	27.0	2.2
195.6	45.5	3.7	900.6	26.2	2.1
200.6	45.8	3.7	950.6	25.3	2.1
210.6	43.8	3.6	1000.6	24.5	2.0
 $\text{Xe}^{7+} \rightarrow \text{Xe}^{8+}$					
105.6	1.14	0.89	240.6	23.8	2.0
110.6	3.41	0.81	260.6	23.2	1.9
115.6	7.93	1.3	280.6	23.2	1.9
120.6	9.81	1.2	300.6	22.8	1.9
125.6	16.4	1.7	330.6	22.1	1.8
130.6	19.4	2.0	360.6	21.5	1.8
135.6	19.5	1.8	400.6	20.7	1.7
140.6	19.7	1.8	450.6	20.1	1.6
145.6	20.1	1.7	500.6	19.2	1.6
150.6	21.5	1.8	550.6	18.4	1.5
160.6	22.1	1.8	600.6	17.6	1.4
170.6	24.6	2.0	650.6	17.6	1.4
180.6	23.5	2.0	700.6	16.5	1.3
190.6	23.6	2.0	750.6	15.8	1.3
200.6	23.8	2.0	800.6	15.4	1.3
220.6	23.9	2.0	850.6	15.0	1.2

**Table D.1**(continued)

Collision energy (eV)	Cross section ( $10^{-18}\text{cm}^2$ )	Total error	Collision energy (eV)	Cross section ( $10^{-18}\text{cm}^2$ )	Total error
$\text{Xe}^{8+} \rightarrow \text{Xe}^{9+}$					
120.7	0.338	0.19	300.7	10.8	0.88
130.7	1.57	0.21	320.7	10.6	0.87
140.7	2.92	0.33	340.7	10.7	0.87
150.7	3.16	0.32	360.7	10.7	0.87
160.7	3.69	0.38	380.7	10.5	0.86
170.7	3.84	0.37	400.7	10.6	0.86
180.7	4.12	0.36	430.7	10.4	0.85
190.7	6.14	0.51	460.7	10.1	0.83
200.7	7.20	0.60	500.7	10.1	0.83
210.7	8.37	0.69	550.7	9.76	0.79
220.7	8.76	0.73	600.7	9.52	0.77
230.7	9.21	0.77	650.7	9.24	0.76
240.7	9.88	0.80	700.7	9.04	0.74
250.7	10.1	0.82	750.7	8.83	0.72
260.7	10.2	0.83	800.7	8.61	0.70
270.7	10.4	0.84	850.7	8.39	0.69
280.7	10.5	0.85	900.7	8.08	0.66
290.7	10.6	0.86	1000.7	7.58	0.63
$\text{Xe}^{9+} \rightarrow \text{Xe}^{10+}$					
200.7	0.280	0.20	320.7	6.34	0.55
205.7	0.647	0.16	340.7	6.46	0.55
210.7	1.23	0.19	360.7	6.72	0.58
215.7	1.85	0.24	380.7	6.66	0.57
220.7	2.68	0.28	400.7	6.60	0.57
225.7	3.37	0.32	430.7	6.79	0.58
230.7	3.88	0.37	460.7	6.76	0.58
235.7	4.03	0.36	500.7	6.66	0.55
245.7	4.84	0.42	550.7	6.54	0.54
250.7	4.85	0.42	600.7	6.49	0.54
255.7	5.02	0.44	650.7	6.63	0.55
260.7	5.24	0.45	700.7	6.41	0.53
270.7	5.74	0.49	750.7	6.29	0.51
280.7	5.80	0.50	800.7	6.11	0.50
290.7	5.97	0.51	900.7	5.85	0.48
300.7	6.06	0.52	1000.7	5.54	0.46

**Table D.1**(continued)

Collision energy (eV)	Cross section ( $10^{-18}\text{cm}^2$ )	Total error	Collision energy (eV)	Cross section ( $10^{-18}\text{cm}^2$ )	Total error
$\text{Xe}^{10+} \rightarrow \text{Xe}^{11+}$					
220.8	0.0460	0.075	500.8	5.06	0.43
230.8	0.498	0.078	550.8	5.09	0.42
240.8	1.85	0.16	600.8	5.05	0.43
260.8	3.08	0.28	650.8	5.11	0.43
280.8	3.69	0.34	700.8	5.11	0.44
300.8	4.06	0.34	750.8	5.02	0.43
330.8	4.55	0.39	800.8	4.90	0.41
360.8	4.83	0.41	850.8	4.83	0.41
400.8	4.79	0.41	900.8	4.66	0.39
450.8	4.96	0.42	950.8	4.67	0.39
			1000.8	4.42	0.37
$\text{Xe}^{11+} \rightarrow \text{Xe}^{12+}$					
150.9	-0.00723	-0.036	380.9	3.61	0.30
160.9	0.0111	0.022	400.9	3.67	0.30
170.9	0.0361	0.022	450.9	3.83	0.31
180.9	0.0895	0.020	500.9	3.96	0.32
190.9	0.101	0.019	550.9	3.98	0.32
200.9	0.124	0.021	600.9	4.05	0.33
220.9	0.139	0.017	650.9	4.31	0.35
240.9	0.145	0.019	700.9	4.16	0.34
260.9	0.888	0.074	750.9	4.21	0.34
280.9	2.03	0.17	800.9	4.14	0.34
300.9	2.60	0.21	850.9	3.99	0.33
320.9	2.98	0.24	900.9	3.94	0.32
340.9	3.23	0.26	950.9	3.85	0.31
360.9	3.47	0.28	1000.9	3.72	0.30
$\text{Xe}^{12+} \rightarrow \text{Xe}^{13+}$					
190.9	0.0113	0.016	450.9	2.93	0.24
200.9	0.0775	0.016	500.9	3.04	0.25
220.9	0.0925	0.020	550.9	3.25	0.27
240.9	0.108	0.021	600.9	3.25	0.26
260.9	0.125	0.014	650.9	3.43	0.28
280.9	0.333	0.030	700.9	3.37	0.28
300.9	1.38	0.11	750.9	3.42	0.28
320.9	1.89	0.15	800.9	3.41	0.28
340.9	2.23	0.18	850.9	3.35	0.27

**Table D.1**(continued)

Collision energy (eV)	Cross section ( $10^{-18}\text{cm}^2$ )	Total error	Collision energy (eV)	Cross section ( $10^{-18}\text{cm}^2$ )	Total error
360.9	2.43	0.20	900.9	3.27	0.27
380.9	2.60	0.21	950.9	3.26	0.27
400.9	2.70	0.22	1000.9	3.16	0.26
$\text{Xe}^{13+} \rightarrow \text{Xe}^{14+}$					
220.9	0.0199	0.023	500.9	2.23	0.18
240.9	0.0497	0.018	550.9	2.60	0.21
260.9	0.0390	0.018	600.9	2.52	0.20
280.9	0.0647	0.018	650.9	2.61	0.21
300.9	0.0778	0.012	700.9	2.78	0.23
320.9	0.585	0.051	750.9	2.89	0.24
340.9	1.14	0.094	800.9	2.87	0.23
360.9	1.46	0.12	850.9	2.78	0.23
380.9	1.70	0.14	900.9	2.74	0.22
400.9	1.85	0.15	950.9	2.69	0.22
450.9	2.13	0.17	1000.9	2.61	0.21
$\text{Xe}^{14+} \rightarrow \text{Xe}^{15+}$					
281.0	0.0307	0.020	551.0	1.81	0.15
301.0	0.0372	0.023	601.0	1.95	0.16
321.0	0.0617	0.022	651.0	2.20	0.18
341.0	0.140	0.016	701.0	2.33	0.19
361.0	0.675	0.058	751.0	2.29	0.19
381.0	1.01	0.085	801.0	2.36	0.19
401.0	1.20	0.098	851.0	2.34	0.19
451.0	1.49	0.12	901.0	2.30	0.19
501.0	1.64	0.13	951.0	2.27	0.18
			1001.0	2.24	0.18
$\text{Xe}^{15+} \rightarrow \text{Xe}^{16+}$					
321.0	0.0389	0.035	601.0	1.81	0.15
341.0	0.0454	0.022	651.0	1.75	0.14
361.0	0.0550	0.022	701.0	1.84	0.15
381.0	0.254	0.030	751.0	1.92	0.16
401.0	0.598	0.053	801.0	1.94	0.16
451.0	0.927	0.079	851.0	2.00	0.16
501.0	1.28	0.11	901.0	1.98	0.16
551.0	1.31	0.11	951.0	1.97	0.16
			1001.0	1.94	0.16

**Table D.1**(continued)

Collision energy (eV)	Cross section ( $10^{-18}\text{cm}^2$ )	Total error	Collision energy (eV)	Cross section ( $10^{-18}\text{cm}^2$ )	Total error
$\text{Xe}^{16+} \rightarrow \text{Xe}^{17+}$					
339.9	0.0919	0.018	599.9	1.34	0.11
359.9	0.0950	0.019	649.9	1.37	0.12
379.9	0.126	0.017	699.9	1.51	0.13
399.9	0.127	0.017	749.9	1.69	0.14
424.9	0.394	0.036	799.9	1.84	0.16
449.9	0.557	0.050	849.9	1.80	0.15
499.9	0.856	0.077	899.9	1.78	0.15
549.9	1.01	0.089	949.9	1.79	0.15
			999.9	1.74	0.15
$\text{Xe}^{17+} \rightarrow \text{Xe}^{18+}$					
379.9	0.0980	0.017	649.9	0.994	0.085
399.9	0.0895	0.021	699.9	1.21	0.10
429.9	0.122	0.017	749.9	1.28	0.11
459.9	0.278	0.027	799.9	1.48	0.13
499.9	0.371	0.035	849.9	1.49	0.13
549.9	0.573	0.051	899.9	1.51	0.13
599.9	0.811	0.070	949.9	1.55	0.13
			999.9	1.54	0.13
$\text{Xe}^{18+} \rightarrow \text{Xe}^{19+}$					
480.0	0.150	0.016	750.0	1.13	0.096
500.0	0.214	0.020	800.0	1.13	0.097
530.0	0.265	0.024	850.0	1.25	0.11
560.0	0.379	0.033	900.0	1.38	0.12
650.0	0.697	0.060	950.0	1.37	0.12
700.0	0.951	0.082	1000.0	1.40	0.12
$\text{Xe}^{19+} \rightarrow \text{Xe}^{20+}$					
500.1	0.0348	0.0047	750.1	0.855	0.073
530.1	0.0934	0.0093	800.1	1.08	0.092
560.1	0.176	0.016	850.1	1.07	0.091
600.1	0.231	0.021	900.1	1.13	0.096
650.1	0.464	0.041	950.1	1.20	0.10
700.1	0.648	0.055	1000.1	1.20	0.10
$\text{Xe}^{20+} \rightarrow \text{Xe}^{21+}$					
500.1	0.0348	0.011	700.1	0.535	0.046

**Table D.1**(continued)

Collision energy (eV)	Cross section ( $10^{-18}\text{cm}^2$ )	Total error	Collision energy (eV)	Cross section ( $10^{-18}\text{cm}^2$ )	Total error
520.1	0.0428	0.010	750.1	0.732	0.063
540.1	0.0645	0.013	800.1	1.11	0.095
560.1	0.0766	0.012	850.1	1.09	0.093
600.1	0.0973	0.016	900.1	1.18	0.10
650.1	0.298	0.028	950.1	1.20	0.10
			1000.1	1.18	0.10
$\text{Xe}^{21+} \rightarrow \text{Xe}^{22+}$					
550.1	0.0265	0.011	800.1	0.857	0.078
600.1	0.139	0.023	850.1	0.990	0.088
650.1	0.159	0.026	900.1	1.16	0.11
700.1	0.433	0.042	950.1	1.17	0.10
750.1	0.730	0.067	1000.1	1.15	0.10
$\text{Xe}^{22+} \rightarrow \text{Xe}^{23+}$					
500.2	0.118	0.034	750.2	0.644	0.062
550.2	0.131	0.046	800.2	0.828	0.077
600.2	0.114	0.032	850.2	0.948	0.085
650.2	0.130	0.025	900.2	0.922	0.084
700.2	0.152	0.031	950.2	1.03	0.094
			1000.2	1.08	0.098
$\text{Xe}^{23+} \rightarrow \text{Xe}^{24+}$					
100.2	1.31	0.63	500.2	0.533	0.11
150.2	0.671	0.36	550.2	0.581	0.083
175.2	0.792	0.26	600.2	0.510	0.080
200.2	0.781	0.29	650.2	0.577	0.093
225.2	0.929	0.22	700.2	0.473	0.077
250.2	0.814	0.22	750.2	0.497	0.076
300.2	0.816	0.16	800.2	0.828	0.100
350.2	0.787	0.17	850.2	1.03	0.10
400.2	0.843	0.17	900.2	1.16	0.12
450.2	0.695	0.12	950.2	1.09	0.11
			1000.2	1.20	0.12
$\text{Xe}^{24+} \rightarrow \text{Xe}^{25+}$					
100.3	1.29	0.56	550.3	1.14	0.13
150.3	1.75	0.39	600.3	1.03	0.12
200.3	1.63	0.31	650.3	0.987	0.11

**Table D.1**(continued)

Collision energy (eV)	Cross section ( $10^{-18}\text{cm}^2$ )	Total error	Collision energy (eV)	Cross section ( $10^{-18}\text{cm}^2$ )	Total error
250.3	1.13	0.26	700.3	0.869	0.097
300.3	1.35	0.19	750.3	0.880	0.092
350.3	1.39	0.19	800.3	0.872	0.087
400.3	1.22	0.18	850.3	1.08	0.11
450.3	1.45	0.17	900.3	1.16	0.11
500.3	1.04	0.14	950.3	1.25	0.11
			1000.3	1.30	0.13
 $\text{Xe}^{25+} \rightarrow \text{Xe}^{26+}$					
100.4	0.834	1.4	500.4	0.953	0.12
150.4	1.74	0.41	600.4	0.912	0.11
200.4	1.09	0.28	700.4	0.837	0.098
250.4	1.18	0.23	800.4	0.697	0.080
300.4	1.10	0.24	850.4	0.649	0.073
350.4	1.06	0.17	900.4	0.748	0.083
400.4	1.11	0.15	950.4	0.767	0.077
			1000.4	0.824	0.086

**Table D.2:** Absolute cross-section values of electron-impact double ionization of xenon ions

Collision energy (eV)	Cross section ( $10^{-19}\text{cm}^2$ )	Total error	Collision energy (eV)	Cross section ( $10^{-19}\text{cm}^2$ )	Total error
$\text{Xe}^+ \rightarrow \text{Xe}^{3+}$					
54.3	7.78	1.2	115.3	454	37
55.3	12.7	1.8	120.3	459	37
56.3	18.5	2.4	125.3	450	37
57.3	23.5	2.5	135.3	428	35
58.3	30.2	3.0	135.3	427	35
59.3	35.7	3.3	140.3	407	33
60.3	44.0	4.0	145.3	401	33
61.3	47.1	4.2	150.3	389	32
62.3	55.0	4.9	160.3	363	30
63.3	62.1	5.5	170.3	348	28
64.3	66.8	5.8	180.3	336	27
65.3	71.5	6.1	190.3	322	26
67.3	78.2	6.8	200.3	312	25
69.3	86.8	7.3	220.3	297	24
71.3	91.0	7.8	240.3	292	24
73.3	104	8.9	260.3	291	24
75.3	119	10	280.3	289	24
77.3	143	12	300.3	283	23
79.3	167	14	330.3	283	23
81.3	182	15	360.3	281	23
83.3	202	17	400.3	272	22
85.3	224	18	450.3	264	22
87.3	249	20	500.3	259	21
89.3	271	22	550.3	250	20
91.3	296	24	600.3	241	20
93.3	321	26	650.3	234	19
95.3	340	28	700.3	231	19
97.3	357	30	750.3	221	18
100.3	386	32	800.3	217	18
105.3	420	34	900.3	208	17
110.3	446	36	1000.3	198	16
$\text{Xe}^{2+} \rightarrow \text{Xe}^{4+}$					
74.2	11.4	1.3	239.2	294	25
79.2	70.1	7.0	259.2	296	25
84.2	125	12	279.2	296	25

**Table D.2**(continued)

Collision energy (eV)	Cross section ( $10^{-19}\text{cm}^2$ )	Total error	Collision energy (eV)	Cross section ( $10^{-19}\text{cm}^2$ )	Total error
89.2	175	17	299.2	297	25
94.2	225	22	329.2	294	25
99.2	267	25	399.2	287	24
109.2	323	30	359.2	293	25
119.2	347	32	449.2	278	24
129.2	353	32	499.2	267	23
139.2	350	32	549.2	258	22
149.2	341	31	599.2	251	21
159.2	340	30	649.2	243	21
169.2	337	30	699.2	236	20
179.2	323	29	749.2	229	19
189.2	311	27	799.2	224	19
199.2	304	27	849.2	217	18
219.2	295	26	899.2	211	18
			999.2	201	17
 $\text{Xe}^{3+} \rightarrow \text{Xe}^{5+}$					
93.2	3.36	0.57	259.2	227	20
95.2	4.74	0.55	279.2	229	20
97.2	10.0	1.2	299.2	226	19
99.2	20.5	2.1	329.2	230	20
104.2	52.4	5.0	359.2	222	19
109.2	87.3	8.3	399.2	219	19
119.2	137	13	449.2	210	18
129.2	173	16	499.2	205	17
139.2	194	18	549.2	198	17
149.2	217	19	599.2	191	16
159.2	240	21	649.2	188	16
169.2	251	22	699.2	182	16
179.2	253	22	749.2	174	15
189.2	249	22	799.2	172	15
199.2	243	21	849.2	165	14
219.2	237	21	899.2	162	14
239.2	229	20	999.2	152	13
 $\text{Xe}^{4+} \rightarrow \text{Xe}^{6+}$					
107.3	0.558	0.092	259.3	103	9.0
109.3	0.721	0.11	279.3	99.1	8.7
114.3	1.33	0.13	299.3	94.7	8.4

**Table D.2**(continued)

Collision energy (eV)	Cross section ( $10^{-19}\text{cm}^2$ )	Total error	Collision energy (eV)	Cross section ( $10^{-19}\text{cm}^2$ )	Total error
119.3	2.56	0.26	329.3	91.9	8.1
124.3	8.00	0.75	359.3	89.7	7.9
129.3	15.7	1.5	399.3	84.1	7.4
134.3	26.0	2.4	449.3	85.3	7.5
139.3	37.2	3.4	499.3	81.4	7.2
144.3	45.3	4.1	549.3	77.7	6.8
149.3	57.3	5.1	599.3	74.1	6.5
159.3	76.4	6.8	649.3	71.4	6.3
169.3	93.9	8.3	699.3	68.7	6.1
179.3	102	9.0	749.3	66.3	5.9
189.3	107	9.4	799.3	64.7	5.7
199.3	109	9.7	849.3	60.5	5.4
219.3	110	9.7	899.3	59.9	5.3
239.3	108	9.6	999.3	55.4	4.9
$\text{Xe}^{5+} \rightarrow \text{Xe}^{7+}$					
149.3	0.600	0.073	399.3	55.2	4.7
159.3	1.09	0.14	449.3	55.7	4.7
169.3	11.0	1.0	499.3	53.4	4.6
179.3	24.3	2.3	549.3	51.1	4.3
189.3	36.7	3.3	599.3	49.3	4.2
199.3	44.5	3.9	649.3	47.4	4.0
219.3	54.4	4.7	699.3	46.9	4.0
239.3	58.5	5.0	749.3	45.0	3.8
259.3	59.3	5.1	799.3	43.2	3.7
279.3	59.1	5.1	849.3	41.9	3.6
299.3	58.5	5.0	899.3	40.8	3.5
329.3	57.8	4.9	949.3	39.1	3.3
359.3	56.8	4.9	999.3	37.8	3.2
$\text{Xe}^{6+} \rightarrow \text{Xe}^{8+}$					
179.4	0.0512	0.030	449.4	31.7	2.7
189.4	0.491	0.078	499.4	31.3	2.7
199.4	2.71	0.26	549.4	30.6	2.6
209.4	7.27	0.68	599.4	29.3	2.5
219.4	13.6	1.3	649.4	29.9	2.6
239.4	21.1	1.8	699.4	29.0	2.5
259.4	25.2	2.2	749.4	28.7	2.5

**Table D.2**(continued)

Collision energy (eV)	Cross section ( $10^{-19}\text{cm}^2$ )	Total error	Collision energy (eV)	Cross section ( $10^{-19}\text{cm}^2$ )	Total error
279.4	27.8	2.4	799.4	27.5	2.4
299.4	29.5	2.5	849.4	27.3	2.3
329.4	30.6	2.6	899.4	26.6	2.3
359.4	31.6	2.7	949.4	25.7	2.2
399.4	32.3	2.8	999.4	24.8	2.1
$\text{Xe}^{7+} \rightarrow \text{Xe}^{9+}$					
219.4	0.0102	0.0082	419.4	7.14	0.61
229.4	0.0404	0.0093	439.4	7.60	0.66
239.4	0.0908	0.011	459.4	7.85	0.67
249.4	0.107	0.012	499.4	8.26	0.71
259.4	0.148	0.015	549.4	8.44	0.72
269.4	0.205	0.022	599.4	8.53	0.73
279.4	0.285	0.029	649.4	8.85	0.76
289.4	0.414	0.042	699.4	9.22	0.79
299.4	1.23	0.11	749.4	9.76	0.84
319.4	3.14	0.27	799.4	10.0	0.86
339.4	4.58	0.40	849.4	10.1	0.86
359.4	5.56	0.48	899.4	10.4	0.88
379.4	6.31	0.54	949.4	10.1	0.86
399.4	6.74	0.58	999.4	10.1	0.86
$\text{Xe}^{8+} \rightarrow \text{Xe}^{10+}$					
299.5	0.00337	0.0026	479.5	1.97	0.17
329.5	0.0432	0.0063	499.5	2.15	0.19
339.5	0.131	0.013	529.5	2.30	0.20
349.5	0.240	0.025	559.5	2.49	0.22
359.5	0.367	0.035	599.5	2.65	0.23
369.5	0.479	0.044	649.5	2.85	0.25
379.5	0.552	0.050	699.5	3.30	0.28
389.5	0.670	0.059	749.5	3.86	0.33
399.5	0.809	0.071	799.5	4.17	0.36
419.5	1.18	0.10	849.5	4.60	0.39
439.5	1.51	0.13	899.5	4.86	0.41
459.5	1.78	0.15	949.5	5.25	0.45
			999.5	5.42	0.46
$\text{Xe}^{9+} \rightarrow \text{Xe}^{11+}$					
399.5	0.0194	0.0041	649.5	1.38	0.12

**Table D.2**(continued)

Collision energy (eV)	Cross section ( $10^{-19}\text{cm}^2$ )	Total error	Collision energy (eV)	Cross section ( $10^{-19}\text{cm}^2$ )	Total error
419.5	0.0269	0.0042	699.5	1.65	0.14
439.5	0.0689	0.0073	749.5	2.19	0.19
459.5	0.254	0.023	799.5	2.52	0.22
479.5	0.415	0.037	849.5	2.92	0.25
499.5	0.582	0.051	899.5	3.34	0.29
549.5	0.838	0.073	949.5	3.90	0.34
599.5	1.03	0.089	999.5	4.16	0.36
$\text{Xe}^{10+} \rightarrow \text{Xe}^{12+}$					
489.6	0.0269	0.0066	699.6	1.11	0.096
499.6	0.0723	0.0084	749.6	1.54	0.13
509.6	0.132	0.014	799.6	1.92	0.17
524.6	0.205	0.020	824.6	2.19	0.19
549.6	0.311	0.029	849.6	2.68	0.23
599.6	0.551	0.050	899.6	2.85	0.24
649.6	0.700	0.061	949.6	3.23	0.28
			999.6	3.64	0.32
$\text{Xe}^{11+} \rightarrow \text{Xe}^{13+}$					
558.8	0.0679	0.0084	758.8	1.15	0.10
578.8	0.153	0.015	778.8	1.36	0.12
598.8	0.202	0.020	798.8	1.50	0.13
618.8	0.260	0.025	828.8	1.95	0.17
638.8	0.361	0.033	858.8	2.13	0.19
658.8	0.494	0.046	878.8	2.30	0.21
678.8	0.531	0.049	898.8	2.97	0.26
698.8	0.639	0.058	948.8	3.03	0.27
718.8	0.836	0.074	973.8	3.24	0.29
738.8	0.973	0.087	998.8	3.54	0.31
$\text{Xe}^{12+} \rightarrow \text{Xe}^{14+}$					
618.8	0.0476	0.0063	758.8	0.758	0.069
638.8	0.131	0.013	778.8	0.825	0.075
658.8	0.195	0.019	798.8	0.984	0.089
678.8	0.246	0.023	828.8	1.48	0.13
698.8	0.302	0.029	858.8	1.63	0.15
718.8	0.454	0.042	898.8	2.06	0.19
738.8	0.712	0.064	948.8	2.66	0.24
			998.8	3.15	0.28

**Table D.2**(continued)

Collision energy (eV)	Cross section ( $10^{-19}\text{cm}^2$ )	Total error	Collision energy (eV)	Cross section ( $10^{-19}\text{cm}^2$ )	Total error
<b>Xe<sup>13+</sup> → Xe<sup>15+</sup></b>					
678.8	0.0383	0.0062	798.8	0.698	0.063
698.8	0.0897	0.010	828.8	0.905	0.081
718.8	0.187	0.019	858.8	1.25	0.11
738.8	0.273	0.026	898.8	1.66	0.15
758.8	0.437	0.040	948.8	2.17	0.19
778.8	0.462	0.043	998.8	2.80	0.25
<b>Xe<sup>14+</sup> → Xe<sup>16+</sup></b>					
718.9	0.0115	0.0040	828.9	0.450	0.045
738.9	0.0574	0.0078	858.9	0.810	0.074
758.9	0.130	0.014	898.9	1.10	0.10
778.9	0.231	0.024	948.9	1.63	0.15
798.9	0.277	0.029	998.9	2.11	0.19
<b>Xe<sup>15+</sup> → Xe<sup>17+</sup></b>					
798.9	0.0292	0.0050	898.9	0.486	0.045
818.9	0.0816	0.011	923.9	0.699	0.064
838.9	0.126	0.014	948.9	0.846	0.077
858.9	0.268	0.028	973.9	1.19	0.11
878.9	0.382	0.038	998.9	1.35	0.12
<b>Xe<sup>16+</sup> → Xe<sup>18+</sup></b>					
799.0	0.00040	0.0059	899.0	0.0838	0.012
839.0	0.00894	0.0066	919.0	0.115	0.015
859.0	0.0217	0.0074	939.0	0.181	0.018
879.0	0.0415	0.0092	959.0	0.282	0.029
			999.0	0.484	0.047
<b>Xe<sup>17+</sup> → Xe<sup>19+</sup></b>					
949.2	0.0168	0.0035	974.2	0.0502	0.0057
			999.2	0.0709	0.0084

**Table D.3:** Absolute cross-section values of electron-impact triple ionization of xenon ions

Collision energy (eV)	Cross section ( $10^{-20}\text{cm}^2$ )	Total error	Collision energy (eV)	Cross section ( $10^{-20}\text{cm}^2$ )	Total error
$\text{Xe}^+ \rightarrow \text{Xe}^{4+}$					
80.3	-0.0592	-1.0	145.3	736	61
82.3	0.154	0.50	150.3	764	65
84.3	0.130	0.46	160.3	862	71
86.3	0.391	0.33	170.3	961	80
88.3	0.942	0.28	180.3	1046	87
90.3	0.818	0.27	190.3	1089	90
92.3	1.24	0.36	200.3	1099	89
94.3	2.04	0.54	220.3	1050	85
96.3	2.65	0.55	240.3	994	83
98.3	8.27	1.4	260.3	945	77
100.3	18.8	2.1	280.3	896	74
102.3	38.1	3.7	300.3	891	73
104.3	59.4	5.6	330.3	864	70
106.3	89.3	7.7	360.3	823	67
108.3	125	11	400.3	772	63
110.3	165	14	450.3	701	57
113.3	228	19	500.3	717	58
116.3	294	25	550.3	669	54
119.3	352	30	600.3	645	52
122.3	415	35	650.3	611	49
125.3	473	40	700.3	583	47
130.3	564	47	750.3	557	45
135.3	621	52	800.3	530	43
140.3	678	56	900.3	488	40
			1000.3	451	36
$\text{Xe}^{6+} \rightarrow \text{Xe}^{9+}$					
379.4	0.186	0.022	649.4	13.3	1.1
399.4	1.27	0.12	699.4	14.7	1.3
429.4	3.85	0.35	749.4	17.2	1.5
459.4	6.23	0.56	799.4	19.7	1.7
499.4	8.41	0.73	849.4	21.9	1.9
529.4	9.51	0.81	899.4	24.3	2.1
549.4	10.1	0.86	949.4	27.3	2.3
599.4	11.1	0.95	999.4	29.0	2.5

**Table D.3**(continued)

Collision energy (eV)	Cross section ( $10^{-20}\text{cm}^2$ )	Total error	Collision energy (eV)	Cross section ( $10^{-20}\text{cm}^2$ )	Total error
$\text{Xe}^{7+} \rightarrow \text{Xe}^{10+}$					
501.2	0.0588	0.011	751.2	3.65	0.31
526.2	0.278	0.030	801.2	4.83	0.41
551.2	0.621	0.057	851.2	6.27	0.54
601.2	1.20	0.11	901.2	9.32	0.80
651.2	1.94	0.17	951.2	10.6	0.91
701.2	2.64	0.23	1001.2	13.0	1.1

**Table D.4:** Absolute cross-section values of electron-impact fourfold ionization of xenon ions

Collision energy (eV)	Cross section ( $10^{-20}\text{cm}^2$ )	Total error	Collision energy (eV)	Cross section ( $10^{-20}\text{cm}^2$ )	Total error
$\text{Xe}^+ \rightarrow \text{Xe}^{5+}$					
140.3	0.115	0.22	270.3	279	23
145.3	0.0907	0.11	280.3	283	23
150.3	0.0222	0.11	290.3	289	24
155.3	0.416	0.19	300.3	276	22
160.3	2.53	0.52	320.3	275	23
165.3	7.33	1.0	340.3	283	23
170.3	16.6	1.6	360.3	291	24
175.3	29.3	2.9	380.3	295	24
180.3	44.8	4.1	400.3	292	24
185.3	62.0	5.7	450.3	284	23
190.3	83.6	7.8	500.3	286	23
195.3	106	9.2	550.3	279	23
200.3	123	11	600.3	263	21
210.3	162	14	650.3	250	20
220.3	196	17	700.3	249	20
230.3	226	19	750.3	245	20
240.3	254	22	800.3	238	19
250.3	267	22	900.3	225	18
260.3	274	23	1000.3	199	16
$\text{Xe}^{6+} \rightarrow \text{Xe}^{10+}$					
639.4	0.0420	0.0062	799.4	0.642	0.058
669.4	0.119	0.012	849.4	0.916	0.081
699.4	0.209	0.020	899.4	1.27	0.11
729.4	0.321	0.030	949.4	2.09	0.18
759.4	0.434	0.040	999.4	3.04	0.26
$\text{Xe}^{7+} \rightarrow \text{Xe}^{11+}$					
779.4	0.0205	0.0049	899.4	0.227	0.021
799.4	0.0359	0.0065	949.4	0.359	0.032
849.4	0.0899	0.0100	999.4	0.644	0.056

**Table D.5:** Absolute cross-section values of electron-impact fivefold ionization of xenon ions

Collision energy (eV)	Cross section ( $10^{-20}\text{cm}^2$ )	Total error	Collision energy (eV)	Cross section ( $10^{-20}\text{cm}^2$ )	Total error
$\text{Xe}^+ \rightarrow \text{Xe}^{6+}$					
240.3	0.455	0.047	500.3	41.5	3.4
260.3	3.06	0.25	550.3	41.5	3.4
280.3	8.73	0.71	600.3	41.5	3.4
300.3	15.9	1.3	650.3	40.8	3.3
320.3	22.8	1.9	700.3	40.7	3.3
340.3	28.3	2.3	750.3	42.9	3.5
360.3	32.4	2.6	800.3	43.6	3.6
380.3	35.3	2.9	850.3	43.6	3.6
400.3	37.1	3.0	900.3	42.8	3.5
450.3	40.6	3.3	950.3	42.7	3.5
			1000.3	42.2	3.4

**Table D.6:** Absolute cross-section values of electron-impact sixfold ionization of xenon ions

Collision energy (eV)	Cross section ( $10^{-20}\text{cm}^2$ )	Total error	Collision energy (eV)	Cross section ( $10^{-20}\text{cm}^2$ )	Total error
$\text{Xe}^+ \rightarrow \text{Xe}^{7+}$					
360.3	0.0699	0.012	650.3	3.89	0.32
380.3	0.265	0.025	700.3	4.33	0.35
400.3	0.598	0.052	750.3	5.29	0.43
450.3	1.66	0.14	800.3	5.86	0.48
500.3	2.61	0.21	850.3	6.42	0.53
550.3	3.23	0.26	900.3	7.00	0.57
600.3	3.63	0.30	950.3	7.57	0.62
			1000.3	8.66	0.71

**Table D.7:** Absolute cross-section values of electron-impact sevenfold ionization of xenon ions

Collision energy (eV)	Cross section ( $10^{-22}\text{cm}^2$ )	Total error	Collision energy (eV)	Cross section ( $10^{-22}\text{cm}^2$ )	Total error
$\text{Xe}^+ \rightarrow \text{Xe}^{8+}$					
700.3	12.9	1.3	850.3	72.7	6.0
750.3	33.2	3.0	900.3	92.8	7.6
800.3	53.4	4.4	950.3	117	9.6
			1000.3	181	15

**Table D.8:** Absolute cross-section values of electron-impact eightfold ionization of xenon ions

Collision energy (eV)	Cross section ( $10^{-23}\text{cm}^2$ )	Total error	Collision energy (eV)	Cross section ( $10^{-23}\text{cm}^2$ )	Total error
$\text{Xe}^+ \rightarrow \text{Xe}^{9+}$					
708.4	0.889	0.31	898.4	22.6	2.3
728.4	2.28	0.51	948.4	38.8	3.9
748.4	3.13	0.55	998.4	91.2	9.1
798.4	7.04	0.86	998.4	92.2	8.9
848.4	14.2	1.5	998.4	91.7	9.0

**Table D.9:** Absolute cross-section values of electron-impact ninefold ionization of xenon ions

Collision energy (eV)	Cross section ( $10^{-24}\text{cm}^2$ )	Total error	Collision energy (eV)	Cross section ( $10^{-24}\text{cm}^2$ )	Total error
$\text{Xe}^+ \rightarrow \text{Xe}^{10+}$					
948.4	0.574	0.33	998.4	7.14	0.94

**Table D.10:** Absolute cross-section values of electron-impact single ionization of tin ions

Collision energy (eV)	Cross section ( $10^{-18}\text{cm}^2$ )	Total error	Collision energy (eV)	Cross section ( $10^{-18}\text{cm}^2$ )	Total error
<b>Sn<sup>+</sup> → Sn<sup>2+</sup></b>					
15.2	84.2	11	108.2	221	18
16.2	120	14	118.2	211	17
17.2	160	17	128.2	200	16
18.2	172	16	138.2	193	16
20.2	202	18	148.2	188	15
22.2	236	20	158.2	182	15
24.2	238	20	168.2	177	14
26.2	246	20	178.2	170	14
28.2	255	21	188.2	168	14
30.2	264	22	198.2	163	13
32.2	268	22	218.2	156	13
34.2	268	22	238.2	150	12
36.2	268	22	258.2	146	12
38.2	279	23	278.2	142	12
40.2	270	22	298.2	138	11
42.2	274	23	348.2	128	10
44.2	273	23	398.2	120	9.7
46.2	272	22	448.2	114	9.2
48.2	273	23	498.2	106	8.6
53.2	272	22	548.2	102	8.2
58.2	267	22	598.2	96.7	7.8
63.2	264	22	648.2	92.3	7.5
68.2	260	21	698.2	88.3	7.1
73.2	252	21	748.2	84.6	6.8
78.2	248	20	798.2	81.7	6.6
83.2	242	20	848.2	77.3	6.3
88.2	243	20	898.2	74.7	6.0
93.2	236	19	948.2	71.7	5.8
98.2	226	18	998.2	69.5	5.6
<b>Sn<sup>2+</sup> → Sn<sup>3+</sup></b>					
25.3	16.4	2.8	98.3	128	10
26.3	18.0	3.0	108.3	125	10
27.3	20.6	3.0	118.3	119	9.7
28.3	25.4	2.9	128.3	116	9.4
29.3	29.3	3.0	138.3	110	9.0
30.3	33.1	3.1	148.3	106	8.6

**Table D.10**(continued)

Collision energy (eV)	Cross section ( $10^{-18}\text{cm}^2$ )	Total error	Collision energy (eV)	Cross section ( $10^{-18}\text{cm}^2$ )	Total error
31.3	37.7	3.3	158.3	103	8.4
32.3	42.4	3.6	168.3	100	8.2
33.3	44.9	3.8	178.3	98.8	8.0
34.3	48.7	4.1	188.3	96.8	7.9
35.3	54.6	4.5	198.3	95.0	7.7
36.3	59.8	5.0	218.3	92.9	7.6
37.3	62.6	5.2	238.3	91.8	7.4
38.3	64.8	5.4	258.3	90.0	7.3
40.3	74.8	6.1	278.3	88.3	7.2
42.3	79.8	6.5	298.3	86.6	7.0
44.3	85.9	7.0	348.3	82.4	6.7
46.3	90.6	7.4	398.3	78.7	6.4
48.3	95.4	7.8	448.3	75.5	6.1
51.3	102	8.3	498.3	72.4	5.9
54.3	109	8.9	548.3	69.4	5.6
58.3	115	9.4	598.3	66.4	5.4
63.3	122	9.9	648.3	64.5	5.2
68.3	125	10	698.3	64.0	5.2
73.3	129	11	748.3	62.5	5.1
78.3	131	11	798.3	60.2	4.9
83.3	130	11	848.3	57.8	4.7
88.3	132	11	898.3	57.8	4.7
93.3	129	10	948.3	55.3	4.5
			998.3	54.1	4.4
 $\text{Sn}^{3+} \rightarrow \text{Sn}^{4+}$					
41.4	10.7	1.1	178.4	83.3	6.8
43.4	32.7	2.9	188.4	86.1	8.2
46.4	46.8	4.0	198.4	81.2	6.6
49.4	61.9	5.1	218.4	79.4	6.5
52.4	69.3	5.7	238.4	76.9	6.3
55.4	77.7	6.3	258.4	74.8	6.1
58.4	82.7	6.8	278.4	72.6	5.9
63.4	88.2	7.2	298.4	72.2	5.9
68.4	93.6	7.6	348.4	69.4	5.7
73.4	95.5	7.8	398.4	66.8	5.4
78.4	99.7	8.1	448.4	63.0	5.1
83.4	104	8.4	498.4	60.8	5.0
88.4	105	8.5	548.4	58.3	4.7

**Table D.10**(continued)

Collision energy (eV)	Cross section ( $10^{-18}\text{cm}^2$ )	Total error	Collision energy (eV)	Cross section ( $10^{-18}\text{cm}^2$ )	Total error
93.4	106	8.6	598.4	56.0	4.6
98.4	106	8.6	648.4	53.7	4.4
108.4	105	8.6	698.4	53.2	4.3
118.4	105	8.6	748.4	52.8	4.3
128.4	100	8.1	798.4	51.8	4.2
138.4	93.9	7.6	848.4	49.7	4.0
148.4	88.9	7.3	898.4	48.5	3.9
158.4	85.6	7.0	948.4	47.6	3.9
168.4	85.6	7.0	998.4	46.2	3.7
$\text{Sn}^{4+} \rightarrow \text{Sn}^{5+}$					
53.3	2.38	0.32	178.3	57.6	4.7
54.3	9.04	1.1	188.3	56.7	4.6
55.3	14.5	1.5	198.3	56.6	4.6
56.3	17.7	1.6	218.3	54.6	4.5
59.3	24.0	2.0	238.3	53.4	4.4
62.3	26.5	2.2	258.3	52.6	4.3
65.3	29.4	2.4	278.3	51.7	4.2
68.3	32.1	2.7	298.3	50.9	4.2
73.3	33.6	2.8	328.3	50.1	4.1
78.3	37.1	3.1	358.3	48.7	4.0
83.3	43.8	3.6	398.3	46.9	3.8
88.3	48.2	4.0	448.3	44.6	3.6
93.3	51.5	4.2	498.3	43.3	3.5
98.3	55.3	4.5	548.3	41.3	3.4
108.3	59.6	4.9	598.3	40.0	3.3
118.3	60.8	5.0	648.3	38.3	3.1
128.3	62.3	5.1	698.3	37.8	3.1
138.3	62.1	5.1	748.3	36.3	3.0
148.3	62.0	5.1	798.3	34.5	2.8
158.3	60.6	5.0	848.3	33.4	2.7
168.3	58.8	4.8	898.3	32.2	2.6
			948.3	30.9	2.5
$\text{Sn}^{5+} \rightarrow \text{Sn}^{6+}$					
65.4	0.235	0.057	198.4	33.3	2.7
68.4	1.19	0.13	218.4	33.4	2.7
71.4	2.81	0.25	238.4	32.0	2.6
74.4	3.70	0.32	258.4	31.9	2.6

**Table D.10**(continued)

Collision energy (eV)	Cross section ( $10^{-18}\text{cm}^2$ )	Total error	Collision energy (eV)	Cross section ( $10^{-18}\text{cm}^2$ )	Total error
77.4	4.81	0.41	278.4	31.1	2.5
79.4	5.32	0.44	298.4	31.1	2.5
83.4	5.80	0.48	328.4	29.9	2.4
88.4	6.34	0.52	358.4	29.3	2.4
93.4	6.98	0.57	398.4	28.0	2.3
98.4	13.2	1.1	448.4	27.0	2.2
103.4	19.9	1.6	498.4	26.0	2.1
108.4	23.7	1.9	548.4	25.2	2.1
118.4	28.7	2.3	598.4	24.4	2.0
128.4	32.6	2.7	648.4	22.9	1.9
138.4	34.1	2.8	698.4	22.4	1.8
148.4	34.5	2.8	748.4	21.7	1.8
158.4	34.6	2.8	798.4	21.1	1.7
168.4	34.2	2.8	848.4	20.5	1.7
178.4	34.2	2.8	898.4	19.8	1.6
188.4	34.2	2.8	948.4	19.2	1.6
			998.4	18.6	1.5
 $\text{Sn}^{6+} \rightarrow \text{Sn}^{7+}$					
88.6	0.390	0.059	258.6	18.7	1.5
93.6	0.680	0.072	278.6	18.3	1.4
98.6	0.752	0.077	298.6	17.9	1.4
103.6	0.838	0.087	318.6	17.5	1.4
108.6	0.919	0.097	338.6	17.3	1.3
113.6	2.82	0.25	358.6	16.9	1.3
118.6	6.82	0.55	378.6	16.5	1.3
123.6	9.71	0.78	398.6	16.4	1.3
128.6	12.3	0.98	448.6	15.6	1.2
133.6	14.2	1.1	498.6	15.0	1.2
138.6	15.6	1.2	548.6	14.3	1.1
143.6	16.2	1.3	598.6	13.8	1.1
148.6	17.2	1.3	648.6	13.2	1.0
158.6	18.3	1.4	698.6	12.7	0.98
168.6	18.6	1.5	748.6	12.2	0.98
178.6	19.1	1.5	798.6	11.8	0.91
188.6	18.8	1.5	848.6	11.3	0.88
198.6	19.0	1.5	898.6	10.9	0.84
218.6	18.9	1.5	948.6	10.6	0.82
238.6	18.8	1.5	998.6	10.3	0.80

**Table D.10**(continued)

Collision energy (eV)	Cross section ( $10^{-18}\text{cm}^2$ )	Total error	Collision energy (eV)	Cross section ( $10^{-18}\text{cm}^2$ )	Total error
<b>Sn<sup>7+</sup> → Sn<sup>8+</sup></b>					
143.6	7.60	0.60	358.6	13.8	1.1
133.6	1.72	0.15	398.6	13.4	1.0
138.6	5.35	0.43	448.6	12.9	1.00
148.6	9.01	0.71	498.6	12.4	0.96
158.6	11.2	0.88	548.6	11.9	0.92
168.6	12.5	0.98	598.6	11.5	0.89
178.6	13.3	1.0	648.6	11.1	0.86
198.6	14.3	1.1	698.6	10.6	0.82
218.6	14.5	1.1	748.6	10.2	0.79
238.6	14.6	1.1	798.6	9.93	0.77
258.6	14.7	1.1	848.6	9.57	0.74
278.6	14.6	1.1	898.6	9.19	0.71
298.6	14.5	1.1	948.6	8.92	0.69
328.6	14.2	1.1	998.6	8.56	0.66
<b>Sn<sup>8+</sup> → Sn<sup>9+</sup></b>					
148.7	0.217	0.030	358.7	9.88	0.77
153.7	1.02	0.085	398.7	9.67	0.75
158.7	2.45	0.20	448.7	9.31	0.72
163.7	3.70	0.29	498.7	9.14	0.71
168.7	5.15	0.40	548.7	8.85	0.69
178.7	7.03	0.55	598.7	8.52	0.66
188.7	7.95	0.62	648.7	8.17	0.63
198.7	8.82	0.69	698.7	7.96	0.62
218.7	9.47	0.74	748.7	7.69	0.60
238.7	9.67	0.75	798.7	7.41	0.57
258.7	9.88	0.77	848.7	7.20	0.56
278.7	10.0	0.78	898.7	6.99	0.54
298.7	9.99	0.78	948.7	6.77	0.52
328.7	9.95	0.77	998.7	6.53	0.51
<b>Sn<sup>9+</sup> → Sn<sup>10+</sup></b>					
168.7	0.0744	0.011	338.7	6.60	0.52
173.7	0.150	0.017	358.7	6.62	0.52
176.7	0.366	0.034	378.7	6.66	0.52
178.7	0.641	0.051	398.7	6.71	0.53
178.7	0.658	0.057	418.7	6.53	0.51
180.7	1.07	0.085	448.7	6.50	0.51

**Table D.10**(continued)

Collision energy (eV)	Cross section ( $10^{-18}\text{cm}^2$ )	Total error	Collision energy (eV)	Cross section ( $10^{-18}\text{cm}^2$ )	Total error
183.7	1.91	0.16	498.7	6.63	0.52
188.7	3.00	0.24	548.7	6.46	0.50
198.7	4.01	0.32	598.7	6.19	0.48
208.7	4.84	0.39	648.7	6.04	0.47
218.7	5.34	0.42	698.7	5.91	0.46
238.7	6.00	0.47	748.7	5.63	0.44
258.7	6.32	0.50	798.7	5.45	0.43
278.7	6.50	0.51	848.7	5.29	0.41
298.7	6.53	0.52	898.7	5.12	0.40
318.7	6.59	0.52	948.7	4.99	0.39
			998.7	4.93	0.38
<b>Sn<sup>10+</sup> → Sn<sup>11+</sup></b>					
193.8	0.0984	0.021	398.8	4.79	0.37
198.8	0.150	0.024	428.8	4.90	0.38
203.8	0.452	0.042	458.8	4.99	0.39
208.8	1.16	0.094	498.8	5.13	0.40
218.8	2.21	0.17	548.8	4.98	0.39
228.8	2.87	0.22	598.8	4.95	0.38
238.8	3.31	0.26	648.8	4.74	0.37
258.8	3.93	0.31	698.8	4.59	0.36
278.8	4.21	0.33	748.8	4.45	0.35
298.8	4.44	0.34	798.8	4.34	0.34
318.8	4.55	0.35	848.8	4.23	0.33
338.8	4.61	0.36	898.8	4.12	0.32
358.8	4.67	0.36	948.8	4.01	0.31
378.8	4.85	0.38	998.8	3.90	0.30
<b>Sn<sup>11+</sup> → Sn<sup>12+</sup></b>					
218.8	0.110	0.020	398.8	3.38	0.26
223.8	0.129	0.019	448.8	3.70	0.29
228.8	0.270	0.029	498.8	3.89	0.30
233.8	0.704	0.059	548.8	4.07	0.32
238.8	1.08	0.087	598.8	3.89	0.30
248.8	1.66	0.13	648.8	3.81	0.30
258.8	2.08	0.16	698.8	3.71	0.29
278.8	2.62	0.21	748.8	3.56	0.28
298.8	2.85	0.22	798.8	3.46	0.27
318.8	3.06	0.24	848.8	3.39	0.26

**Table D.10**(continued)

Collision energy (eV)	Cross section ( $10^{-18}\text{cm}^2$ )	Total error	Collision energy (eV)	Cross section ( $10^{-18}\text{cm}^2$ )	Total error
338.8	3.18	0.25	898.8	3.28	0.25
358.8	3.33	0.26	948.8	3.18	0.25
378.8	3.35	0.26	998.8	3.13	0.24
$\text{Sn}^{12+} \rightarrow \text{Sn}^{13+}$					
258.9	0.418	0.041	458.9	2.69	0.21
268.9	0.953	0.078	498.9	2.92	0.23
278.9	1.28	0.10	548.9	3.13	0.24
288.9	1.52	0.12	598.9	3.06	0.24
298.9	1.67	0.13	648.9	3.11	0.24
318.9	1.87	0.15	698.9	3.01	0.23
338.9	2.06	0.16	748.9	2.94	0.23
358.9	2.14	0.17	798.9	2.85	0.22
378.9	2.30	0.18	848.9	2.76	0.21
398.9	2.40	0.19	898.9	2.67	0.21
428.9	2.56	0.20	948.9	2.62	0.20
			998.9	2.55	0.20
$\text{Sn}^{13+} \rightarrow \text{Sn}^{14+}$					
273.9	0.211	0.030	468.9	2.15	0.17
278.9	0.215	0.030	498.9	2.01	0.16
283.9	0.308	0.037	548.9	2.28	0.18
288.9	0.438	0.043	598.9	2.59	0.20
298.9	0.639	0.056	648.9	2.60	0.20
318.9	0.812	0.068	698.9	2.58	0.20
338.9	0.945	0.078	748.9	2.51	0.19
358.9	1.16	0.093	798.9	2.46	0.19
378.9	1.25	0.100	848.9	2.38	0.18
398.9	1.62	0.13	898.9	2.29	0.18
418.9	1.56	0.12	948.9	2.26	0.18
438.9	1.63	0.13	998.9	2.18	0.17

**Table D.11:** Absolute cross-section values of electron-impact double ionization of tin ions

Collision energy (eV)	Cross section ( $10^{-19}\text{cm}^2$ )	Total error	Collision energy (eV)	Cross section ( $10^{-19}\text{cm}^2$ )	Total error
$\text{Sn}^+ \rightarrow \text{Sn}^{3+}$					
45.2	0.767	0.76	108.2	260	21
46.2	1.69	0.52	113.2	261	21
47.2	2.50	0.70	118.2	261	21
48.2	5.53	1.2	123.2	269	22
49.2	7.67	1.4	128.2	275	22
50.2	12.3	1.5	133.2	272	22
51.2	16.4	2.1	138.2	267	22
52.2	21.0	2.3	143.2	259	21
53.2	25.9	2.6	148.2	253	21
54.2	34.2	3.0	153.2	249	20
55.2	37.4	3.6	158.2	244	20
56.2	44.6	4.2	163.2	238	19
57.2	48.2	4.1	168.2	232	19
58.2	53.0	4.6	178.2	207	17
60.2	67.0	5.9	188.2	211	17
62.2	77.9	6.6	198.2	207	17
64.2	91.8	7.8	218.2	197	16
68.2	116	9.6	238.2	192	16
66.2	101	8.5	258.2	183	15
70.2	123	10	278.2	178	14
72.2	131	11	298.2	174	14
74.2	151	12	348.2	161	13
76.2	158	13	398.2	149	12
78.2	163	13	448.2	139	11
80.2	167	14	498.2	129	10
82.2	176	14	548.2	122	9.8
84.2	184	15	598.2	114	9.3
86.2	187	15	648.2	109	8.8
88.2	197	16	698.2	105	8.5
90.2	210	17	748.2	101	8.2
92.2	214	17	798.2	95.0	7.7
94.2	221	18	848.2	91.5	7.4
96.2	233	19	898.2	88.3	7.1
98.2	237	19	948.2	84.8	6.9
103.2	250	20	998.2	81.0	6.6

**Table D.11**(continued)

Collision energy (eV)	Cross section ( $10^{-19}\text{cm}^2$ )	Total error	Collision energy (eV)	Cross section ( $10^{-19}\text{cm}^2$ )	Total error
<b>Sn<sup>2+</sup> → Sn<sup>4+</sup></b>					
71.2	8.80	1.5	148.2	226	18
72.2	9.60	1.5	158.2	236	19
73.2	12.3	1.6	168.2	230	19
74.2	15.3	1.8	178.2	227	19
76.2	20.9	2.2	188.2	221	18
78.2	27.6	2.7	198.2	213	17
80.2	35.3	3.3	218.2	200	16
82.2	42.7	4.0	238.2	191	16
84.2	48.5	4.4	258.2	184	15
86.2	57.2	5.2	278.2	179	15
88.2	62.2	5.4	298.2	177	14
90.2	71.0	6.2	348.2	170	14
92.2	78.0	6.6	398.2	158	13
94.2	85.5	7.2	448.2	152	12
96.2	91.8	7.7	498.2	143	12
98.2	100	8.4	548.2	138	11
103.2	118	9.6	598.2	134	11
108.2	136	11	648.2	128	10
113.2	152	12	698.2	121	9.8
118.2	170	14	748.2	117	9.5
123.2	182	15	798.2	112	9.1
128.2	195	16	848.2	107	8.7
133.2	203	17	898.2	104	8.5
138.2	213	17	948.2	99.6	8.1
143.2	219	18	998.2	97.2	7.9
<b>Sn<sup>3+</sup> → Sn<sup>5+</sup></b>					
118.3	3.16	0.35	298.3	107	8.8
123.3	13.9	1.2	348.3	103	8.4
128.3	27.6	2.4	398.3	100	8.2
133.3	41.7	3.5	448.3	96.9	8.0
138.3	53.7	4.5	498.3	92.6	7.7
143.3	66.4	5.5	548.3	88.4	7.2
148.3	76.7	6.3	598.3	84.5	6.9
158.3	94.3	7.9	648.3	81.8	6.6
168.3	107	8.9	698.3	79.4	6.5
178.3	111	9.3	748.3	75.6	6.2
188.3	114	9.5	798.3	73.5	6.0

**Table D.11**(continued)

Collision energy (eV)	Cross section ( $10^{-19}\text{cm}^2$ )	Total error	Collision energy (eV)	Cross section ( $10^{-19}\text{cm}^2$ )	Total error
198.3	117	9.7	848.3	71.9	5.9
223.3	116	9.5	898.3	68.8	5.6
248.3	112	9.3	948.3	66.4	5.4
273.3	109	8.9	993.3	63.4	5.2
$\text{Sn}^{4+} \rightarrow \text{Sn}^{6+}$					
153.3	1.28	0.35	358.3	39.9	3.3
158.3	3.64	0.74	398.3	38.9	3.2
163.3	6.26	0.80	448.3	37.9	3.1
168.3	8.81	1.0	498.3	36.5	3.0
173.3	11.5	1.2	548.3	35.6	2.9
178.3	14.0	1.5	598.3	34.7	3.0
188.3	21.3	1.8	648.3	33.9	2.8
198.3	26.5	2.3	698.3	31.8	2.6
218.3	35.2	3.0	748.3	31.6	2.6
238.3	38.9	3.3	798.3	31.5	2.6
258.3	41.1	3.4	848.3	29.0	2.4
278.3	41.1	3.4	898.3	29.8	2.5
298.3	41.5	3.5	948.3	27.5	2.3
328.3	40.5	3.4	998.3	26.9	2.2
$\text{Sn}^{5+} \rightarrow \text{Sn}^{7+}$					
188.4	0.310	0.085	288.4	14.8	1.2
193.4	0.533	0.075	298.4	15.3	1.3
198.4	0.898	0.10	318.4	16.0	1.3
203.4	1.10	0.12	338.4	16.4	1.4
208.4	1.48	0.14	358.4	16.6	1.4
213.4	2.20	0.20	398.4	17.0	1.4
218.4	3.37	0.31	448.4	17.2	1.4
223.4	4.66	0.42	498.4	17.2	1.4
228.4	6.17	0.53	548.4	17.6	1.4
233.4	7.69	0.66	598.4	17.6	1.4
238.4	8.80	0.75	648.4	17.5	1.4
243.4	9.94	0.84	698.4	17.7	1.4
248.4	10.7	0.90	748.4	17.6	1.4
253.4	11.5	0.97	798.4	17.3	1.4
258.4	12.3	1.0	848.4	17.0	1.4
263.4	12.7	1.1	898.4	16.6	1.4
268.4	13.5	1.1	948.4	16.3	1.3

**Table D.11**(continued)

Collision energy (eV)	Cross section ( $10^{-19}\text{cm}^2$ )	Total error	Collision energy (eV)	Cross section ( $10^{-19}\text{cm}^2$ )	Total error
278.4	14.3	1.2	998.4	16.1	1.3
<b>Sn<sup>6+</sup> → Sn<sup>8+</sup></b>					
243.6	0.135	0.016	498.6	8.43	0.61
258.6	0.977	0.075	548.6	9.33	0.68
278.6	3.21	0.23	598.6	9.87	0.71
298.6	4.82	0.35	648.6	10.4	0.75
323.6	5.93	0.43	698.6	10.5	0.76
348.6	6.57	0.48	748.6	10.7	0.78
373.6	7.06	0.51	798.6	10.7	0.77
398.6	7.16	0.52	848.6	10.7	0.77
428.6	7.86	0.57	898.6	10.7	0.77
458.6	8.01	0.58	948.6	10.6	0.76
			998.6	10.4	0.75
<b>Sn<sup>7+</sup> → Sn<sup>9+</sup></b>					
298.6	0.245	0.033	548.6	5.36	0.42
308.6	0.743	0.067	598.6	6.19	0.49
318.6	1.24	0.11	648.6	6.78	0.53
338.6	2.01	0.17	698.6	7.32	0.57
358.6	2.60	0.21	748.6	7.68	0.60
378.6	2.88	0.23	798.6	7.81	0.61
398.6	3.14	0.25	848.6	7.97	0.62
428.6	3.51	0.28	898.6	8.01	0.62
458.6	3.77	0.30	948.6	7.99	0.62
498.6	4.16	0.33	998.6	8.05	0.63
<b>Sn<sup>8+</sup> → Sn<sup>10+</sup></b>					
338.7	0.0214	0.0045	598.7	4.13	0.32
358.7	0.358	0.029	648.7	4.73	0.37
378.7	0.680	0.055	698.7	5.68	0.44
398.7	0.988	0.079	748.7	5.84	0.46
428.7	1.29	0.10	798.7	6.20	0.48
458.7	1.55	0.12	848.7	6.38	0.50
498.7	2.18	0.17	898.7	6.50	0.50
548.7	3.04	0.24	948.7	6.61	0.51
			998.7	6.74	0.52

**Table D.11**(continued)

Collision energy (eV)	Cross section ( $10^{-19}\text{cm}^2$ )	Total error	Collision energy (eV)	Cross section ( $10^{-19}\text{cm}^2$ )	Total error
<b>Sn<sup>9+</sup> → Sn<sup>11+</sup></b>					
390.7	0.0335	0.0069	528.7	1.50	0.12
388.7	0.0216	0.0055	558.7	2.39	0.19
393.7	0.0597	0.0086	598.7	3.01	0.23
398.7	0.0923	0.011	648.7	4.11	0.32
408.7	0.185	0.018	698.7	4.85	0.38
418.7	0.284	0.026	748.7	5.51	0.43
438.7	0.455	0.039	798.7	5.94	0.46
458.7	0.742	0.061	848.7	6.24	0.49
478.7	0.900	0.072	898.7	6.44	0.50
498.7	1.30	0.10	948.7	6.59	0.51
			998.7	6.71	0.52
<b>Sn<sup>10+</sup> → Sn<sup>12+</sup></b>					
448.8	0.0577	0.0086	598.8	2.33	0.19
458.8	0.105	0.013	648.8	3.12	0.25
468.8	0.186	0.019	698.8	3.89	0.31
478.8	0.269	0.026	748.8	4.71	0.37
498.8	0.604	0.052	798.8	5.41	0.42
518.8	0.650	0.055	848.8	5.88	0.46
538.8	0.908	0.074	898.8	6.20	0.49
558.8	1.35	0.11	948.8	6.29	0.49
578.8	1.80	0.15	998.8	6.55	0.51
<b>Sn<sup>11+</sup> → Sn<sup>13+</sup></b>					
498.8	0.0483	0.012	648.8	2.25	0.18
518.8	0.132	0.014	698.8	3.30	0.26
538.8	0.257	0.024	748.8	4.14	0.33
558.8	0.536	0.045	798.8	4.88	0.39
578.8	0.918	0.075	848.8	5.64	0.44
598.8	1.09	0.088	898.8	5.94	0.47
618.8	1.43	0.11	948.8	6.29	0.49
			998.8	6.48	0.51
<b>Sn<sup>12+</sup> → Sn<sup>14+</sup></b>					
538.9	0.0149	0.0040	698.9	1.66	0.13
558.9	0.0661	0.0089	748.9	2.54	0.20
578.9	0.166	0.015	798.9	3.36	0.26
598.9	0.256	0.022	848.9	4.03	0.31

**Table D.11**(continued)

Collision energy (eV)	Cross section ( $10^{-19}\text{cm}^2$ )	Total error	Collision energy (eV)	Cross section ( $10^{-19}\text{cm}^2$ )	Total error
623.9	0.409	0.038	898.9	4.58	0.36
648.9	0.837	0.067	948.9	5.00	0.39
673.9	1.15	0.092	998.9	5.37	0.42

## E Calculated lifetimes of excited states

This appendix contains results of the investigations of the lifetimes of excited states of the studied  $\text{Xe}^{q+}$  and  $\text{Sn}^{q+}$  ions performed using the Cowan code [110]. These are presented in Tab. E.1 and Tab. E.2 which contain columns with the investigated primary ions, electron configurations, excited states, excitation energies (in electronvolts) as well as the estimated lifetimes (in seconds). The last column contains separately estimated times (in seconds) which are required for certain ion species to pass from the ion source to the point of intersection with the electron beam in the interactions chamber.

For all of the listed excited states (except those marked with (\*)), corresponding evidences in the studied cross sections have been revealed. The excited states marked with (\*) are the states for which the evidences in the measured cross section are expected to be located below the investigated energy intervals.

For  $\text{Xe}^{17+}$ , the Cowan code failed to calculate a reasonable value of the lifetime of the  $4p^6 5s^2 S_{1/2}$  excited state, hence, no number is given. However, since the dipole decay of this state is allowed neither to the ground state, nor to any other lower excited state, we strongly believe its lifetime to be long enough to "survive" the passage from the ion source into the interaction chamber.

**Table E.1:** Calculated lifetimes of excited states of the studied xenon ions.

Primary ion	Configuration	Metastable state	Excitation energy (eV)	Life time (s)	Flight time (s)
$\text{Xe}^+$	$5s^2 5p^5$	$^2P_{1/2}$	1.26	5.36[-2]	3.17[-5]
		$^4F_{9/2}$	12.29	3.13	
		$^4F_{7/2}$	13.39	1.65	
$\text{Xe}^{2+}$	$5s^2 5p^4$	$^3P_0$	1.08	15.21	2.24[-5]
		$^3P_1$	1.12	6.5[-2]	
		$^1D_2$	1.51	4.3[-2]	
		$^1S_0$	4.95	4.4[-3]	
	$5s^2 5p^3 5d$	$^5D_4$	13.22	433.59	
		$^3G_4$	16.08	0.14	
		$^3G_5$	16.31	0.51	
$\text{Xe}^{3+}$	$5s^2 5p^3$	$^1G_4$	16.47	0.18	
		$^2D_{3/2}$	1.87	5.24[-2]	1.83[-5]

Table E.1(continued)

Primary ion	Configuration	Metastable state	Excitation energy (eV)	Life time (s)	Flight time (s)		
Xe <sup>4+</sup>	5s <sup>2</sup> 5p <sup>2</sup> 5d	<sup>2</sup> D <sub>5/2</sub>	2.37	0.44			
		<sup>2</sup> P <sub>1/2</sub>	3.94	1.54[-2]			
		<sup>2</sup> P <sub>3/2</sub>	4.71	6.4[-3]			
		<sup>4</sup> F <sub>9/2</sub>	17.77	0.46			
		<sup>2</sup> G <sub>9/2</sub>	20.36	2.1[-2]			
	5s <sup>2</sup> 5p <sup>2</sup>	<sup>3</sup> P <sub>1</sub>	1.00	0.11	1.59[-5]		
		<sup>3</sup> P <sub>2</sub>	1.70	0.50			
		<sup>1</sup> D <sub>2</sub>	3.61	1.86[-2]			
		<sup>1</sup> S <sub>0</sub>	6.09	3.3[-3]			
		<sup>3</sup> F <sub>4</sub>	20.76	8.7[-2]			
Xe <sup>5+</sup>	5s <sup>2</sup> 5p	<sup>2</sup> P <sub>3/2</sub>	2.31	3.45[-2]	1.42[-5]		
	5s5p5d	<sup>4</sup> F <sub>9/2</sub>	32.62	5.83[-2]			
Xe <sup>6+</sup>	5s5p	<sup>3</sup> P <sub>2</sub>	12.51	4.86[-2]	1.29[-5]		
Xe <sup>7+</sup>	4d <sup>10</sup> 4f	<sup>2</sup> F <sub>7/2</sub>	32.71	91.34	1.2[-5]		
	4d <sup>9</sup> 5s5p	<sup>4</sup> F <sub>9/2</sub>	67.84	3.13[-2]			
		<sup>4</sup> H <sub>11/2</sub>	83.06	1.08			
		<sup>4</sup> H <sub>9/2</sub>	83.43	0.39			
		<sup>4</sup> H <sub>7/2</sub>	84.13	0.14			
		<sup>2</sup> H <sub>11/2</sub>	84.46	0.94			
		<sup>4</sup> F <sub>9/2</sub>	84.57	1.51			
		<sup>2</sup> H <sub>9/2</sub>	85.00	3.55[-2]			
		<sup>4</sup> G <sub>11/2</sub>	85.39	5.08[-2]			
		<sup>2</sup> H <sub>9/2</sub>	86.03	2.52[-2]			
		<sup>4</sup> G <sub>9/2</sub>	86.31	1.05[-2]			
		<sup>4</sup> G <sub>11/2</sub>	86.51	1.15[-2]			
		<sup>2</sup> G <sub>9/2</sub>	87.38	8.8[-3]			
		<sup>2</sup> G <sub>9/2</sub>	88.04	6.8[-3]			
		Xe <sup>8+</sup>	4d <sup>9</sup> 5s	<sup>3</sup> D <sub>1</sub>	58.71	2.12[-2]	1.12[-5]
			4d <sup>9</sup> 4f	<sup>3</sup> H <sub>5</sub>	84.51	1.11[-3]	
				<sup>1</sup> H <sub>5</sub>	86.55	1.23[-3]	
		Xe <sup>9+</sup>	4d <sup>9</sup>	<sup>3</sup> G <sub>5</sub>	87.79	8.53[-4]	
			4d <sup>8</sup> 5s	<sup>2</sup> D <sub>3/2</sub>	1.99	1.5[-2]	1.06[-5]
<sup>4</sup> F <sub>9/2</sub>	62.15			1[-4]			
4d <sup>8</sup> 4f	<sup>4</sup> P <sub>1/2</sub>		66.72	2.90[-5]			
	<sup>4</sup> I <sub>13/2</sub>		85.51	5.52[-2]			
	<sup>4</sup> H <sub>13/2</sub>		86.07	3.53[-2]			
	<sup>2</sup> I <sub>13/2</sub>		87.80	3.52[-3]			
	<sup>2</sup> K <sub>13/2</sub>		89.45	7.17[-3]			
	<sup>2</sup> K <sub>15/2</sub>		89.54	6.07[-3]			
	<sup>2</sup> I <sub>13/2</sub>		93.56	2.62[-3]			

Table E.1(continued)

Primary ion	Configuration	Metastable state	Excitation energy (eV)	Life time (s)	Flight time (s)		
Xe <sup>10+</sup>	4d <sup>8</sup>	<sup>3</sup> F <sub>3</sub>	1.79	1.31[-2]	1[-5]		
		<sup>3</sup> F <sub>2</sub>	1.86	163.44			
		<sup>3</sup> P <sub>2</sub>	3.52	1.47[-2]			
		<sup>3</sup> P <sub>0</sub>	4.53	4.43			
		<sup>3</sup> P <sub>1</sub>	4.72	2.01[-2]			
		<sup>1</sup> G <sub>4</sub>	5.48	1.26[-2]			
		<sup>1</sup> D <sub>2</sub>	5.52	4.9[-3]			
		<sup>1</sup> S <sub>0</sub>	11.98	1[-3]			
	4d <sup>7</sup> 4f	<sup>5</sup> I <sub>8</sub>	87.63	2.43			
		<sup>3</sup> K <sub>8</sub>	91.02	4.23[-3]			
		<sup>3</sup> L <sub>9</sub>	91.75	5.76[-2]			
		<sup>1</sup> L <sub>8</sub>	91.97	2.23[-2]			
		<sup>3</sup> K <sub>8</sub>	93.71	4.98[-3]			
		<sup>3</sup> K <sub>8</sub>	94.25	3.52[-3]			
		Xe <sup>11+</sup>	4d <sup>7</sup>	<sup>4</sup> F <sub>7/2</sub>	1.61	1.45[-2]	9.6[-6]
				<sup>4</sup> F <sub>5/2</sub>	2.24	0.16	
<sup>4</sup> F <sub>3/2</sub>	2.53			1.89			
<sup>4</sup> P <sub>3/2</sub>	3.56			4[-2]			
<sup>4</sup> P <sub>5/2</sub>	4.01			3.08[-2]			
<sup>2</sup> G <sub>9/2</sub>	4.18			7.3[-3]			
<sup>4</sup> P <sub>1/2</sub>	4.80			2.05[-2]			
<sup>2</sup> G <sub>7/2</sub>	5.57			1.23[-2]			
<sup>2</sup> H <sub>11/2</sub>	5.60			0.11			
<sup>4</sup> P <sub>3/2</sub>	6.17			4[-3]			
<sup>2</sup> D <sub>5/2</sub>	6.47			2.6[-3]			
<sup>2</sup> P <sub>1/2</sub>	7.25			6.5[-3]			
<sup>2</sup> H <sub>9/2</sub>	7.33			6.8[-3]			
<sup>2</sup> F <sub>5/2</sub>	8.50			1.22[-2]			
<sup>2</sup> D <sub>3/2</sub>	8.88			2.8[-3]			
<sup>2</sup> F <sub>7/2</sub>	9.47			5.7[-3]			
4d <sup>6</sup> 4f	<sup>2</sup> D <sub>3/2</sub>	13.27	1.6[-3]				
	<sup>2</sup> D <sub>5/2</sub>	14.02	1.6[-3]				
	<sup>4</sup> L <sub>17/2</sub>	93.33	7.16[-2]				
	<sup>4</sup> K <sub>17/2</sub>	94.40	2.28[-2]				
	<sup>2</sup> L <sub>17/2</sub>	95.24	2.00[-2]				
	<sup>2</sup> M <sub>17/2</sub>	96.70	5.34[-3]				
	<sup>2</sup> M <sub>19/2</sub>	96.96	3.76[-3]				
	<sup>2</sup> L <sub>17/2</sub>	97.27	3.74[-3]				
Xe <sup>12+</sup>	4d <sup>6</sup>	<sup>2</sup> L <sub>17/2</sub>	98.75	3.02[-3]	9.2[-6]		
		<sup>5</sup> D <sub>3</sub>	1.17	3.58[-2]			

Table E.1(continued)

Primary ion	Configuration	Metastable state	Excitation energy (eV)	Life time (s)	Flight time (s)
		$^5D_2$	1.37	4.47	
		$^5D_1$	1.89	0.17	
		$^5D_0$	2.02	6.73	
		$^3H_4$	4.14	7.9[-3]	
		$^3H_6$	4.83	3655	
		$^3H_5$	4.88	0.12	
		$^3P_2$	4.98	2.7[-3]	
		$^3F_3$	5.76	6[-3]	
		$^3F_2$	6.02	9.7[-3]	
		$^3H_4$	6.35	4.4[-3]	
		$^1S_0$	7.02	2.5[-3]	
		$^3G_5$	7.07	1.07[-2]	
		$^3G_4$	7.33	1.26[-2]	
		$^3D_1$	7.36	3[-3]	
		$^3D_2$	7.76	1[-2]	
		$^3G_3$	7.85	7.4[-3]	
		$^3D_3$	8.12	[-3]	
		$^1I_6$	8.21	1[-2]	
		$^3D_1$	8.61	2.7[-3]	
		$^1G_4$	9.56	3.1[-3]	
		$^3P_0$	9.89	5.9[-3]	
		$^1F_3$	10.17	1.02[-2]	
		$^1D_2$	10.36	3[-3]	
		$^3P_1$	11.89	1.9[-3]	
		$^3F_4$	12.54	2.4[-3]	
		$^3P_0$	12.59	1[-3]	
		$^3F_2$	12.71	2.5[-3]	
		$^3F_3$	13.78	2.1[-3]	
		$^3P_2$	13.93	2.1[-3]	
		$^1G_4$	14.49	2[-3]	
		$^1D_2$	18.35	1.8[-3]	
		$^1S_0$	23.53	7[-4]	
	$4d^54f$	$^5K_9$	95.31	4.84[-2]	
		$^3M_9$	98.39	7.82[-3]	
		$^3M_{10}$	98.96	4.61[-2]	
		$^3L_9$	99.68	1.13[-2]	
		$^3L_9$	102.90	8.26[-4]	
Xe <sup>13+</sup>	$4d^5$	$^4G_{5/2}$	5.38	8[-3]	8.8[-6]
		$^4G_{7/2}$	6.24	9.54[-2]	
		$^4G_{11/2}$	6.42	1.62[9]	

Table E.1(continued)

Primary ion	Configuration	Metastable state	Excitation energy (eV)	Life time (s)	Flight time (s)
		$^4G_{5/2}$	6.57	4.5[-3]	
		$^4G_{9/2}$	6.60	1.09	
		$^4P_{3/2}$	6.64	3.9[-3]	
		$^4P_{1/2}$	7.29	0.14	
		$^4D_{7/2}$	7.95	1.67[-2]	
		$^4D_{5/2}$	8.60	4.5[-3]	
		$^4D_{1/2}$	8.85	1.07[-2]	
		$^2I_{11/2}$	9.09	1.59[-2]	
		$^4D_{3/2}$	9.14	4[-3]	
		$^2I_{13/2}$	9.79	0.12	
		$^4F_{7/2}$	10.03	2.13[-2]	
		$^4F_{3/2}$	10.18	4[-3]	
		$^2G_{9/2}$	10.21	1.31[-2]	
		$^4P_{5/2}$	10.33	1.8[-3]	
		$^4F_{5/2}$	11.31	4[-3]	
		$^2H_{9/2}$	11.60	3.3[-3]	
		$^2G_{7/2}$	12.00	4.8[-3]	
		$^2D_{3/2}$	12.36	4.3[-3]	
		$^2F_{7/2}$	12.58	3[-3]	
		$^2F_{5/2}$	12.67	3.5[-3]	
		$^2H_{11/2}$	13.19	2.1[-3]	
		$^2F_{7/2}$	13.45	5.1[-3]	
		$^2G_{9/2}$	13.56	5.3[-3]	
		$^2S_{1/2}$	14.09	2.6[-3]	
		$^2F_{5/2}$	14.53	1.5[-3]	
		$^2D_{3/2}$	15.63	1.8[-3]	
		$^2D_{5/2}$	16.47	1.6[-3]	
		$^2G_{9/2}$	17.25	3.4[-3]	
		$^2G_{7/2}$	17.63	2.4[-3]	
		$^2P_{3/2}$	20.20	2.7[-3]	
		$^2P_{1/2}$	20.97	1.7[-3]	
		$^2D_{5/2}$	22.62	1[-3]	
		$^2D_{3/2}$	23.14	1.1[-3]	
	$4d^44f$	$^4K_{17/2}$	100.41	3.4[-2]	
		$^4L_{17/2}$	102.94	2.23[-2]	
		$^4L_{19/2}$	103.26	3.04[-2]	
		$^4K_{17/2}$	104.90	9[-3]	
		$^2L_{17/2}$	105.42	5.6[-3]	
		$^2L_{17/2}$	106.52	3.9[-3]	
		$^2M_{19/2}$	107.07	3.1[-3]	

Table E.1(continued)

Primary ion	Configuration	Metastable state	Excitation energy (eV)	Life time (s)	Flight time (s)
Xe <sup>14+</sup>	4d <sup>4</sup>	<sup>2</sup> L <sub>17/2</sub>	107.54	3.2[-3]	
		<sup>5</sup> D <sub>1</sub>	0.81	7.96[-2]	8.5[-6]
		<sup>5</sup> D <sub>2</sub>	1.63	6.77[-2]	
		<sup>5</sup> D <sub>3</sub>	2.35	0.12	
		<sup>5</sup> D <sub>4</sub>	2.94	0.39	
		<sup>3</sup> P <sub>0</sub>	4.92	1.7[-3]	
		<sup>3</sup> H <sub>4</sub>	5.28	1.67[-2]	
		<sup>3</sup> G <sub>3</sub>	6.38	6.3[-3]	
		<sup>3</sup> H <sub>5</sub>	6.47	3.59[-2]	
		<sup>3</sup> P <sub>1</sub>	6.66	2.4[-3]	
		<sup>3</sup> F <sub>2</sub>	6.69	4.7[-3]	
		<sup>3</sup> H <sub>6</sub>	7.03	0.77	
		<sup>3</sup> G <sub>4</sub>	7.67	5.1[-3]	
		<sup>3</sup> P <sub>2</sub>	8.20	1.03[-2]	
		<sup>3</sup> G <sub>4</sub>	8.24	5.4[-3]	
		<sup>3</sup> F <sub>3</sub>	8.59	5.3[-3]	
		<sup>3</sup> D <sub>3</sub>	9.13	3[-3]	
		<sup>3</sup> G <sub>5</sub>	9.38	7.6[-3]	
		<sup>3</sup> D <sub>2</sub>	9.77	2.3[-3]	
		<sup>1</sup> I <sub>6</sub>	9.96	6.5[-3]	
		<sup>3</sup> D <sub>1</sub>	10.17	2[-3]	
		<sup>1</sup> G <sub>4</sub>	11.41	2.9[-3]	
		<sup>1</sup> S <sub>0</sub>	11.74	1.7[-3]	
		<sup>1</sup> D <sub>2</sub>	11.98	2.4[-3]	
		<sup>1</sup> F <sub>3</sub>	12.62	3[-3]	
		<sup>3</sup> P <sub>2</sub>	13.76	3[-3]	
		<sup>3</sup> F <sub>4</sub>	14.30	1.5[-3]	
		<sup>3</sup> F <sub>2</sub>	14.86	1.8[-3]	
		<sup>3</sup> F <sub>3</sub>	15.06	3.4[-3]	
		<sup>3</sup> P <sub>1</sub>	15.33	1.8[-3]	
		<sup>3</sup> P <sub>0</sub>	16.10	2.5[-3]	
		<sup>1</sup> G <sub>4</sub>	16.28	1.8[-3]	
		<sup>1</sup> D <sub>2</sub>	20.35	1.3[-3]	
<sup>1</sup> S <sub>0</sub>	25.73	6[-4]			
Xe <sup>15+</sup>	4d <sup>3</sup> 4f	<sup>3</sup> K <sub>8</sub>	102.40	4.1[-3]	
		<sup>3</sup> K <sub>8</sub>	104.40	3[-3]	
		<sup>3</sup> L <sub>8</sub>	106.63	3.5[-3]	
		<sup>3</sup> L <sub>9</sub>	106.63	6.2[-3]	
		<sup>1</sup> L <sub>8</sub>	108.30	2.3[-3]	
Xe <sup>15+</sup>	4d <sup>3</sup>	<sup>4</sup> F <sub>5/2</sub>	1.31	2.19[-2]	8.2[-6]

Table E.1(continued)

Primary ion	Configuration	Metastable state	Excitation energy (eV)	Life time (s)	Flight time (s)		
Xe <sup>16+</sup>	4d <sup>2</sup> 4f	<sup>4</sup> F <sub>7/2</sub>	2.48	3.08[-2]			
		<sup>4</sup> F <sub>9/2</sub>	3.38	0.12			
		<sup>4</sup> P <sub>3/2</sub>	3.93	1.05[-2]			
		<sup>4</sup> P <sub>1/2</sub>	4.43	5.91[-2]			
		<sup>2</sup> G <sub>7/2</sub>	5.66	4.5[-3]			
		<sup>2</sup> H <sub>9/2</sub>	5.82	6.6[-3]			
		<sup>4</sup> P <sub>5/2</sub>	6.11	1.4[-2]			
		<sup>4</sup> P <sub>3/2</sub>	6.98	2[-3]			
		<sup>2</sup> P <sub>1/2</sub>	7.41	4.6[-3]			
		<sup>2</sup> H <sub>11/2</sub>	7.90	1.49[-2]			
		<sup>2</sup> D <sub>5/2</sub>	8.68	3.2[-3]			
		<sup>2</sup> G <sub>9/2</sub>	8.83	2.8[-3]			
		<sup>2</sup> P <sub>3/2</sub>	10.01	2[-3]			
		<sup>2</sup> F <sub>5/2</sub>	10.46	6.8[-3]			
		<sup>2</sup> F <sub>7/2</sub>	10.54	5.9[-3]			
		<sup>2</sup> D <sub>3/2</sub>	15.73	1.5[-3]			
		<sup>2</sup> D <sub>5/2</sub>	15.80	9[-4]			
		<sup>4</sup> I <sub>15/2</sub>	101.33	1.83[-2]			
		<sup>2</sup> K <sub>15/2</sub>	107.97	4.2[-3]			
		Xe <sup>17+</sup>	4d <sup>2</sup>	<sup>3</sup> F <sub>3</sub>	2.10	8.9[-3]	7.9[-6]
<sup>3</sup> F <sub>4</sub>	3.85			1.92[-2]			
<sup>3</sup> P <sub>0</sub>	4.11			1.02			
<sup>1</sup> D <sub>2</sub>	4.74			7.4[-3]			
<sup>3</sup> P <sub>1</sub>	5.34			3.68[-2]			
<sup>1</sup> G <sub>4</sub>	7.38			4.4[-3]			
<sup>3</sup> P <sub>2</sub>	7.68			3.5[-3]			
<sup>1</sup> S <sub>0</sub>	14.43			7[-4]			
<sup>3</sup> H <sub>6</sub>	102.49			2.21[-2]			
<sup>2</sup> D <sub>5/2</sub>	2.73			8.6[-3]	7.7[-6]		
<sup>4</sup> G <sub>9/2</sub>	83.00			5.75[-2]			
<sup>4</sup> G <sub>11/2</sub>	83.84			0.16			
<sup>4</sup> F <sub>9/2</sub>	87.60			2.1[-3]			
Xe <sup>18+</sup>	4p <sup>6</sup> 5s	<sup>2</sup> H <sub>11/2</sub>	88.33	5.6[-3]			
		<sup>2</sup> G <sub>9/2</sub>	91.59	2.8[-3]			
		<sup>2</sup> G <sub>9/2</sub>	101.62	3.1[-5]			
		<sup>2</sup> H <sub>9/2</sub>	105.88	2.8[-5]			
		<sup>2</sup> S <sub>1/2</sub>	130.62	—			
		<sup>3</sup> F <sub>3</sub>	84.15	2.87[-2]	7.5[-6]		
		<sup>3</sup> P <sub>2</sub>	84.20	5.6[-3]			
		<sup>3</sup> F <sub>4</sub>	85.00	0.22			
		Xe <sup>18+</sup>	4p <sup>5</sup> 4d	<sup>3</sup> F <sub>3</sub>	84.15	2.87[-2]	7.5[-6]
				<sup>3</sup> P <sub>2</sub>	84.20	5.6[-3]	

Table E.1(continued)

Primary ion	Configuration	Metastable state	Excitation energy (eV)	Life time (s)	Flight time (s)	
Xe <sup>19+</sup>	4p <sup>5</sup> 4p <sup>4</sup> 4d	<sup>1</sup> D <sub>2</sub>	86.47	5.4[-3]	7.2[-6]	
		<sup>3</sup> D <sub>3</sub>	89.79	1.5[-3]		
		<sup>2</sup> P <sub>1/2</sub>	15.45	2.83[-5]		
		<sup>4</sup> D <sub>7/2</sub>	81.84	3.53[-2]		
		<sup>4</sup> F <sub>9/2</sub>	85.01	1.1[-2]		
		<sup>2</sup> F <sub>7/2</sub>	85.35	1.53[-2]		
		<sup>4</sup> F <sub>7/2</sub>	98.47	4.07[-5]		
		<sup>2</sup> G <sub>7/2</sub>	100.05	5.33[-5]		
Xe <sup>20+</sup>	4p <sup>4</sup>	<sup>2</sup> F <sub>7/2</sub>	107.20	3.58[-5]	7.1[-6]	
		<sup>3</sup> P <sub>0</sub>	5.34	0.34		
		<sup>3</sup> P <sub>1</sub>	14.60	3.07[-5]		
	4p <sup>3</sup> 4d	<sup>1</sup> D <sub>2</sub>	17.89	4.59[-5]		
		<sup>5</sup> D <sub>4</sub>	86.21	8.7[-3]		
		<sup>3</sup> G <sub>4</sub>	99.46	5.77[-5]		
		<sup>3</sup> F <sub>4</sub>	100.97	1[-4]		
		<sup>1</sup> G <sub>4</sub>	102.91	3[-4]		
	4s4p <sup>4</sup> 4d	<sup>3</sup> G <sub>5</sub>	103.68	2[-4]		
		<sup>5</sup> D <sub>4</sub> (*)	146.58	2.93[-5]		
<sup>5</sup> F <sub>5</sub> (*)		149.93	5.7[3]			
<sup>3</sup> G <sub>5</sub> (*)		173.11	3.81[-5]			
Xe <sup>21+</sup>		4p <sup>3</sup>	<sup>2</sup> D <sub>3/2</sub>	14.83	3.92[-5]	6.9[-6]
			<sup>2</sup> D <sub>5/2</sub>	18.29	2[-4]	
			<sup>2</sup> P <sub>1/2</sub>	22.89	3.07[-5]	
		4p <sup>2</sup> 4d	<sup>2</sup> P <sub>3/2</sub>	35.98	1.16[-5]	
	<sup>4</sup> F <sub>9/2</sub>		105.30	1.7[3]		
	<sup>2</sup> D <sub>3/2</sub>		122.57	2.51[-5]		
	4s4p <sup>3</sup> 4d		<sup>6</sup> D <sub>9/2</sub> (*)	146.42	1.98[-4]	
		<sup>4</sup> G <sub>9/2</sub> (*)	164.77	1.78[-5]		
		<sup>4</sup> G <sub>11/2</sub> (*)	169.67	1[-4]		
		<sup>2</sup> G <sub>9/2</sub> (*)	628.72	3.58[-5]		
<sup>6</sup> G <sub>13/2</sub> (*)		693.50	1.35[-2]			
<sup>6</sup> G <sub>13/2</sub> (*)		707.77	2.16[-5]			
<sup>4</sup> H <sub>13/2</sub> (*)		710.06	9.37[-5]			
3d <sup>9</sup> 4s <sup>2</sup> 4p <sup>4</sup> 3d <sup>9</sup> 4s <sup>2</sup> 4p <sup>3</sup> 4d	<sup>2</sup> I <sub>13/2</sub> (*)	712.24	7.74[-5]			
	<sup>4</sup> I <sub>17/2</sub> (*)	712.59	7.67[-5]			
	<sup>4</sup> H <sub>13/2</sub> (*)	714.96	7.78[-5]			
	<sup>4</sup> I <sub>13/2</sub> (*)	726.54	1.56[-5]			
	Xe <sup>22+</sup>	4p <sup>2</sup>	<sup>3</sup> P <sub>1</sub>	13.60	5.3[-5]	6.7[-6]
			<sup>1</sup> D <sub>2</sub>	16.38	4.66[-3]	

Table E.1(continued)

Primary ion	Configuration	Metastable state	Excitation energy (eV)	Life time (s)	Flight time (s)		
Xe <sup>23+</sup>	4s <sup>2</sup> 4p4d	<sup>3</sup> F <sub>4</sub> (*)	119.18	6.21[-5]			
	4s4p <sup>2</sup> 4d	<sup>5</sup> F <sub>5</sub> (*)	163.62	3.14[-4]			
	3d <sup>9</sup> 4s <sup>2</sup> 4p <sup>3</sup>		<sup>3</sup> G <sub>5</sub> (*)	183.19	1.26[-5]		
			<sup>5</sup> D <sub>4</sub> (*)	629.23	3.58[-5]		
			<sup>3</sup> F <sub>4</sub> (*)	633.29	1.50[-4]		
			<sup>3</sup> G <sub>5</sub> (*)	633.47	1.42[-4]		
			<sup>3</sup> G <sub>4</sub> (*)	646.71	3.59[-5]		
			<sup>3</sup> F <sub>4</sub> (*)	652.77	1.05[-5]		
	3d <sup>9</sup> 4s <sup>2</sup> 4p <sup>2</sup> 4d		<sup>5</sup> H <sub>7</sub> (*)	719.04	9.69[-5]		
			<sup>3</sup> I <sub>7</sub> (*)	735.27	1.22[-5]		
	Xe <sup>23+</sup>	4s <sup>2</sup> 4p	<sup>2</sup> P <sub>3/2</sub>	17.09	4.18[-5]	6.6[-6]	
		4s4p4d	<sup>4</sup> F <sub>9/2</sub> (*)	163.92	2.64[-5]		
		3d <sup>9</sup> 4s <sup>2</sup> 4p <sup>2</sup>		<sup>4</sup> D <sub>7/2</sub> (*)	623.38	5.72[-5]	
				<sup>2</sup> G <sub>9/2</sub> (*)	626.84	3.87[-3]	
			<sup>2</sup> F <sub>7/2</sub> (*)	628.62	2.85[-4]		
			<sup>2</sup> G <sub>7/2</sub> (*)	640.19	3.98[-5]		
			<sup>4</sup> F <sub>9/2</sub> (*)	643.54	1.99[-5]		
			<sup>2</sup> F <sub>7/2</sub> (*)	644.50	2.26[-5]		
			<sup>2</sup> G <sub>7/2</sub> (*)	657.52	1.28[-5]		
			<sup>4</sup> H <sub>13/2</sub> (*)	728.79	3.16[-5]		
Xe <sup>24+</sup>	3d <sup>9</sup> 4s <sup>2</sup> 4p4d	<sup>3</sup> P <sub>1</sub>	47.67	3.63[-3]			
	3d <sup>9</sup> 4s <sup>2</sup> 4p		<sup>3</sup> F <sub>3</sub> (*)	619.27	1.639	6.5[-6]	
			<sup>3</sup> F <sub>2</sub> (*)	631.87	4.59[-5]		
			<sup>3</sup> F <sub>4</sub> (*)	635.98	4.11[-5]		
			<sup>1</sup> D <sub>2</sub> (*)	637.48	4.61[-5]		
			<sup>3</sup> D <sub>3</sub> (*)	638.86	3.08[-5]		
			<sup>3</sup> P <sub>0</sub> (*)	647.38	2.56[-5]		
			<sup>3</sup> F <sub>3</sub> (*)	650.17	1.94[-5]		
			<sup>3</sup> D <sub>2</sub> (*)	651.77	2.04[-5]		
			<sup>4</sup> F <sub>9/2</sub> (*)	644.03	2.68[-5]	6.3[-6]	
Xe <sup>25+</sup>	3d <sup>9</sup> 4s4p	<sup>4</sup> F <sub>9/2</sub> (*)	644.03	2.68[-5]	6.3[-6]		

**Table E.2:** Calculated lifetimes of excited states of the studied tin ions.

Primary ion	Configuration	Metastable state	Excitation energy (eV)	Life time (s)	Flight time (s)
Sn <sup>+</sup>	5s <sup>2</sup> 5p	<sup>2</sup> P <sub>3/2</sub>	0.16	1.78	3.02[-5]
Sn <sup>2+</sup>	5s5p	<sup>3</sup> P <sub>2</sub>	6.00	1.97	2.14[-5]
Sn <sup>3+</sup>	4d <sup>9</sup> 5s <sup>2</sup>	<sup>2</sup> D <sub>5/2</sub>	21.57	1.17[-4]	1.75[-5]
		<sup>2</sup> D <sub>3/2</sub>	22.58	9.34[-5]	
	4d <sup>9</sup> 5s5p	<sup>4</sup> F <sub>9/2</sub>	28.31	4.00	
Sn <sup>4+</sup>	4d <sup>9</sup> 5s	<sup>3</sup> D <sub>2</sub>	23.18	1.76[-4]	1.51[-5]
		<sup>3</sup> D <sub>1</sub>	23.88	0.19	
		<sup>1</sup> D <sub>2</sub>	24.34	4.62[-5]	
Sn <sup>5+</sup>	4d <sup>9</sup>	<sup>2</sup> D <sub>3/2</sub>	0.62	0.11	1.35[-5]
	4d <sup>8</sup> 5s	<sup>4</sup> F <sub>9/2</sub>	26.57	5.15[-3]	
		<sup>4</sup> F <sub>7/2</sub>	27.08	1.01[-4]	
		<sup>4</sup> F <sub>5/2</sub>	27.63	4.74[-4]	
		<sup>4</sup> F <sub>3/2</sub>	27.86	2.85[-4]	
		<sup>2</sup> F <sub>7/2</sub>	28.17	1.53[-5]	
		<sup>2</sup> F <sub>5/2</sub>	28.65	2.11[-5]	
		<sup>4</sup> P <sub>5/2</sub>	29.28	3.10[-5]	
		<sup>4</sup> P <sub>3/2</sub>	29.46	4.16[-5]	
		<sup>4</sup> P <sub>1/2</sub>	29.86	1.52[-3]	
		<sup>4</sup> P <sub>3/2</sub>	30.03	4.73[-5]	
		<sup>2</sup> D <sub>5/2</sub>	30.44	3.04[-5]	
		<sup>2</sup> D <sub>9/2</sub>	30.90	2.47[-5]	
		<sup>2</sup> D <sub>7/2</sub>	30.91	2.79[-5]	
Sn <sup>6+</sup>	4d <sup>8</sup>	<sup>3</sup> F <sub>3</sub>	0.87	9.34[-2]	1.23[-5]
		<sup>3</sup> F <sub>2</sub>	1.18	2.3	
		<sup>3</sup> P <sub>2</sub>	2.38	6.16[-2]	
		<sup>3</sup> P <sub>1</sub>	3.26	0.13	
		<sup>3</sup> P <sub>0</sub>	3.27	8.21	
		<sup>1</sup> D <sub>2</sub>	3.54	3.08[-2]	
		<sup>1</sup> G <sub>4</sub>	3.92	5.78[-2]	
		<sup>1</sup> S <sub>0</sub>	8.96	4.07[-3]	
	4d <sup>7</sup> 5s	<sup>5</sup> F <sub>5</sub>	32.60	5.67[-4]	
		<sup>5</sup> F <sub>4</sub>	33.18	9.40[-5]	
		<sup>5</sup> F <sub>3</sub>	33.64	2.67[-4]	
		<sup>5</sup> F <sub>2</sub>	33.93	3.41[-4]	
		<sup>5</sup> F <sub>1</sub>	34.10	3.25[-4]	
		<sup>5</sup> P <sub>3</sub>	35.55	7.26[-5]	
		<sup>5</sup> P <sub>1</sub>	35.88	5.79[-5]	
		<sup>3</sup> G <sub>5</sub>	36.08	1.40[-5]	
		<sup>3</sup> G <sub>3</sub>	36.84	1.44[-5]	

Table E.2(continued)

Primary ion	Configuration	Metastable state	Excitation energy (eV)	Life time (s)	Flight time (s)	
Sn <sup>7+</sup>	4d <sup>7</sup> 4f	<sup>5</sup> I <sub>8</sub>	60.97	8.21		
		<sup>3</sup> K <sub>8</sub>	63.58	1.67[-2]		
		<sup>3</sup> L <sub>9</sub>	64.18	0.31		
		<sup>3</sup> L <sub>8</sub>	64.34	0.13		
		<sup>1</sup> L <sub>8</sub>	65.25	1.79[-3]		
		<sup>3</sup> K <sub>8</sub>	65.63	3.35[-4]		
	4d <sup>7</sup>	<sup>4</sup> F <sub>7/2</sub>	0.81	0.11	1.14[-5]	
		<sup>4</sup> F <sub>5/2</sub>	1.25	0.42		
		<sup>4</sup> F <sub>3/2</sub>	1.51	1.87		
		<sup>4</sup> P <sub>3/2</sub>	2.78	0.27		
		<sup>4</sup> P <sub>7/2</sub>	2.96	0.24		
		<sup>2</sup> G <sub>9/2</sub>	3.09	3.26[-2]		
		<sup>4</sup> P <sub>1/2</sub>	3.43	0.18		
		<sup>2</sup> G <sub>7/2</sub>	3.86	5.27[-2]		
		<sup>2</sup> H <sub>11/2</sub>	4.13	0.51		
		<sup>4</sup> P <sub>3/2</sub>	4.26	2.01[-2]		
		<sup>2</sup> D <sub>5/2</sub>	4.61	1.28[-2]		
		<sup>2</sup> P <sub>1/2</sub>	4.94	3.77[-2]		
		<sup>2</sup> H <sub>9/2</sub>	4.99	4.02[-2]		
		<sup>2</sup> D <sub>3/2</sub>	5.95	1.18[-2]		
		<sup>2</sup> F <sub>5/2</sub>	6.57	5.14[-2]		
		<sup>2</sup> F <sub>7/2</sub>	7.01	2.78[-2]		
		<sup>2</sup> D <sub>3/2</sub>	10.23	7[-3]		
		<sup>2</sup> D <sub>5/2</sub>	10.62	5.7[-3]		
		4d <sup>6</sup> 5s	<sup>6</sup> D <sub>9/2</sub>	38.65	3.14[-4]	
			<sup>6</sup> D <sub>7/2</sub>	39.14	1.85[-4]	
			<sup>6</sup> D <sub>5/2</sub>	39.42	2.11[-4]	
<sup>6</sup> D <sub>3/2</sub>	39.61		2.03[-4]			
<sup>6</sup> D <sub>1/2</sub>	39.73		2.34[-4]			
4d <sup>6</sup> 4f	<sup>4</sup> L <sub>17/2</sub>		67.55	6.88[-4]		
	<sup>4</sup> L <sub>19/2</sub>	67.64	8.68[-4]			
	<sup>4</sup> K <sub>17/2</sub>	68.16	7.27[-4]			
	<sup>2</sup> L <sub>17/2</sub>	68.81	5.28[-4]			
	<sup>4</sup> K <sub>17/2</sub>	69.84	5.48[-4]			
	<sup>2</sup> M <sub>19/2</sub>	69.96	8.26[-4]			
	<sup>2</sup> M <sub>17/2</sub>	70.08	5.26[-4]			
	<sup>2</sup> L <sub>17/2</sub>	71.19	4.94[-4]			
	Sn <sup>8+</sup>	4d <sup>6</sup>	<sup>5</sup> D <sub>3</sub>	0.59	0.28	1.06[-5]
			<sup>5</sup> D <sub>2</sub>	0.83	2.30	
<sup>5</sup> D <sub>1</sub>			1.04	2.11		

Table E.2(continued)

Primary ion	Configuration	Metastable state	Excitation energy (eV)	Life time (s)	Flight time (s)
		$^5D_0$	1.13	17.9	
		$^3H_4$	3.51	3.75[-2]	
		$^3H_6$	3.75	3.39[3]	
		$^3H_5$	3.82	1.42	
		$^3P_2$	3.84	1.22[-2]	
		$^3F_3$	4.41	2.49[-2]	
		$^3H_4$	4.57	2.12[-2]	
		$^3F_2$	4.62	4.56[-2]	
		$^3G_5$	5.09	6.25[-2]	
		$^3P_0$	5.30	1.12[-2]	
		$^3P_1$	5.35	9.13[-3]	
		$^3G_4$	5.41	6.19[-2]	
		$^3G_3$	5.61	3.90[-2]	
		$^3D_2$	5.98	3.81[-2]	
		$^1I_6$	6.05	4.86[-2]	
		$^3D_3$	6.16	1.81[-2]	
		$^3D_1$	6.22	2.01[-2]	
		$^1G_4$	6.81	1.29[-2]	
		$^3P_0$	7.67	9.82[-3]	
		$^1D_2$	7.75	1.24[-2]	
		$^1F_3$	8.13	4.21[-2]	
		$^3P_0$	9.22	5.84[-3]	
		$^3P_1$	9.41	8.74[-3]	
		$^3F_4$	9.76	9.74[-3]	
		$^3F_2$	9.83	1.03[-2]	
		$^3F_3$	10.26	9.17[-3]	
		$^3P_2$	10.47	9.61[-3]	
		$^1G_4$	11.18	8.45[-3]	
		$^1D_2$	14.52	5.26[-3]	
		$^1S_0$	18.72	2.39[-3]	
	$4d^5 5s$	$^7S_3$	43.27	3[-4]	
	$4d^5 4f$	$^5K_9$	70.61	0.287	
		$^3M_9$	73.10	4.66[-2]	
		$^3M_{10}$	73.36	0.45	
		$^3L_9$	73.83	5.45[-2]	
		$^1M_9$	74.54	2.75[-2]	
		$^3L_9$	76.06	3.54[-3]	
$Sn^{9+}$	$4d^5$	$^4G_{5/2}$	4.97	7.13[-2]	1.01[-5]
		$^4G_{7/2}$	5.24	2.38	
		$^4G_{11/2}$	5.30	2.53[11]	

Table E.2(continued)

Primary ion	Configuration	Metastable state	Excitation energy (eV)	Life time (s)	Flight time (s)
		$^4G_{9/2}$	5.36	20.2	
		$^4P_{5/2}$	5.53	1.29[-2]	
		$^4P_{3/2}$	5.72	1.54[-2]	
		$^4P_{1/2}$	6.05	0.10	
		$^4D_{7/2}$	6.47	9.67[-2]	
		$^4D_{1/2}$	6.93	6.61[-2]	
		$^4D_{5/2}$	6.97	1.75[-2]	
		$^4D_{3/2}$	7.12	1.80[-2]	
		$^2I_{11/2}$	7.47	9.38[-2]	
		$^2I_{13/2}$	7.82	1.09	
		$^2F_{5/2}$	8.24	6.93[-3]	
		$^4F_{3/2}$	8.39	1.84[-2]	
		$^4F_{7/2}$	8.48	7.74[-2]	
		$^4F_{9/2}$	8.52	4.89[-2]	
		$^4F_{5/2}$	9.00	2.95[-2]	
		$^2H_{9/2}$	9.34	1.52[-2]	
		$^2F_{7/2}$	9.42	1.07[-2]	
		$^4F_{3/2}$	9.60	1.83[-2]	
		$^2G_{7/2}$	9.90	3.08[-2]	
		$^2H_{11/2}$	10.13	8.97[-3]	
		$^2F_{5/2}$	10.15	1.46[-2]	
		$^2G_{9/2}$	10.49	2.53[-2]	
		$^2F_{7/2}$	10.63	2.75[-2]	
		$^2F_{5/2}$	10.88	7.85[-3]	
		$^2S_{1/2}$	11.40	1.10[-2]	
		$^2D_{3/2}$	12.66	7.85[-3]	
		$^2D_{5/2}$	13.00	6.27[-3]	
		$^2G_{9/2}$	13.93	1.20[-2]	
		$^2G_{7/2}$	14.08	8.92[-3]	
		$^2P_{3/2}$	16.62	7.32[-3]	
		$^2P_{1/2}$	16.93	5.27[-3]	
		$^2D_{5/2}$	18.34	3.79[-3]	
		$^2D_{3/2}$	18.56	3.74[-3]	
	$4d^44f$	$^4K_{17/2}$	76.29	0.16	
		$^4L_{17/2}$	78.29	8.56[-2]	
		$^4L_{19/2}$	78.49	8.88[-2]	
		$^4K_{17/2}$	79.90	2.10[-2]	
		$^2L_{17/2}$	80.24	1.79[-2]	
		$^2L_{17/2}$	80.85	1.32[-2]	
		$^2M_{19/2}$	81.33	9.76[-3]	

Table E.2(continued)

Primary ion	Configuration	Metastable state	Excitation energy (eV)	Life time (s)	Flight time (s)
Sn <sup>10+</sup>	4d <sup>4</sup>	<sup>2</sup> M <sub>17/2</sub>	81.55	1.07[-2]	
		<sup>5</sup> D <sub>1</sub>	0.31	1.27	9.5[-6]
		<sup>5</sup> D <sub>2</sub>	0.71	0.54	
		<sup>5</sup> D <sub>3</sub>	1.13	0.58	
		<sup>5</sup> D <sub>4</sub>	1.55	1.05	
		<sup>3</sup> P <sub>0</sub>	3.71	6.88[-3]	
		<sup>3</sup> H <sub>4</sub>	3.98	8.72[-2]	
		<sup>3</sup> H <sub>5</sub>	4.59	0.31	
		<sup>3</sup> P <sub>1</sub>	4.74	8.91[-3]	
		<sup>3</sup> G <sub>3</sub>	4.76	2.46[-2]	
		<sup>3</sup> H <sub>6</sub>	4.95	2.52	
		<sup>3</sup> F <sub>2</sub>	4.96	2.20[-2]	
		<sup>3</sup> F <sub>4</sub>	5.32	1.61[-2]	
		<sup>3</sup> P <sub>2</sub>	5.86	2.31[-2]	
		<sup>3</sup> G <sub>4</sub>	5.89	3.61[-2]	
		<sup>3</sup> F <sub>3</sub>	5.99	1.94[-2]	
		<sup>3</sup> G <sub>5</sub>	6.40	4.23[-2]	
	<sup>3</sup> D - 3	6.75	1.61[-2]		
	<sup>1</sup> I <sub>6</sub>	6.98	3.17[-2]		
	<sup>3</sup> D <sub>2</sub>	7.01	1.11[-2]		
	<sup>3</sup> D <sub>1</sub>	7.26	1.01[-2]		
	<sup>1</sup> G <sub>4</sub>	7.90	9.77[-3]		
	<sup>1</sup> S <sub>0</sub>	8.42	6.66[-3]		
	<sup>1</sup> D <sub>2</sub>	8.72	9.39[-3]		
	<sup>1</sup> F <sub>3</sub>	9.36	1.33[-2]		
	<sup>3</sup> P <sub>2</sub>	10.51	1.10[-2]		
	<sup>3</sup> F <sub>4</sub>	10.76	6.92[-3]		
	<sup>3</sup> F <sub>2</sub>	11.01	7.18[-3]		
	<sup>3</sup> F <sub>3</sub>	11.18	1.20[-2]		
	<sup>3</sup> P <sub>1</sub>	11.43	7.25[-3]		
	<sup>3</sup> P <sub>0</sub>	11.91	9.21[-3]		
	<sup>1</sup> G <sub>4</sub>	12.30	6.93[-3]		
	<sup>1</sup> D <sub>2</sub>	15.81	4.05[-3]		
	<sup>1</sup> S <sub>0</sub>	20.23	1.91[-3]		
4d <sup>3</sup> 4f	<sup>5</sup> I <sub>8</sub>	75.00	0.17		
	<sup>3</sup> K <sub>8</sub>	78.01	1.78[-2]		
	<sup>3</sup> K <sub>8</sub>	79.91	1.09[-2]		
	<sup>3</sup> L <sub>8</sub>	81.35	1.77[-2]		
	<sup>3</sup> L <sub>9</sub>	81.42	2.99[-2]		
	<sup>1</sup> L <sub>8</sub>	82.74	1.14[-2]		

Table E.2(continued)

Primary ion	Configuration	Metastable state	Excitation energy (eV)	Life time (s)	Flight time (s)			
Sn <sup>11+</sup>	4d <sup>3</sup>	<sup>4</sup> F <sub>5/2</sub>	0.65	0.17	9.1[-6]			
		<sup>4</sup> F <sub>7/2</sub>	1.33	0.15				
		<sup>4</sup> F <sub>9/2</sub>	1.97	0.3				
		<sup>4</sup> P <sub>3/2</sub>	3.11	5.84[-2]				
		<sup>4</sup> P <sub>1/2</sub>	3.33	0.49				
		<sup>2</sup> G <sub>7/2</sub>	3.99	2.18[-2]				
		<sup>2</sup> H <sub>9/2</sub>	4.14	2.60[-2]				
		<sup>4</sup> P <sub>5/2</sub>	4.25	8.59[-2]				
		<sup>2</sup> D <sub>3/2</sub>	4.95	8.41[-3]				
		<sup>2</sup> P <sub>1/2</sub>	5.23	2.32[-2]				
		<sup>2</sup> H <sub>11/2</sub>	5.58	7.56[-2]				
		<sup>2</sup> G <sub>9/2</sub>	5.89	1.50[-2]				
		<sup>2</sup> D <sub>5/2</sub>	6.13	1.16[-2]				
		<sup>2</sup> P <sub>3/2</sub>	6.78	8.72[-3]				
		<sup>2</sup> F <sub>7/2</sub>	7.92	2.24[-2]				
		<sup>2</sup> F <sub>5/2</sub>	7.99	2.87[-2]				
		<sup>2</sup> D <sub>5/2</sub>	12.03	3.38[-3]				
		<sup>2</sup> D <sub>3/2</sub>	12.12	4.76[-3]				
		Sn <sup>12+</sup>	4d <sup>2</sup>	<sup>4</sup> I <sub>15/2</sub>		77.98	4.71[-2]	8.7[-6]
				<sup>2</sup> K <sub>15/2</sub>		83.68	8.53[-3]	
<sup>3</sup> F <sub>3</sub>	1.13			5.48[-2]				
<sup>3</sup> F <sub>4</sub>	2.20			7.89[-2]				
<sup>3</sup> P <sub>0</sub>	3.27			1.70				
<sup>1</sup> D <sub>2</sub>	3.42			2.82[-2]				
<sup>3</sup> P <sub>1</sub>	3.86			0.24				
<sup>3</sup> P <sub>2</sub>	5.14			1.73[-2]				
<sup>1</sup> G <sub>4</sub>	5.27			2.02[-2]				
<sup>1</sup> S <sub>0</sub>	11.08			2.20[-3]				
Sn <sup>13+</sup>	4d4f 4d 4p <sup>6</sup> 4d <sup>2</sup>	<sup>3</sup> H <sub>6</sub>	79.92	6.9[-2]	8.4[-6]			
		<sup>2</sup> D <sub>5/2</sub>	1.56	4.60[-2]				
		<sup>4</sup> G <sub>9/2</sub>	67.56	0.16				
		<sup>4</sup> G <sub>11/2</sub>	67.88	2.54				
		<sup>4</sup> F <sub>9/2</sub>	70.91	4.88[-3]				
		<sup>2</sup> H <sub>11/2</sub>	71.86	2.28[-2]				
		<sup>2</sup> H <sub>9/2</sub>	74.57	6.99[-3]				
		<sup>2</sup> G <sub>9/2</sub>	79.83	1.27[-4]				
		<sup>2</sup> G <sub>9/2</sub>	83.31	1.20[-4]				



## F Ionization energies

There are threshold energies for ground-state single- and multiple ionization of the studied xenon and tin ions presented in this appendix. Tables F.1 through F.5 contain the values for  $\text{Xe}^{q+}$  ions calculated using the LANL Atomic Physics Code package [111] as well as the values available from the NIST Atomic Spectra Database [112]. In Tab. F.6 and Tab. F.7 the threshold energies for single- and double ionization of  $\text{Sn}^{q+}$  ions calculated using the LANL Atomic Physics Code package [111] are tabulated. Experimental values of these are unknown.

**Table F.1:** Threshold energies for ground-state single ionization of the studied  $\text{Xe}^{q+}$  ions.

Primary ion	LANL code (eV)	NIST ASD (eV)	Primary ion	LANL code (eV)	NIST ASD (eV)
$\text{Xe}^+$	21.73	20.98	$\text{Xe}^{13+}$	313.51	–
$\text{Xe}^{2+}$	31.72	31.05	$\text{Xe}^{14+}$	342.37	–
$\text{Xe}^{3+}$	42.36	40.91	$\text{Xe}^{15+}$	371.97	–
$\text{Xe}^{4+}$	53.58	54.14	$\text{Xe}^{16+}$	402.23	–
$\text{Xe}^{5+}$	65.33	66.70	$\text{Xe}^{17+}$	433.2	–
$\text{Xe}^{6+}$	90.56	91.60	$\text{Xe}^{18+}$	556.27	–
$\text{Xe}^{7+}$	105.09	105.98	$\text{Xe}^{19+}$	589.18	–
$\text{Xe}^{8+}$	179.26	179.84	$\text{Xe}^{20+}$	622.59	–
$\text{Xe}^{9+}$	205.23	201.72	$\text{Xe}^{21+}$	656.49	–
$\text{Xe}^{10+}$	231.18	229.02	$\text{Xe}^{22+}$	690.88	–
$\text{Xe}^{11+}$	257.87	–	$\text{Xe}^{23+}$	725.75	–
$\text{Xe}^{12+}$	285.32	–	$\text{Xe}^{24+}$	819.22	–
			$\text{Xe}^{25+}$	857.42	857

**Table F.2:** Threshold energies for ground-state double ionization of the studied  $\text{Xe}^{q+}$  ions.

Primary ion	LANL code (eV)	NIST ASD (eV)	Primary ion	LANL code (eV)	NIST ASD (eV)
$\text{Xe}^+$	53.45	52.03	$\text{Xe}^{9+}$	436.46	430.74
$\text{Xe}^{2+}$	74.08	71.36	$\text{Xe}^{10+}$	489.05	–
$\text{Xe}^{3+}$	95.94	95.05	$\text{Xe}^{11+}$	543.19	–
$\text{Xe}^{4+}$	118.91	120.84	$\text{Xe}^{12+}$	598.83	–
$\text{Xe}^{5+}$	155.89	158.3	$\text{Xe}^{13+}$	655.88	–
$\text{Xe}^{6+}$	195.65	198.58	$\text{Xe}^{14+}$	714.34	–
$\text{Xe}^{7+}$	284.35	285.82	$\text{Xe}^{15+}$	774.2	–
$\text{Xe}^{8+}$	384.49	381.56	$\text{Xe}^{16+}$	835.43	–
			$\text{Xe}^{17+}$	989.47	–

**Table F.3:** Threshold energies for ground-state triple ionization of the studied  $\text{Xe}^{q+}$  ions.

Primary ion	LANL code (eV)	NIST ASD (eV)
$\text{Xe}^+$	95.81	92.94
$\text{Xe}^{6+}$	374.91	377.42
$\text{Xe}^{7+}$	489.58	487.54

**Table F.4:** Threshold energies for ground-state fourfold ionization of the studied  $\text{Xe}^{q+}$  ions.

Primary ion	LANL code (eV)	NIST ASD (eV)
$\text{Xe}^+$	149.39	147.08
$\text{Xe}^{6+}$	580.14	579.14
$\text{Xe}^{7+}$	720.76	716.56

**Table F.5:** Threshold energies for ground-state multiple-ionization of  $\text{Xe}^+$  ion.

Ionization multiplicity	LANL code (eV)	NIST ASD (eV)
Fivefold	214.72	213.78
Sixfold	305.28	305.38
Sevenfold	410.37	411.36
Eightfold	589.63	591.2
Ninefold	794.86	792.92

**Table F.6:** Threshold energies for ground-state single ionization of the studied  $\text{Sn}^{q+}$  ions.

Primary ion	LANL code (eV)	Primary ion	LANL code (eV)
$\text{Sn}^+$	14.40	$\text{Sn}^{7+}$	137.83
$\text{Sn}^{2+}$	29.36	$\text{Sn}^{8+}$	160.02
$\text{Sn}^{3+}$	40.07	$\text{Sn}^{9+}$	183.02
$\text{Sn}^{4+}$	76.51	$\text{Sn}^{10+}$	206.79
$\text{Sn}^{5+}$	96.02	$\text{Sn}^{11+}$	231.33
$\text{Sn}^{6+}$	116.48	$\text{Sn}^{12+}$	256.59
		$\text{Sn}^{13+}$	282.58

**Table F.7:** Threshold energies for ground-state double ionization of the studied  $\text{Sn}^{q+}$  ions.

Primary ion	LANL code (eV)	Primary ion	LANL code (eV)
$\text{Sn}^+$	43.76	$\text{Sn}^{7+}$	297.85
$\text{Sn}^{2+}$	69.43	$\text{Sn}^{8+}$	343.04
$\text{Sn}^{3+}$	116.58	$\text{Sn}^{9+}$	389.81
$\text{Sn}^{4+}$	173.02	$\text{Sn}^{10+}$	438.12
$\text{Sn}^{5+}$	212.5	$\text{Sn}^{11+}$	487.92
$\text{Sn}^{6+}$	254.31	$\text{Sn}^{12+}$	539.17



## **Acknowledgements**

Throughout five years of my life in graduate school in Germany I have been very fortunate to receive a tremendous amount of support from the people around me. It has been an incredible experience for me. I would like to acknowledge my friends for all they have done.

First and foremost I would like to thank my advisor, Prof. Dr. Alfred Müller, for giving me the opportunity to perform this exciting work at Institut für Atom- und Molekülphysik, for his invaluable guidance, support and patience.

I am indebted to Prof. Dr. Stefan Schippers for co-advising me throughout my thesis, as well as for his reasonable critiques and valuable and interesting discussions.

I am grateful to Mr. Heinz-Jürgen Schäfer for great all-around support regarding the experimental setup, sometimes even beyond working hours. I would also like to acknowledge Dr. Kurt Huber's assistance with regard to the data acquisition system.

I very much appreciate the assistance from Dr. Mohammad Gharaibeh, Dr. Sándor Ricz, B.Sc. Joachim Rausch, Dipl.Phys. Jan Rudolph, Dipl.Phys. Pierre-Michel Hillenbrand and B.Sc. Diego Caballero in performing long-continued measurements and repair work. I am also thankful for Dipl.Phys. Alexander Titte's, Dipl.Phys. Patrick Löffler's and Dipl.Phys. Jan Jung's guidance in laboratory during the first time.

Likewise, I also thank Dr. Eike Schmidt-Naujok, Dipl.Phys. Kristof Holste, Dipl.Phys. Dietrich Bernhardt and other present and previous members of the Institut für Atom- und Molekülphysik for their support and friendship.

I would like to give my special thanks to my family for their encouraging support and especially to my father for lots of shared experimental-work experience.

Finally, I thank all my friends in Germany and in Ukraine for supporting me during these years.

## **Erklärung**

Ich versichere, dass ich diese Arbeit selbständig geschrieben habe und keine anderen als die angegebenen Hilfsmittel verwendet habe.